Evaluation of optical biosensing techniques towards point-of-care diagnosis of active TB

Student: Charles Maphanga
(221116891)

Supervisor: Prof. Patience Mthunzi-Kufa
Co-supervisor: Dr. Yaseera Ismail
Co-supervisor: Dr. Saturnin Ombinda-Lemboumba

A thesis submitted in fulfilment of the requirement for the
degree of
Doctor of Philosophy in Physics

School of Chemistry and Physics
University of KwaZulu-Natal
South Africa

August 2024

As the candidate's supervisor, I, **Patience Mthunzi-Kufa**, agree to the submission of this dissertation.

Signed:..... ..... Date:16 August 24.....

I, **Charles Maphanga** declare that the work contained in herein has not been submitted in any form for any degree or diploma to any other institution.

Signed:. ..... Date:16 August 2024.....

Preface

The research discussed in this dissertation was carried out at the Council for Scientific and Industrial Research (CSIR) Photonics Centre's Biophotonics research group in collaboration with College of Agriculture, Engineering and Science of the University of Kwa-Zulu Natal, Durban, from January 2020 until March 2023 by Charles Maphanga under the supervision of Prof. Patience Mthunzi-Kufa and co-supervised by Dr. Yaseera Ismail, and Dr. Saturnin Ombinda-Lemboumba.

As the candidate's supervisor, I, Patience Mthunzi-Kufa, agree to the submission of this dissertation.

Signed:..... ..... Date:16 August 24.....

As the candidate's co-supervisor, I, Yaseera Ismail, agree to the submission of this dissertation.

Signed:.. ..... Date:16 August 2024.....

As the candidate's co-supervisor, I, Saturnin Ombinda-Lemboumba, agree to the submission of this dissertation.

Signed:..... ..... Date:16 August 2024.....

I, Charles Maphanga, hereby declare that all the material incorporated in this dissertation are my own original work, except where acknowledgement is made by name or in the form of a reference. The work contained in herein has not been submitted in any form for any degree or diploma to any other institution.

Signed:..... ..... Date:16 August 2024.....

Abstract

Tuberculosis (TB) remains one of the leading causes of mortality and morbidity globally even though it is a treatable disease. South Africa is one of 22 countries with a high TB burden that accounts for 83% of worldwide TB cases. Recent innovations in "near-patient" or point-of-care (POC) diagnostic technologies for TB have resulted in early treatment initiation. For instance, the roll-out of GeneXpert MTB/RIF devices in resource-limited countries has resulted in improved rapid and accurate diagnosis of TB and rifampicin resistance testing. Regardless, these devices also have limitations, for example, requirements for specialized infrastructure, operation by highly trained personnel, and high costs per test. This is a significant setback, especially in developing countries. Thus, a rapid and effective diagnosis of TB is a crucial intervention strategy for reducing the burden of TB. As a result, there is a need for a cost-effective, user-friendly, and robust POC TB diagnostic device with high sensitivity and specificity. Hence, this study focuses on the evaluation of optical biosensing techniques for the development of a POC device for TB diagnosis. Biosensors offer great advantages over conventional analytical techniques. Specifically, they can provide multiple capabilities such as user-friendly operation, real-time analysis, rapid response, high sensitivity and specificity, portability, label-free detection, and cost-effectiveness. This diagnostic approach possesses suitable features to develop POC diagnostics and monitoring technologies. A novel optical biosensor chip was developed to monitor biomolecular interactions between mycolic acid antigens and anti-*mycobacterium tuberculosis* antibodies. Mycolic acid was successfully immobilized on a gold-coated surface and a photonic crystal-based surface and allowed to react with anti-*mycobacterium tuberculosis* antibody as an analyte. The biosensor chip surface was characterized using various tests, including atomic force microscopy (AFM), scanning electron microscopy (SEM), and energy dispersive X-ray (EDX) spectroscopy. To enhance the detection signal from biomolecular binding events, gold nanoparticles (AuNPs) were bioconjugated with

goat anti-rabbit IgG H&L secondary antibody and introduced on the biosensing surface. Characterization of the AuNPs before and after bioconjugation was performed using ultraviolet-visible (UV-vis) absorption spectroscopy, dynamic light scattering (DLS), transmission electron microscopy (TEM), and further analyzed using Fourier-transform infrared (FTIR) spectroscopy. The gold-coated biosensor chip was analyzed using a custom-built nanoplasmonic biosensing setup to differentiate the experiment from control groups, and the photonic crystal-based biosensor chip was analyzed using a similar setup using a white light source. The obtained results showed that mycolic acid was successfully immobilized on the biosensing surface and made it possible to capture anti-*mycobacterium tuberculosis* antibodies. The nanoplasmonic optical biosensing technique was indeed successful in the detection of anti-*mycobacterium tuberculosis* antibodies.

Keywords: Biomarker, Biosensor, Optical biosensing, Bioconjugation, Gold nanoparticle, Localized surface plasmon resonance, Photonic crystal, Transmission spectroscopy, Fluorescence microscopy, UV-vis absorption spectroscopy, Dynamic light scattering, Fourier-transform infrared spectroscopy, Scanning electron microscopy, Energy dispersive X-ray spectroscopy, Atomic force microscopy, Mycolic acid, *Mycobacterium tuberculosis*

Dedication

This thesis is dedicated to my brother Bro Scotch.

Thank you for your unconditional love.

Your wisdom and kindness keep me going and you will always have a special place in my heart.

Through you, I have seen an angel in human form.

I love you, brother!

Declaration 1 - Plagiarism

I, **Charles Maphanga**, declare that.

1. The research reported in this thesis, except where otherwise indicated, is my original research.
2. This thesis has not been submitted for any degree or examination at any other university.
3. This thesis does not contain other persons' data, pictures, graphs or other information, unless specifically acknowledged as being sourced from other persons.
4. This thesis does not contain other persons' writing, unless specifically acknowledged as being sourced from other researchers. Where other written sources have been quoted, then:
   (a) Their words have been re-written, but the general information attributed to them has been referenced,
   (b) Where their exact words have been used, then their writing has been placed in italics and inside quotation marks and referenced.
5. This thesis does not contain text, graphics or tables copied and pasted from the Internet, unless specifically acknowledged, and the source being detailed in the thesis and in the references sections.

Signed..  .....Date.....16 August 2024.....

Declaration 2 - Publications

DETAILS OF CONTRIBUTION TO PUBLICATIONS that form part and/or include research presented in this thesis.

Peer-reviewed journals:

1. C. Maphanga, S. Manoto, S. Ombinda-lemboumba, Y. Ismail, Sensing and Bio-Sensing Research Localized surface plasmon resonance biosensing of Mycobacterium tuberculosis biomarker for TB diagnosis, Sens. Bio-Sensing Res. 39 (2023) 100545. https://doi.org/10.1016/j.sbsr.2022.100545.
2. M.A. Tjale, S. Ombinda-Lemboumba, C. Maphanga, P. Mthunzi-Kufa, TB diagnostic insights, progress made on point of care diagnostics and bioinformatics as an additional tool for improvement, Indian J. Tuberc. (2023). https://doi.org/10.1016/j.ijtb.2023.03.023.

Other peer-reviewed journals published during PhD study:

1. C. Maphanga, S. Manoto, C. Mabena, S. Ombinda-Lemboumba, M. Maaza, P. Mthunzi-Kufa, Laser-enabled delivery of antiretroviral drugs into HIV-1 infected TZM-bl cells, J. Biophotonics. 15 (2022) 1–11. https://doi.org/10.1002/jbio.202200043.

Peer-reviewed conference proceedings:

1. Charles Maphanga, Saturnin Ombinda-Lemboumba, Yaseera Ismail, Patience Mthunzi-Kufa, Photonic crystal-based biosensing for TB detection, South African Institute of Physics (SAIP) Proceeding (2023) (In Press). https://events.saip.org.za/event/239/papers/9027/

2. C.P. Maphanga, S.L. Manoto, S.S. Ombinda-Lemboumba, Y. Ismail, P.T. Mthunzi-Kufa, Optical biosensing of mycolic acid biomarker for TB diagnosis, Proc. SPIE 12387, Opt.

Diagnostics Sens. XXIII Towar. Point-of-Care Diagnostics. (2023) 25. https://doi.org/10.1117/12.2650013.

3. C.P. Maphanga, S.S. Ombinda-Lemboumba, Y. Ismail, P.T. Mthunzi-Kufa, Photonic crystal-based biosensor chip development for TB diagnosis, Proc. SPIE 12387, Opt. Diagnostics Sens. XXIII Towar. Point-of-Care Diagnostics. (2023) 33. https://doi.org/10.1117/12.2650057.

4. Charles Maphanga, Saturnin Ombinda-Lemboumba, Sello Manoto, Patience Mthunzi-Kufa, "Surface plasmon resonance (SPR) based biosensor for mycobacterium tuberculosis diagnosis," Proc. SPIE 11651, Optical Diagnostics and Sensing XXI: Toward Point-of-Care Diagnostics, 1165103 (5 March 2021); doi: 10.1117/12.2578728

5. Charles Maphanga, Sello Manoto, Saturnin Ombinda-Lemboumba, Patience Mthunzi-Kufa, "Detection of mycobacterium tuberculosis using gold nanoparticles conjugated to TB antibodies," Proc. SPIE 11651, Optical Diagnostics and Sensing XXI: Toward Point-of-Care Diagnostics, 116510X (5 March 2021); doi: 10.1117/12.2578789

6. M. Y. Lugongolo, S. L. Manoto, C. Maphanga, S. Ombinda-Lemboumba, S. L. Thobakgale, P. Mthunzi-Kufa, "Label-free detection of mutations in the HIV genome using a surface plasmon resonance biosensor," Proc. SPIE 11661, Plasmonics in Biology and Medicine XVIII, 116610M (5 March 2021); doi: 10.1117/12.2578317

7. Charles Maphanga, Sello Manoto, Saturnin Ombinda-Lemboumba, Lerato Hlekelele, Patience Mthunzi-Kufa, "Optical biosensing of mycobacterium tuberculosis for point-of-care diagnosis," Proc. SPIE 11251, Label-free Biomedical Imaging and Sensing (LBIS) 2020, 112510R (20 February 2020); doi: 10.1117/12.2545842

8. Saturnin Ombinda-Lemboumba, Sello Manoto, Charles Maphanga, Rudzani Malabi, Patience Mthunzi-Kufa, "Development of collinear transmission plasmonic biosensor for detection of HIV-1," Proc. SPIE 11257, Plasmonics in Biology and Medicine XVII, 112570L

(21 February 2020); doi: 10.1117/12.2546496

9. Saturnin Ombinda-Lemboumba, Sello Manoto, Charles Maphanga, Rudzani Malabi, Lebogang Thobakgale, Masixole Y. Lugongolo, Patience MthunziKufa, "Raman spectroscopy and gold thin film for biosensing and detection," Proc. SPIE 11251, Label-free Biomedical Imaging and Sensing (LBIS) 2020, 112512P (20 February 2020); doi: 10.1117/12.2546617

Signed.  .....Date.....16 August 2024.....

Achievements:

1. July 2022: Best Oral Presentation by PhD student, Council for Scientific and Industrial Research (CSIR), Emerging Researchers Symposium.

2. December 2021: Biggest Impact Research by PhD student, University of KwaZulu-Natal, College of Agriculture, Engineering and Science, School of Chemistry and Physics, UKZN Postgraduate Research and Innovation Symposium.

3. June 2019: Mail&Guardian 200 Young South Africans (Health Category)

4. December 2017: Best masters' studentship, National Laser Centre (NLC) excellence awards, Council for Scientific and Industrial Research (CSIR), Pretoria, South Africa.

Acknowledgements

First and foremost, I would like to thank GOD for the wisdom, grace, and strength that has carried me throughout my studies. I am truly grateful to my supervisor Prof. Patience Mthunzi-Kufa for giving me a chance to pursue a PhD degree within the Biophotonics research group of the CSIR's Photonics Centre. It has been a great journey from MSc to PhD. I am very thankful to my co-supervisors Dr. Saturnin Ombinda Lemboumba and Dr. Yaseera Ismail for their guidance and support. Thank you all for the opportunities you exposed me to during my studies. I am so grateful to the Biophotonics research team for their continued support. You guys rock! To the staff at the UKZN School of Chemistry and Physics, thank you very much. To my family, I am still standing today, and it is because of your support, especially my brother Bro Scotch, I love you so much. To my nephews and nieces, I appreciate how you are so proud of me, and I wish the Almighty blesses you in your respective life journeys. To everyone in my circle, thank you for listening, encouraging, and believing in me. I thank the CSIR, NRF, and the DSI for the financial support. And lastly, I would like to say, "I love you so much" to my late mom Makhapa Rebecca Pebetsi Nkoshana Moela. You will always live in my heart "kgarebe ya Bakwena ba Moela meetse a pula".

List of Acronyms

1-dimensional	1-D
1-Ethyl-3-(3-dimethylaminopropyl)-carbodiimide	EDC
2019 coronavirus disease	COVID-19
3-Aminopropyl triethoxysilane	APTES
Acid-fast bacilli	AFB
Acquired immunodeficiency syndrome	AIDS
Aluminium	Al
Amikacin	AMK
Antigen85	Ag85
Arabinogalactan	AG
Atomic force microscopy	AFM
Bacillus Calmette-Guerin	BCG
Backward inner primer	BIP
Backward loop primer	BLP
Base pair	bp
Biosafety level	BSL
Bovine serum albumin	BSA
Calcium	Ca
Capreomycin	CPR
Centimeter	cm
Centipoise	cP
Charge-coupled device	CCD
Ciprofloxacin	CPFX
Cluster of differentiation 4	CD4

Colony forming unit	CFU
Culture filtrate protein	CFP
Cycloserine	CYS
Cysteamine	Cys
Deoxyribonucleic acid	DNA
Drug sensitivity test	DST
Dynamic light scattering	DLS
Early secreted antigen target	ESAT
Electromagnetic wave	EMW
Energy-dispersive X-ray	EDX
Enzyme-linked immunosorbent assay	ELISA
Ethambutol	EMB
Ethionamide	ETA
Extensively drug-resistant	XDR
Extrapulmonary TB	EPTB
Fluorescent microscopy	FM
Forward inner primer	FIP
Forward loop primer	FLP
Fourier-transform infrared	FTIR
Gas chromatography	GC
Genomic DNA	gDNA
Gold	Au
Gold nanoparticle	AuNP
High-resolution transmission electron microscope	HRTEM
Human immunodeficiency virus	HIV
Isoniazid	INH

Kanamycin	KM
Kilohertz	kHz
Kilojoule	kJ
Kilovolt	KV
Light-emitting diode	LED
Limit of detection	LOD
Line probe assay	LPA
Lipoarabinomannan	LAM
Lipomannan	LM
Localized surface plasmon resonance	LSPR
Loop-mediated isothermal amplification	LAMP
Lowenstein-Jensen	LJ
Magnesium	Mg
Mass spectrometry	MS
Mercury vapour lamp	MVP
Methyl nicotinate	MN
Methyl *p*-anisate	MP
Methyl phenylacetate	MPA
Meter	m
Milligram	mg
Millilitre	ml
Milliwatt	mW
Micrometer	μm
Multidrug resistant	MDR
Mutant	MUT
Mycobacterial growth indicator tube	MGIT

Mycobacterium tuberculosis complex	MTBC
Mycobacterium tuberculosis	MTB
Mycolic acid	MA
Mycolyl-arabinogalactan-peptidoglycan	mAGP
Nanometer	nm
N-hydroxysuccinimide	NHS
Nucleic acid amplification test	NAAT
o-phenylanisole	OPA
Outer backward primer	B3
Outer forward primer	F3
Palladium	Pd
para-Aminosalicylic acid	PAS
Peptidoglycan	PG
Phosphate buffered saline	PBS
Photonic band gap	PBG
Photonic crystal	PhC
Physical vapour deposition	PVD
Platinum	Pt
Point-of-care	POC
Polyethylene glycol	PEG
Polymerase chain reaction	PCR
Pulmonary TB	PTB
Pyrazinamide	PZA
Refractive Index Unit	RIU
Rifampicin	RIF
Scanning electron microscopy	SEM

Second-line injectable drug	SLID
Self-assembled monolayer	SAM
Silver	Ag
Sputum smear microscopy	SSM
Stearic acid	STA
Surface plasmon resonance	SPR
Titanium	Ti
Transmission electron microscopy	TEM
Transrenal DNA	Tr-DNA
Tuberculin skin test	TST
Tuberculosis	TB
Ultra-violet visible	UV-vis
Volatile organic compound	VOC
Wild-type	WT
World Health Organization	WHO
Ziehl-Neelsen	ZN

List of Figures

TABLE OF CONTENTS

INTRODUCTION

i. Background and motivation

Tuberculosis (TB) is a contagious disease and one of the world's deadliest infectious diseases caused by the *Mycobacterium tuberculosis* (MTB) pathogen [1,2]. It is an airborne bacillus and can spread through microscopic droplets or particles called droplet nuclei generated when a person with untreated active pulmonary tuberculosis (PTB) coughs, sneezes, talks, or sings [3,4]. People who become infected with TB have approximately a 10% risk of developing active TB during their lives, with greater risk in the first two years after infection and much greater risk in HIV-co-infected individuals [5]. The infection usually lasts throughout life as a latent infection in more than 90% of infected individuals [6]. MTB typically affects the lungs as PTB; however, it can also occur in other organs of the body as extrapulmonary TB (EPTB) infection [1,6–8]. When TB infection occurs in combination with other serious infections, such as human immunodeficiency virus (HIV), it can severely compromise the host immune system and complicate effective forms of therapy [6].

TB infections remain a major public health problem worldwide, especially in developing and some industrialized countries, associated with high morbidity and mortality rates. According to the World Health Organization (WHO), despite the availability of treatment that is curative in about ninety percent of detected cases, approximately one-third of the world's population is affected by TB, and new infections occur in about one percent of the population each year [9]. About one-third of TB cases are undetected, and these cases pose serious hurdles for TB control. Therefore, early, rapid, and accurate TB diagnosis is essential in lowering the global burden of the disease [10,11]. The estimated incidence of TB infections remains high in both Asia and Africa, and sub-Saharan Africa has the highest estimated TB incidence [12]. The notable high rate of TB in sub-Saharan Africa is influenced by a high prevalence of HIV infections [12].

Despite a slow decline in global TB rates, the progress in closing detection/diagnosis and treatment gaps is notably slow, particularly in Africa [12]. Regardless of the improvements in TB control programs, active disease cases in many regions remain at unacceptable levels [13]. Advances in TB diagnosis in recent years have contributed to increased survival rates; however, there are still reported limitations associated with early diagnosis [14].

Currently, the WHO has endorsed several TB diagnostic methods for TB diagnosis. These include light-emitting diode (LED) fluorescence microscopy, TB culture using the BACTEC MGIT960 instrument, urine lipoarabinomannan (LAM) assay, and various nucleic acid amplification tests (NAATs) for TB detection and drug sensitivity testing (DST) [13–15]. There are also commonly used indirect immunological screening methods which include tuberculin skin test (TST) and interferon gamma release assays; however not endorsed by the WHO but are commonly used to screen for TB exposure in developed countries [13]. However, some of these tests are expensive, require specialized infrastructure, sophisticated equipment, and trained personnel, and thus hinder TB diagnosis, particularly in resource-limited settings [14].

For these reasons, the WHO recognizes the need for new and more sensitive and specific techniques to improve early TB diagnosis, such as the use of point-of-care (POC) devices [16]. Herein, a custom-designed optical biosensor chip was developed and analyzed using a custom-built optical biosensing transmission spectroscopy platform. For biosensor chip analysis, localized surface plasmon resonance (LSPR) biosensing and photonic crystal (PhC) biosensing are applied toward the development of a point-of-care TB diagnostic device platform. The LSPR method, over other label-free biosensing techniques, offers the advantage of obtaining results in real-time, is robust, precise, and has high sensitivity [16,17]. In biosensing, LSPR sensors can monitor a variety of binding events, including protein-ligand interaction, deoxyribonucleic acid (DNA) hybridization, and biomarker interaction [18]. Like other optical biosensors, PhC-based

biosensors have also been utilized as label-free biosensors for various biomolecular assays. They can detect biomolecular interactions on the surface of a transducer [19]. In contrast to other optical detection techniques, which measure layer thickness for detection, PhC biosensing is primarily based on refractive index change induced by the adsorption of biomolecules and allows direct measurement of the binding affinities and binding kinetics to characterize biomolecular interactions in real-time [19–23]. With variations in refractive index on the biosensing surface, the resonant wavelength shifts. This resonant wavelength shift is preferred in biosensing as an indication and measure of sensitivity, which forms the basis of detection in label-free PhC-based biosensing [22].

The diagnostic approach applied in this study aims to use a TB pathogen-specific biomarker immobilized on a biosensor chip to detect anti-*mycobacterium tuberculosis* antibodies. To functionalize the biosensor chip, mycolic acid TB antigen was immobilized on a gold-coated and PhC biosensing surface of the chip as the biorecognition element to react with the anti-*mycobacterium tuberculosis* antibody as the analyte of interest. To enhance the detection signal on the biosensing surface, gold nanoparticles (AuNPs) were covalently conjugated with a secondary antibody, also called signal antibody, and subsequently introduced on the biosensing surface. The AuNPs were further optimized for changes in refractive index before and after bioconjugation using ultraviolet-visible (UV-vis) absorption spectroscopy and for changes in hydrodynamic size using dynamic light scattering (DLS). The biosensing surface was characterized using scanning electron microscopy (SEM), energy-dispersive X-ray (EDX) spectroscopy, and atomic force microscopy (AFM). The optimized biosensor chip was further analyzed using the custom-built optical biosensing setup to perform nanoplasmonic biosensing, and the acquired data were analyzed using OriginPro software. The obtained spectra of the reference, control, and experiment samples were interpreted for the detection of the anti-*mycobacterium tuberculosis* antibody.

ii. Research aims and objectives:

The proposed research study aims to evaluate two optical biosensing techniques for detecting anti-*mycobacterium tuberculosis* antibodies.

The objectives of this study are:

i. Design and development of a custom-built optical biosensing setup.
ii. Development of a novel biosensor chip for the detection of anti-*mycobacterium tuberculosis* antibodies.
iii. Evaluation of a localized surface plasmon resonance optical biosensor for the detection of anti-*mycobacterium tuberculosis* antibody.
iv. Evaluation of a Photonic crystal-based optical biosensor for the detection of anti-*mycobacterium tuberculosis* antibody.

iii. Synopsis of the thesis

This thesis contains five chapters. **Chapter 1** gives an overview of *Mycobacterium tuberculosis* as the causative agent for TB and its microscopic structural arrangement focusing on the cell envelope. It continues to provide the state of TB epidemiology, the various types of TB biomarkers, and the current WHO-endorsed TB diagnostic methods. Since this study focuses on optical biosensing techniques, this chapter provides a detailed summary of biosensors, transducer methods, applications of optical biosensors in diagnostics, and the role of LSPR and PhC biosensing in diagnostics.

Chapter 2 primarily focuses on research study preparations. It particularly focuses on biosensing surface coating for LSPR biosensor chips and characterization of the coated surface. Fluorescence microscopy is introduced for a proof-of-concept experiment between the biorecognition element and the analyte of interest to test for reactivity or binding. It also provides an overview of the design and development of a custom-built optical biosensing detection setup. Additionally, various protocols are optimized in this chapter, including optimization of the bioconjugation method protocol, preparation of the microscope glass surface protocol, which is also used for PhC surface functionalization, and, lastly, optimization of the gold-coated surface protocol.

Chapter 3 provides an overview of how the optimized protocols are applied to perform LSPR biosensing of anti-*mycobacterium tuberculosis* antibodies. In this chapter, various characterization techniques are used to perform the characterization of AuNPs before and after bioconjugation. The biosensing surface is also characterized using various techniques before LSPR biosensing is performed.

Chapter 4 focuses on the application of a PhC-based optical biosensing platform for the detection of anti-*mycobacterium tuberculosis* antibodies using optimized protocols from Chapter 2 and characterization techniques from Chapter 3. In this chapter, a white light source was used instead of the green light source used in Chapter 3. The 1-dimensional (1-D) PhCs used in this chapter are detected at a resonance wavelength between 636 – 651 nanometers (nm) range, hence the use of white light.

Lastly, **Chapter 5** summarizes the contents of the thesis while putting special emphasis on the significance of optical biosensing platforms in the detection of biomolecules and their potential for the future development of POC diagnostic devices.

CHAPTER 1:

LITERATURE REVIEW

This chapter provides an overview of the discovery of *Mycobacterium tuberculosis* as a causative agent for TB. The pathogenesis, clinical symptoms, transmission, and global epidemiology of TB infection, focusing primarily on active TB. The current TB diagnostic platforms endorsed by the WHO, with their advantages and limitations, are explored. This chapter also investigates the discovery and significance of TB biomarkers used in diagnostics and their potential applications in the development of POC diagnostic devices, emphasizing mycolic acid as a recommended biomarker for TB diagnosis. Furthermore, optical biosensors, mainly LSPR and PhC-based optical biosensing platforms, are presented as potential optical detection techniques for the possible development of a POC TB diagnostic device.

1.1. Introduction to TB

1.1.1. TB as a global pandemic

TB is an airborne infection caused by *Mycobacterium tuberculosis.* Until the 2019 coronavirus disease (COVID-19) pandemic, TB was the leading cause of death from a single infectious agent, ranking above HIV, acquired immunodeficiency syndrome (HIV/AIDS) [24]. TB primarily affects the lungs as pulmonary TB and constitutes about 80% of total TB cases [13,25]. TB can affect other sites of the body and is referred to as extrapulmonary TB. It can affect the bones, joints, meninges, lymph nodes, kidneys, intestines, and the skin [13]. Approximately one in four people worldwide demonstrate an immunological response to MTB infection, which can remain dormant (TB infection) or later progress into active TB disease. Patients with TB infection may present with no signs or symptoms of TB disease and have a 5-10% lifetime risk of developing TB disease, which increases in varying states of immunodeficiency up to 16%

annual risk in HIV patients [26]. According to the global report released by the WHO in 2022, there were an estimated 1.4 million deaths among HIV-negative people and 187 000 deaths among HIV-positive people in 2021, for a combined total of 1.6 million. This represents an increase from 1.5 million in 2020 and 1.4 million in 2019. This reported increase in TB mortality has been severely impacted by the COVID-19 pandemic [24]. South Africa is counted among the high TB-burden countries [27]. In 2021, approximately 2.5 million people in Africa contracted TB, resulting in about 500 000 deaths [28]. The estimated number of deaths in 2021 in the Democratic Republic of Congo, Nigeria, and South Africa accounted for 48% of all TB deaths in the African continent [28]. The high prevalence of HIV in Africa is directly reflected in the 20% of new TB cases reported among people living with HIV and AIDS [28]. Drug-resistant TB is also an increasing concern in the management of TB, with 450 000 cases of rifampicin-resistant TB and 77 000 cases of multi-drug-resistant TB reported. Of these, 53% of cases are reported from Nigeria and South Africa [28].

1.1.2. Mycobacterium tuberculosis discovery

Mycobacterium tuberculosis pathogen belongs to the *Actinomycetales* order, *Actinomycetes* class, *Mycobacteriaceae* family, and in the genus *Mycobacterium* which comprises more than 170 species which are environmental organisms [29,30]. On the evening of 24 March 1882, German doctor Robert Koch made a presentation to the Berlin Physiological Society and announced that he had successfully identified the tubercle bacillus [31]. After centuries of speculations and uncertainty as to the possible direct cause of TB, Koch, in his presentation, proved conclusively from his findings that the cause of the disease was a microorganism that he successfully isolated and cultured [32]. To achieve this discovery, Koch and his research team stained the *Mycobacterium tuberculosis* to determine the presence of unique or foreign parasitic structures indicative of the pathogen. Koch developed the staining methods for *Mycobacterium tuberculosis* used to date as an improvement of previously used stains which were unsuccessful

in the detection of this pathogen [33]. Koch reported using the new staining methods that the tubercle bacteria are rod-shaped microorganisms when observed under the microscope. He embarked on his second innovation by isolating the bacilli in pure solid culture instead of the liquid broths used at that time. He used heat-sterilized solidified cow or sheep serum, poured and solidified in slanted tubes for a larger surface area for inoculation [33]. After inoculation, tubes were incubated at 37 – 38 °C, and growing colonies were detected by the naked eye over a few days. Koch further demonstrated the mode of transmission of the illness in animal studies and based on his understanding of the spread of the disease, recommended the isolation of patients with TB. Koch was awarded a Nobel Prize of Medicine in 1905 for his inventions and discoveries about TB and gained a global reputation in the scientific community to date [33,34].

1.1.3. Structure of Mycobacterium tuberculosis

A mycobacteria cell typically measures 0.5 – 3 µm and is classified as an acid-fast gram-positive bacterium with a unique cell wall structure essential to its survival [4,35]. The cell envelope consists of a plasma membrane (PM), periplasm, cell wall, and the outermost layer capsule only present in pathogenic mycobacteria species (Figure 1). Additionally, the cell envelope constituents are involved in adhesion, motility, cell division, and the cellular transport mechanism of solutes, ions, and proteins [36]. The bacterial cell wall, defined as the structure that surrounds the cytosol, is of great research interest and imperative for the pathogen's physiology because various crucial biological processes take place in this compartment. It specifically contributes to the microorganism's shape, and mechanical resistance and forms protection against hostile environments [36]. It forms a barrier responsible for resistance against antibiotics and hosts defense mechanisms [4]. The mycobacteria cell wall is a complex constituted of a 7 – 8 nm thick outer membrane (also called mycomembrane) like that of the plasma membrane, arabinogalactan (AG), and peptidoglycan (PG). The composition of the cell wall of mycobacteria and related genera differs from those of other Gram-positive and Gram-

negative bacteria significantly. The cell wall is key to the survival of mycobacteria, and its various components interfere with the host defense pathways to establish its survival within phagosomes [4,35]. The peptidaglycan is just external to the plasma membrane, responsible for cell wall rigidity, and also a contributing structure to the permeability barrier of mycobacteria [4]. Mycolic acids form the inner leaflet of the mycomembrane, covalently attached to AG, which is covalently linked to PG and forming a complex polymer called A1γ representing mycolyl-arabinogalactan-peptidoglycan (mAGP) formerly known as the cell wall skeleton [36]. Mycobacterial cell wall is composed of over 60% of lipids. The lipid content of MTB comprises three major components, namely mycolic acid, cord factor, and wax-D [35]. These lipids are species-specific and, therefore, can be used as biomarkers to detect mycobacterial infections and to determine the species responsible for the infections. Of interest, mycolic acids are unique alpha-, keto-, and methoxy-branched lipids present in the cell wall of *Mycobacterium* and *Corynebacterium*. Their hydrophobic nature allows them to act as primary permeability determinants of the mycobacterial cell wall and are also considered to be important virulence factors of *Mycobacterium tuberculosis* [35].

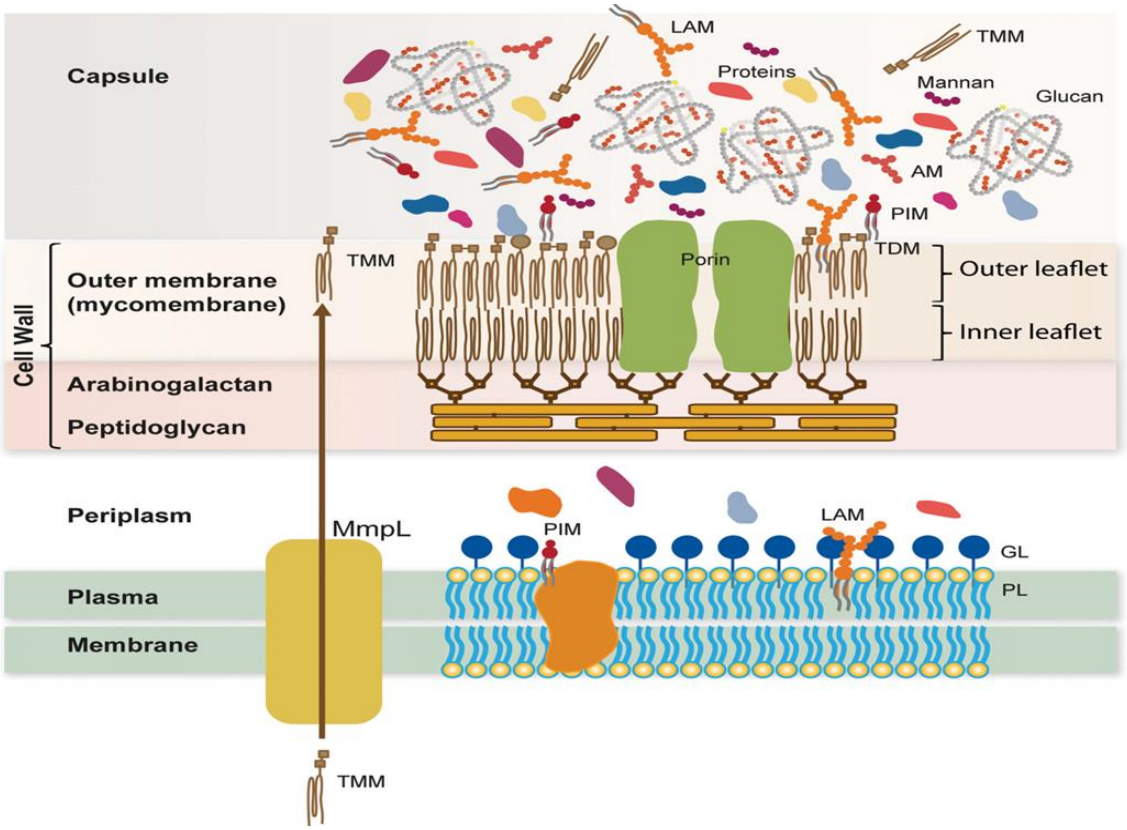

Figure 1: Model of the mycobacterial cell envelope [37]. The cell envelope consists of a phospholipid bilayer plasma membrane, periplasmic space, cell wall, and the outermost capsule responsible for the pathogen's virulence. The periplasm consists of a granular layer. The cell wall is formed by peptidoglycan, arabinogalactan, and mycolic acid residues. The capsule is composed of proteins, lipopolysaccharides, and some lipids. (TMM: Trehalose monomycolate, PL: Phospholipid, GL: Granular layer, LAM: Lipoarabinomannan, PIM: Phosphatidyl inositol mannose, MmpL: Mycobacterial membrane protein large, TDM: Trehalose dimycolate, AM: Arabinomannan).

The abundance of mycolic acids in the cell wall thus forms a barrier responsible for most of the medically challenging physiological characteristics of TB, including resistance to antibiotics and host immune responses [4,38]. The mycobacteria plasma membrane is formed by a phospholipid bilayer. It acts as a separation barrier between the inner cytosol of the bacterial cell and the periplasmic space located between the plasma membrane and the peptidoglycan layer [36,39]. It consists of phospholipids and proteins specific to the cell's metabolic functions. Additionally, it acts as the active site for the cell's anabolic and catabolic functioning, responsible for allowing essential nutrients to flow into the cell [36,39].

This bilayer structure is like that of other Gram-positive and Gram-negative mycobacteria. It consists of diphosphatidylglycerol, phosphatidylethanolamine, phosphatidylinositol, and phosphatidylmannoside family (PIMs) as the main phospholipids (Figure 1) [39]. These lipids contribute to the integrity of the membrane and have significant physiological functions [36]. LAM and lipomannan (LM) lipopolysaccharides are found in the outer leaflet of the PM. LAM is a carbohydrate structural antigen also present in the capsular layer. It is immunogenic and facilitates the survival of the pathogen within infected macrophages [4].

Several transmembrane proteins, such as mycobacterial membrane protein large (MmpL), are also present in the plasma membrane and are involved in the transport of various lipids across the membrane [36]. The outermost capsular layer is a matrix of proteins as the main components, (lipo)polysaccharides, and rarely present small amounts of lipids [36]. Several studies have also demonstrated that the outermost capsular layer of the mycobacterial cell envelope plays a role in TB pathogenesis and modulates the uptake of the pathogen by lung cells [40]. The mycobacteria cell envelope structure is of great research interest since it consists of significant immunogenic components that can be used as biomarkers to develop TB diagnostic assays.

1.1.4. Mycobacterium tuberculosis transmission

Mycobacterium tuberculosis bacilli can be transmitted as droplet nuclei that are residues of dried respiratory droplets (Figure 2). The droplet nuclei are small airborne particles that contain 1 – 10 TB bacilli of 1 – 5 µm in diameter expectorated by individuals with active pulmonary TB, typically when the person coughs [5,41]. Other reported effective aerosol-generating activities include sneezing, talking, and singing [4,42–45]. Due to their small size, the droplet nuclei can remain suspended in the air for several minutes (min) to hours [5]. On the other hand, respiratory droplets that are greater than 100 µm will fall to the ground within 1 meter (m) from the source and will be deposited in the upper airway [41].

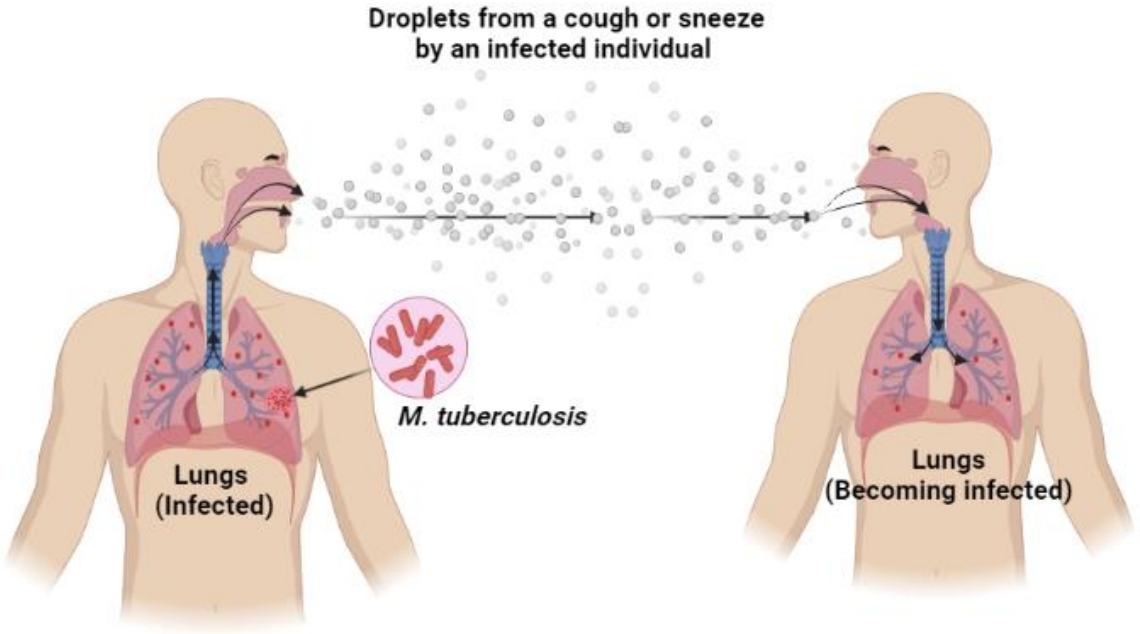

Figure 2: Illustration of how *Mycobacterium tuberculosis* spreads through the air from one person to another. Droplet nuclei are released from an infected person with TB disease through coughing, speaking, or singing. After inhalation of *Mycobacterium tuberculosis* by an uninfected person, the bacilli settle throughout the airways, and infection is initiated.

Respiratory secretions surrounding droplet nuclei protect the TB bacilli from UV light, dehydration, oxygen injury, and other potential environmental stresses [41]. Transmission or the risk of infection is influenced by several factors, such as the number of bacilli in the droplet, the bacillary load inhaled, the degree of exposure, exposure of the bacilli to natural irradiation, the degree of virulence of the bacteria, poor ventilation, and the immune status of the potential host [4,5,46].

1.1.5. TB pathogenesis

The primary route of infection involves the lungs in most TB cases. After inhalation of *Mycobacterium tuberculosis* within aerosols of droplet nuclei, the bacilli settle throughout the airways [4]. Typically, the bacilli are trapped in the upper, containing mucus-secreting goblet cells. In the upper airway or oropharynx, *Mycobacterium tuberculosis* can potentially cause TB

of the oropharynx or cervical lymph nodes [47]. The mucus produced by goblet cells traps foreign bodies, and the cilia on the surface of goblet cells continuously beat the mucus and its entrapped particles upward for removal [4]. This mucociliary system is the host's initial defense against invading foreign bodies and potentially prevents infection in most TB-exposed individuals. The bacilli that bypass the mucociliary system and reach distant segments of the bronchoalveolar tree, particularly in the lower lobes of the lungs, are phagocytosed by alveolar macrophages (the most abundant immune effector cells present in alveolar spaces) as the first line of defense or innate immune response that most often can kill the invading bacteria [4,46,48–50].

Macrophages are phagocytic cells that destroy most pathogens, requiring no previous exposure to the microorganism [4]. Within macrophages, *Mycobacterium tuberculosis* resides primarily inside phagosomes [51]. Several mechanisms (e.g., the complement system) and macrophage receptors are involved in phagocytosis of this pathogen. The outcome of bacterial control at this level is essentially determined by the quality of host defenses and the balance between the host defense mechanism and the virulence of the invading mycobacteria. Should the bacilli escape the first line of defense, it starts actively replicating in macrophages and diffuses to nearby cells, including epithelial and endothelial cells [49]. Within a few weeks of exponential growth, a high bacterial burden is established to fully elicit the cell-mediated immune response, which can be detected by a tuberculin skin test. During these early stages of infection, the pathogen can diffuse to other organs through lymphatic and hematogenous dissemination affecting multiple organs, which may eventually result in extrapulmonary TB disease [46,49]. For individuals with intact cell-mediated immunity, local pro-inflammatory responses lead to the recruitment of additional neutrophils, T-lymphocytes, and other immune cells (e.g. dendritic cells), which in turn assemble around infected macrophages to contain MTB within an organized cellular structure known as a granuloma (nodular-type lesion) (Figure 3) [4,49,52].

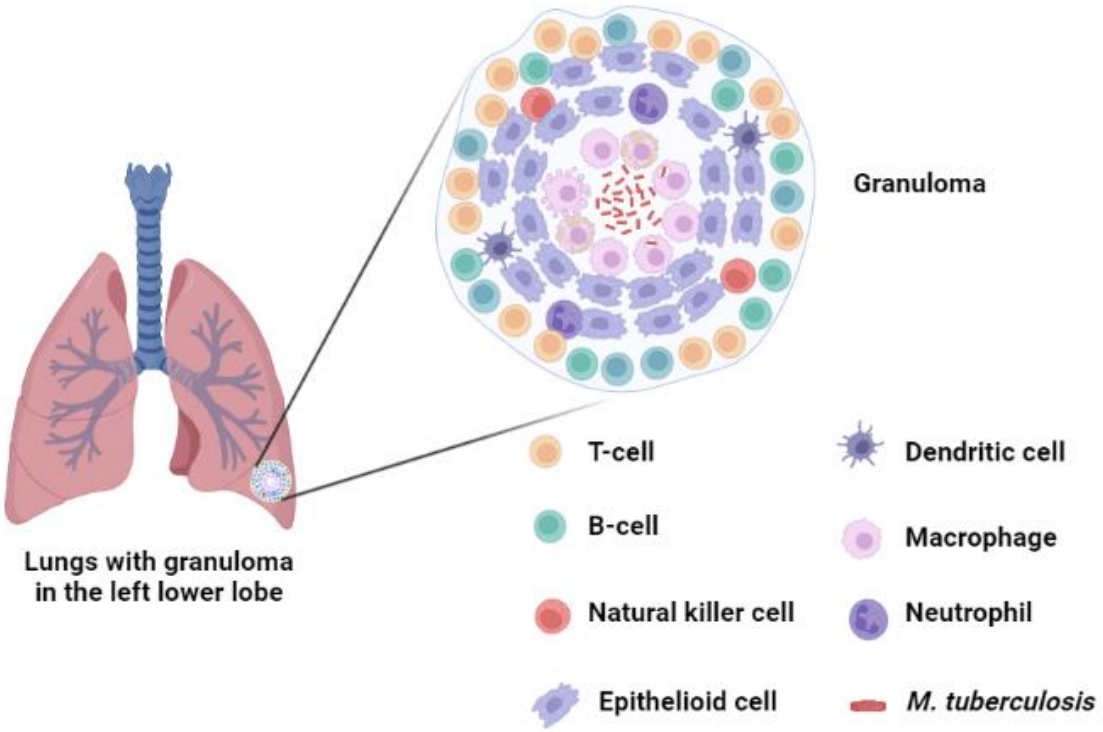

Figure 3: An illustration of how a granuloma is formed. The granuloma is formed by various immune cells, thus creating a microenvironment that slows down the replication and spread of MTB. This environment destroys infected macrophages and produces early solid necrosis at the center of the lesion; however, the bacilli can adapt and survive. When the immune system is compromised, the wall of the granuloma loses integrity, and the bacilli can escape and spread.

The granuloma creates a microenvironment that limits replication and the spread of MTB. This environment destroys the infected macrophages and produces early solid necrosis at the center of the lesion; however, the bacilli can adapt and survive. Over time (by two to three weeks), the necrotic environment resembles soft cheese, commonly referred to as caseous necrosis, and is characterized by low oxygen levels, low pH, and limited nutrients. Subsequently, these conditions restrict further growth, establish latency, and MTB persists in a prolonged state of slowed replication in immunocompetent individuals [4,52]. In the majority of individuals, the disease stays dormant indefinitely; however, a defect in cell-mediated immunity in weaker immune systems may result in reactivation [5]. When the immune system is compromised, the wall of the granuloma loses integrity, and the bacilli can escape and spread [4]. Persons at risk

for reactivation include end-stage renal disease patients, silicosis (prevalent in mine workers due to exposure to silica dust), HIV-infected individuals, the elderly, patients with diabetes, prisoners (due to poor ventilation), illicit-drug users, homeless individuals, malnutrition patients, healthcare workers, and medical students [9,46]. These risk groups populations should be prioritized in the primary healthcare system for clinical management of latent TB to prevent reactivation and many individuals with active disease.

1.1.6. Signs and symptoms

A large percentage of individuals are latently infected and have no clinical signs of TB. Pulmonary TB typically develops slowly with no precise date of onset. Unless the disease is far advanced, symptoms are very minimal and often attributed to other cases such as excessive smoking, pregnancy, and other conditions [45,53]. The frequency and severity of symptoms may differ according to whether the patient has primary TB or reactivation. Patients with primary TB infection present with minimal symptoms and, in other cases, may be asymptomatic. Symptoms and signs of active pulmonary TB include cough (commonly hemoptysis), and fever, which develop in the evening and may lead to classic "night sweats" and loss of appetite resulting in weight loss, wasting, fatigue, and dyspnea [13,53,54]. Patients with a full spectrum of symptoms are rare in developed countries, and commonly found in developing countries, typically among very poor people and those who are severely malnourished and HIV-positive [54]. Hence TB is referred to as the disease of the poor.

1.1.7. TB prevention through vaccination

In high-prevalence countries especially developing countries, the WHO and the International Union Against Tuberculosis and Lung Disease still recommend the neonatal Bacillus Calmette-Guerin (BCG), pending the development of a more effective vaccine [54]. The BCG, an attenuated strain of *Mycobacterium bovis* (*M. bovis*), remains the only licensed vaccine against

TB. Vaccination with BCG can provide protection, especially from severe forms of TB in children, but has variable efficiency in preventing pulmonary disease in children and adults [24,25]. BCG vaccination in children provided protection against severe forms of TB, especially against the deadly TB meningitis and disseminated TB [54].

1.1.8. TB treatment

Treatment of TB is a challenging task for both the healthcare system and the patient. It requires the administration of multiple antibiotics over an extended period. The administration of multiple antibiotics in treating active TB, as opposed to treatment with one antibiotic in latent TB treatment, is implemented to reduce the risk of drug resistance [9]. Treatment with antibiotics is the most effective regimen against actively replicating MTB. Treatment challenges originate from the uncommon structural and chemical composition of the MTB cell envelope described in section 1.1.3, which hinders the entry of drugs and subsequently complicates treatment. TB is treated over six months. A combination of first-line anti-TB drugs, which include isoniazid (INH), rifampicin (RIF), pyrazinamide (PZA), and ethambutol (EMB) is administered for the first two months, followed by a continuation phase treatment with INH and RIF for four months [9]. Mycolic acid synthesis inhibition is one of the primary effects of INH [37]. Of note, RIF reduces the efficacy of oral contraceptives and may result in unplanned pregnancies and EMB should not be given to children younger than eight years. In the case of laboratory-diagnosed multidrug-resistant TB (MDR-TB) and extensively drug-resistant TB (XDR-TB), second-line anti-TB drugs are administered. The second-line anti-TB drugs may be less effective than the first-line anti-TB drugs; hence they are administered over a period longer than six months. Additionally, they may have toxic side effects (e.g. cycloserine) and may be unavailable in most developing countries [9]. The second-line anti-TB drugs include amikacin (AMK), kanamycin (KM), para-Aminosalicylic acid (PAS) (also known as 4-Aminosalicylic acid), cycloserine (CYS), ethionamide (ETA), capreomycin (CPR), and ciprofloxacin (CPFX) [9].

1.2. Biomarkers of active TB infection

1.2.1. Breath biomarkers

Volatile organic compounds (VOC) metabolites

The detection of MTB-specific VOCs for early diagnosis of TB has been a topic of research interest recently [55]. During infection, specific VOC metabolites are released by the host (in response to microbial infection) or pathogen and can be qualitatively detected or quantitatively measured to provide information on the disease and its prognosis [56]. This can be used to determine the physiological reflection of host-pathogen interaction during infection or treatment. It is believed that VOCs are transported from various organs via blood to the lungs and subsequently excreted from the lungs by diffusing across the pulmonary alveolar membrane and exhaled via breath [57]. VOCs represent a wide range of stable chemicals that are volatile at ambient temperature and can be detected in exhaled breath, sweat, urine, and stool specimens [57]. Although VOCs are detectable in different specimens, an exhaled breath sample is recommended for the diagnosis of pulmonary TB [56,58,59]. Exhaled breath is considered a lung-derived biological specimen, easy to collect, non-invasive, and therefore an ideal sample for TB diagnosis in children and critically ill patients [56]. Four VOCs produced exclusively by the metabolism of *M. tuberculosis* and *M. bovis*, that have not been associated with nontuberculous mycobacteria or other respiratory pathogens have been identified. These are methyl phenylacetate (MPA), methyl nicotinate (MN), methyl *p*-anisate (MP), and *o*-phenylanisole (OPA) [55,59–61]. Methyl nicotinate is the most representative TB breath biomarker [55]. Gas chromatography and mass spectrometry (GC-MS) are commonly used for the detection of TB-related VOCs. However, analysis using these techniques is time-consuming and requires trained personnel [55]. The initial investment in the instrument is not cost-effective, and breath analysis can also be limited by the loss of analytes and contamination from the collection device [61]. To date, limited progress has been made in diagnosing TB using *M.*

tuberculosis-related VOCs.

1.2.2. Urine biomarkers

1.2.2.1. Lipoarabinomannan (LAM)

LAM is a 17.5 kD amphiphilic glycolipid found in the capsular layer (outer layer) of mycobacterial species [15,62–64]. It is a major constituent of the cell wall and constitutes up to 15% of the total bacterial cell weight [10,65–68]. LAM is one of the three interrelated polysaccharides within the mycobacterial cell wall. These three molecules are non-covalently linked to the mycobacterial plasma membrane through the glycophospholipid anchor and extend to the surface of the cell wall [15,69]. LAM is immunogenic and a major mycobacterial virulence factor promoting the survival of the microorganism within the host. During mycobacterial infection, LAM is released from metabolically active or degrading mycobacterial cells and is present in body fluids [66,70,71]. It is, therefore, a potentially significant biomarker for identifying infected individuals. Additionally, the immune responds by producing anti-LAM antibodies during mycobacterial infection to circulating LAM in body fluids, and therefore it can also serve as a crucial diagnostic marker [65,72]. LAM is filtered by the kidneys and detectable in urine samples of severely immunosuppressed individuals [62,73]. Urine specimens are commonly used for LAM detection in lateral flow assays; however, these biomarkers can also be detected from sputum and blood specimens using enzyme-linked immunosorbent assay (ELISA) [74]. Since it is a carbohydrate (polysaccharide) antigen, it is inherently heat stable and can still be detected even after heat treatment (when required) of urine samples [75,76].

1.2.2.2. Transrenal DNA

Mycobacterial transrenal DNA (Tr-DNA) are small fragments of DNA originating from the mycobacterial genome [77]. These small DNA fragments are derived from cell-free nucleic acids in plasma and blood, resulting from the breakdown of dying human cells and

microorganisms [78–82]. However, the quantity of Tr-DNA in urine is significantly lower than cell-free nucleic acids in plasma and blood. TB-related Tr-DNA is released during mycobacterial cell lysis. It can bypass the glomerulus and be detected in urine samples of patients with active TB [77]. Tr-DNA is considered much smaller than genomic DNA (gDNA), which is believed to be the reason why it can pass through the kidneys into the urine (Figure 4) [78]. These Tr-DNA fragments are usually less than 200 base pairs (bp) in size [83]. Like other NAATs, the molecular detection of Tr-DNA can be much more sensitive than sputum smear microscopy. However, the cost and complexity of the test will limit its applications in resource-limited settings and countries with a high prevalence of TB, providing fewer chances of developing a POC diagnostic test [78]. To date, only a few studies have looked at the diagnostic efficacy of urine-detectable mycobacterial Tr-DNA fragments as biomarkers for diagnostic purposes, and no Tr-DNA diagnostic test is yet commercially available [77].

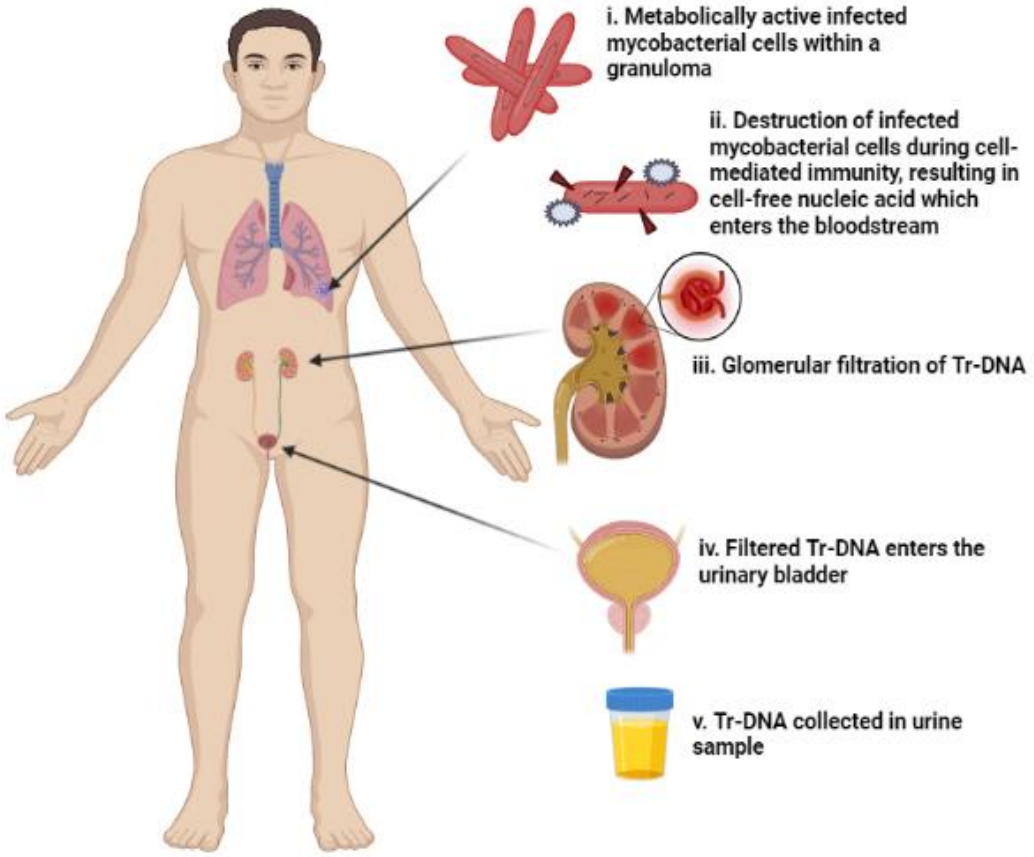

Figure 4: Illustration of the process of Transrenal (Tr) DNA production in a patient with pulmonary tuberculosis. *Mycobacterium tuberculosis* bacilli in the lungs are destroyed by the immune cells, thus releasing cell-free nucleic acids in plasma. Small-sized cell-free nucleic acids pass through the kidneys during glomerular filtration to produce Tr-DNA detectable in urine.

1.2.3. Sputum biomarkers

1.2.3.1. Mycolic acid

Mycolic acids are a complex group of long-chain (60 – 90 carbons long) highly hydrophobic branched α-alkyl β-hydroxy fatty acids found in the cell wall of bacteria belonging to the mycolate family of actinomycetes, which includes *Rhodococcus* and *Mycobacterium* [84–88]. Mycolic acid consists of a long saturated 2-alkyl branch and a long fatty alcohol part known as a “mero” chain. It is an asymmetrical structure consisting of a hydrophilic head group (C-C with COOH and OH), as shown in Figure 5, and the COOH acts as the antibody binding site [85].

Initially, they were first isolated from a human strain of *M. tuberculosis*; however, they have since been found in a variety of *Mycobacteria* species [89]. To date, several mycolic acids have been isolated and characterized, and they have been found to possess the same basic structure with differences in functional groups (e.g. carbonyl, carboxyl, methoxyl branches, cyclopropane rings, and carbon-carbon double bonds) used to differentiate between species [89]. The functional groups vary in type, stereochemistry, spacing, and the number of carbon atoms also varies between genera. The mycolic acids of mycobacteria have a large diversity of chain lengths and chemical functions that result in different classes of mycolic acids (e.g. alpha, keto, and methoxy) (Figure 5) [85]. The alpha-mycolates contain no oxygen substitutions in their meromycolic chains and are the most widely distributed type of mycolic acids [84].

The keto and methoxy-mycolates are characterized by *cis* and *trans* cyclopropane rings in the proximal positions of their chains and are notably less common forms of mycolic acids [84]. Within the cell wall, mycolic acids are arranged orderly in parallel and covalently attached to peptidoglycan via arabinogalactan, as seen in Figure 1 in 1.1.3. Besides being an important component of the mycobacterial cell wall, mycolic acid has also been reported as being a virulence factor of *M. tuberculosis*. Mycolic acids are immunogenic and capable of eliciting a cellular and humoral response [86,87]. Several studies have also shown the prevalence of anti-mycolic acid antibodies in TB patient's sera using ELISA [90].

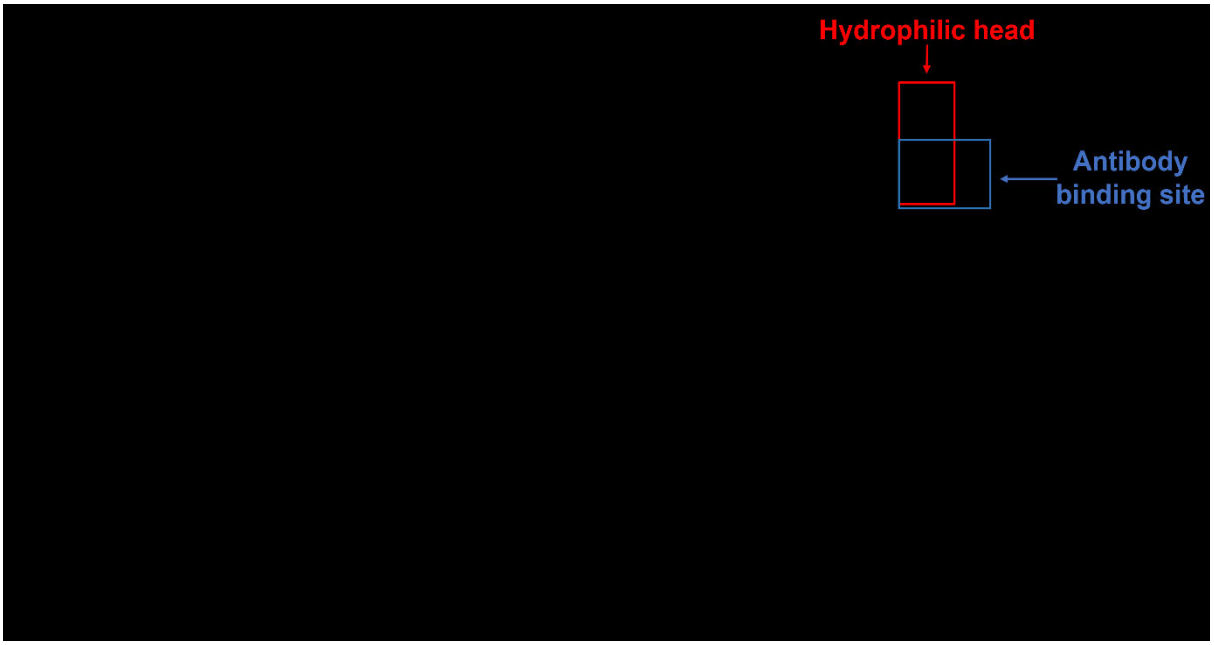

Figure 5: Chemical structures of alpha, keto, and methoxy-mycolic acid derived from *Mycobacterium tuberculosis*.

Mycolic acids seem to be relevant diagnostic indicators for various reasons. Firstly, they are pathogen-derived diagnostic markers and not produced by the host; hence are considered classic indicators of active infection. Secondly, they are present in high concentrations regardless of bacterial growth conditions. Lastly, they are chemically stable and can be easily extracted from the bacterial cell wall [84]. Although it has been demonstrated in various studies that MAs are secreted during mycobacterial infection, no standardized immunoassay enabling the detection of such antibodies has been developed to date. Hence, this study aims to develop and/or evaluate mycolic acid as a potential biomarker for use in optical biosensing immunoassay techniques for the detection of anti-*mycobacterium tuberculosis* antibodies.

1.2.3.2. Early secreted antigenic target - 6

The 6 kDa (kilo Dalton) early secreted antigenic target (ESAT-6) is a crucial secretory antigen and a major virulence factor of *M. tuberculosis*. It is detectable in the sputum and blood specimens of TB patients during the acute phase of active infection [91]. It has also been reported

to be prominent during the progression to TB infection, hence considered a key mediator in mycobacterial virulence [91–93]. It is secreted only by the pathogenic *Mycobacterium* species, thus a potential biomarker for active TB diagnosis [91]. There are several advantages of using ESAT-6 as a biomarker for TB. It is detectable in the early stages of TB infection and has been easily detected using immunoassays in infected patients; however, it often results in false positives in individuals vaccinated with BCG [94]. This antigen is detectable in individuals with latent and active TB, and, therefore, not the best biomarker for the detection of TB disease [95]. It is commonly used in most immunological studies, including vaccine designs, and in the blood, it forms a heterodimer with another antigenic protein secreted by M. tuberculosis called 10 kDa culture filtrate protein (CFP-10), leading to virulence [93,96]. The ESAT-6/CFP-10 complex induces a significant T-cell response in the blood and is a common target for interferon-gamma release assay (IGRA) used for the diagnosis of latent TB [97].

1.2.4. Blood biomarkers

Antigen85 (Ag85)

The antigen85 complex represents the most abundant secreted protein antigens of actively replicating *M. tuberculosis* of all mycobacterial species and is not detectable in non-*M. tuberculosis* complex strains [98–101]. It plays a significant role in the pathogenicity of M. tuberculosis [101]. The complex comprises Ag85A (30 kDa), Ag85B (32.5 kDa), and Ag85C (32.5 kDa) that are encoded by genes *FbpA*, *FbpB* and *FbpC2* respectively [99]. These proteins belong to the *Corynebacterium*, *Mycobacterium,* and *Norcadia* genera, all characterized by the presence of mycolic acids on the surface of the cell wall [100]. The Ag85A is involved in the survival of tubercle bacilli within cultured macrophages. Ag85B has the greatest expression levels and is the most abundant secreted protein compared to Ag85A and C, making it a potential biomarker for TB diagnostics. Ag85C is the most biologically active of the three [99,102]. The

Ag85 complex possesses a mycolyltransferase activity that is essential for the biosynthesis of the mycobacterial cell wall and survival of the mycobacteria [98,99,103,104]. This complex is involved in the final step of assembly and is required to maintain the bacterial cell envelope integrity, thus stimulating humoral and cell-mediated immune response [105]. The production and abundance of anti-Ag85 antibodies in TB patients support the use of Ag85 as a promising TB diagnostic biomarker [106]. Several studies have reported elevated levels of Ag85 complex TB meningitis patients, suggesting the possibility of using this secreted protein complex for diagnosing extrapulmonary TB meningitis [99,107]. Various immunodiagnostic tests such as ELISA, direct liquid chromatography-tandem mass spectroscopy, immunoblotting, and waveguide-based biosensor assays have been reported for the detection of Ag85 [98]. However, these tests are complicated laboratory-based assays that cannot be performed in a point-of-care setting.

1.3. Current TB diagnostic methods

Difficulty in TB diagnosis is one of the main contributing factors in the struggle to control TB [108]. As indicated in section 1.1.8, individuals who develop active pulmonary TB disease can be treated; however, rapid and early detection of TB, especially in the point-of-care setting, is required to reduce the interval between infection and treatment initiation [109]. Therefore, TB diagnostics need to provide timely, accurate, cost-effective results in settings where access to electricity, equipment, and technical expertise remains a challenge. Currently, there are numerous methods used for screening and diagnosis of TB. TB diagnostic tests recommended and endorsed by the WHO include LED fluorescence microscopy, commercial liquid culture and drug susceptibility testing, rapid speciation strip technology for identification of *M. tuberculosis*, Xpert MTB/RIF, lateral flow urine LAM assay to detect TB in severely ill HIV patients or those with cluster of differentiation 4 (CD4) count ≤ 100 cells/μL, loop-mediated

isothermal amplification (LAMP), line probe assay to detect resistance to INH and RIF in the smear-positive specimen or cultured colonies, and second-line line probe assays (SL-LPA) to detect fluoroquinolone and second-line injectable drug (SLID) resistance assays [13]. The availability of these advanced tools comes with limitations, especially where the TB burden is high, and most of them require specialized infrastructure, power, and trained personnel, are costly, and cannot be performed in a point-of-care setting [13,26,110,111]. Hence this study focuses on the use of optical biosensing techniques for the detection of anti-*mycobacterium tuberculosis* antibodies as an alternative.

1.3.1. WHO-accredited active TB diagnostic tests

1.3.1.1. Microscopy

Direct sputum smear microscopy (SSM) detecting acid-fast bacilli (AFB) in smears is the most commonly used diagnostic test for the evaluation of patients with symptoms suggestive of pulmonary TB in most resource-limited settings, particularly in developing countries [112–115]. In general, microscopy examination of smears can be performed using conventional light microscopy, acid staining Ziehl-Neelsen (ZN), and fluorescent microscopy using auramine O (Figure 6) [116]. SSM is used in most primary healthcare laboratories at the health center level [117]. In these settings, conventional light microscopy is used to examine ZN-stained direct smears. This technique has shown to be highly specific, especially in areas with a high prevalence of TB, but with varying sensitivity (20 – 80%) [117]. Additionally, the sensitivity of this technique is reduced further in child and TB patients co-infected with HIV [113,118]. The sensitivity of this assay is limited by the requirement for high bacillary content of 5000 – 10 000 colony forming units (CFU)/milliliter (ml) [13]. Fluorescent microscopy (FM) has advantages over conventional light microscopy. It uses an acid-fast fluorochrome dye and a high-pressure mercury vapour lamp (MVP) as a light source [113]. The higher contrast obtained in FM allows

the user to lower the power magnification, reducing the time required to screen each slide. The increased contrast in FM reduces operator fatigue and has been reported to increase detection sensitivity [116]. However, its low sensitivity and requirement for high bacilli count is a major limitation. The MVP-FM can only be used in a dark room [118]. The use of MVP light source in FM poses major cost limitations, especially for initial investment (purchase) and ongoing maintenance costs [116]. MVP lamps are costly, require an expensive power supply, and have a short lifespan (200 – 300 hours). MVP lamp lifespan is also affected by switching on and off, emitting UV rays as by-products, and MVP may release toxic mercury, which is a health hazard to the operator [113,116].

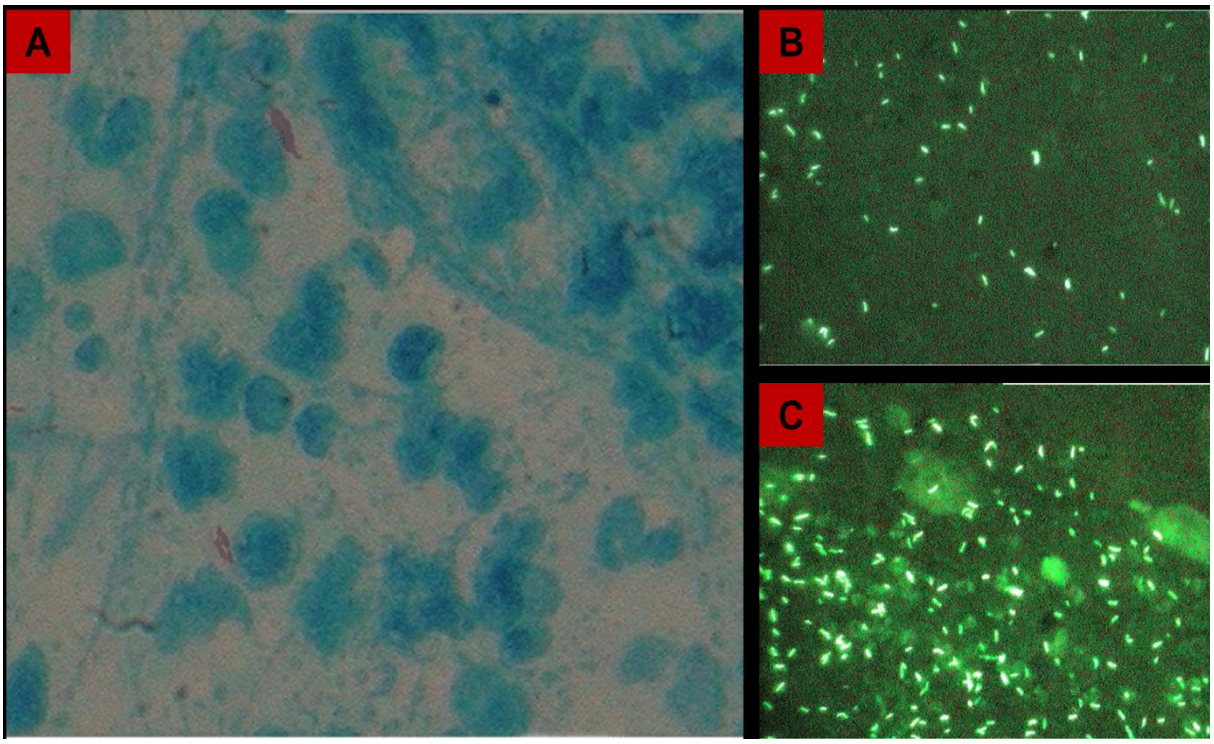

Figure 6: Photomicrographs of TB bacilli. A) Ziehl-Neelsen stain sputum smear showing TB bacilli stained red against a blue background, B) Conventional fluorescent micrograph of Auramine O stain sputum smear, C) Light Emitting Diode (LED) fluorescent micrograph of Auramine O stain sputum smear showing brighter spots of TB bacilli compared to conventional fluorescent microscopy [119].

In 2010, the WHO recommended that conventional fluorescence microscopy (MVP-FM) be replaced with LED-FM in all settings where MVP-FM is used, including both high and low-volume laboratories, and that LED-FM be used as an alternative to ZN microscopy [120]. The LEDs used in LED-FM can produce very narrow spectrum light and can excite auramine O and other commonly used fluorescent dyes/stains used in FM. The LED-FM has several advantages over MPV-FM. It does not require operation in a dark room and can still produce high-resolution quality images. It has a bulb lifespan of approximately 50 000 hours (compared to 200 - 300 hours in MVP-FM), does not produce UV light, has low power consumption, and can be solar or battery-operated. LED-FM produces minimal heat and contains no life-threatening hazardous materials [112,117,118,120,121]. Several studies have demonstrated similar sensitivity between the MVP-FM and the LED-FM [120]. These advantages and cost benefits make LED-FM suitable for high TB burden resource-limited settings [122].

1.3.1.2. TB culture

Culture remains the gold standard for the diagnosis of TB and drug resistance detection of existing and emerging mutations [15]. This sputum culture bacterial isolation method can detect a minimum of 10 – 100 viable bacilli in cultured material. Traditional egg-based Lowenstein-Jensen (LJ) and agar-based Middlebrook 7H10/11 media are used. The LJ medium is commonly used for the isolation of human strains of *M. tuberculosis* and most other mycobacteria [13]. Bacterial growth in LJ medium takes 4 – 8 weeks, with an additional four weeks for drug sensitivity testing using the conventional culture method [15]. The presence of glycerol in the LJ medium improves the growth of *M. tuberculosis*. When formed, colonies appear dry, raised, rough, and irregular with wrinkled surfaces [13]. They are creamy white initially and become yellowish or buff-colored over time [13]. *M. tuberculosis* bacilli is an obligate aerobe that grows optimally at 37 °C (range: 20°C - 40°C) and at a pH of 6.4 – 7.0. It is a slow-growing

microorganism with a generation time of 14 – 15 hours, and the colonies appear in approximately two weeks and, if delayed up to 6 – 8 weeks, which is a major limitation for treatment initiation. Other limitations include the requirement for specialized infrastructure with biosafety facilities and highly trained laboratory personnel to perform the tests [15].

In 2007 the WHO endorsed a liquid culture system for the identification and DST of TB [13]. Initially, the semi-automated radiometric BACTEC 460 TB system (Becton Dickson Diagnostic System, Sparks, MD, USA) was used as the gold standard for DST for both first-line and second-line anti-TB drugs. However, this system has limitations, including using radiometric materials, inconvenient manual loading and unloading of samples, risk of cross-contamination, and lack of computerized data management [123]. Recently, the BACTEC Mycobacteria Growth Indicator Tube (MGIT) system (Becton Dickson Diagnostic System, Sparks, MD, USA) was introduced as an alternative to the radiometric BACTEC 460 for growth and detection of TB, and drug sensitivity testing of *M. tuberculosis* isolates [13,123,124]. It is a non-radioactive, fully automated, and continuously monitoring system [123]. For *M. tuberculosis* detection, it utilizes a 7 mL modified 7H9 Middlebrook broth base containing 0.25% glycerol containing oxygen quenching fluorescent sensor embedded in silicon at the bottom to detect microbial growth directly from clinical specimens [125,126]. The fluorescent sensor responds to the concentration of oxygen in the culture media [127]. As the microorganisms grow in the media utilizing oxygen, the oxygen gets depleted, and fluorescence is released and detected automatically by the photodetector every 60 min. When a certain level of fluorescence is reached, the instrument indicates that a specific vial has a positive result [15,126,127].

1.3.1.3. Lateral flow urine lipoarabinomannan assay

The DETERMINE TB-LAM Ag test (Alere, Waltham, MA, USA) assay was recently commercialized for POC testing of TB (Figure 7). It is a lateral flow immunochromatographic strip test used to detect mycobacterial LAM antigen biomarkers released from metabolically

active and degrading mycobacterial cells during TB infection [10,73]. It can provide results in 20 - 30 min [15,63,73].

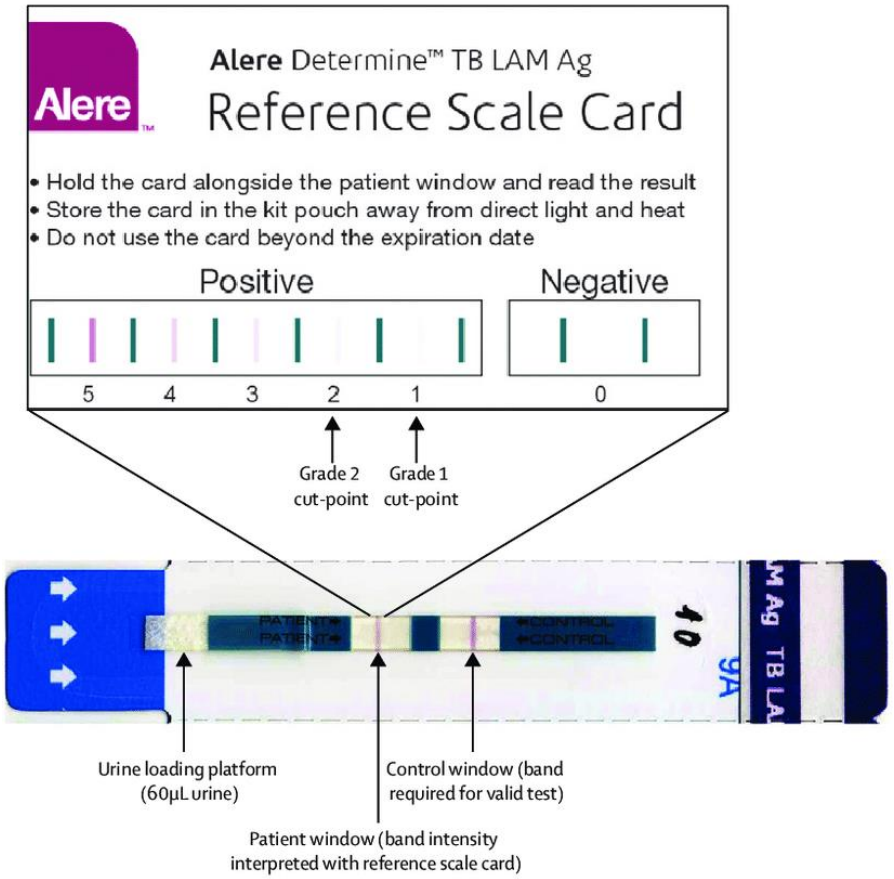

Figure 7: The Alere DETERMINE TB-LAM lateral flow antigen test. It was recently commercialized for point-of-care testing of TB to detect mycobacterial lipoarabinomannan antigen biomarkers present in the urine of severely immunocompromised HIV patients.

The detection of LAM in urine samples has several potential advantages. Urine is easy to collect, process, and store. There are fewer infection control measures to consider when compared to sputum. It is a convenient specimen for young children who often cannot produce sputum and bedridden patients who are severely ill or in a coma [10]. The WHO recommends that this test should not be used for TB diagnosis. However, it should only be used to diagnose TB in HIV in-patients with signs and symptoms of pulmonary and/or extrapulmonary TB, who have a CD4

cell count of ≤ 100 cells/μL, or severely ill HIV-patients regardless of CD4 count [15].

1.3.1.4. Xpert MTB/RIF and Xpert MTB/RIF Ultra

In 2010 the WHO approved the molecular test Xpert MTB/RIF assay (Cepheid, Sunnyvale, CA, USA) as the preferred initial test for the diagnosis of pulmonary TB, extrapulmonary TB, TB meningitis, and RIF susceptibility testing [114,128,129]. This invention was a major breakthrough for TB diagnosis and DST, and the requirement for sophisticated infrastructure with mycobacterial culture capabilities and the need for highly skilled lab technicians was no longer significant [130]. Xpert MTB/RIF is a cartridge-based, fully automated semi-nested polymerase chain reaction (PCR) test. This assay has a limit of detection (LOD) of ~116 colony-forming units (CFU) per mL, thus remaining less sensitive than TB culture with an LOD of ~1 – 10 CFU/mL [131]. The assay targets a single copy gene (rpoB) for RIF resistance testing [131]. Xpert MTB/RIF's sensitivity for TB detection is limited in clinical specimens with few bacilli count, and this limits its usefulness in patients with sputum smear-negative results and extrapulmonary TB, especially children, and HIV co-infected individuals [130,132]. For the detection of RIF susceptibility, Xpert can give false-positive results for strains that carry phenotypically silent mutations or if the bacillary burden is relatively low. However, this is rare [132].

To circumvent these limitations, Cepheid re-engineered a new Xpert MTB/RIF Ultra assay to improve the analytical sensitivity for MTB and RIF resistance detection [129,131,133]. Xpert Ultra was approved by the WHO in March 2017. It uses the same diagnostic platform as Xpert MTB/RIF, incorporating a few changes [130]. To improve the sensitivity and RIF resistance testing, two additional hybridization targets (IS6110 and IS1081 genes) intended to reduce the LOD of bacterial CFU, a larger DNA reaction chamber (50μL PCR reaction in Ultra versus 25μL reaction in Xpert MTB/RIF), fully-nested nucleic amplification, more rapid thermal cycling, improved fluidics and enzymes [128,134]. This has resulted in Ultra having a LOD of

~16 CFU/mL, better than Xpert MTB/RIF's LOD of ~116 CFU/mL and approaching TB culture's LOD of ~1 – 10 CFU/mL [131,133–135]. The LOD of Ultra, which is getting closer to the LOD of TB culture, is only valid for respiratory specimens [131]. To improve the accuracy of RIF resistance detection, Ultra incorporates melting curve analysis of molecular probes to detect mutations in the active site of the rpoB gene involved in RIF resistance. In contrast, Xpert MTB/RIF relied on real-time PCR cycle threshold (Ct) values to detect mutations, which could potentially result in false-positive results mainly due to insufficient amounts of DNA [131]. Ultra is expected to improve the diagnosis of TB because of its increased sensitivity for MTB DNA detection and its improved specificity for the detection of rpoB mutations [131]. In general, Xpert MTB/RIF and Ultra, and developing countries will feel the cost burden for initial investment of these devices, maintenance, and cost of reagents. Therefore, other affordable POC diagnostic devices need to be developed.

1.3.1.5. Loop-mediated isothermal amplification (LAMP)

TB-LAMP assay is a relatively new, specific, and sensitive NAAT. The Loopamp™ *Mycobacterium tuberculosis* complex (MTBC) detection kit (TB-LAMP) (Eiken Chemical Company, Tokyo, Japan) test was endorsed by the WHO in 2016 for the detection of MTBC in sputum as a follow-up test after a negative sputum smear microscopy result [136–138]. LAMP-based assays can be performed for confirmation of various infections using relevant primer sets [139]. LAMP is an isothermal (65 °C) DNA amplification test that uses two or three sets of primers to amplify small quantities of DNA extracted from PTB specimens. This test can be performed in a laboratory water bath, heating block, or thermal cycler [140]. The 25 µL reaction mastermix for DNA amplification contains a buffer, target DNA, DNA polymerase enzyme, primers, and a DNA intercalating fluorescent dye. The primers are synthesized specifically for detecting the pathogen of interest and include forward inner primer (FIP), backward inner primer

(BIP), outer forward primer (F3), outer backward primer (B3), forward loop primer (FLP), and backward loop primer (BLP) [137,141]. The fluorescent dye can be added during or after the experiment, before confirmation of positive and negative samples through the naked eye or UV light [142]. Results can be obtained in 35 - 60 min [15]. This method is mainly used for diagnosing pulmonary TB, and its role in diagnosing extrapulmonary TB is not well-researched [142]. It is a very economical assay with minimal requirements for laboratory infrastructure and limited biosafety hazards [142,143]. However, the TB-LAMP assay remains underutilized [110]

1.3.1.6. Line probe assay (LPA)

The LPA is a strip-based genotype test used to detect TB DNA and genetic mutations associated with drug resistance to INH and RIF first-line anti-TB drugs [15,142]. In 2008, the WHO certified and endorsed commercial LPAs following a systematic review at that time, evaluating the diagnostic accuracy of the GenoType MTBDRplus (version 1) (Hain Lifescience, Nehren, Germany) and the INNO-LiPA Rif.TB assay (Innogenetics, Ghent, Belgium) [144]. The LPA can be performed using smear-positive sputum specimens, culture isolates, or PCR amplicons of DNA extracted from culture isolates [15]. The turnaround time (TAT) for this assay as per WHO guidelines, is two to three days [145].

This is a DNA hybridization assay and drug resistance is identified by detecting the hybridization of DNA from the patient specimen to the mutant (resistant) probe and/or failure of DNA hybridization to the wild-type probe (sensitive) [14]. Each detection strip consists of 27 reaction zones or bands, including six control bands (conjugate, amplification, MTBC, rpoB, katG, and inhA controls), eight rpoB wild-type (WT) and four mutants (MUT) probes, one katG WT and two MUT, and two inhA WT and four MUT probes [15]. Generally, LPAs are as complex to perform as conventional culture requiring highly trained laboratory personnel to perform the test

and read the significantly complex test strip to make a diagnosis. However, it has a lower biosafety risk compared to conventional culture [14]. To perform this test, the laboratory needs to be spacious and designed for biosafety level 2 or 3 (BSL-2/3) with a Class II biological safety cabinet to reduce the risk of contamination and false-positive results [15]. Although excellent diagnostic accuracy in detecting rifampicin resistance was reported for the two first-generation LPAs endorsed in 2008 by WHO, both tests had lower sensitivity, despite excellent specificity. Subsequent performance data have since been published on the use of LPAs, and newer versions have been developed, including GenoType MTBDRplus version 2 (Hain Lifescience, Nehren, Germany) and the Nipro NTM+MDRTB detection kit 2 (Tokyo, Japan) [110,144,146]. The GenoType MTBDRplus version 2 assay can detect genetic mutations associated with second-line anti-TB drugs used to treat MDR-TB, including fluoroquinolones (FLQs), second-line injectables, amikacin, kanamycin, capreomycin. This assay is mainly used to guide treatment initiation for MDR-TB; however, TB culture still remains the reference standard for DST [14,110].

1.4. Introduction to biosensors and biosensing technique

Biosensing is an emerging analytical field for detecting and analyzing biomolecular or biochemical interactions of various analytes using various transduction mechanisms [147]. These transduction mechanisms are used to translate changes or detectable variations on the transducer surface into readable and quantifiable signals [147]. Biosensing has rapidly advanced over the last few decades due to applications in various disciplines, such as health diagnostics, environmental monitoring, and food quality [148]. A biosensor is an analytical device incorporating a biorecognition element (receptor or biomarker), a transducer system, and a signal output detector [149–151]. The biorecognition element compliments and detects the analyte of interest. The transducer translates or converts the biological information during the interaction

between the biorecognition element and the analyte on the biosensing surface into a detectable signal, and a signal processing unit processes the signal into a readable outcome [20,152–154]. The biorecognition element may be a biological material such as antibodies, nucleic acids, cell receptors, microorganisms, or enzymes; or a biologically derived material such as engineered proteins, functional nucleic acids, and functional nucleic acids [150,151].

When successfully immobilized on the biosensor surface, the biorecognition element captures the analyte (target molecule), thus providing biochemical specificity of the biosensor [155]. The immobilization of biorecognition elements on the biosensing surface is a very crucial step in the design and development of biosensors. The applied surface chemistry used to functionalize the biosensor chip is critical in obtaining sensitive detection signals. To date, there are different and well-described techniques used for surface functionalization, such as covalent immobilization chemistry and physical adsorption [151].

Besides receptor-analyte biorecognition and binding, a fundamental part of biosensing is the signal transduction mechanism, through which binding events are converted into a detectable output signal. This requires a transducer system which may be optical, electrochemical, magnetic, thermometric, or micromechanical [150]. Among the various transduction approaches, optical biosensors have attained great attention in the past decades as powerful analytical and detection tools with vast applications in healthcare (e.g. diagnosis and monitoring of diseases and drug discovery), environmental applications (e.g. environmental detection of pollutants and/or biological agents), and in biotechnology [151,156,157]. Optical biosensors can operate in different modes, including transmission, absorption, and reflection of light waves. Unlike biochemical methods, detection is label-free, making them environmentally friendly [158]. Label-free optical biosensing is a rapidly emerging research focus area with potential applications in clinical diagnostics, pharmaceutical screening, and fundamental research towards the development of portable and easy-to-use point-of-care devices [159]. Optical biosensors

offer significant advantages over conventional analytical techniques because they enable direct, real-time, label-free detection and multiplexing capabilities. They also have the potential for miniaturization into portable, robust, user-friendly, and cost-effective point-of-care devices [150,151,156,160,161].

1.5. Optical biosensing techniques used in this study to detect anti-*mycobacterium tuberculosis* antibodies

1.5.1. Localized surface plasmon resonance biosensing

The LSPR method has emerged as a leader among label-free biosensing techniques offering real-time, robust, precise, and high-sensitivity detection [162,163]. It is an optical phenomenon caused by the interaction of incident photons and metallic nanoparticles [17]. It is also a surface plasmon resonance (SPR) phenomenon existing in metallic nanoparticles instead of thin film metals [164]. During LSPR biosensing, the incident light induces collective oscillations of valence electrons, subsequently increasing the intensity of the electric field at the sensor and creating a characteristic extinction peak at the plasmonic resonance frequency. LSPR biosensors differ from SPR-based biosensors as the induced plasmons oscillate locally around the metallic nanoparticle instead of propagating along the metal-dielectric interface [16,17]. Upon analyte attachment to the nanoparticle, the refractive index change causes a wavelength shift in the extinction spectrum, thus making the LSPR platform suitable for label-free detection and quantification of biorecognition events [16]. During LSPR biosensing, changes in the refractive index of the surrounding media enable the application of this method in biosensing, chemical sensing, and gas sensing [165]. In biosensing, LSPR sensors can monitor a variety of binding events, including protein-ligand interactions, DNA hybridization, and biomarker interactions

[18]. When binding events occur, changes in LSPR properties manifesting as a shift in the extinction peak can be easily measured by UV-vis spectroscopy [18].

1.5.2. Photonic crystal-based biosensing

Over the last three decades, biosensors based on PhCs have been developed and continue to receive significant recognition owing to their distinctive electromagnetic properties and broad applications domain [166]. PhCs are spatially arranged periodic structures made of low and high-refractive index materials, providing high-efficiency reflection at specific wavelengths [147,167]. The existence of a forbidden frequency range called a photonic band gap (PBG) is one of the most significant and special properties of PhCs. In this frequency range, the propagation of electromagnetic waves (EMWs) is prohibited [168]. In practice, this means if the radiation with a wavelength inside the PBG is incident on the PhC it experiences a strong reflection from the PhC; hence a PhC can act as an optical filter [158,168]. PhCs can be designed in one-dimensional (1-D), two-dimensional (2-D), or three-dimensional (3-D) depending on the number of directions with a periodic repetition [20,152,169,170]. The 1-D PhCs, also known as dielectric mirrors or Bragg mirrors, are simple multilayer stacks and can be used as biosensors [20,152]. In this work, a 1-D PhC was modified and used as a biosensor chip. The optical detection was based on refractive index changes on the functionalized 1-D PhC biosensing surface. Studies that have used refractive index as a parameter to design optical biosensing devices based on PhCs have resulted in sensitive optical devices with quick response time for small variations in samples [171]. In this study, for the first time, PhC biosensing towards the diagnosis of TB using a pathogen-specific biomarker was studied based on the detection of refractive index changes on functionalized biosensing surfaces detailed in Chapter 4.

In conclusion, the current WHO-endorsed TB diagnostic platforms described in Section 1.3 are limited by various requirements that hinder their application, especially in resource-limited settings. In general, the limitations are associated with infrastructure requirements, electricity, associated costs in terms of initial investment and ongoing maintenance of the instruments, high costs for reagents, and highly trained personnel needed to perform the tests. This is often not achievable in regions with a high burden of TB. Moreover, most of these advanced diagnostic methods cannot be performed in point-of-care settings, thus contributing to delays in TB diagnosis and treatment initiation. As an alternative approach, optical biosensing emerges as a promising solution for biomarker detection towards TB diagnosis. Optical biosensors described in Section 1.5, incorporating biorecognition elements and transduction systems can operate in label-free modes, allowing for real-time and direct detection of analytes. Their potential for miniaturization makes them suitable candidates for point-of-care applications. Hence the subsequent chapters focus on exploring the capability and potential of using LSPR and PhC-based optical biosensing techniques to detect anti-*mycobacterium tuberculosis* antibodies.

CHAPTER 2:

BIOSENSING SURFACE COATING AND OPTIMIZATION OF CHARACTERIZATION TECHNIQUES

2.1. INTRODUCTION

This chapter covers biomolecular interactions, substrate coating with metals, design, and development of a custom-built optical biosensing setup for biosensor chip analysis in Chapters 3 and 4. For molecular interaction experiments, fluorescence microscopy will be used as a proof-of-concept experiment to test the reaction, interaction, or binding between the mycolic acid biorecognition element and the anti-mycobacterium tuberculosis antibodies. To perform substrate coating with metals, the physical vapour deposition (PVD) technique will be used to coat glass substrates with Au to generate surface plasmons during LSPR experiments, and the thin film Au-coated layer will be characterized using SEM to visualize the gold distribution on the surface. Additionally, AuNPs will be bioconjugated using physical and covalent bioconjugation strategies to determine an efficient method for bioconjugation and UV-vis absorption spectroscopy will be used to determine successful bioconjugation. To study the morphology of the AuNPs that will be used in this study, TEM will be used. Lastly, a custom-built optical biosensing setup will be designed and developed for applications in Chapters 3 and 4.

The PVD is a vacuum-based dry-coating technique used to create thin films of various materials (e.g., Au, Ag, and titanium) on solid substrates (e.g., glass slides) [172–174]. In PVD, the material to be deposited is first vaporized in a vacuum chamber, and then the vaporized atoms or molecules condense onto the substrate, forming a thin film. The deposition process in PVD is primarily driven by physical mechanisms, such as evaporation, sputtering, or thermal decomposition, rather than chemical reactions [172]. During sputtering, Argon gas is first

introduced into the vacuum chamber. A high voltage is applied to the gas, causing it to ionize and form a plasma. The plasma consists of positively charged argon ions and free electrons [172]. The target material (Ti) is then exposed to the high-energy ions from the inert gas (Argon) plasma, causing atoms or ions from the target to be ejected and deposited onto the substrate. The sputtered species (Ti) travel in a straight-line path and form a thin film on the substrate [172]. To create the Au thin film, the electron beam evaporation technique was used. This method involves the use of an electron beam as a heating source to vaporize the material in a vacuum chamber, followed by condensation onto the substrate made of Ti layer to form a stable Au thin film [172]. Physical vapor deposition allows the deposition of a wide range of materials, and the deposited films can exhibit excellent adhesion, uniformity, and density, thus making them widely used in industries such as electronics, optics, and coatings [172,175,176].

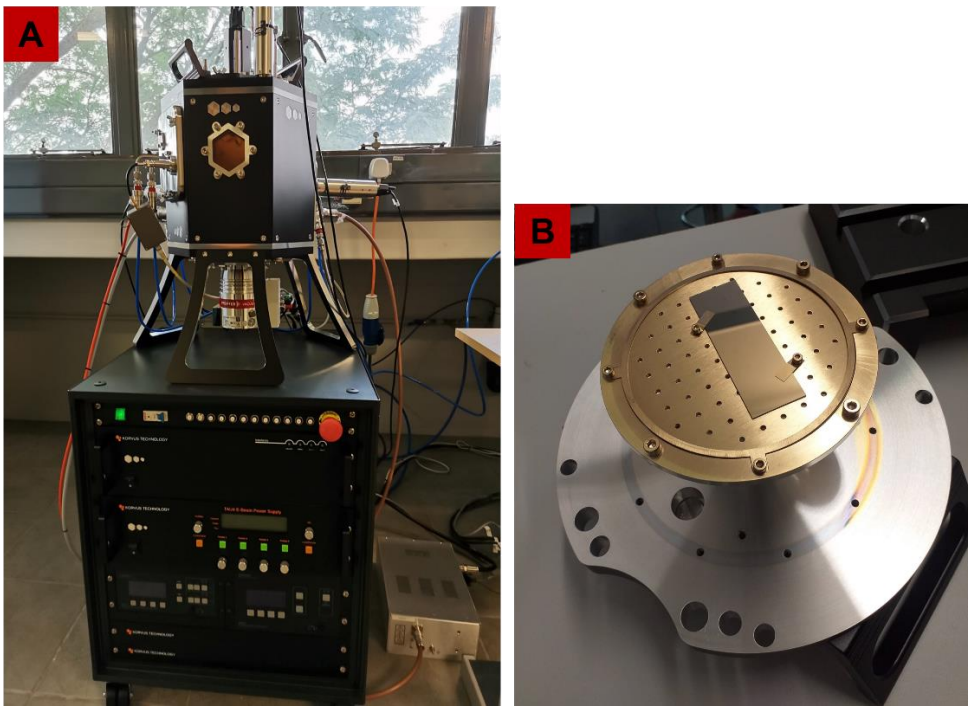

Figure 8: The HEX benchtop thin film deposition system used to develop Au-coated slide (A). (B) The Au-coated slide.

For signal enhancement during the analysis of the biosensor chip, bioconjugated AuNPs are commonly introduced on the surface of the chip. Bioconjugation refers to the process of linking molecules of biological or chemical origin to form a single complex or conjugate [177–179]. It involves the modification of biomolecules, such as proteins, antibodies, nucleic acids, or carbohydrates, by attaching synthetic molecules or functional groups, labels, or probes [177]. The resulting bioconjugates combine the properties of both components, enabling a wide range of applications in various fields, including biosensing, diagnostics, imaging, and targeted drug delivery [180,181]. To perform bioconjugation, molecules can be linked via physical or covalent conjugation. Covalent conjugation refers to the formation of a stable chemical bond between two molecules through covalent bonding [177]. It involves the joining of functional groups or reactive moieties on one molecule with complementary reactive groups on another molecule. Covalent conjugation, therefore, provides a versatile and robust approach for the synthesis of conjugates with desired properties and functionalities [177,179].

Physical conjugation refers to the non-covalent association or attachment of molecules or entities through physical interactions without the formation of strong chemical bonds [179]. It involves reversible interactions such as electrostatic interactions, hydrophobic interactions, hydrogen bonding, or van der Waals forces or interactions [179]. Unlike covalent conjugation, physical conjugation does not involve the formation of permanent chemical bonds and is generally less stable. Physical conjugation offers advantages such as ease of assembly, reversibility, and the ability to preserve the individual properties of the conjugated entities [179]. Both conjugation techniques were tested in this study to functionalize AuNPs.

2.2. MATERIALS AND METHODS

2.2.1. Characterization of functionalized glass surface using fluorescence microscopy

To functionalize the microscope glass slide in preparation for fluorescence microscopy, the hydrophobic glass slides were washed thoroughly with absolute ethanol, blow-dried with nitrogen gas (N_2), and exposed to oxygen plasma treatment to make them hydrophilic. After the activation procedure, the activated glass slides were immersed in (3-Aminopropyl) triethoxysilane (APTES) (1%, v/v) (Sigma-Aldrich, A3648) in a vertical Coplin jar and incubated at room temperature overnight. Post incubation, the glass slides were washed thoroughly by sonication in absolute ethanol for 5 min and followed by sonication in ultrapure water for 5 min. The clean glass slides were blown with N_2 gas and further dried at 90°C for 1 hour. Silanized glass slides were used immediately to immobilize stearic acid (STA) (141 mM) (Sigma-Aldrich, S4745) on the glass surface or stored in a vacuum for future use. A self-assembled monolayer (SAM) of mycolic acid from *M. tuberculosis* (bovine strain) (0.5 mg/mL) (Sigma-Aldrich, M4537) used as TB antigens were formed on the STA monolayer by incubating the slide in a solution of mycolic acid dissolve in hexane (1mg MA, 2mL hexane: molecular weight = 86,18 g/mol) (Sigma-Aldrich, 34859) overnight at room temperature. Post incubation, the slide was rinsed thoroughly with 1x PBS (Sigma-Aldrich, D1283) to remove physically adsorbed mycolic acid. Subsequently incubated in a solution of bovine serum albumin (BSA) (1%, v/v) (Roche Diagnostics, 10711454001) blocking agent in 1x PBS for an hour before the addition of anti-*mycobacterium tuberculosis* antibody (Abcam, ab905) (8.8 mg/ml) prepared in 1x PBS acting as primary antibody. This antibody was introduced on the mycolic acid monolayer and incubated overnight. For fluorescence staining, to test for the successful reaction between mycolic acid and the primary antibody, a secondary fluorescently labeled goat anti-rabbit IgG H&L (Alexa Fluor) (2 mg/mL, 1:200 dilution in 1x PBS) (Abcam, ab150077) was introduced to the surface. The excitation and emission wavelengths of the goat anti-rabbit IgG H&L (Alexa Fluor) are $495_{Ex}/519_{Em}$ nm. Fluorescence was visualized using an inverted microscope (Wirsam

Olympus® CKX41) with a mounted reflected fluorescence system.

2.2.2. Au-coating of glass substrates

To coat the glass substrates with Au, a HEX benchtop thin film deposition system (Korvus Technology Ltd, United Kingdom) was used. The glass substrates were washed thoroughly with absolute ethanol, rinsed with ultrapure water, and blow-dried with N_2 gas flow. Subsequently, a two-step PVD deposition process was performed, which included sputtering titanium (Ti) directly to the clean glass substrate, followed by electron beam evaporation of approximately 40 nm of Au to the Ti layer.

2.2.3. Characterization of the untreated gold-coated surface

To characterize the Au-coated slides developed using the HEX benchtop thin film deposition system detailed in section 2.1, SEM was used. The Au thin film was washed thoroughly with absolute ethanol, rinsed with ultrapure water, and blow-dried with nitrogen gas flow before SEM analysis. The SEM data was acquired using the JSM-IT800 Schottky field emission scanning electron microscope (JEOL Ltd, Japan). SEM data was performed without coating the slides.

2.2.4. Transmission electron microscopy (TEM) characterization of AuNPs

The morphological analysis of the AuNPs was performed using a High-Resolution Transmission Electron Microscope (HRTEM) (JEOL JEM-2100, Japan) operated at a voltage of 200 Kilovolt (KV). A copper grid was used for sample preparation and dipped into a sample of AuNPs suspended in PBS. The HRTEM operates at an imaging mode with high magnification, thus enabling high-resolution imaging of the crystallographic structure of nanomaterials at the atomic scale level. In this analysis, the HRTEM analysis was used for analyzing the morphology, particle size, and shape to confirm the structural properties of the AuNPs for subsequent studies.

2.2.5. Evaluation of bioconjugation strategies

2.2.5.1. Covalent conjugation

To perform covalent conjugation, N-hydroxysuccinimide (NHS) (13 mM) (Sigma-Aldrich, 56480) and 1-Ethyl-3-(3-dimethylaminopropyl)-carbodiimide) (EDC) (5 mM) (Sigma-Aldrich, E7750) with similar molar ratio were added to heterobifunctional polyethylene glycol (PEG) (SH-PEG-COOH) (10 mg diluted in 10 mL ultrapure water) (Sigma-Aldrich, 757845) in ultrapure water and shaken for an hour on an orbital shaker. PEG is light-sensitive; therefore, samples must be wrapped in foil throughout the experiment. 10x PBS was added to the solution to adjust the pH of the reaction mixture to 7.4. The anti-*mycobacterium tuberculosis* antibody was introduced to the reaction mixture and incubated for 2 hours before filtering the solution with a 50 kDa filter to remove any by-products. The final SH-PEG-IgG bioconjugated solution was obtained after washing with 1x PBS twice. Then, 12µL of the SH-PEG-IgG complex was added to 200 µL of AuNPs and incubated for an hour on an orbital shaker to form the TB-bioconjugate complex (AuNPs-IgG). The samples were analyzed on a NanoDrop 800 spectrophotometer.

2.2.5.2. Physical conjugation

To perform direct adsorption or physical conjugation, the anti-*mycobacterium tuberculosis* antibody was added directly to 200 µL AuNPs. The mixture was wrapped in foil and incubated on an orbital shaker at room temperature for 30 min to form AuNPs-IgG bioconjugate. Additionally, AuNPs were used as a reference. Successful AuNPs bioconjugation was confirmed using NanoDrop 8000 spectrophotometer (Thermo Fisher Scientific, United States) measuring UV-vis absorption. Several absorption spectra (~4) of the AuNPs were recorded to determine the redshift before and after bioconjugation.

2.3. RESULTS

2.3.1. Fluorescence microscopy

To perform fluorescence microscopy, two sample groups were prepared, an experiment and a control sample (Figure 9). In the experiment sample, green fluorescence was detected (Figure 9A). In the control sample group (Figure 9B), no fluorescence was detected. The experiment sample surface consisted of mycolic acid used as a biorecognition element, an anti-*mycobacterium tuberculosis* primary antibody, and a fluorescent-labeled goat anti-rabbit IgG H&L (Alexa Fluor) secondary antibody. The control sample surface consisted of the components in the experimental samples except for the anti-*mycobacterium tuberculosis* primary antibody. The observed green fluorescence in the experiment sample is an indication of the successful binding of the secondary fluorescently-labelled antibody to the mycolic acid/primary antibody complex. The absence of fluorescence in the control sample is a result of the lack of binding of the secondary fluorescently-labelled antibody directly to mycolic acid.

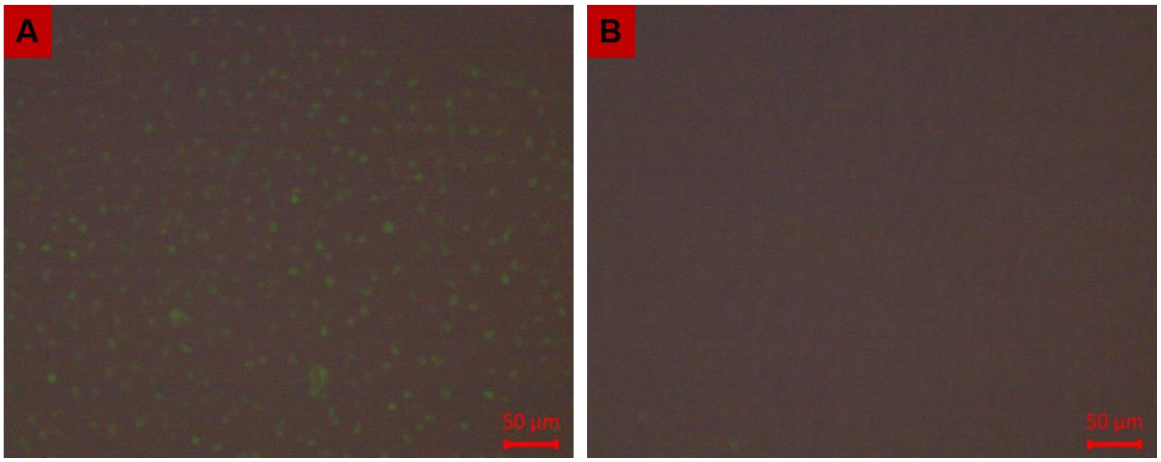

Figure 9: Fluorescence images of mycolic acid TB antigen reaction with anti-*mycobacterium tuberculosis* antibody used as primary antibody. Image A, showing green fluorescence, is the experiment sample consisting of SAM of mycolic acid, a primary antibody, and a fluorescent-labeled goat anti-rabbit IgG H&L (Alexa Fluor) secondary antibody. Image B shows the control sample with SAM of mycolic acid and the goat anti-rabbit IgG H&L (Alexa Fluor) antibody introduced on the surface in the absence of an anti-*mycobacterium tuberculosis* antibody. No fluorescence was observed in the control sample. Images were captured with a CKX41 Olympus microscope, and the length of the scale bar is 50µm.

2.3.2. SEM analysis of the gold-coated thin film surface

The SEM analysis of the Au thin film deposited using the PVD surface coating technique was performed to study the distribution of Au microparticles on the surface and to look for surface contaminants. The elemental composition of the surface was studied using EDX spectroscopy and detailed in chapter 3, section 3.3.4. The Au thin film is resembled by a homogenous layer of tightly packed Au microstructures (Figure 10). The surface contains no signs of contaminants.

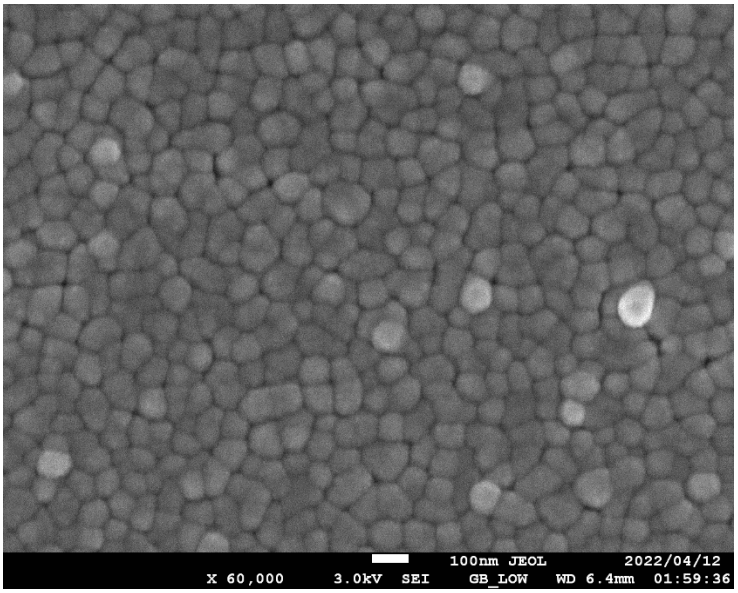

Figure 10: The SEM image of untreated gold-coated thin film surface captured with the JSM-IT800 Schottky field emission scanning electron microscope. The surface shows the distribution of tightly packed Au microstructures. There are no signs of surface contaminants.

2.3.3. Transmission electron microscopy (TEM)

The morphology and size of AuNPs were evaluated. Figure 11 shows the TEM image of bare AuNPs, specifically Au NanoUrchins used in this study. Under TEM analysis, the AuNPs appeared multibranched with spiky uneven surfaces. The AuNPs had an average size of 60 nm.

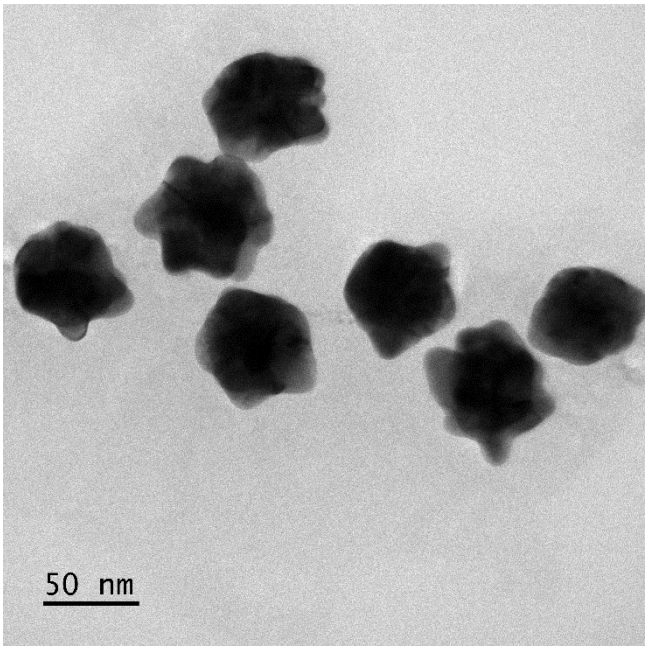

Figure 11: Transmission electron micrograph of gold NanoUrchins. The nanoparticles displayed a multibranched, spiky, uneven surface morphology with an average size of 60nm. The length of the scale bar is 50nm.

2.3.4. UV-vis absorption spectroscopy

To characterize the AuNPs before and after bioconjugation using covalent conjugation chemistry and physical conjugation, UV-vis absorption spectroscopy was performed (Figure 12). The covalent bioconjugation chemistry uses NHS and EDC to enhance the binding of antibodies to PEG which acts as a linker molecule between the antibodies and AuNPs. However, in physical bioconjugation, the antibodies are directly attached to the AuNPs using intermolecular forces. In Figure 12, the absorption peaks between 250 nm – 350 nm represents the concentration of proteins (antibodies) in the samples. Proteins specifically absorb at 280 nm. The absorption peaks between 500 nm and 750 nm represent the absorption wavelength of the gold nanoparticles and the bioconjugate (nanoparticles functionalized with antibodies). At 250 nm – 350 nm, there is no absorption peak for the AuNPs. At 250 nm – 350 nm, the high absorption intensity of antibodies physically conjugated (TB-Bioconjugate-P) to the AuNPs was detected, and lower absorption intensity was recorded for the covalently bioconjugated

antibodies (TB-Bioconjugate-C). At 500 nm – 750 nm, approximately 645 nm absorbance peak for the AuNPs was detected, and a redshift in both the covalent and physically conjugated AuNPs was detected. In this region, a notable difference in absorbance intensity was also recorded between the AuNPs, TB-Bioconjugate-P, and TB-Bioconjugate-C. The absence of a peak for the AuNPs at 250 nm – 350 nm is due to the absence of proteins on the surface of the AuNPs, as this wavelength range is indicative of protein presence. For the physically conjugated AuNPs, the high absorption peak between 250 nm and 350 nm compared to the covalently conjugated method suggests a significant concentration of antibodies in the sample. The higher peak between 500 nm and 750 nm compared to the covalently conjugated method, particularly around 650 nm, shows the characteristic absorption of conjugated AuNPs and indicates that the binding of antibodies affects the optical properties of the nanoparticles, resulting in a reduction in absorbance intensity. For the covalently conjugated AuNPs, the lower absorption peak between 250 nm and 350 nm indicates a lower concentration of antibodies compared to the physically conjugated method. The lower peak between 500 nm and 750 nm compared to the physically conjugated AuNPs and the further redshift indicates higher binding affinity of the method compared to the physical conjugation.

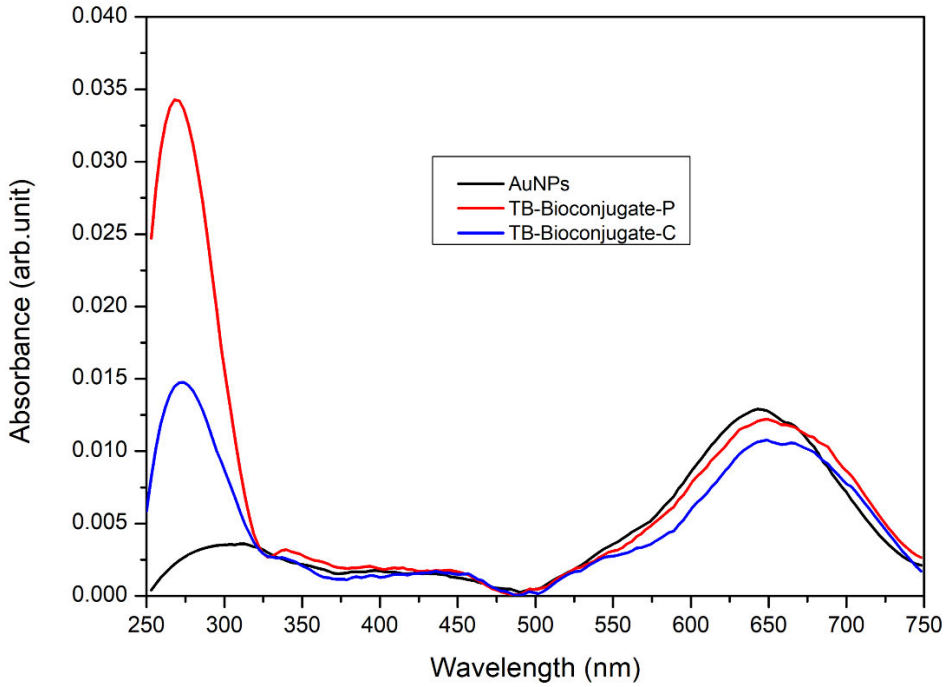

Figure 12: Absorbance spectra of AuNPs, covalent conjugated AuNPs (TB-Bioconjugate-C), and physical bioconjugated AuNPs (TB-Bioconjugate-P). There are clear differences in absorbance intensity of the antibody (A250 nm – 350 nm) and the AuNPs (A500 nm – 750 nm) when comparing the two bioconjugation techniques.

2.4. DISCUSSION

Fluorescent microscopy was used in this study for proof of concept to visually confirm the specificity of mycolic acid binding to the anti-*mycobacterium tuberculosis* antibody. Also, since PhCs are costly, it was crucial to optimize the functionalization protocol on a microscope glass slide before implementing it in PhC-based biosensing. In these techniques, when the mycolic acid is successfully immobilized on the surface, the complementary anti-*mycobacterium tuberculosis* primary antibody will bind to the surface. Upon immobilization of the goat anti-rabbit IgG H&L (Alexa Fluor) secondary antibody specifically designed to bind to the anti-*mycobacterium tuberculosis* antibody, a fluorescence signal is expected. Fluorescence was detected in the experiment sample (Figure 9A) and not in the control sample (Figure 9B), thus confirming the presence of the primary antibody on the surface attached to the mycolic acid biorecognition element. These results also confirm the specificity of mycolic acid to the anti-*mycobacterium tuberculosis* antibody.

To prepare the biosensing surface for LSPR biosensing, a 40 nm Au thin film was deposited on a glass substrate containing a 5 nm layer of Ti. The surface was further characterized using SEM before the immobilization of the biorecognition element. Characterization of the surface is essential for understanding the film's properties and to optimize its performance for optical biosensing. In Figure 10, the Au thin film surface shows no signs of contaminants. The presence of surface contaminants or irregularities can affect the optical properties (e.g., reflectivity, transmission, and other optical phenomena) during analysis and negatively impact the performance and reliability of optical biosensing systems. Surface contaminants can introduce unwanted signal interference, leading to inaccurate or unreliable measurements. Contaminants can absorb or scatter light, altering the optical properties of the sensing surface [182]. Consequently, this interference can result in decreased sensitivity, increased noise, and reduced signal-to-noise ratio, making it challenging to detect the target analyte accurately. Surface contaminants can also contribute to non-specific binding, where molecules in the sample adhere to the sensing surface nonspecifically, even in the absence of the target analyte. This can lead to false-positive signals and reduced selectivity or specificity [183,184]. Contaminants as simple as dust particles can serve as binding sites for non-target molecules, resulting in unreliable and non-reproducible findings. Contaminants can potentially create a physical barrier between the target analyte and the sensing surface, hindering the interaction and detection of the analyte. To mitigate the impact of surface contaminants in optical biosensing, several strategies can be employed, including proper cleaning and surface treatment protocols and the implementation of appropriate controls and reference measurements.

The use of noble metal nanoparticles in biosensing has grown immensely in recent years, particularly for LSPR biosensing applications. Several elements have been demonstrated to support localized surface plasmons, including palladium (Pd), platinum (Pt), silver (Ag), and gold (Au) [17]. Both Ag and Au nanostructures are intensely researched for their role in

biosensing, with their popularity stemming from their high refractive index sensitivity values. Gold is 44 nm/refractive index unit (RIU), and silver is 161 nm/RIU, although gold has a lower sensitivity than silver nanostructures, it is mostly preferred for biosensing applications due to its biocompatibility with biological material and is prone to less oxidation [17]. In this study, AuNPs were used to enhance the detection signal during optical biosensing, detailed in chapters 3 and 4. In these chapters, the AuNPs were characterized using TEM to obtain detailed information about their size, shape, and morphology. This characterization is essential for understanding their properties and tailoring their applications in optical biosensing. On TEM, the AuNPs appeared multibranched with a spiky uneven surface. Multibranched and spiky AuNPs have a highly porous and rough surface structure, providing a significantly larger surface area compared to their spherical counterparts [185]. This increased surface area allows for more efficient immobilization of biomolecules, leading to enhanced sensitivity in biosensing applications. The larger surface area also results in improved binding affinity, thus improving the detection limits of the biosensor [185]. The unique surface morphology of multibranched and spiky AuNPs can lead to signal amplification in biosensing. The presence of multiple branches or spikes on the nanoparticles creates numerous nanogaps, which can trap and amplify the signal produced during the sensing process. This amplification effect enhances the detection sensitivity and improves the signal-to-noise ratio of the biosensor [185–187].

The AuNPs were further functionalized with a signal or secondary antibody using both the covalent and physical bioconjugation techniques. Bioconjugation occurs upon successful binding of the antibodies to the AuNPs surface, thus resulting in LSPR spectrum red-shift which is an increase in wavelength by a few nanometers [177]. From the findings, it was realized that covalent conjugation resulted in high binding efficiency of antibodies to the surface of the AuNPs indicated by the sharp decline in the absorption intensity of the antibodies at 250 nm – 350 nm, and a redshift in the wavelength at 500 nm – 750 nm (Figure 12). The physical

conjugation strategy resulted in lower binding efficiency of antibodies to AuNPs indicated by the high absorbance intensity of the antibodies at 250 nm – 350 nm, and a less prominent redshift in the wavelength at 500 nm – 750 nm (Figure 12). The AuNPs do not absorb at A250 nm – 350 nm; hence no absorption peak was detected. In chapters 3 and 4, the functionalized AuNPs are introduced on the biosensing surface for both LSPR and PhC-based biosensing.

In conclusion, this chapter has successfully reported on a biomolecular interaction experiment, substrate coating with metals, and the design and development of a custom-built optical biosensing setup. The application of fluorescence microscopy as a proof-of-concept experiment has allowed for the visualization and confirmation of the specificity of mycolic acid antigen binding to anti-*mycobacterium tuberculosis* antibodies. This was confirmed with a green fluorescence detected in the experiment samples and absent in the control samples. This step is essential in establishing reproducibility of the biorecognition element immobilization on the biosensing surface, especially in subsequent chapters where the fluorescently labeled secondary antibody is substituted with a non-fluorescently labeled secondary antibody functionalized with AuNPs. While fluorescence microscopy can confirm the specificity of mycolic acid binding to anti-mycobacterium tuberculosis antibodies by differentiating between positive and negative samples, the principal objective of this study is to investigate optical biosensing techniques. The ultimate goal is to pave the way for future applications in the development of point-of-care (POC) diagnostic devices for TB diagnosis. The application of the PVD technique for coating glass substrates with Au was achieved and will be executed in Chapter 3 to induce surface plasmons during LSPR biosensing experiments. Characterization of the Au thin film using SEM provided essential insights into the spatial distribution of gold on the surface of the glass substrate. Additionally, physical and covalent bioconjugation strategies were studied for efficient binding of AuNPs with antibodies and the covalent bioconjugation strategy proved to be an efficient technique for bioconjugation confirmed by UV-vis absorption spectroscopy and

used throughout the study as the recommended method. The inclusion of noble metal nanoparticles, specifically AuNPs, in biosensing applications, demonstrated in the study, aligns with the growing trend in LSPR biosensing. The unique surface characteristics of these commercial AuNPs display multibranched, spiky, and uneven surfaces when characterized using TEM. This highlights their potential for signal amplification. Finally, the designed and developed custom-built optical biosensing setup lay the foundation for subsequent experiments in Chapters 3 and 4, expanding the scope of optical biosensing applications using lasers in Chapter 3 to perform LSPR biosensing, and white light in Chapter 4 to perform PhC-based biosensing.

CHAPTER 3:

LSPR BIOSENSING OF ANTI-MYCOBACTERIUM TUBERCULOSIS ANTIBODIES USING A CUSTOM-BUILT OPTICAL SETUP

3.1. INTRODUCTION

This chapter focuses on the use of optical biosensing, specifically LSPR to detect anti-*mycobacterium tuberculosis* antibodies. Most studies focus on using electrochemical biosensing to detect anti-mycobacterium tuberculosis antibodies and optical biosensing has not been explored [88]. The mycolic acid biorecognition element is immobilized on a gold thin film and anti-mycobacterium tuberculosis antibodies are allowed to react with the biorecognition element. Furthermore, AuNPs bioconjugated with a secondary antibody are introduced on the surface. Before optical biosensing, the biosensor chip is characterized using the characterization techniques optimized in Chapter 2.

Photonics-based optical detection systems leverage the properties of light to enable sensitive and accurate detection of various analytes. These systems utilize the interaction between light and target molecules to provide valuable information for a wide range of applications. In this chapter, the significance and development process of a custom-built optical biosensing setup is explored, including its applications in the detection of biomolecular interactions. The role of surface coating in the development of a biosensor chip and the significance of bioconjugation in optical biosensing are detailed.

Custom-built optical biosensing setups are specialized instrumentation or systems that are designed and assembled to enable the detection and analysis of biological molecules or analytes using optical techniques [188–190]. They are tailored to specific biosensing applications and are assembled according to the unique requirements of the research experiment. Typically, they

include a range of optical components, such as light sources, lenses, filters, detectors, and spectroscopic instruments, and data acquisition modules. These systems are designed to facilitate the interactions between the analyte of interest and the optical detection mechanism, allowing the measurement of specific optical properties or signals indicative of the presence/absence of the target analyte [161,191]. They can be used in a wide range of applications, including but not limited to biomolecular interaction analysis, to study the interactions between biomolecules such as proteins, nucleic acids, and small molecules. This includes determining binding kinetics, affinity measurements, and characterization of molecular interactions [192–195]. These setups provide flexibility in choosing optical techniques, measurement parameters, and experimental conditions. This flexibility allows researchers and scientists to customize the system to meet their specific needs, optimizing the sensitivity, specificity, and accuracy of their measurements. Such setups are essential for advancing biosensing technologies, supporting research, and enabling applications across various fields [194].

The SPR and LSPR are both optical phenomena related to the interaction of light with metal surfaces or nanoparticles [196–199]. However, they differ in their underlying principles and the scale at which they occur. A few key differences exist between SPR and LSPR. Surface Plasmon Resonance occurs when polarized light strikes a thin metal film, usually gold or silver, and couples with the collective oscillations of free electrons (referred to as plasmons) at the metal-dielectric interface. It is based on the excitation of propagating surface plasmons [200–202]. The SPR effect occurs on a larger scale, involving the interaction of light with a macroscopic metal surface or thin film. It can cover a relatively large area, such as the surface of a biosensor chip or a prism surface [200]. The thin metal film on a biosensor chip acts as the sensing region that allows for the interaction of light with the analyte or biomolecules immobilized on its surface [203]. The sensing is based on changes in the refractive index or thickness of the analyte layer. SPR sensors are known for their high sensitivity in detecting changes in refractive index at the

metal-dielectric interface. They are widely used in label-free biomolecular interactions, such as antibody-antigen interactions, protein-protein interactions, DNA hybridization, and drug discovery studies [203,204].

On the other hand, LSPR refers to the excitation of localized plasmons in metallic nanoparticles (e.g., gold or silver nanoparticles), which act as sensing elements [205–208]. In LSPR, the nanoparticles are much smaller than the wavelength of the incident light [209]. Hence, LSPR operates on a nanoscale, where the localized plasmons are confined to the surface of individual nanoparticles [205]. These nanoparticles are functionalized with specific biomolecules or receptors that interact with the analyte of interest. The LSPR signal occurs when incident light interacts with the nanoparticle's surface, causing the electrons to collectively oscillate and generate a resonance response (Figure 13) [206].

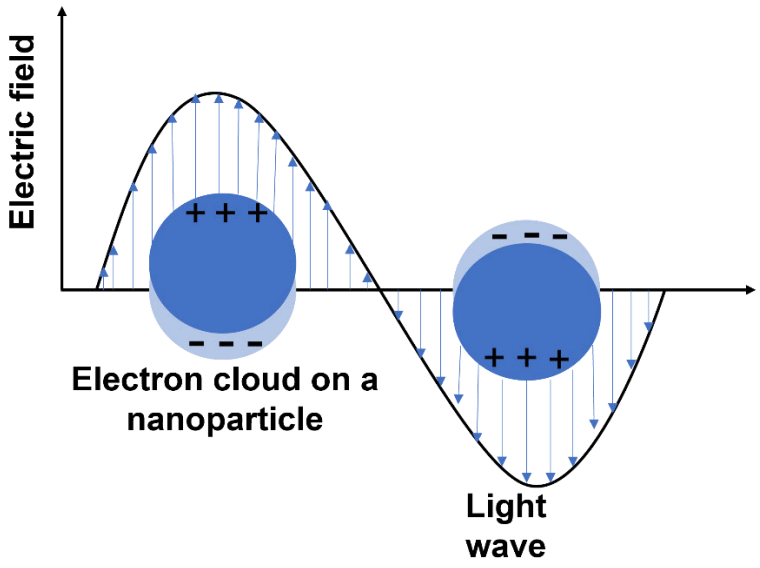

Figure 13: Schematic illustration of plasmon oscillation around a nanoparticle, showing the displacement of the electron charge cloud relative to the nanoparticle.

The signal is highly localized to the vicinity of the nanoparticles and is strongly influenced by their size, shape, and composition [207]. The LSPR response is sensitive to changes in the local refractive index, providing information on molecular binding events [205,210,211]. LSPR-based biosensors have been employed in a range of applications, including label-free biosensing, pathogen detection, disease biomarker analysis, drug monitoring, and allergen detection. In pathogen detection, these biosensors can identify pathogens such as bacteria or viruses using specific antibodies or aptamers as biorecognition elements that bind to target biomolecules [212–214]. This interaction causes a change in the LSPR signal, enabling sensitive and rapid pathogen detection [206,207].

In disease biomarker analysis, LSPR-based biosensors can detect and quantify biomarkers like antigenic proteins, nucleic acids, and infected cells, which are indicative of specific diseases or conditions[215]. The selective binding of biomarkers to the functionalized nanoparticles results in measurable changes in the LSPR signal, allowing for point-of-care diagnosis. [215]. In drug monitoring, these biosensors are promising for tracking drug levels in patient samples. By functionalizing nanoparticles with molecules that interact with specific drugs, changes in the LSPR signal can indicate drug concentrations in real-time, facilitating personalized medicine and therapeutic drug monitoring. [216]. Finally, in allergen detection, LSPR-based biosensors can detect allergens in food or environmental samples by using nanoparticles functionalized with allergen-specific antibodies. The binding of allergens alters the LSPR signal, enabling sensitive and selective detection of allergenic substances.[217,218].

These applications demonstrate the potential of LSPR for developing of point-of-care diagnostic devices, enabling rapid, sensitive, and specific detection of different types of analytes. Further research aiming to optimize the performance and practicality of LSPR-based biosensors is ongoing for practical point-of-care diagnostics. Both SPR and LSPR are valuable in biosensing

and have overlapping applications. Their distinct principles and sensing mechanisms make them suitable for different scenarios. The choice between SPR and LSPR depends on factors such as the desired spatial scale, sensing region, sensitivity requirements, and specific applications. In this chapter, LSPR-based transmission configuration optical biosensing is applied for the label-free detection of anti-*mycobacterium tuberculosis* antibodies. The LSPR-based biosensing technique was chosen over the SPR because it is much more compact and easy to miniaturize. Additionally, the LSPR signal can be significantly improved based on the size, shape, composition, and refractive index of the AuNPs. These properties allow LSPR sensors to detect even minimal changes during biosensing.

3.2. MATERIALS AND METHODS

3.2.1. Gold-coated slide surface functionalization

To functionalize the gold-coated slide surface as illustrated in Figure 14, briefly, the gold thin layer was washed with absolute ethanol and blow-dried with N_2 gas before incubation with 10 mM cysteamine (Cys) (Sigma-Aldrich, M9768) dissolved in nitrogen-saturated absolute ethanol for 18 hours at room temperature to form a gold-cysteamine monolayer. NHS (13 mM) (EDC) (5 mM) with similar molar ratios were used for covalent attachment of stearic acid using carbodiimide coupling chemistry to form an amide bond. After the formation of the cysteamine-stearic acid monolayer, the modified gold-coated surface was washed thoroughly with 70% ethanol and water to remove physically adsorbed stearic acid species. Mycolic acid biorecognition element was enabled to form a self-assembled monolayer on stearic acid by incubating the biosensor chip in a solution of 0.5 mg/ml of mycolic acid in hexane overnight at room temperature. Post incubation, the biosensor chip was rinsed thoroughly with 1x PBS to remove physically adsorbed mycolic acid, and subsequently incubated in a solution of bovine serum albumin (BSA, 1%, v/v) blocking agent for an hour before the addition of the primary

anti-*mycobacterium tuberculosis* antibody. To enhance the sensitivity of the biosensor chip, a goat anti-rabbit IgG H&L secondary antibody (2.1 mg/ml) (Abcam, ab6702) was covalently bioconjugated to gold nanoparticles (AuNPs) (60 nm NanoUrchins) (Cytodiagnostics, 2459298_60U) and herein called TB bioconjugate (AuNPs-IgG). The bioconjugation strategies are described in section 2.1.

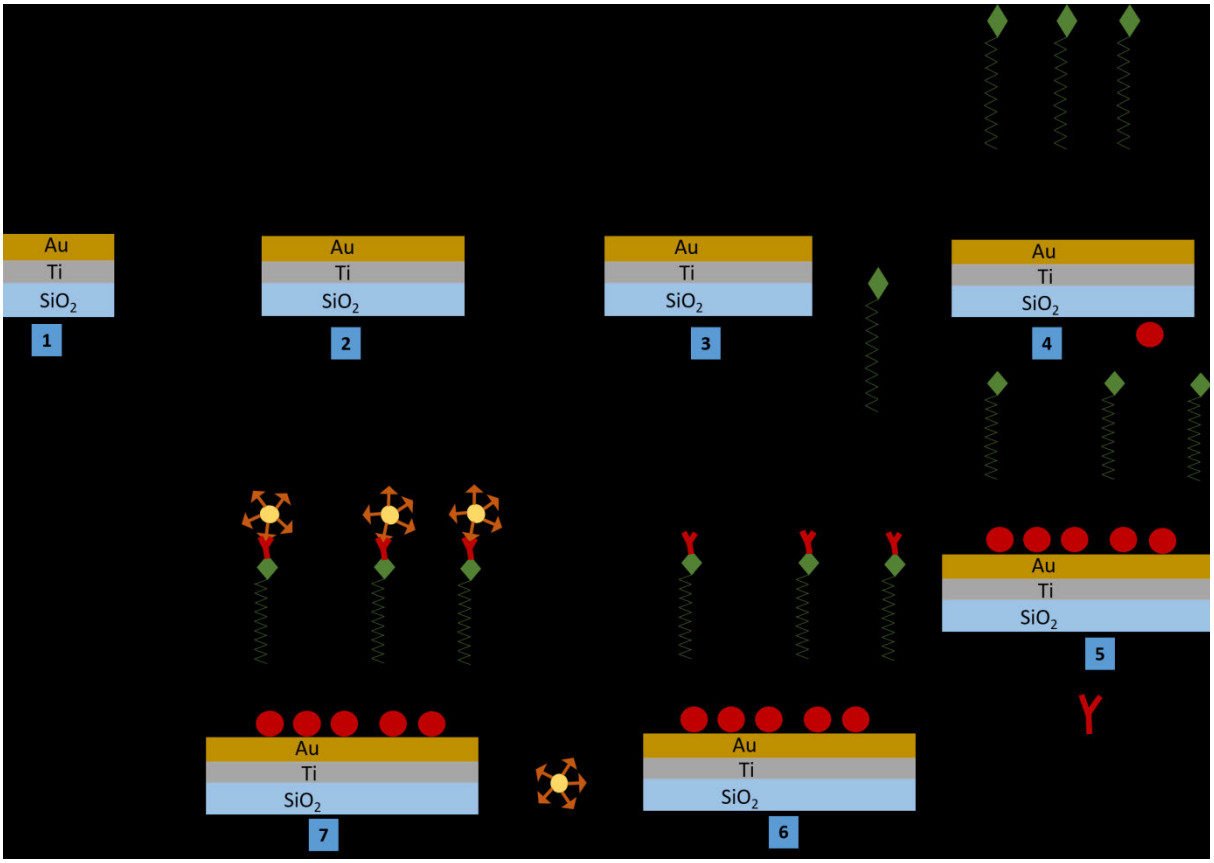

Figure 14: A schematic representation of the gold-coated slide functionalization steps. Schematic key steps include the following: (1) a biosensor chip with a layer of gold deposited on a thin layer of Ti sputtered on a glass substrate, (2) immobilization of cysteamine monolayer on the thin gold surface, (3) covalent attachment of STA to cysteamine and formation of amide bonds using NHS and EDC, (4) development of a SAM of mycolic acid through inter-molecular forces existing between stearic acid and mycolic acid, (5) introduction of BSA to prevent non-specific binding of molecules, (6) binding of anti-*mycobacterium tuberculosis* primary antibody to mycolic acid, (7) binding of gold-bioconjugated secondary antibody to the primary antibody. (BSA: Bovine serum albumin)

3.2.2. Characterization of gold nanoparticles before and after bioconjugation

3.2.2.1. Ultraviolet-visible absorption spectroscopy

UV-vis absorption spectroscopy was performed to characterize the AuNPs before and after bioconjugation. Covalent bioconjugation chemistry optimized in section 2.2.4.1 was adapted to bioconjugate AuNPs to goat anti-rabbit IgG H&L secondary antibody (2.1 mg/ml). UV-vis absorption spectroscopy measurements were obtained using the NanoDrop 8000 spectrophotometer. The data were further analyzed using OriginPro software.

3.2.2.2. Dynamic light scattering (DLS)

DLS was performed to monitor changes in size distribution by intensity before and after bioconjugation of AuNPs with a secondary antibody. Malvern Zetasizer Nano ZS (Malvern Instruments Ltd, United Kingdom) was used to perform DLS. AuNPs, bioconjugated AuNPs with anti-*mycobacterium tuberculosis* (referred to as TB-bioconjugate), and bioconjugated AuNPs with mycolic acid TB antigen were analyzed. Samples were analyzed in triplicates and repeated three times ($n=3$) at 25°C, and the dispersant refractive index was 1.330 with a viscosity of 0.8872 cP.

3.2.3. Characterization of the functionalized gold biosensing surface

3.2.3.1. Scanning electron microscopy

Gold-coated biosensor chip was developed using the HEX benchtop thin film deposition system (Korvus Technology Ltd, United Kingdom) as previously described. Briefly, a gold evaporation slug (Merck Millipore, 373168-6.4G) was used to form the thin gold film. A 5 nm layer of Ti was sputtered on the SiO_2 substrate before Au deposition (~40 nm) using e-beam evaporation. Three sample groups, including the bare Au-thin film sample, experiment, and control samples,

were analyzed. The Experiment sample consisted of mycolic acid, anti-*mycobacterium tuberculosis* antibody, and goat anti-rabbit IgG H&L secondary antibody bioconjugated to AuNPs (referred to as TB-bioconjugate). The control sample did not have an anti-*mycobacterium tuberculosis* antibody on the biosensing surface. The SEM data were acquired using the JSM-IT800 Schottky field emission scanning electron microscope (JEOL Ltd, Japan). All samples were analyzed for SEM without coating.

3.2.3.2. Energy-dispersive X-ray spectroscopy

EDX spectroscopy was performed to study the different elements present on the biosensing surface, and both EDX and SEM techniques were used to characterize the functionalized biosensing surface. The gold-coated biosensor chip functionalized in section 3.2.1 was used to perform SEM and EDX spectroscopy. This gold-coated biosensor chip consisted of a glass substrate (1 mm thick); a 40 nm Au thin layer deposited on a 5 nm thin layer of Ti. EDX was performed using the SEM instrument, and each sample was analyzed for both SEM and EDX spectroscopy.

3.2.3.3. Atomic force microscopy

Atomic force microscopy (AFM) was used for surface morphology studies to perform layer-by-layer characterization of the biosensing surface of the biosensor chips at different stages of functionalization. The AFM images were captured with a Vecco AFM system (Digital Instruments, USA) using a silicon cantilever tip. The tip has a curvature radius of 10 nm and is n-doped silicon, with a resonance frequency of 204-497 kHz and a force constant of approximately 10-130 N/m. Images acquired by the AFM instrument were analyzed using Nanoscope software.

3.2.4. Fourier-transform infrared spectroscopy detection of anti-*mycobacterium tuberculosis* antibody

The FTIR measurements of AuNPs, TB-bioconjugate, and TB-bioconjugate reacted with mycolic acid TB antigen were analyzed in transmission mode using a Perkin Elmer Spectrum 100 FTIR spectrometer equipped with a DTGS detector. The spectra were measured in the 4000 to 550 cm^{-1} wavenumber regions. Before data acquisition, the spectrometer plate and crystal were thoroughly cleaned with tissue and isopropanol and cleaned in between sample analyses. The spectrum of air was used as background before each sample analysis. The background and sample spectra were taken in a room with a temperature around 21 - 23°C, at a spectral resolution of 4 $cm^{-1,}$ and to each measurement, 32 scans were co-added and averaged to achieve an acceptable signal-to-noise ratio. In all cases, spectra resolution was maintained at 16 cm^{-1}. The original FTIR spectra were baseline-corrected using Perkin Elmer Spectrum software.

3.2.5. LSPR biosensing and detection of anti-*mycobacterium tuberculosis* antibodies

A custom-built transmission spectroscopy configuration optical biosensing setup was used to perform LSPR biosensing. The setup was assembled using a 512 nm green light source with a power of 3.1 milliwatts (mW). The light was collimated using collimating lenses and focused on the biosensor chip sample placed on the sample stage. Transmitted light was collected through a 10x microscope objective, and a 50/50 beam splitter directed the light to the imaging system and the spectrometer through a fiber. The imaging system was formed by a charge-coupled device (CCD) camera (Watec, Pine Bush, New York) connected to a computer and was used to visualize events taking place on the sample stage. Sample groups were prepared in triplicates under the same conditions and repeated three times ($n=3$). During sample analysis, background measurements were taken at the same setting before each recording. Transmitted light was focused into the fiber using a focusing lens and directed to the USB 4000 portable

spectrometer (Ocean Optics Inc, United States) connected to the computer for data acquisition and data analysis (Figure 15). Further data analysis was performed using OriginPro software.

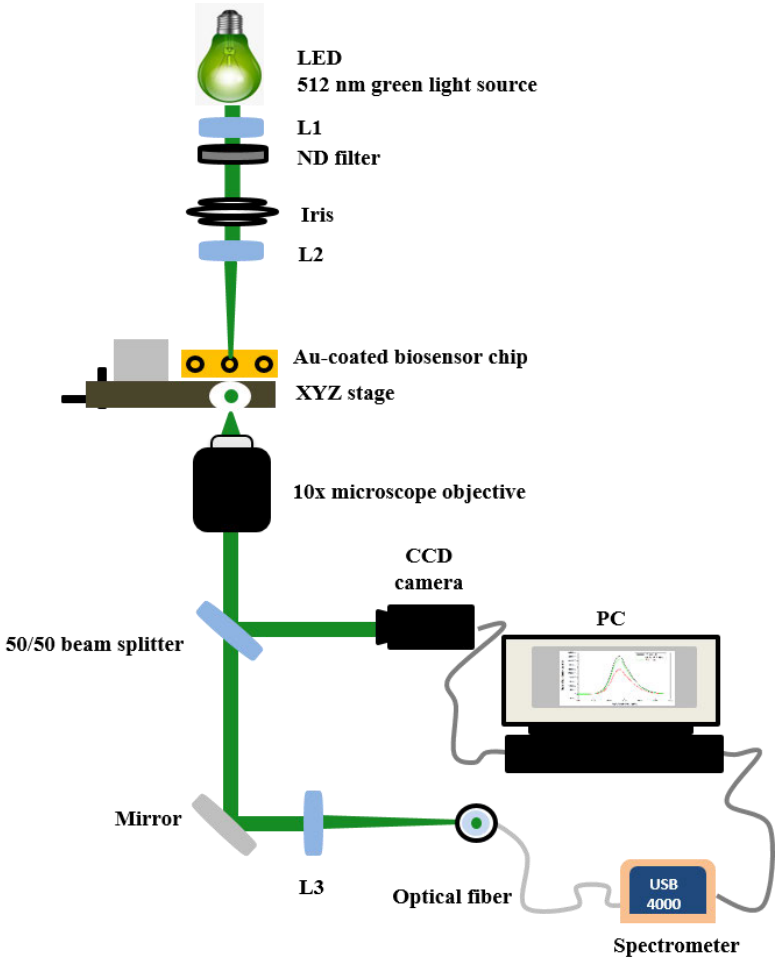

Figure 15: Experimental setup of the transmission spectroscopy setup used for LSPR biosensing. The setup consists of a 512 nm green light source with a power of 3.1 mW, collimating lenses (L1 and 2), XYZ stage, a 10x microscope objective, and an imaging system consisting of a CCD camera and computer, focusing lens (L3), an optical fiber, and a portable USB spectrometer connected to a computer.

3.3. RESULTS

3.3.1. UV-vis absorption spectroscopy

UV-vis absorption spectroscopy was used to characterize AuNPs before and after bioconjugation to goat anti-rabbit IgG H&L secondary antibody. Changes in peak wavelength and absorption intensity between the AuNPs and the functionalized AuNPs were detected.

Figure 16 shows the absorption spectrum of AuNPs before bioconjugation (black spectrum) and the spectrum of AuNPs after bioconjugation (red spectrum). Bioconjugation or binding of the secondary antibody to the AuNPs resulted in a 10nm redshift in the absorption spectrum wavelength. The AuNPs showed absorption peak intensity at 575 nm before bioconjugation and 585 nm after bioconjugation.

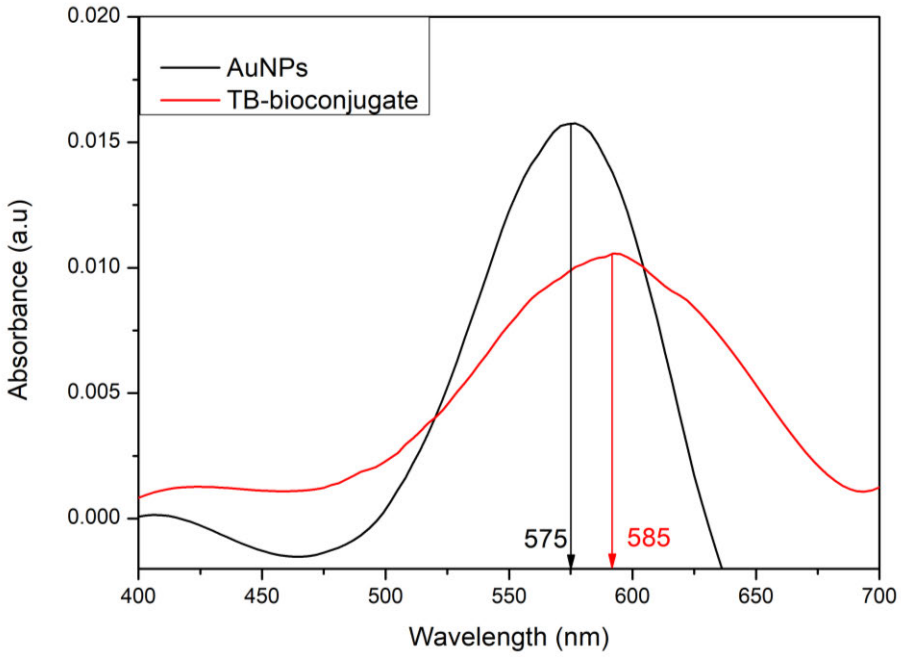

Figure 16: A graphical representation of UV-vis absorption spectrograph for the bioconjugation of AuNPs to goat anti-rabbit IgG H&L secondary antibody. Measurements were taken before and after bioconjugation. The black line represents the spectrum of AuNPs before conjugation, and the red line represents the spectrum of AuNPs after bioconjugation with a secondary antibody.

3.3.2. Dynamic light scattering

Further characterization of AuNPs was performed to determine the particle size distribution using dynamic light scattering (DLS). The DLS measurements of changes in size distribution by intensity were used to study the AuNPs before and after bioconjugation with the secondary antibody. Sample groups included AuNPs, TB-bioconjugate, and TB-bioconjugate in the presence of mycolic acid (Figure 17). The Z-average value of the AuNPs before bioconjugation was 164 d.nm and increased to 190 d.nm after bioconjugation (Figure 17B). The average peak

intensity of the AuNPs, TB-bioconjugate, and TB-bioconjugate in the presence of mycolic acid was 11.3, 9.65, and 8.9, respectively.

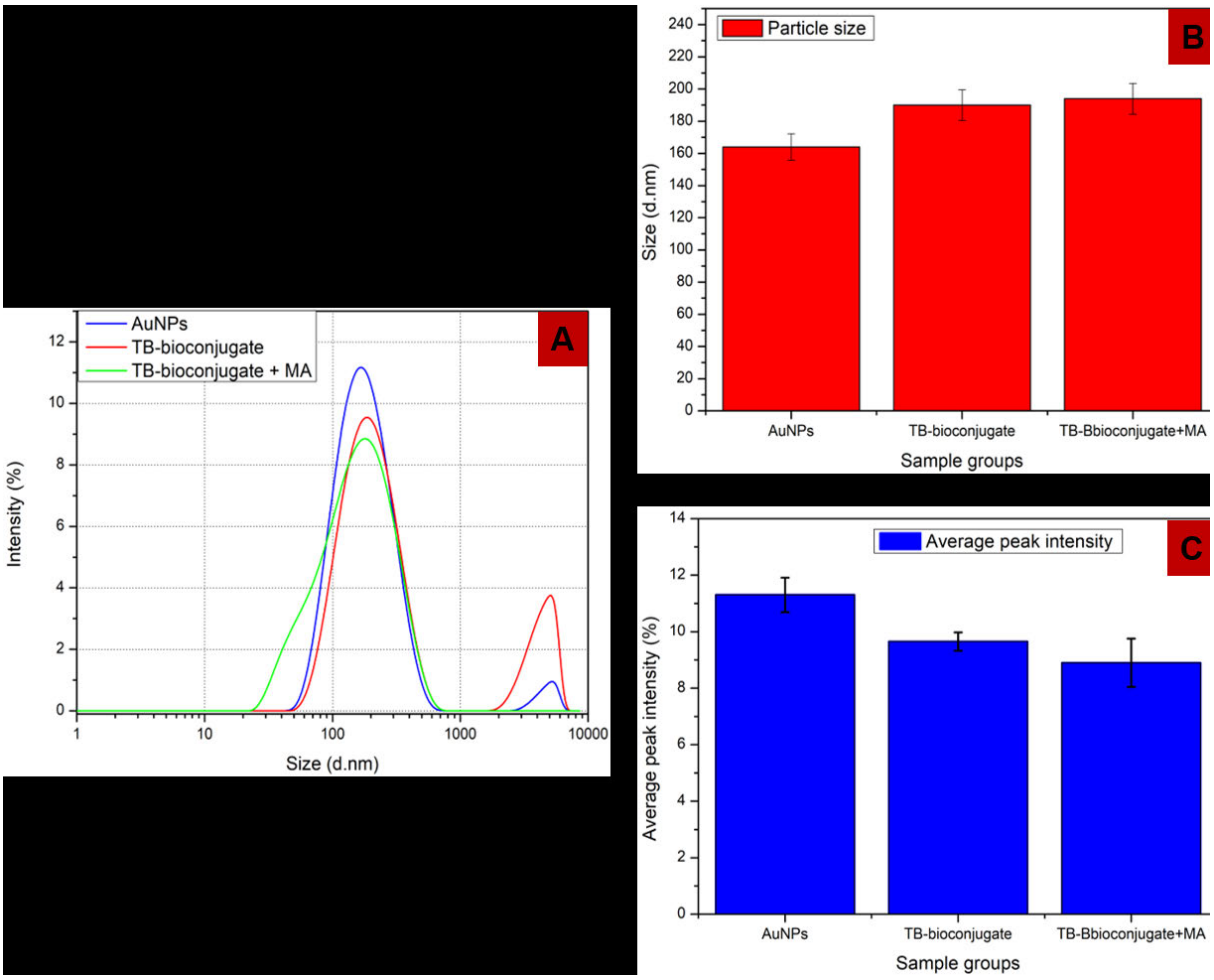

Figure 17: DLS data showing (A) size distribution by the intensity of AuNPs before and after bioconjugation (TB-Bioconjugate) and bioconjugate in the presence of mycolic acid, (B) particle size differences, and (C) average peak intensity differences. DLS was performed on a Zetasizer instrument using water as a dispersant at 25°C. Samples were analyzed in triplicates and repeated three times (n=3).

3.3.3. Scanning electron microscopy

The SEM end-point analysis was performed to characterize the biosensing surface, specifically to visualize the presence or absence of AuNPs (NanoUrchins) on the biosensing surface. To perform SEM, three sample groups were prepared, namely a thin gold film surface, the experiment sample, and the control sample. The experiment and control samples were prepared on a thin gold film surface. The thin gold sample with an approximately 40nm Au layer was

used as a reference to visualize the distribution of Au on the surface. The experiment sample surface consisted of mycolic acid TB antigen, anti-*mycobacterium tuberculosis* primary antibody, and AuNPs bioconjugated with goat anti-rabbit IgG H&L secondary antibody. There was no anti-*mycobacterium tuberculosis* antibody on the biosensing surface of the control sample. The control sample was used to test for the specificity of the mycolic acid biorecognition element to the primary antibody. SEM images were obtained without coating the samples. A uniform, evenly distributed, closely, and densely packed layer of gold was observed in the SEM image of the Au thin film reference sample (Figure 18A). The film shows a columnar layer represented by round-shaped structures. Spiky, uneven, and multi-branched Au NanoUrchins structures were observed in high quantities on the surface of the experiment sample (Figure 18B) and in small traces on the surface of the control sample (Figure 18C). The visualized Au NanoUrchins are evenly dispersed, with no signs of agglomerations observed on the surface.

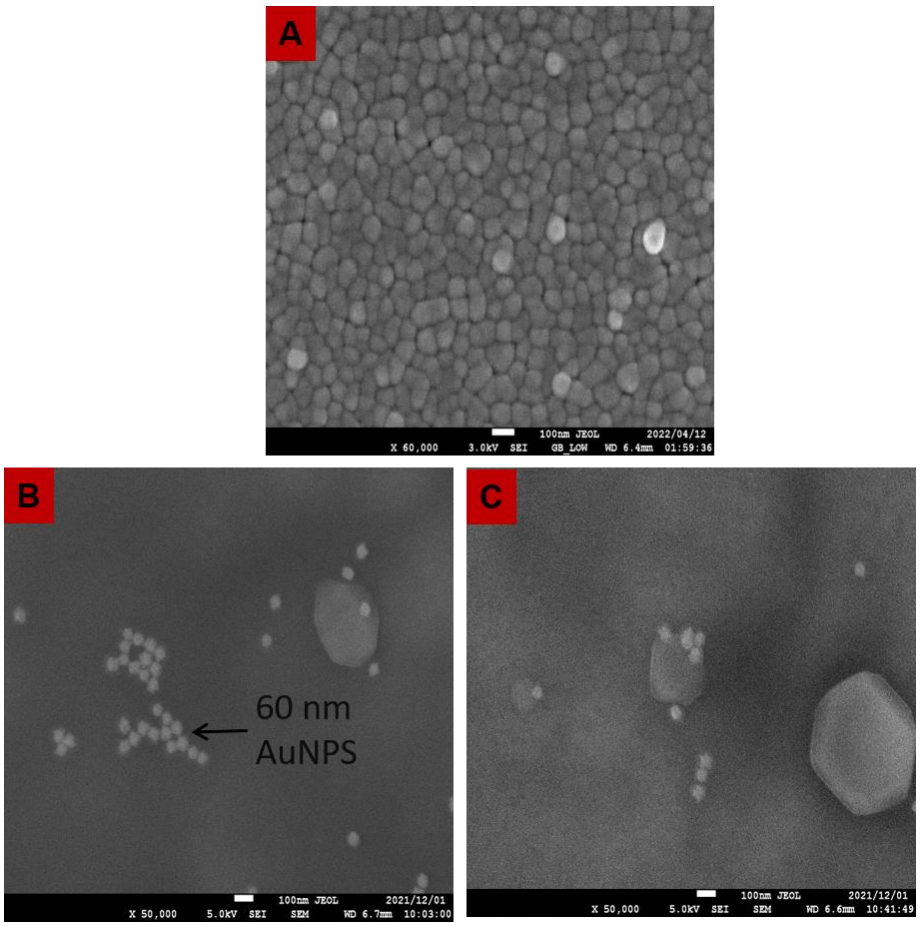

Figure 18: SEM images of the biosensing surface of the thin bare gold surface (A), experiment sample (B)) and control sample (C). The experiment sample surface consists of a self-assembled monolayer of mycolic acid TB antigen, anti-*mycobacterium tuberculosis* antibody, and a secondary antibody bioconjugated to AuNPs. The control sample lacks an anti-*mycobacterium tuberculosis* antibody on the surface. The AuNPs (NanoUrchins) under SEM are visualized as tiny bright spots resembling stars. A small number of bioconjugated AuNPs were observed on the biosensing surface of the control sample.

3.3.4. Energy-dispersive X-ray spectroscopy

EDX spectroscopy was specifically used to qualitatively determine the elemental composition between the reference sample (Au thin film), experiment, and control samples. The elemental composition, as per Figure 19A - C, shows that Au and Si dominate over all the other elements detected on the biosensor chip and are present in all sample groups. Si is from the SiO_2 glass substrate, and Au is from the Au thin film and/or AuNPs. Si was detected at a weight percentage lower than gold in all sample groups; however, its atomic percentage was higher than Au in all the samples.

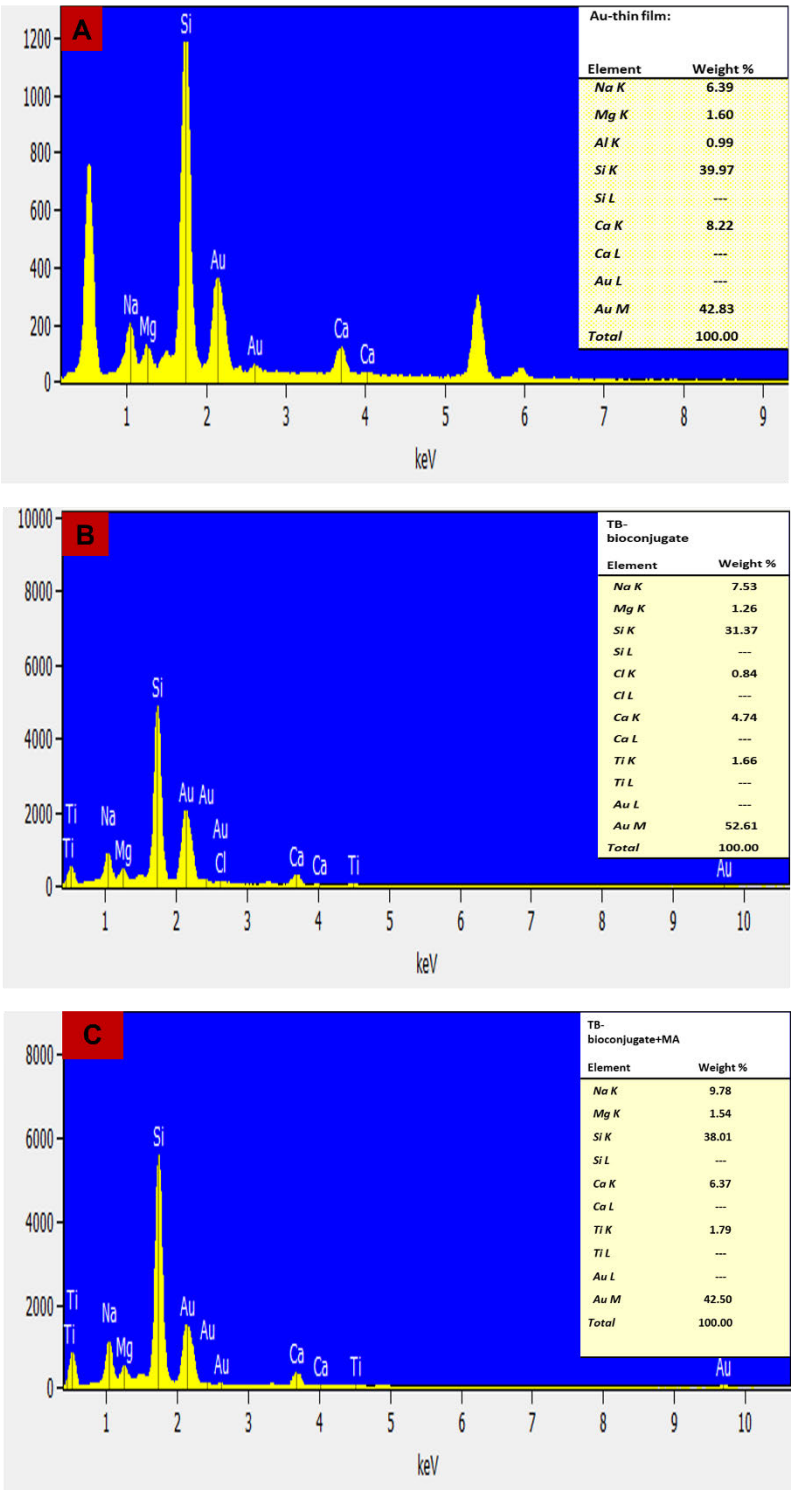

Figure 19: EDX spectrographs of the bare gold-coated surface (A), the experiment sample (B), and the control sample (C). The biosensing surface of the experiment sample consisted of mycolic acid TB antigen, an anti-*mycobacterium tuberculosis* primary antibody, and a goat anti-rabbit IgG H&L secondary antibody bioconjugated to AuNPs. The main elements obtained from all three samples are Au, Si, Ti, Na, Mg, Ca, and Cl. There were significant differences in the weight and atomic percentage of Au detected between the experimental sample compared to the control and reference samples which had approximately similar percentages.

The weight percentage of Au in the reference sample, experiment, and control sample was 42.83, 52.62, and 42.50, and the atomic percentage was 9.77, 13.77, and 9.57, respectively. The weight and atomic percentage of Au were higher on the experiment sample containing immobilized bioconjugated AuNPs, as seen on SEM (Figure 18B). Common elements detected in all sample groups were magnesium (Mg), sodium (Na), and calcium (Ca). In addition, chlorine (Cl) was detected only in the experiment sample, and aluminium (Al) was detected at very low levels in the reference sample instead of Ti detected in both the experiment and control samples.

3.3.5. Atomic force microscopy

Atomic force microscopy (AFM) was used to perform layer-by-layer characterization during the process of functionalizing the biosensor chip. Changes in height and surface roughness at various stages of biosensor chip functionalization were studied. The images taken using AFM are shown in Figure 20, and each of the scans represents a 5µm X 5µm lateral area that was scanned. AFM was used to characterize surfaces of the Au thin film layer, MA, MA+1^0 Ab, MA+1^0 Ab+2^0Ab, and MA+2^0Ab (table 1).

Table 1: List of sample groups and their full descriptions

MA	Mycolic acid
MA+1^0 Ab	Mycolic acid + anti-mycobacterium tuberculosis primary antibody
MA+1^0 Ab+2^0Ab	Mycolic acid + anti-mycobacterium tuberculosis primary antibody + goat anti-rabbit IgG H&L secondary antibody
MA+2^0Ab	Mycolic acid + goat anti-rabbit IgG H&L secondary antibody

The Au-thin layer, referred to as the background sample, had nothing immobilized on the surface. The mycolic acid sample, referred to as the reference sample, consisted of mycolic acid immobilized on a surface consisting of cysteamine. The cysteamine was used as a linker for mycolic acid, which is the biorecognition element. Stearic acid was covalently attached to the cysteamine before the introduction of mycolic acid. The MA+1^0 Ab sample had an anti-*mycobacterium tuberculosis* antibody introduced onto the mycolic acid surface. The MA+1^0 Ab+2^0Ab referred to as the experiment sample, consisted of AuNPs bioconjugated with goat anti-rabbit IgG H&L secondary antibody and added to the surface containing the primary antibody. Lastly, the MA+2^0Ab sample, referred to as the control sample, was used to test for non-specific binding. It consisted of AuNPs bioconjugated with goat anti-rabbit IgG H&L secondary antibody applied to a mycolic acid-containing surface in the absence of the anti-*mycobacterium tuberculosis* primary antibody.

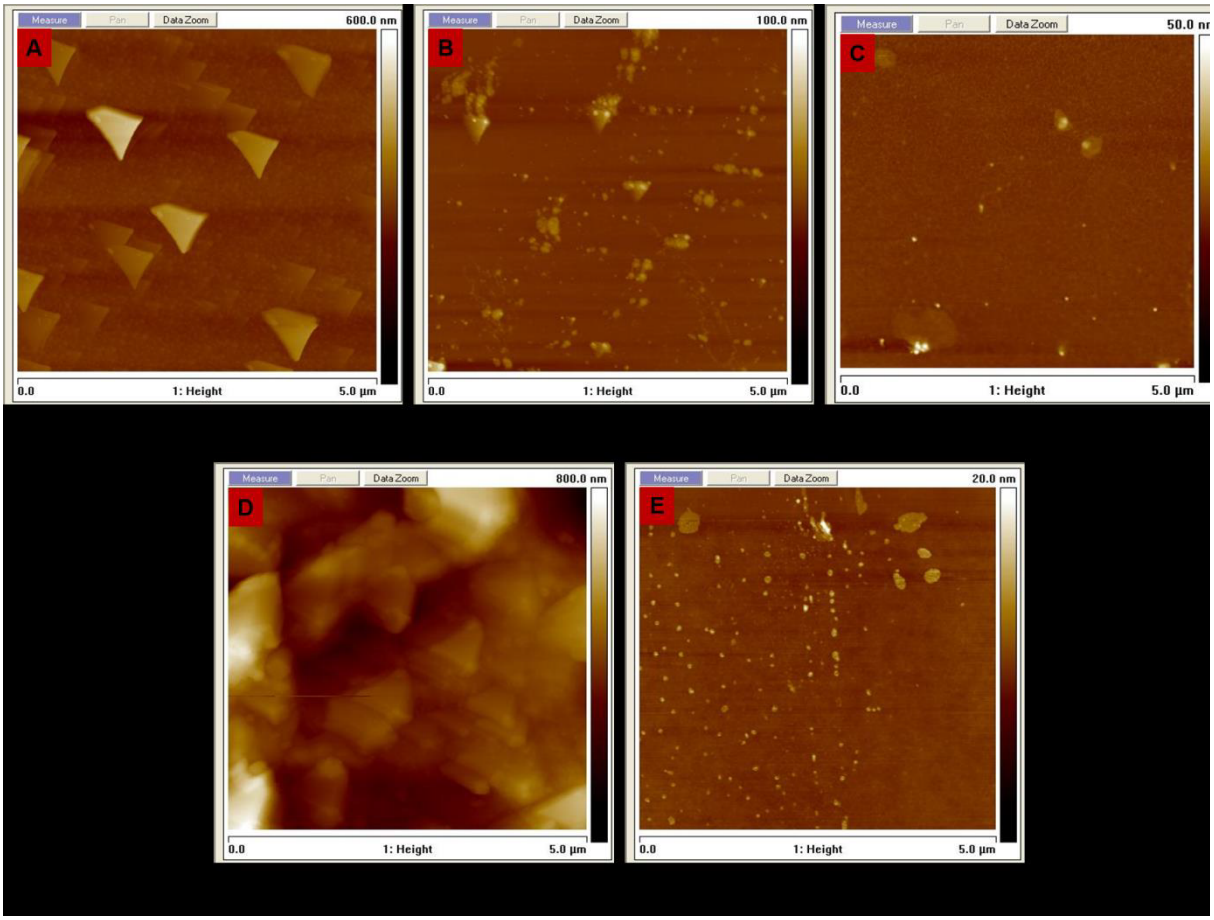

Figure 20: Atomic force microscopy micrographs of the five sample groups captured at different stages of the biosensor chip functionalization. Sample groups include Au thin film layer (A), MA (B), MA+1^0Ab (C), MA+1^0Ab+2^0Ab (D), and MA+2^0Ab (E). A sharp increase in height and surface roughness was observed in MA+1^0 Ab+2^0Ab sample (D), confirming the successful binding of the bioconjugated AuNPs with the goat anti-rabbit IgG H&L secondary antibody added on a surface containing anti-*mycobacterium tuberculosis* primary antibody. The binding of the bioconjugated AuNPs to the surface is critical for detection signal enhancement during optical biosensing.

Homogenous and smooth coverage of the surface was observed in the Au thin film sample (Figure 20A). Numerous islands were formed on the surface when mycolic acid was introduced (Figure 20B). A similar pattern was observed when the bioconjugated antibody was introduced on the mycolic acid surface and subsequently washed. Interestingly, when the primary antibody was introduced to react with mycolic acid, the islands disappeared, and the surface displayed a smooth morphology (Figure 20C). On the contrary, various large and rough structures were visualized in the MA+1^0 Ab+2^0Ab sample (Figure 20D). The roughness of the surface increased

significantly on the surface containing AuNPs bioconjugated to goat anti-rabbit IgG H&L secondary antibody (Figure 20D). The Z-range increased from 289 nm in the Au thin film sample (Figure 20A) to 681 nm in the MA+1^0 Ab+2^0Ab sample containing immobilized bioconjugated AuNPs (Figure 20D).

3.3.6. Fourier-transform infrared spectroscopy detection of anti-*mycobacterium tuberculosis* antibody

FTIR spectroscopy analysis is a qualitative optical detection technique used to examine the existence of surface functional groups [219]. FTIR was carried out to identify the possible functional groups formed during the bioconjugation of AuNPs with anti-*mycobacterium tuberculosis* antibody and monitor spectral changes due to the interaction between the anti-*mycobacterium tuberculosis* antibody and mycolic acid TB antigen. A sample of AuNPs was used as a reference (Figure 21A). FTIR was performed using evaporated samples of AuNPs, TB-bioconjugate, and the TB-bioconjugate reacted with mycolic acid TB antigen. Figure 21 shows the FTIR spectra of the three sample groups. The AuNPs (Figure 21A) presented prominent peaks at 2983 cm^{-1}, 2923.2 cm^{-1}, 2830.4 cm^{-1} wavenumbers indicating alkane C-H stretching; 2287.8 cm^{-1} indicating the presence of O=C=O; 1558.6.6 cm^{-1} representing N-O stretching, and 1400.8 cm^{-1} representing C-H bending. The TB-bioconjugate (Figure 21B) displayed a very similar spectra pattern to the AuNPs, however, with reduced percentage transmittance and the introduction of very few new wavenumbers. The 2983 cm^{-1} also present in AuNPs spectra represents C-H stretching, 1980.7 cm^{-1} for C-H bending, 1656.6 cm^{-1} C=C stretching, and 1388 cm^{-1} for O-H bending. When mycolic acid was added to the bioconjugated AuNPs (Figure 21C), strong bands were yielded at 3337 cm^{-1}, 2958 cm^{-1}, 2922 cm^{-1}, 2956 cm^{-1}, 1638 cm^{-1}, 1462 cm^{-1}, and 1378 cm^{-1}.

The FTIR analysis was successful in identifying functional groups involved in the bioconjugation of AuNPs with anti-*mycobacterium tuberculosis* antibodies and monitored spectral changes upon interaction with the mycolic acid TB antigen. The spectra of AuNPs, used as a reference sample, showed some characteristic peaks similar to the TB-bioconjugate, with some reduced transmittance and a few new wavenumbers. This suggests successful bioconjugation and supports the UV-vis absorption spectroscopy results (section 3.3.1). Upon the addition of mycolic acid to the TB-bioconjugate, significant new bands were observed, indicating further interaction between the antigen and the bioconjugated gold nanoparticles.

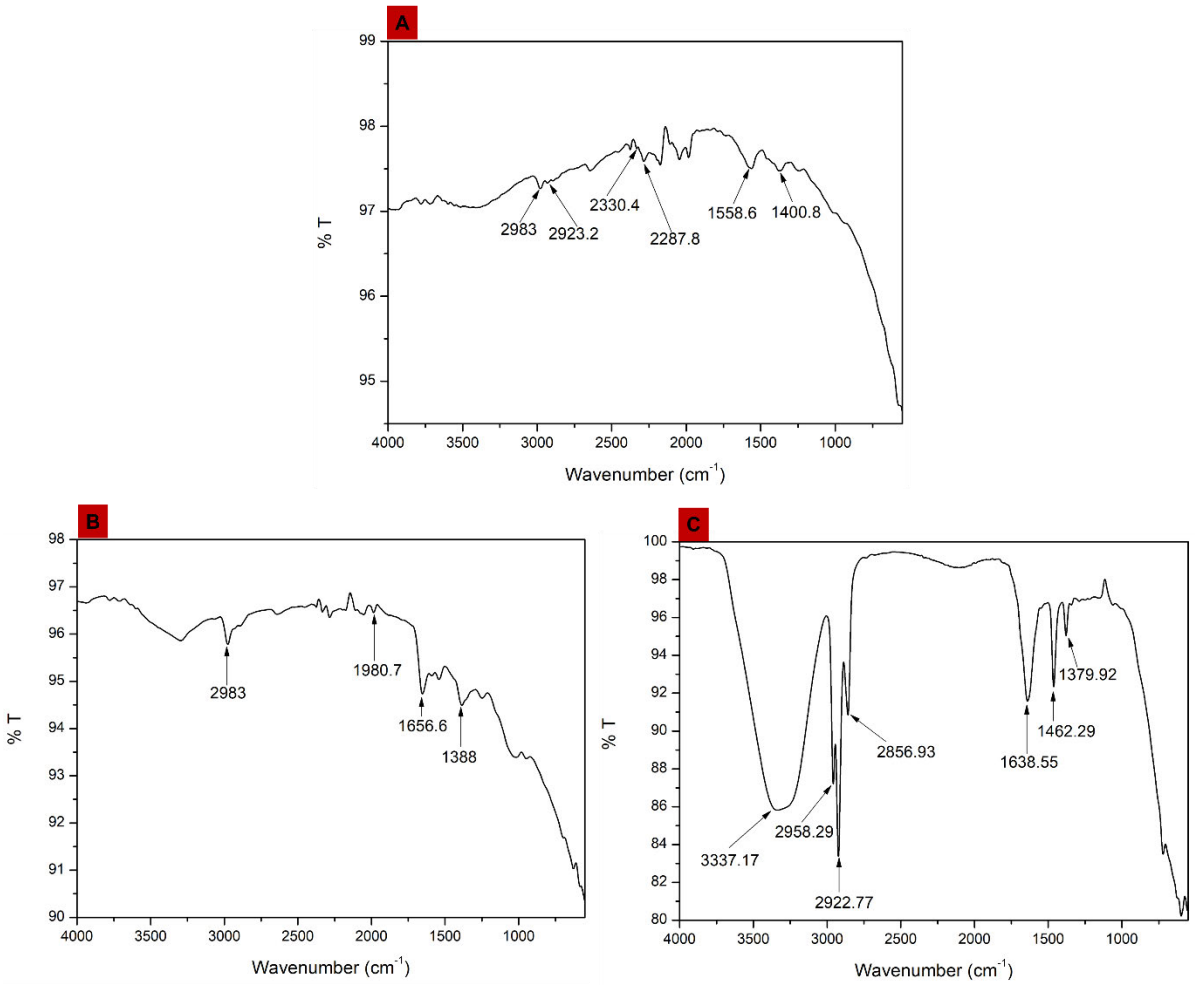

Figure 21: FTIR spectra of AuNPs (A), TB-bioconjugate (B), and the TB-bioconjugate reacted with mycolic acid TB antigen (C) dissolved in hexane.

3.3.7. Localized surface plasmon resonance biosensing and detection of anti-*mycobacterium tuberculosis* antibodies

The optimized biosensor chip was analyzed using a custom-built LSPR biosensing experimental setup (Figure 15). Samples were prepared in triplicates under the same conditions and repeated three times (*n=3*). The transmitted intensity between the five sample groups was measured. Sample groups included Au-thin layer, MA, MA+1^0 Ab, MA+1^0 Ab+2^0Ab, and MA+2^0Ab. Refer to section 3.3.5 Table 1 for a full description of the sample groups. Measurements of transmitted intensity of the five sample groups are depicted in Figure 22A. The transmitted intensity measurements of the five sample groups demonstrated that there was a higher percentage of light transmitted in the Au-thin film sample used as the background. The mycolic acid sample transmitted less light compared to the untreated gold surface. The MA+2^0Ab sample used to test for non-specific binding transmitted less light compared to the MA. The MA+1^0 Ab sample transmitted less light compared to the MA+2^0Ab. The MA+1^0 Ab+2^0Ab sample reported the lowest transmitted intensity.

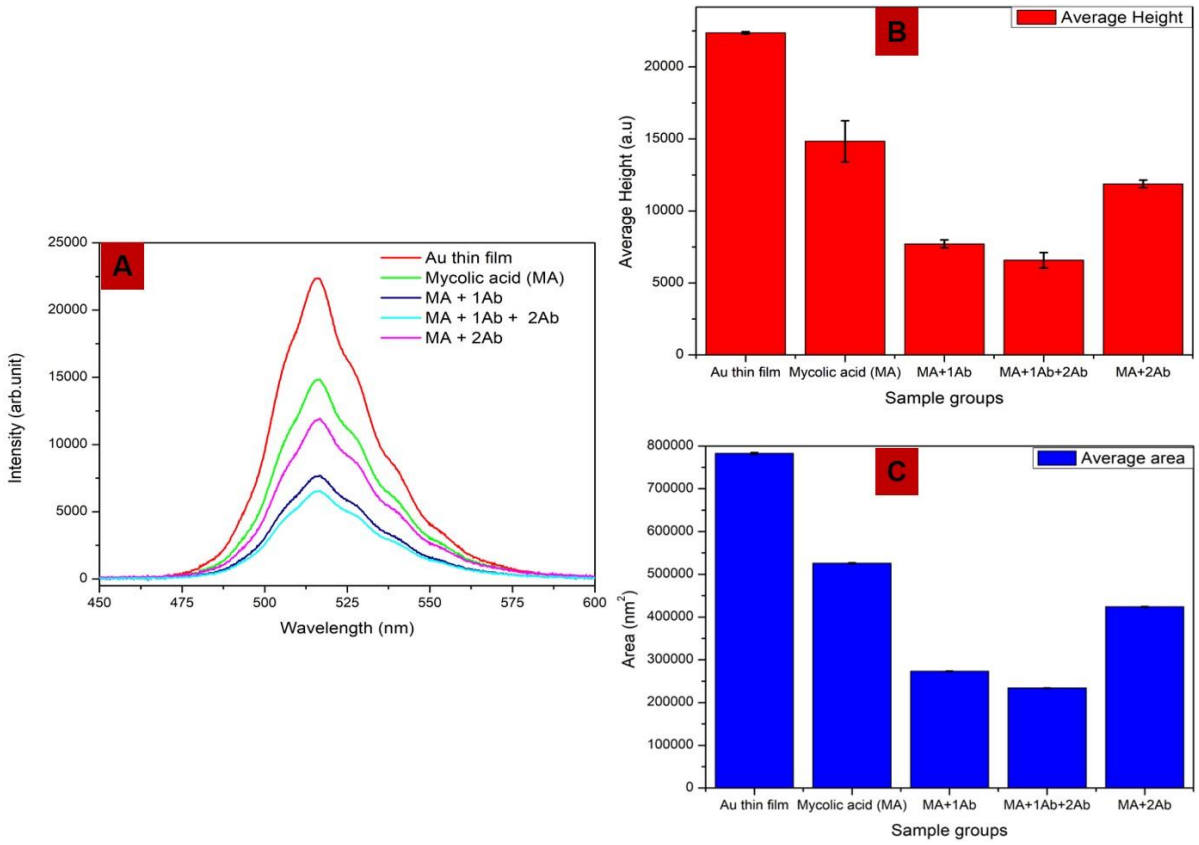

Figure 22: Transmitted intensity measurements for LSPR biosensing of anti-*mycobacterium tuberculosis* antibody. The transmitted intensity between the Au thin film layer, MA, MA+1Ab, MA+1Ab+2Ab, and MA+2Ab. The Au-thin layer was used as the background sample since all the sample groups were developed from it. The MA sample was used as a reference sample since all the sample groups except the background sample have MA on the surface as the biorecognition element. (A) shows transmitted intensity peaks of the five sample groups, whereby the Au-thin layer transmitted a high percentage of light, followed by MA, MA+2Ab, MA+1Ab, and the MA+1Ab+2Ab sample reported the lowest transmitted intensity. (B) show differences in height (B) and area under graph (C) for each sample group spectrum observed in (A). Sample groups were prepared in triplicates under the same conditions and repeated three times (n=3).

3.4. DISCUSSION

In this chapter, a custom-made optical biosensor chip consisting of a thin gold-coated layer deposited on a Ti layer on a glass substrate was developed using the Korvus Technology HEX benchtop thin film deposition system. The developed biosensor chip was subsequently functionalized with mycolic acid pathogen-specific TB antigens for the detection of anti-*mycobacterium tuberculosis* antibodies. Functionalized and characterized AuNPs were

introduced to the biosensing surface before detection measurements using the custom-built LSPR biosensing setup. The AuNPs were characterized before and after bioconjugation using UV-vis absorption spectroscopy and dynamic light scattering. The introduction of the functionalized AuNPs to the biosensing surface plays a crucial role in changing the material refractive index, thus enhancing the detection signal of the biosensor chip.

AuNPs have unique optical properties that can be easily manipulated compared to bulk gold. These special characteristics provide a plethora of advantages, especially in biosensing and diagnostic imaging. One of the major attributes is the interaction of light with electrons on its exterior [220]. The resonance wavelength and bandwidth of the AuNPs are dependent on the shape, particle size, refractive index of the surrounding media, and temperature [220]. Herein, Covalent conjugation chemistry was applied for the bioconjugation of AuNPs with the secondary antibody. EDC and NHS chemistry were used to bind goat anti-rabbit IgG H&L secondary antibody to PEG. In this chemistry, EDC and NHS activate the carboxyl groups of the AuNP surface to form an intermediate that interacts with the amine group (NH_2) on the antibody [219]. Bioconjugation occurs upon successful binding of the antibody to the AuNPs surface, thus resulting in a redshift in absorption spectrum by a few nanometers when analyzed using UV-vis absorption spectroscopy [221]. This was observed in section 3.3.1 (Figure 16). The observed UV-vis reduction in absorption intensity and a detectable 10 nm redshift in the wavelength in Figure 16 is an indication of successful bioconjugation of the AuNPs to the secondary antibody. The redshift detected in the AuNPs-IgG bioconjugate complex might be a result of the changes in the dielectric environment surrounding the AuNPs [224,225].

Light in the near-UV and visible range of the electromagnetic spectrum has an energy of about 150 - 400 kJ mol^{-1} [222]. This energy promotes electrons from the ground state to an excited state. A spectrum is obtained when the absorption of light is measured as a function of its

frequency or wavelength [222]. Molecules with electrons in delocalized aromatic systems often absorb light in the near-UV (150–400 nm) or the visible (400–800 nm) region. Absorption spectroscopy is usually performed with molecules dissolved in a transparent solvent. The absorbance of a solute depends primarily on its concentration; hence absorption spectroscopy is ideal for quantitative measurements [223]. Spectroscopic measurements are very sensitive and non-destructive and only require small amounts of sample for analysis [222]. Absorption spectroscopy is, therefore, an excellent technique for analyzing, amongst others, ligand-binding reactions. The spectrophotometer can identify components in a solution mainly based on their unique absorbance characteristics [224].

The increase in hydrodynamic particle size observed on dynamic light scattering between the AuNPs, TB-bioconjugate, and TB-bioconjugate in the presence of an analyte (Figure 17) supports the UV-vis absorption spectroscopy findings. Therefore, the wavelength redshift on UV-vis absorption spectroscopy observed after bioconjugation indicates successful bioconjugation of AuNPs with secondary antibodies. There were no detectable significant differences in hydrodynamic size when mycolic acid was introduced to the TB-bioconjugate (Figure 17B). However, changes in average peak intensity were observed between the three sample groups (Figure 17C). High peak intensity was observed in AuNPs before bioconjugation, and a notable decline in intensity was observed after TB-bioconjugation and further decline upon introduction of mycolic acid to the TB-bioconjugate (Figure 17A). This is indicative of antibody binding on the surface of AuNPs and binding of mycolic acid to antibodies present on the surface of the AuNPs, thus resulting in light absorption and reduction in dynamic light scattering average peak intensity.

SEM analysis is an essential technique used to visualize small-scale nanomaterials such as AuNPs. In this study, functionalized gold NanoUrchins were introduced on the surface of the

biosensor chip mycolic acid and/or anti-*mycobacterium tuberculosis* primary antibody. Gold NanoUrchins have unique optical properties as compared to spherical gold nanoparticles with the same diameter. NanoUrchins have a spiky uneven surface which causes a red shift in the surface plasmon peak and a larger enhancement of electromagnetic fields at the tips of the NanoUrchin spikes as compared to that of a spherical particle. The 60 nm NanoUrchins used in this study were chosen because they have the same absorption wavelength as the gold deposited on the glass substrate. The smooth, densely packed, and evenly distributed columnar structure resembled by round-shaped structures observed in the gold thin film reference sample (Figure 18A) agrees with what has been documented in the literature [226]. The nano-interspaces between the columnar structures support what has been detected in other studies, and this is an indication that the film is robust and can be used to develop biosensing platforms [227]. The spiky, uneven, and multi-branched structures observed in high quantities in the experiment samples (Figure 18B) are a typical morphology of the Au NanoUrchins [228]. The spikes found on gold Nanourchins cause a redshift in the surface plasmon peak and a larger enhancement of the electromagnetic field at the tips of the spikes compared to spherical nanoparticles [229].

The addition of bioconjugated gold NanoUrchins in the control sample (Figure 18C) was not expected to bind to the surface unless there was non-specific binding. The non-specific binding or physically adsorbed gold NanoUrchins could potentially result from inadequate wash steps. However, the few traces of Au NanoUrchins detected on the biosensing surface of the control sample were confirmed by EDX to be insignificant (Figure 19C). Herein, the percentage of Au for both the Au thin film reference sample and the control sample containing few traces of gold NanoUrchins was 42.83 (Figure 19A) and 42.50 (Figure 19C) respectively. Gold quantity was the main detectable element of interest used to distinguish between the experiment and the control sample based on the successful attachment of Au NanoUrchins to the biosensing surface. The high percentage of Au detected in the experiment group (Figure 19B) was attributed to the

significant amount of AuNPs detected on the biosensing surface as visualized on SEM (Figure 18). These results confirm the successful binding of bioconjugated AuNPs on surfaces containing immobilized anti-*mycobacterium tuberculosis* antibodies and support the specificity of mycolic acid reaction with anti-*mycobacterium tuberculosis* antibodies.

For layer-by-layer characterization of the biosensor chip, atomic force microscopy was performed. The Atomic force microscopy analysis is a quantitative technique and provides direct information on the height of the surface structures. This is a crucial technique in the process of functionalizing a biosensor chip to confirm the surface binding of structures. During immobilization of the mycolic acid biorecognition element, the successful binding of mycolic acid to the cysteamine/stearic acid complex (Figure 20B) may be associated with the strong Van der Waal's hydrophobic attractive forces existing between the alkyl chains of the MA and stearic acid [88]. The surface containing mycolic acid (Figure 20B) and the one where a bioconjugated secondary antibody was introduced to the surface (Figure 20E) had surface visual similarities, surface roughness, and thickness. This may be due to the absence of a complementary primary antibody on the surface to react with the bioconjugated secondary antibody; consequently, the secondary antibody was washed off following wash steps before sample analysis. In the presence of mycolic acid biorecognition element, primary antibody, and secondary antibody bioconjugated to AuNPs, rough structures were detected on the surface (Figure 20D). This may be the resemblance of AuNP-antibody complexes. This also supports findings by Lee et al., 2015 who demonstrated the possibility of visualizing AuNP-antibody complexes as a result of the presence of immobilized AuNPs. This shows that immobilization of the secondary antibody to the AuNPs was achieved, and the secondary antibody on the surface of the AuNPs was able to react with the primary antibody on the surface of the biosensor chip. This finding supports the UV-vis absorption spectroscopy findings in section 3.3.1, the SEM results in section 3.3.3, and the EDX spectroscopy results in section 3.3.4.

FTIR assay was performed to determine the molecular bonds formed between the AuNPs, anti-*mycobacterium tuberculosis* antibody, and mycolic acid. FTIR spectroscopy is one of the most powerful techniques used for the structural and spectral recognition of biological materials and their interactions [231]. It is a technique used to obtain an infrared spectrum of absorption or emission of a solid, liquid, or gas. It detects biochemical compositions, including proteins, lipids, nucleic acids, and carbohydrates within biological samples by specifically identifying molecular conformations, bonding types, functional groups, and intermolecular interactions of the sample under study [232,233]. FTIR Spectroscopy relies on the fact that most biological material absorbs light in the mid-infrared (IR) region (4000 – 400 cm^{-1}) of the electromagnetic spectrum [233–235]. The region of significant interest is between 1800 and 900 cm^{-1} and is called the bio-fingerprint region because it provides a large amount of information and representation of the composition of samples under study based on the vibrational modes of chemical bonds [235]. Other spectral regions of interest include amide I and II regions (1700 – 1500 cm^{-1}), higher-wavenumber regions (3500 – 2550 cm^{-1}) associated with stretching vibrations including C-H, O-H, N-H, and S-H, while lower-wavenumber regions are associated with bending and skeletal fingerprint vibrations [233]. In this instance, a reduction in percentage transmittance in the TB-bioconjugate (Figure 21B) was observed when compared to the AuNPs (Figure 21A).

This finding supports the UV-vis absorption spectroscopy results from section 3.3.1, whereby a reduction in absorption intensity was observed when anti-*mycobacterium tuberculosis* antibodies were bioconjugated to AuNPs. The absorption band at 3337 cm^{-1} (Figure 21C) corresponds to carboxyl and hydroxyl functional groups [236,237]. In addition, the absorption bands at 2958 cm^{-1}, 2922 cm^{-1}, and 2956 cm^{-1} fall within the alkanes and carboxylic acid functional groups and therefore represent alkane (C-H) stretch and carboxylic acid (O-H stretch) [238]. In addition, the absorption band at 1638 cm^{-1} represents vibrational modes of C=C double

bonds of the AuNP/antibody/mycolic acid complex. Lastly, the absorption peak at 1462 cm^{-1} shows the presence of an aromatic (C=C stretch). These findings indicate the presence of mycolic acid in the reaction mixture containing bioconjugated AuNPs; however, it does not confirm direct binding without the support of other qualitative and quantitative characterization tests, including SEM, EDX, AFM, and DLS.

On LSPR biosensing, the higher percentage of transmitted light in the Au-thin film sample used as the background was a result of no substances immobilized on the surface. As substances were covalently attached to the biosensor chip, there was a reduction in the percentage of transmitted light. No significant differences were detected between the MA and MA+2^0Ab samples used to test for non-specific binding when comparing the average peak height (Figure 22B) and the area under the graph (Figure 22C). This shows that the bioconjugated secondary antibody could not bind directly to mycolic acid since it is specifically designed to react with the anti-*mycobacterium tuberculosis* antibody/mycolic acid complex. This proved the specificity of the mycolic acid biorecognition element to the primary antibody. Additionally, the few traces of AuNPs seen on the SEM surface in section 3.3.3 (Figure 18C) may be a result of MA+2^0Ab surface transmitting less light compared to the mycolic acid sample surface. The lowest percentage of transmitted light in the MA+1^0 Ab+2^0Ab sample may be a result of the presence of a bioconjugated secondary antibody on the biosensing surface detected on SEM in section 3.3.3 (Figure 18B). From these results and the AFM results, it is evident that the immobilization of the mycolic acid biorecognition element on the biosensor chip was successful. It enabled the binding or attachment of the targeted anti-*mycobacterium tuberculosis* primary antibody, which subsequently reacted with the secondary antibody bioconjugated to AuNPs. Therefore, the increase in height and roughness detected on AFM in section 3.3.5 (Figure 20D) led to a further reduction in the percentage of transmitted light detected on LSPR biosensing with additional redshift in the wavelength.

In conclusion, based on the data acquired using UV-vis absorption spectroscopy, dynamic light scattering, and FTIR, it was proven that the covalent bioconjugation of AuNPs with antibodies was successful. Furthermore, biosensing surface characterization using SEM showed the presence of the bioconjugated AuNPs on the biosensor chip surface, and the gold percentage on EDX spectroscopy was higher in the experiment group containing AuNPs than in the control group and the Au-coated chip used as reference. On AFM, surface roughness and height increased in the experiment group compared to the control and reference groups. On LSPR biosensing, there was a higher percentage of light transmitted in the reference sample when analyzing peaks based on peak intensity and area under the peaks, followed by the control samples, and the experiment sample transmitted less light.

Overall, it was proven that mycolic acid could be applied as an efficient biomarker to capture anti-*mycobacterium tuberculosis* antibodies. It can be used for the development of biosensor chips for TB diagnosing, and the developed biosensor chip can be successfully analyzed using optical detection techniques such as LSPR for diagnostic purposes. In summary, this chapter introduced novel contributions to the field of optical biosensing for the detection of anti-*mycobacterium tuberculosis* antibodies through LSPR biosensing. A custom-made biosensor chip formed by a thin gold-coated layer on a glass substrate was developed and functionalized with mycolic acid pathogen-specific TB antigens.

The UV-vis absorption spectroscopy, DLS, and FTIR were used to confirm the conjugation/functionalization of the AuNPs with the antibodies. The AFM, SEM, and EDX were used for the characterization of the biosensor chip and will not be performed in a point-of-care setting. These characterization techniques collectively validated the effectiveness of mycolic acid as a biomarker for capturing anti-*mycobacterium tuberculosis* antibodies. The LSPR biosensing technique demonstrates specificity in detecting anti-*mycobacterium tuberculosis*

antibodies, confirming the successful immobilization of mycolic acid on the biosensor chip. This LSPR transmitted intensity (average height) and area under the curve-based approach can potentially contribute significantly to the development of cost-effective, sensitive, and specific diagnostic tools in tuberculosis and infectious disease detection.

CHAPTER 4:

PHOTONIC CRYSTAL-BASED BIOSENSING OF ANTI-MYCOBACTERIUM TUBERCULOSIS ANTIBODIES

4.1. INTRODUCTION

Photonic crystals, which are periodic nanostructures (as detailed in section 1.5.2) that manipulate the flow of light, have garnered significant interest in the field of biosensing and their potential application in the development of point-of-care diagnostic devices. PhC-based biosensing plays a crucial role in the development of point-of-care diagnostics. They can be engineered to exhibit strong light-matter interactions, resulting in enhanced sensitivity for detecting analytes. By tailoring the structural properties of PhCs, such as the periodicity and refractive index contrast, the interaction of light with biomolecules can be optimized, leading to increased sensitivity in detecting molecular binding events [239–241]. PhC-based biosensors offer label-free detection, eliminating the need for fluorescent or radioactive labels [23,159,242]. This simplifies the assay procedure and reduces costs. The interaction of analytes with the PhC structure causes changes in the optical properties, such as the shift in the wavelength or change in intensity, enabling direct detection without the use of additional labels or probes [159].

PhC-based biosensors can also be designed to support multiplexed analysis, allowing the simultaneous detection of multiple analytes in a single assay [153,243]. By functionalizing different regions of the PhC surface with specific capture molecules or biorecognition elements, such as pathogen-specific biomarkers, antibodies, or DNA probes, the biosensor can selectively bind and detect multiple target molecules concurrently. This capability is advantageous for point-of-care diagnostics, where the detection of multiple biomarkers can provide comprehensive diagnostic information. One of the advantages of PhC-based biosensors is their

capability for real-time monitoring of biomolecular interactions. The changes in the optical properties of the PhC structure occur instantaneously upon analyte binding, allowing the detection and analysis of binding kinetics and affinity [159]. Real-time monitoring enables dynamic measurements, enhancing the understanding of biomolecular interactions and enabling timely diagnostic decisions. PhC-based biosensors can be miniaturized into compact and portable devices [244], making them suitable for point-of-care applications. The compact size and portability of PhC-based biosensors facilitate on-site testing, remote healthcare, and decentralized diagnostics. The integration of PhC-based biosensing into point-of-care diagnostic devices holds promise for rapid and sensitive detection of biomarkers in various clinical and environmental applications [244–246].

In this study, 1-D PhCs were functionalized with a pathogen-specific biomarker for label-free detection of anti-*mycobacterium tuberculosis* antibodies. These 1-D PhCs offer unique optical properties that can be harnessed for biosensing applications. They can be designed to act as optical filters or mirrors that selectively transmit or reflect certain wavelengths of light [158,247]. These properties are useful in biosensing applications where specific wavelengths are used for excitation or detection. By incorporating PhCs into optical setups, they can enhance the signal-to-noise ratio and improve the sensitivity of detection systems [154,248]. The 1-D PhCs can amplify fluorescence signals through heightened interactions between light and matter, leading to improved emission at specific wavelengths.The 1-D PhCs can be engineered to exhibit sharp spectral reflectance features, known as photonic stopbands, which are sensitive to changes in the refractive index of the surrounding medium [249–251]. By functionalizing the surface of the PhC with receptors/ capture molecules or biorecognition elements, they can be used for label-free biosensing. The binding of target analytes to the surface causes a shift in the photonic stopband, enabling the detection and quantification of the analytes [251]. These applications highlight the versatility of 1-D PhCs in biosensing and diagnostics. The ability to tailor their

optical properties and combine them with functionalized surfaces or nanoparticles enables improved sensitivity, selectivity, and miniaturization of diagnostic devices. Ongoing research in this field continues to explore novel approaches and applications for 1-D PhCs in advancing biosensing and diagnostic technologies and aims to optimize the performance, manufacturability, and cost-effectiveness of PhC-based biosensors for practical implementation in point-of-care diagnostics.

4.2. MATERIALS AND METHODS

4.2.1. Characterization of AuNPs using UV-vis absorption spectroscopy

UV-vis absorption spectroscopy was performed to characterize the AuNPs before and after bioconjugation following the optimized protocol used in section 2.2.5.1 for covalent conjugation chemistry of the 60nm gold NanoUrchin to the secondary antibody.

4.2.2. Functionalization of the photonic crystal biosensor chip

Functionalization of the 1-D PhC biosensor chip used to capture anti-*mycobacterium tuberculosis* antibodies was performed using the optimized microscope glass slide protocol described in section 2.2.1. For purposes of enhancing the detection signal during PhC optical biosensing, AuNPs were covalently conjugated with the secondary antibody and introduced on the biosensing surface containing the anti-*mycobacterium tuberculosis* antibody. Three sample groups were prepared, namely the untreated 1-D PhC used as a reference sample, the control, and the experiment samples. In the control sample, the primary antibody was not introduced on the surface; however, the TB bioconjugate was introduced on the surface containing mycolic acid to rule out the lack of specificity of the biorecognition element. In the experiment sample, the AuNPs bioconjugated with the goat anti-rabbit IgG H&L secondary antibody herein called

TB bioconjugate (AuNPs-IgG) were introduced on the surface containing the primary antibody. The sample was analyzed using the custom-built PhC-based optical biosensing detection system described in section 4.2.4.1.

4.2.3. Biosensing surface characterization using atomic force microscopy

The AFM was used to perform layer-by-layer characterization of the biosensing surface for surface morphology studies of the PhC biosensor chips at different stages of the functionalization process. AFM images of the untreated PhC biosensor chip (reference sample), control, and experiment, were captured with a Vecco AFM system (Digital Instruments, USA) using a silicon cantilever tip. The tip has a curvature radius of 10 nm and is n-doped silicon, with a resonance frequency of 204-497 kHz and a force constant of approximately 10-130 N/m. Images acquired by the AFM instrument were analyzed using Nanoscope software. The obtained images were specifically analyzed for surface roughness and height between the three sample groups.

4.2.4. Photonic crystal-based optical biosensing and detection of anti-*mycobacterium tuberculosis* antibodies

4.2.4.1. The PhC-based optical biosensing setup

A custom-built optical biosensing setup with a transmission spectroscopy conformation was used to perform PhC biosensing (Figure 23). The setup was assembled using a broadband LED light source to accommodate the 1-D PhC used in this study which is detected at a resonance wavelength between 636 – 651 nm range. The light was collimated using a combination of collimating lenses and focused on the sample stage. Light transmitted through the PhC biosensor chip on the stage was collected using a 10x microscope objective. A 50/50 beam splitter was used to split the beam into the imaging system and the spectrometer. Transmitted light was

focused into the fiber using a focusing lens and directed to the USB 4000 portable spectrometer (Ocean Optics Inc, United States) connected to the computer. The imaging system enabled the visualization of biosensing activities on the sample stage and was formed by a CCD camera connected to a computer. SpectraSuit software was used to perform spectroscopic analysis of the different sample groups. Sample groups were prepared in triplicates under the same conditions, and the analysis was repeated three times ($n=3$). During sample analysis, background measurements were taken before each recording. The acquired data were further analyzed using OriginPro software to plot wavelength-shift differences between the sample groups.

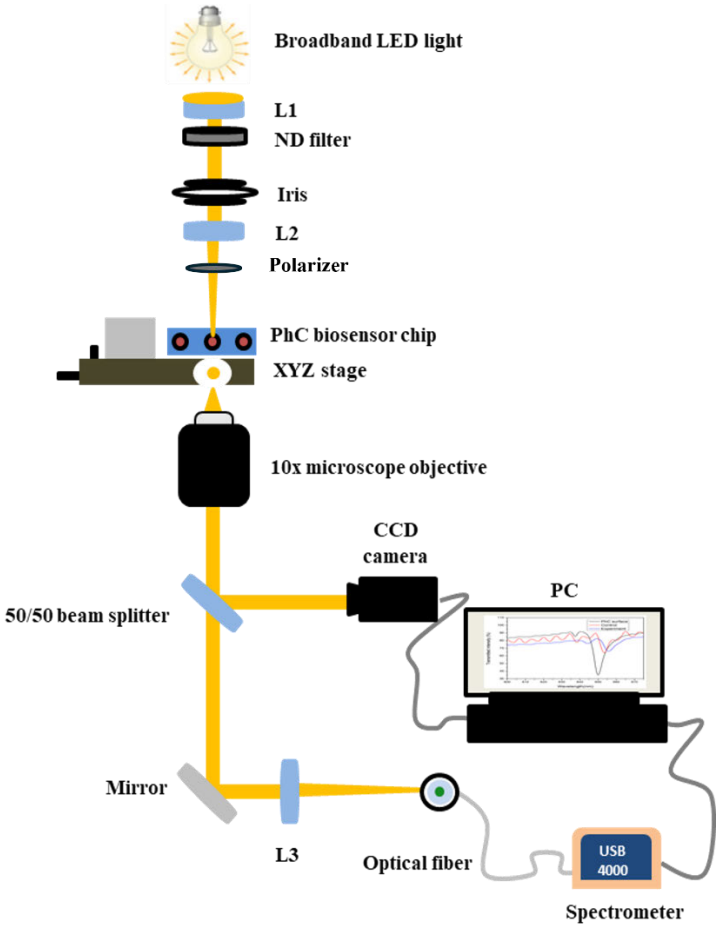

Figure 23: A custom-built photonic crystal biosensing setup used to measure transmitted light. This setup uses a broadband LED light source instead of the 512 nm green light source used on the LSPR-based biosensing setup in Figure 15, collimating lenses (L1 and 2), polarizer, XYZ stage, a 10x microscope objective, and an imaging system consisting of a CCD camera and computer. The focusing lens (L3) was used to focus the light into the optical fiber, and the portable USB spectrometer connected to a computer was used for data acquisition.

4.3. RESULTS

4.3.1. UV-vis absorption spectroscopy

UV-vis absorption spectroscopy was performed to characterize AuNPs before and after bioconjugated to goat anti-rabbit IgG H&L secondary antibody. The bioconjugated AuNPs were subsequently introduced on the biosensing surface. Refer to Chapter 3, section 3.3.1 (Figure 16) for the absorption spectrum of AuNPs before bioconjugation and the spectrum of AuNPs after bioconjugation with goat anti-rabbit IgG H&L secondary antibody.

4.3.2. Atomic force microscopy

Atomic force microscopy was used in this study to perform layer-by-layer characterization of the PhC biosensor chip surface during the chip functionalization process. Sample groups included untreated PhC, control, and experiment samples. The control sample consisted of mycolic acid immobilized on the biosensing surface as the biorecognition element and the goat anti-rabbit IgG H&L secondary antibody bioconjugated to AuNPs (TB-bioconjugate). There was no primary antibody on the surface of the control sample. Mycolic acid used in this study can only bind to the anti-*mycobacterium tuberculosis* antibody, and the secondary antibody is designed to bind to the primary antibody. The experiment sample consisted of mycolic acid, an anti-*mycobacterium tuberculosis* primary antibody, and the TB bioconjugate. The images taken using AFM are shown in Figure 24, and each of the scans represents a 5µm X 5µm lateral area that was scanned.

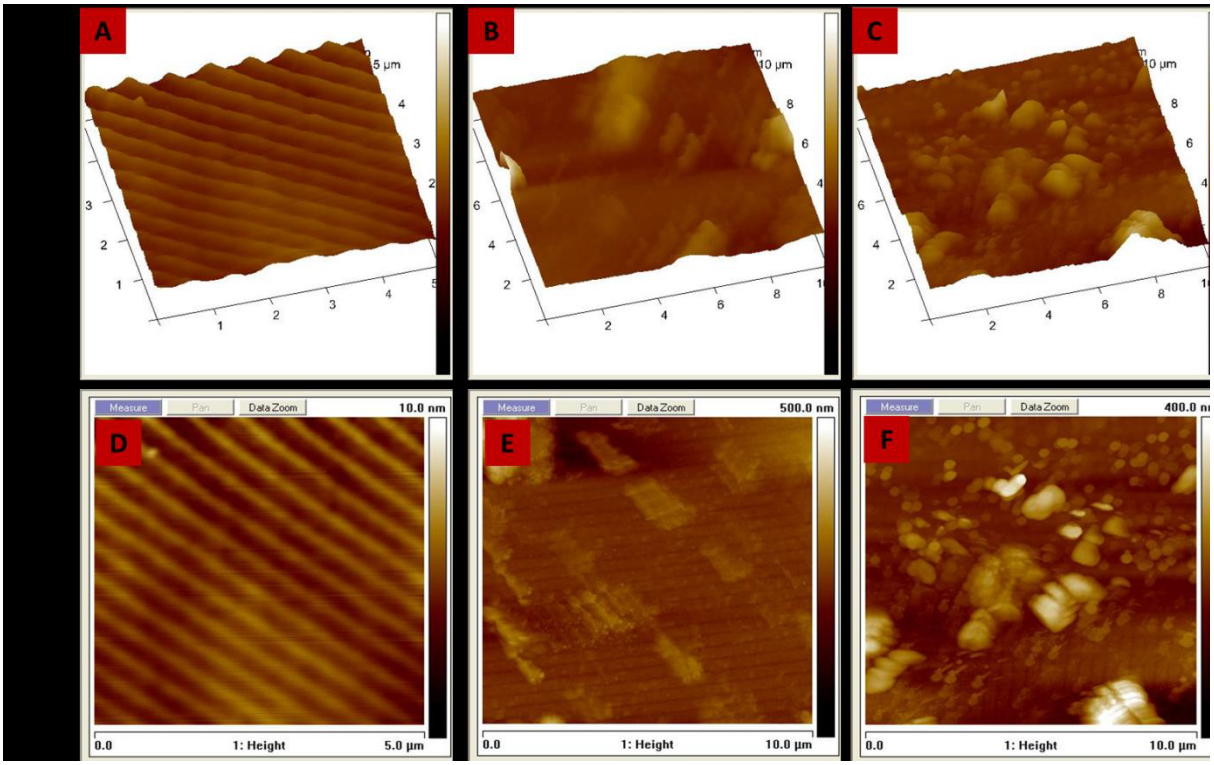

Figure 24: Atomic force microscopy micrographs of the PhC, control, and experiment group displayed in 3-dimensional and 1-dimensional view projection. Figures A and D show the 1-D PhC used as the reference sample displayed in 3-D and 1-D view. Figures B and E show the control sample in 3-D and 1-D view projection. Figures C and F show the experiment sample in 3-D and 1-D view. The PhC surface was smooth with no debris detected on it. The experiment sample displayed much more surface roughness compared to the control sample.

Figure 24A and D shows the untreated PhC surface depicting the band structure representing the periodicity of the PhC. The consistent crest and trough pattern of the PhC periodicity is represented in Figure 24A. The surface is uniform, with no signs of irregularities, defects, or contaminants. Prominent surface roughness was observed in the experiment sample (Figure 24C and F) compared to the control sample (Figure 24B and E). The experiment sample consisted of distinct rough structures on the surface, which were not detected in the control and reference samples. The Z-range increased from 150 nm in the untreated 1-D PhC sample used as a reference to 344 nm in the control sample. The experiment sample containing immobilized bioconjugated AuNPs displayed a z-range of 473 nm.

4.3.3. Photonic crystal-based optical biosensing and detection of anti-*mycobacterium tuberculosis* antibody

A custom-built PhC biosensing setup was used to differentiate and detect differences between the untreated PhC sample, the control, and the experiment samples. Transmitted light intensity was measured between the three sample groups. There were clear wavelength-shift differences between the three samples (Figure 25). The untreated PhC reference sample was detected at a resonance wavelength of 650.08 nm, which corresponds to the manufacturer's recommendations. The control sample with surface-immobilized mycolic acid biorecognition element was detected at a wavelength of 653.48 nm. There was a redshift of 3.4 nm in the wavelength detected between the reference sample and the control.

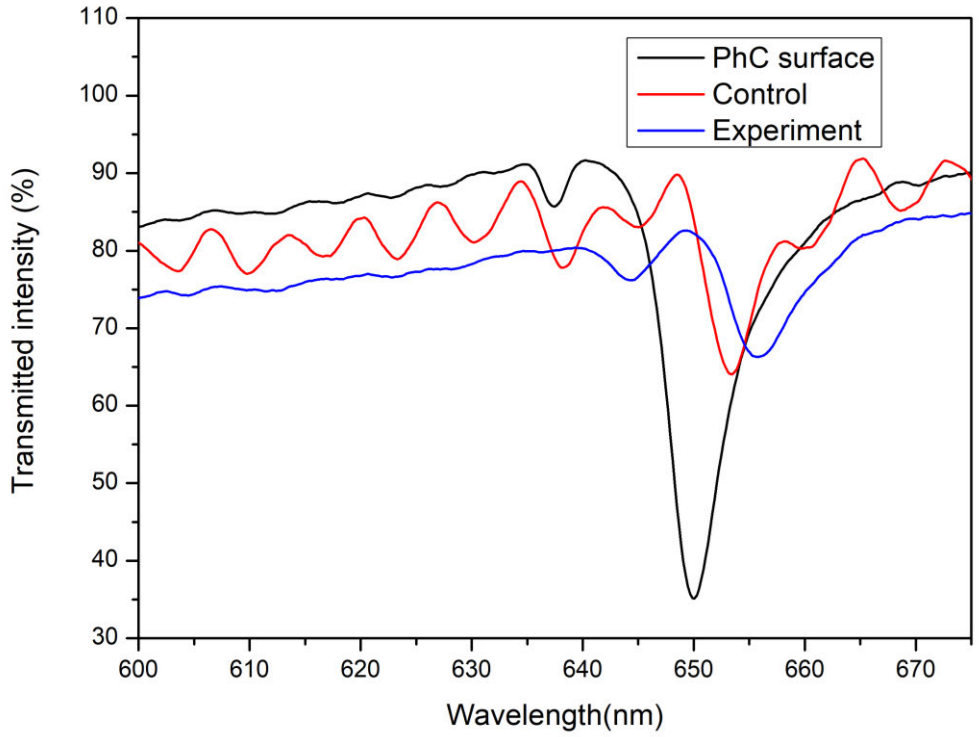

Figure 25: Photonic crystal spectrograph for the detection of anti-mycobacterium tuberculosis antibodies. The untreated PhC spectrum is represented by the black line, the control is represented by the red spectrum, and the experiment is represented by the blue spectrum. There were clear detectable wavelength differences between the three sample groups, and a reduction in transmitted intensity was also recorded.

There was also a significant reduction in transmitted intensity between the untreated PhC and the control. A further reduction in transmitted intensity was detected between the control and the experiment. The resonance peak of the experiment sample was observed at a wavelength of 655.88 nm, and this suggests a redshift of 2.4 nm between the control and the experiment. When the experiment sample was compared to the reference sample, a redshift of 5.8 nm was recorded.

4.4. DISCUSSION

Signal enhancement of the PhC biosensing surface was applied using functionalized AuNPs. These functionalized AuNPs were characterized using a NanoDrop 8000 spectrophotometer device to perform UV-vis absorption spectroscopy. A spectrophotometer can identify components in a solution mainly based on their unique absorbance characteristics [224,252]. To functionalize the AuNPs with the secondary antibody, covalent bioconjugation chemistry was used. In this conjugation technique, NHS and EDC chemistry was used to bind the secondary antibody to PEG. The NHS and EDC activate the carboxyl groups of the PEG (linker molecule) attached to the AuNP surface to form an intermediate that reacts with primary amine groups on the antibody [219]. Bioconjugation occurs upon successful binding of the antibody to the AuNPs surface, thus resulting in a wavelength redshift in the absorption spectrum by a few nanometers [221]. In this study, a 10 nm redshift was observed and is significant enough to confirm refractive index changes on the surface of the AuNPs due to the attachment of the secondary antibody. The resonance wavelength and bandwidth of the AuNPs are dependent on the shape, particle size, refractive index of the surrounding media, and temperature. The shift in the AuNPs-IgG bioconjugate spectra might be a result of the changes in the dielectric environment surrounding the AuNPs [224,225]. Additionally, successful bioconjugation of AuNPs with the secondary antibody plays a crucial role in changing the refractive index when introduced on the biosensing surface of the biosensor chip. As a result, this enhances the detection signal during optical biosensing.

The PhC-based biosensing surface was characterized layer-by-layer using AFM during the functionalization process to confirm the binding of molecules on the surface. Immobilization of molecules on the biosensing surface was achieved through covalent attachment and the formation of self-assembled monolayers. As different elements were immobilized on the biosensor chip surface to distinguish the experiment from the control sample, it was crucial to study the changes in surface morphology, mainly height, and surface roughness, between the different sample groups. Three sample groups, including the untreated PhC, control, and experiment groups, were studied. The untreated PhC was used as the reference sample. Mycolic acid was used as the biorecognition element to capture anti-*mycobacterium tuberculosis* antibodies. It was immobilized on the biosensing surfaces of both the control and experiment samples. However, a complementary primary antibody was not introduced on the surface of the control sample, but rather a non-complimentary TB-bioconjugate (AuNPs functionalized with secondary antibody) was introduced to both the control and experiment samples. In the control sample, the TB-bioconjugate was used to test for the specificity of the biorecognition element. In the absence of a primary antibody on the surface of the control sample, the TB-bioconjugate was not expected to bind to the surface; hence the prominent surface roughness observed in the experiment sample (Figure 24C and F) was not detected in the control sample (Figure 24B and E). Various structures resembling AuNP-antibody complexes were visualized on the surface containing bioconjugated AuNPs in figures 24C and F of the experiment sample. This also supports findings by Lee et al., 2015 who demonstrated the possibility of visualizing AuNP-antibody complexes as a result of the presence of immobilized AuNPs. The increased surface roughness in the experiment sample could be attributed to the immobilization of the AuNPs contained in the TB-bioconjugate bound to the surface of the experiment sample. This is also supported by the Z-range values of 150 nm in the untreated 1-D PhC sample, 344 nm in the control sample, and 473 nm in the experiment sample. This can be an indication that the immobilization of the secondary antibody to the AuNPs was successful, and the secondary

antibody was subsequently attached to the primary antibody on the surface of the biosensor chip in the experiment sample. This finding supports the UV-vis absorption spectroscopy findings in section 3.3.1.

After the characterization of the biosensing surface, PhC-based biosensing of the chip was performed using the custom-built optical biosensing setup. During analysis, wavelength shift due to refractive index changes on the surfaces between the three sample groups was measured. During data acquisition, the samples were placed flat (0° angle) on the sample stage, enabling light to pass directly vertically through the sample. Based on the manufacturer's instruction, the 1-D PhC used in this study provides optimum results at 0° to 10° angles and is detected at a resonance wavelength between 636 – 651 nm range. In this study, 0° angle provided optimum results. There were distinct differences in wavelength redshift between the three samples. The redshift detection is due to changes in the refractive index between samples [252]. The significant reduction in transmitted intensity between the untreated PhC and the control is attributed to the successful immobilization of the biorecognition element in the control sample. Further reduction in transmitted intensity detected between the control and the experiment samples is suggestive of the successful binding of anti-*mycobacterium tuberculosis* to the biosensing surface containing immobilized biorecognition element.

The binding of the TB-bioconjugate containing AuNPs in the experiment sample may also have contributed to the reduction in transmitted intensity. These results fully support the AFM results in section 4.3.2 whereby the immobilization of molecules on the biosensing surface absorbs light and alters the refractive index of the material. From these findings, it is evident that the introduction of elements on the PhC surface changed the refractive index of the material, which contributes directly to changes in detectable wavelength between various sample groups. These findings suggest a possible diagnosis of TB using a label-free PhC optical biosensing platform.

Lastly, the use of white light for the development of a custom-built PhC-based biosensing setup as opposed to the green light source used in Chapter 3 or the traditional use of laser light sources has several advantages besides the distinct resonance wavelength shifts detected between the various sample groups analyzed. Firstly, the utilization of a white light source adds versatility to the biosensor, thus allowing for a broader spectral range of detection. This versatility is particularly advantageous when compared to lasers, which can be more costly and have narrower emission spectra. The cost-effectiveness of employing a white light source is a notable advantage in this study, leading to the potential development of accessible future POC diagnostic biosensing technologies.

CHAPTER 5

CONCLUSION

This chapter presents a conclusion on the four chapters of this thesis and future work regarding the findings. **Chapter 1** focused on three key areas, including an introduction to TB, biomarkers of active TB, and optical biosensing techniques used in this study. An overview of the global pandemic of TB, and *M. tuberculosis* as the causative agent for TB infections, the structural arrangement of the mycobacterial cell envelope, TB spread, prevention, and treatment options were detailed under the introduction to TB. The arrangement of the bacterial cell envelope provided insights regarding the arrangement of certain pathogen-specific biomarkers of TB present on the cell wall. Various biomarkers were explored further to support the selection of mycolic acid as the biomarker of choice for this study. Furthermore, the optical biosensing techniques used in this work, such as LSPR and PhC-based biosensing for the detection of anti-*mycobacterium tuberculosis* were introduced and explored further in the subsequent chapter.

In **Chapter 2,** the design and development of the optical biosensing setup, characterization of the biosensing surface, and characterization of AuNPs before and after bioconjugation were detailed. For proof of concept, fluorescent microscopy was used to confirm the specificity of mycolic acid binding to anti-*mycobacterium tuberculosis* antibodies. This was also done to optimize the functionalization protocol of mycolic acid on a microscope glass slide before implementing it in photonic crystal (PhC)-based biosensing. The presence of fluorescence signal in the experiment sample confirmed the successful immobilization of mycolic acid as the biorecognition element and its binding to the anti-*mycobacterium tuberculosis* antibody.

To characterize the biosensing surface, a 40 nm Au thin film deposited on a glass substrate was characterized using SEM to understand its optical properties and optimize its performance for optical biosensing. The SEM analysis showed a homogenous, tightly packed layer of Au with no signs of contaminants present on the thin film. This is crucial because surface contaminants or irregularities can negatively affect the optical properties of the biosensing system, leading to unwanted signal interference and decreased accuracy.

To characterize the AuNPs, TEM was used and displayed the characteristic multibranched, spiky, uneven morphology of the gold NanoUrchins which provides a larger surface area compared to spherical nanoparticles. This unique surface morphology of Au NanoUrchins resulted in signal enhancement when introduced on the biosensing surface in chapters 3 and 4, improving the detection sensitivity of the biosensor. Additionally, the functionalization of the AuNPs using covalent conjugation resulted in higher binding efficiency, indicated by a significant redshift in the wavelength when characterized using UV-vis absorption spectroscopy, and the protocol was adopted in subsequent chapters. In conclusion, the importance of confirming the specificity of the biorecognition element to the analyte of interest using characterization techniques is critical in biosensing.

In **Chapter 3**, a custom-made biosensor chip was developed using a thin gold-coated layer deposited on a glass substrate. The biosensor chip was functionalized with mycolic acid pathogen-specific TB antigens for the detection of anti-*mycobacterium tuberculosis* antibodies. To enhance the detection signal, functionalized AuNPs were introduced to the biosensing surface. The unique optical properties of AuNPs, including their ability to interact with light, were proven advantageous for biosensing. Various additional characterization techniques were employed to confirm the successful bioconjugation of AuNPs with the secondary antibodies. UV-vis absorption spectroscopy demonstrated a redshift in the absorption spectrum after AuNPs

bioconjugation, indicating the binding of the antibodies to the AuNPs. Dynamic light scattering measurements showed an increase in the hydrodynamic particle size after bioconjugation, further supporting the successful binding. Additionally, SEM images revealed the presence of functionalized AuNPs on the biosensor chip surface, confirming the attachment of the bioconjugated AuNPs to the biosensing surface. The specificity of the mycolic acid biorecognition element to the anti-*mycobacterium tuberculosis* primary antibody was confirmed through the absence of non-specific binding in the control samples. Further analysis using atomic force microscopy provided insights into the surface morphology, focusing on surface roughness and thickness, and subsequently confirmed the binding of mycolic acid, primary antibody, and bioconjugated secondary antibody to the biosensor chip. FTIR spectroscopy was utilized to identify the molecular bonds formed between the AuNPs, antibodies, and mycolic acid. The FTIR results showed specific absorption peaks corresponding to the functional groups present in the mycolic acid/primary antibody/bioconjugated AuNPs complex, providing evidence of the presence of mycolic acid in the reaction mixture.

The LSPR biosensing measurements demonstrated a reduction in the percentage of transmitted light in various sample groups. A redshift in the wavelength was also detected in the mycolic acid/primary antibody/bioconjugated AuNPs complex. The increased surface roughness and height observed on AFM, along with the decrease in transmitted light detected on LSPR biosensing, were suggestive of successful immobilization and binding of the targeted antibodies or analyte. In conclusion, the comprehensive characterization techniques employed in this study confirmed the successful covalent bioconjugation of AuNPs with antibodies confirmation with UV-vis and SEM. Also, the presence of bioconjugated AuNPs on the surface, the higher gold percentage detected, and the increased surface roughness and height demonstrated the successful immobilization of the biomolecules. The use of mycolic acid as a biomarker for capturing anti-*mycobacterium tuberculosis* antibodies was proven effective, and the developed biosensor chip

showed potential for TB diagnosis using optical detection techniques such as LSPR. These findings contribute to the advancement of biosensing technology for improved diagnostic applications.

In **Chapter 4**, photonic crystal-based biosensing was performed to detect anti-*mycobacterium tuberculosis* antibodies. Various techniques were performed towards the development of a biosensor chip and this included covalent bioconjugation of gold-nanoparticles with antibodies and UV-vis absorption spectroscopy to confirm bioconjugation. Surface characterization of the biosensor chip was performed using atomic force microscopy. Covalent bioconjugation chemistry involving NHS and EDC was employed to bind the secondary antibody to the PEG linker molecule attached to the AuNP surface. The functionalized AuNPs were successfully characterized using UV-vis absorption spectroscopy, which identified their unique absorbance characteristics. Successful bioconjugation resulted in a redshift in the absorption spectrum, confirming changes in the refractive index in the bioconjugated AuNPs. Bioconjugated AuNPs were introduced to the experiment sample to form a mycolic acid/primary antibody/bioconjugated AuNPs complex. The PhC biosensing surface was subsequently characterized layer-by-layer at various steps of the surface functionalization process using AFM. Immobilization of molecules was achieved through covalent attachment and the formation of self-assembled monolayers, resulting in changes in surface thickness and roughness. The AFM confirmed the binding of molecules on the surface through detectable changes in the surface thickness. The AFM analysis demonstrated that the introduction of elements on the biosensor chip surface, including the immobilization of bioconjugated AuNPs, led to changes in biosensing surface characteristics. The immobilization of functionalized AuNPs on the PhC biosensing surface, forming a mycolic acid/primary antibody/bioconjugated AuNPs complex, contributed to the increase in surface roughness detected in the experiment sample, thus also contributing to refractive index changes.

The differences in refractive index between the sample groups contributed significantly to detectable or measurable wavelength differences, thus distinguishing negative from positive samples. Therefore, the immobilization of bioconjugated AuNPs further contributed to signal enhancement in the optical biosensing system. The reduction in transmitted intensity observed between the different sample categories also confirmed the successful immobilization of the biorecognition element in the control and experiment samples, and the binding of the TB bioconjugate (bioconjugated AuNPs) to the primary antibody in the experiment sample. The findings from UV-vis absorption spectroscopy and AFM characterization supported the results obtained from the PhC-based optical biosensing measurements. The introduction of elements on the PhC surface altered the refractive index of the material, leading to detectable wavelength shifts between the sample groups. These results indicate the potential of the label-free PhC optical biosensing platform for the detection of anti-*mycobacterium tuberculosis* antibodies. Overall, the functionalization of AuNPs, successful bioconjugation, and careful characterization of the biosensing surface demonstrated enhanced sensitivity and specificity in the PhC-based optical biosensing system, opening up possibilities for the development of accurate and reliable biosensors for disease diagnosis.

Overall, the research presented in this thesis evaluated two optical biosensing techniques, localized surface plasmon resonance and photonic crystal-based methods, for detecting anti-*mycobacterium tuberculosis* antibodies. These techniques were selected to support the hypothesis that optical biosensing techniques can potentially be applied in developing point-of-care diagnostic methods for TB and other infectious diseases. The comprehensive characterization techniques employed throughout this thesis have provided compelling evidence for the successful immobilization of the biorecognition element and the binding of the targeted antibody. The results demonstrate the potential of optical biosensing techniques using LSPR-based and photonic crystal-based biosensing, for the detection of anti-*mycobacterium*

tuberculosis antibodies, paving the way for the development of advanced point-of-care diagnostic tools for infectious diseases. LSPR-based and PhC-based biosensors generate detection signals due to changes in the sample's refractive index. Both methods can analyze similar biological materials but differ in their operating principles, material requirements, and signal readout methods. LSPR-based sensors use metallic nanoparticles (e.g. gold or silver) to generate surface plasmons, responding to changes in refractive index. This sensitivity enables the detection of biomolecular interactions through spectroscopic measurements of resonance shifts. In this study, the LSPR analysis was based on the variation of transmitted intensity variation at a given wavelength. In contrast, PhC-based sensors rely on photonic crystals, which are dielectric materials with periodic nanostructures that create photonic band gaps, and the polization of the light source. These biosensing techniques detect changes in the refractive index by measuring spectral shift. In this study, the transmission spectra were obtained for data analysis on both techniques.

The pronounced differences in refractive index changes detected on the surface of the photonic crystal biosensor chip depicted by a notable resonance wavelength shift in Chapter 4 signify a significant enhancement in the optical biosensing platform. The reduction in transmitted intensity among distinct sample categories also reinforces the efficacy of this approach. While LSPR showed significant differences in transmitted intensity and less prominent differences in wavelength shift when compared to PhC biosensing. It is therefore evident that photonic crystal-based optical biosensing emerges as a superior detection platform compared to LSPR for the accurate and reliable detection of anti-mycobacterium tuberculosis antibodies. These findings contribute to the advancement of biosensing technology and hold promise for improving TB diagnosis. Future work in this field could focus on further optimizing the biosensing setup for real-time detection, incorporating microfluidic technology in the design and development of a multiplex biosensor chip, and investigating additional biomarkers for TB detection, particularly

sputum biomarkers since it is an easily accessible specimen in adults. The integration of these optical biosensing techniques into point-of-care devices could revolutionize TB diagnosis, enabling rapid and sensitive detection, and leading to improved patient outcomes and better control of TB transmission.

6. APPENDICES

6.1. Appendix A: Published peer-reviewed journal articles

Sensing and Bio-Sensing Research 39 (2023) 100545

Contents lists available at ScienceDirect

Sensing and Bio-Sensing Research

journal homepage: www.elsevier.com/locate/sbsr

Localized surface plasmon resonance biosensing of *Mycobacterium tuberculosis* biomarker for TB diagnosis

Charles Maphanga [a,b,*], Sello Manoto [c], Saturnin Ombinda-Lemboumba [a], Yaseera Ismail [b], Patience Mthunzi-Kufa [a,b]

[a] Council for Scientific and Industrial Research, National Laser Centre, P O BOX 395, Pretoria 0001, South Africa
[b] University of KwaZulu-Natal, School of Chemistry and Physics, Westville Campus, University Road, Durban, South Africa
[c] National Research Foundation, CSIR Complex, Meiring Naude Road, Brummeria, Pretoria, Gauteng 0184, South Africa

ARTICLE INFO

Keywords:
Localized surface plasmon resonance
Optical biosensing
Transmission spectroscopy
Scanning electron microscopy
Energy dispersive X-ray
Atomic force microscopy
Mycolic acid
Mycobacterium tuberculosis

ABSTRACT

Biosensors offer great advantages over conventional analytical techniques. Specifically, they can provide multiple capabilities such as user-friendly operation, real-time analysis, rapid response, high sensitivity and specificity, portability, label-free detection, and cost-effectiveness. As a result, this diagnostic approach is a point-of-care (POC) diagnostic and monitoring technology. In this study, for the first time, an optical biosensor chip was developed and analyzed using a localized surface plasmon resonance (LSPR) optical biosensing technique to monitor biomolecular interactions between mycolic acid TB antigen and anti-*Mycobacterium tuberculosis* antibody. Mycolic acid was successfully immobilized on a gold-coated biosensor chip and allowed to react with anti-*Mycobacterium tuberculosis* antibody. To enhance the detection signal from biomolecular binding events, gold nanoparticles (AuNPs) were used and successfully bioconjugated with goat anti-rabbit IgG H&L secondary antibody and characterized using ultraviolet-visible (UV–vis) spectroscopy, dynamic light scattering (DLS), Fourier-transform infrared (FTIR) spectroscopy, and subsequently introduced on the biosensing layer. Scanning electron microscopy (SEM), energy-dispersive X-ray (EDX) spectroscopy, and atomic force microscopy (AFM) were used to characterize the biosensing surface. The optimized biosensor chip was analyzed using a custom-built biosensing transmission spectroscopy setup to perform LSPR biosensing. Our findings showed that mycolic acid was successfully immobilized on the biosensing surface and made it possible to capture anti-*Mycobacterium tuberculosis* antibodies. The LSPR optical biosensing technique was indeed successful in the detection of anti-*Mycobacterium tuberculosis* antibodies.

1. Introduction

Tuberculosis (TB) is a contagious disease and one of the world's deadliest infectious diseases caused by the *Mycobacterium tuberculosis* (MTb) pathogen [1,2]. It is an airborne bacillus and can spread through microscopic droplets or particles called droplet nuclei generated when a person with untreated active pulmonary TB coughs, sneezes, talks, or sings [3,4]. People who become infected with TB have approximately a 10% risk of developing active TB during the course of their lives, with greater risk in the first two years after infection and much greater risk in HIV-co-infected individuals [5]. The infection usually lasts throughout life as a latent infection in more than 90% of infected individuals [6]. MTb typically affects the lungs as pulmonary TB, however, it can also occur in other organs of the body as extrapulmonary TB infection [1,6–8]. When TB infection occurs in combination with other serious infections such as HIV, it can severely compromise the host immune system and complicate effective forms of therapy [6].

TB infections remain a major public health problem worldwide, especially in developing and some industrialized countries associated with high morbidity and mortality rates. According to the World Health Organisation (WHO), approximately 2 billion of the world's population is latently infected with TB, with more than 9 million new infections reported annually [2]. In 2017, TB caused approximately 1.3 million deaths among HIV-negative individuals and an additional 300,000 deaths among HIV-positive individuals [10]. The estimated incidence of TB infections remains high in both Asia and Africa, and sub-Saharan Africa has the highest estimated TB incidence [9]. The notable high rate of TB in sub-Saharan Africa is influenced by a high prevalence of

* Corresponding author at: Council for Scientific and Industrial Research, National Laser Centre, P O BOX 395, Pretoria 0001, South Africa.
E-mail address: cmaphanga@csir.co.za (C. Maphanga).

https://doi.org/10.1016/j.sbsr.2022.100545
Received 5 August 2022; Received in revised form 23 November 2022; Accepted 5 December 2022
Available online 6 December 2022
2214-1804/© 2022 The Authors. Published by Elsevier B.V. This is an open access article under the CC BY-NC-ND license (http://creativecommons.org/licenses/by-nc-nd/4.0/).

HIV infections [9]. Despite a slow decline in global TB rates, the progress in closing detection/diagnosis and treatment gaps is slow particularly in Africa [12]. Regardless of the improvements in TB control programs, active tuberculosis cases in many regions remain at unacceptable levels [13]. Advances in TB diagnosis in recent years contributed to increased survival rates, however, there are still reported limitations associated with early diagnosis [14]. The general impact of any new diagnostic test for active TB or latent TB infection primarily depends on the extent of their uptake into national TB programs, affordability for both the patient and the health system, and the quality and durability of the diagnostic platforms [13].

Currently, several TB diagnostic methods have been approved by WHO for TB diagnosis. These include tuberculin skin test (TST), sputum smear microscopy (SSM), TB culture, and various nucleic acid amplification tests (NAATs) [14,15]. However, some of these tests are expensive, require specialized infrastructure, sophisticated equipment, and trained personnel, and thus hinder TB diagnosis, particularly in resource-limited settings [14,16]. The TST is used for rapid TB screening, however, high false positives have been reported in individuals with prior bacillus Calmette–Guérin (BCG) vaccination [15]. The SSM is a simple direct microscopy test used to identify MTb acid-fast bacilli and remains the preferred method for TB diagnosis in resource-limited settings. It is affordable and can be done in basic laboratories at primary healthcare facilities [17]. However, the sensitivity of the SSM is low in TB patients that are unable to produce sputum or have low bacterial loads (i.e., children, HIV-co-infected persons, and those with extrapulmonary disease) [15,18,19]. TB culture is considered the gold standard for diagnosing TB with relatively high sensitivity and specificity. Although TB culture has been used efficiently for TB diagnosis, it requires specialized infrastructure, poses a high risk to laboratory personnel, and therefore requires highly trained staff to perform tests, and its major setback is turnaround time which may take 2 to 6 weeks to grow mycobacteria [10]. More recently developed nucleic acid amplification tests (NAATs) such as the Xpert MTB/RIF assay and line probe assays (LPAs) as well as MIRU-VNTR genotyping methods have been able to provide rapid and sensitive diagnosis and accuracy of approximately 92–95%. However, these are expensive and require specialized infrastructure with skilled technicians [11]. Thus, it remains a priority to find and/or develop new methods for TB diagnosis. These tests should be sensitive, accurate, cost-effective, and built on an analytical platform that is easy to use [6].

For these reasons, WHO recognizes the need for new and more sensitive and specific techniques to improve early TB diagnosis, such as the use of point-of-care (POC) devices [14]. Herein, we evaluated a custom-made optical biosensor chip and analyzed using a custom-built transmission spectroscopy platform to perform localized surface plasmon resonance (LSPR) biosensing for POC TB diagnostic device development. We used The LSPR method over other label-free biosensing techniques because results are obtained in real-time, are robust, precise, and have high sensitivity [22,23]. LSPR biosensing is an optical phenomenon caused by the interaction of incident photons and metallic nanoparticles [24]. It is also a surface plasmon resonance (SPR) phenomenon existing in metallic nanoparticles instead of thin-film metals [13]. During LSPR biosensing, the incident light induces collective oscillations of valence electrons, subsequently increasing the intensity of the electric field at the sensor and creating a characteristic extinction peak at the plasmonic resonance frequency. LSPR biosensors differ from SPR-based biosensors as the induced plasmons oscillate locally around the metallic nanoparticle instead of propagating along with the metal-dielectric interface [14,15]. Upon analyte attachment to the nanoparticle, the refractive index change causes a wavelength shift in the extinction spectrum or changes in transmitted intensity applied in this study, thus making the LSPR platform suitable for label-free detection and quantification of biorecognition events [14]. During LSPR biosensing, changes in the refractive index of the surrounding media enable the application of this method in biosensing, chemical sensing, and gas sensing [27]. In biosensing, LSPR sensors can monitor a variety of binding events, including protein-ligand interactions, deoxyribonucleic acid (DNA) hybridizations, and biomarker interactions [16]. When binding events occur, changes in LSPR properties manifesting as a shift in the extinction peak can be easily measured by ultraviolet-visible (UV–vis) spectroscopy [16].

To develop the biosensor chip, mycolic acid TB antigen was immobilized on the biosensing surface of the chip as our biorecognition element to react with the anti-*Mycobacterium tuberculosis* antibody as the analyte of interest (Scheme 1). To enhance the detection signal on the biosensing surface, gold nanoparticles (AuNPs) were covalently conjugated with a secondary antibody, also called signal antibody, and subsequently introduced on the biosensing surface. The AuNPs were further optimized before and after bioconjugation using ultraviolet-visible (UV–vis) spectroscopy, dynamic light scattering (DLS), and Fourier-transform infrared (FTIR) spectroscopy. The biosensing surface was characterized using scanning electron microscopy (SEM), energy-dispersive X-ray (EDX) spectroscopy, and atomic force microscopy (AFM). The optimized biosensor chip was further analyzed using the custom-built setup to perform transmission spectroscopy for LSPR detection, and the acquired data were analyzed using OriginPro software.

2. Materials and methods

2.1. Fluorescence microscopy

Fluorescence microscopy was performed to determine the presence of anti-*Mycobacterium tuberculosis* primary antibodies on the surface of the substrate containing immobilized mycolic acid TB antigen. To perform fluorescence microscopy on the glass substrate, the hydrophobic glass slides (SiO_2) were activated with piranha solution (H_2O_2: H_2SO_4, 7:3 *v*/v) for 45 min at 75 °C to generate Si-OH bonds. Subsequently, the glass slides were washed thoroughly with ultrapure water (resistivity of 18 MΩ) and blow-dried with nitrogen gas. After the activation procedure, the activated glass slides were immersed in (3-Aminopropyl) triethoxysilane (APTES) (1%, *v*/v) (Sigma-Aldrich, A3648) in a vertical Coplin jar and incubated at room temperature overnight. Post incubation, the glass slides were washed thoroughly by sonication in absolute ethanol for 5 min and followed by sonication in ultrapure water for 5 min. The clean glass slides were blown with nitrogen (N2) gas and further dried at 90 °C for 1 h. Silanized glass slides were used immediately to immobilize stearic acid (STA) (141 mM) (Sigma-Aldrich, S4745) on the glass surface or stored in a vacuum for future use. A self-assembled monolayer (SAM) of mycolic acid (MA) from *Mycobacterium tuberculosis* (bovine strain) (0.5 mg/mL) (Sigma-Aldrich, M4537) used as TB antigens were formed on the STA monolayer by incubating the slide in a solution of MA dissolve in hexane (1 mg MA, 2 mL hexane: MW 86,18 g/mol) (Sigma-Aldrich, 34,859) overnight at room temperature. Post incubation, the slide was rinsed thoroughly with 1× phosphate buffered saline (PBS) (Sigma-Aldrich, D1283) to remove physically adsorbed MA. Subsequently incubated in a solution of bovine serum albumin (BSA) (1%, *v*/v) (Roche Diagnostics, 10,711,454,001) blocking agent in 1× PBS for an hour before the addition of anti-*Mycobacterium tuberculosis* antibody (Abcam, ab905) (8.8 mg/mL) prepared in 1× PBS (1:100 dilution) was used as primary antibody. This antibody was introduced on the MA monolayer and incubated overnight. For fluorescence staining, to test for the successful reaction between MA and the primary antibody, a secondary fluorescently-labeled goat anti-rabbit IgG H&L (Alexa Fluor) (2 mg/mL, 1:200 dilution in 1× PBS) (Abcam, ab150077) was introduced to the surface. The excitation and emission wavelengths of the goat anti-rabbit IgG H&L (Alexa Fluor) are 495_{Ex} /519_{Em} nm. Fluorescence was visualized using an inverted microscope (Wirsam Olympus® CKX41) with a mounted reflected fluorescence system.

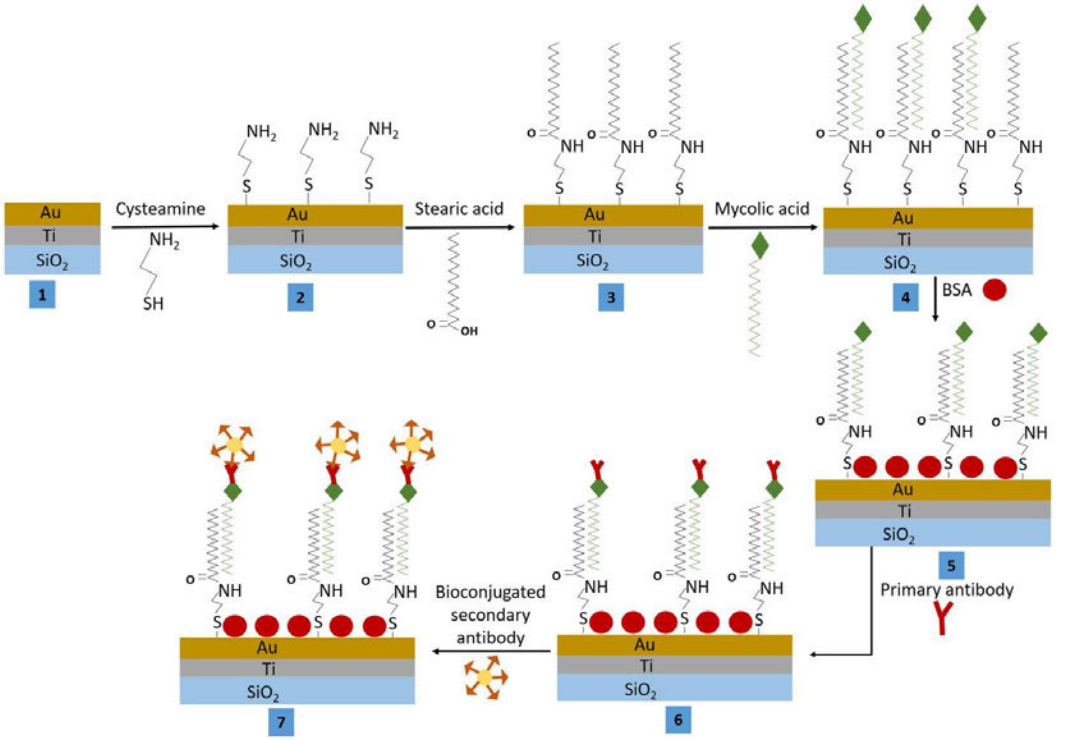

Scheme 1. Schematic representation of the development process of the gold-coated biosensor chip for TB diagnosis. Mycolic acid was used as a biorecognition element and immobilized on the biosensing surface to capture anti-*Mycobacterium tuberculosis* antibodies. Schematic key steps include the following: (1) a biosensor chip with a layer of gold deposited on a thin layer of titanium sputtered on a glass substrate, (2) immobilization of cysteamine monolayer on the thin gold surface, (3) covalent attachment of stearic acid (STA) to cysteamine and formation of amide bonds using N-hydroxysuccinimide (NHS) and 1-Ethyl-3-(3-dimethylaminopropyl)-carbodiimide (EDC), (4) development of a self-assembled monolayer (SAM) of mycolic acid (MA) through inter-molecular forces existing between STA and MA, (5) introduction of 1% bovine serum albumin (BSA) to prevent non-specific binding of molecules, (6) binding of anti-*Mycobacterium tuberculosis* as primary antibody to MA, (7) binding of gold-bioconjugated secondary antibody to the primary antibody.

2.2. UV–vis absorption spectroscopy

UV–vis absorption spectroscopy and dynamic light scattering (DLS) were used to characterize the gold nanoparticles (AuNPs) before and after bioconjugation. To perform covalent bioconjugation of the 60 nm gold NanoUrchins (Cytodiagnostics, 2459298_60U), N-hydroxysuccinimide (NHS) (13 mM) (Sigma-Aldrich, 56,480) and 1-Ethyl-3-(3-dimethylaminopropyl)-carbodiimide) (EDC) (5 mM) (Sigma-Aldrich, E7750) with similar molar ratio were added to heterobifunctional polyethylene glycol (SH-PEG-COOH) (10 mg diluted in 10 mL ultrapure water) (Sigma-Aldrich, 757,845) in ultrapure water and shaken for an hour. The pH of this reaction mixture was adjusted to 7.4 using 10× PBS, and the anti-*Mycobacterium tuberculosis* antibody was added to the solution. The reaction mixture was incubated for additional 2 h before filtering with a 50 kDA filter to remove any by-products. The final SH-PEG-IgG conjugated solution was obtained after washing with 1× PBS twice. Then, 12 μL of the SH-PEG-IgG conjugate was added to 200 μL of AuNPs and incubated for an hour to form the TB-bioconjugate (AuNPs-IgG) confirmed using NanoDrop 8000 spectrophotometer (Thermo Fisher Scientific, United States). Several absorption spectra (ϵ 4) of the AuNPs were recorded using the NanoDrop to determine the redshift before and after bioconjugation. For purposes of introducing bioconjugated AuNPs on the biosensing surface to enhance the detection signal during LSPR biosensing, a complementary secondary goat anti-rabbit IgG H&L antibody was used for bioconjugation to react with the primary anti-*Mycobacterium tuberculosis* antibody immobilized on the biosensor chip surface.

2.3. Dynamic light scattering

DLS was performed to monitor changes in size distribution by intensity before and after bioconjugation of AuNPs with a secondary antibody. Malvern Zetasizer Nano ZS (Malvern Instruments Ltd., United Kingdom) was used to perform DLS. AuNPs, bioconjugated AuNPs with anti-*Mycobacterium tuberculosis* (referred to as TB-bioconjugate), and bioconjugated AuNPs with mycolic acid TB antigen were analyzed. Samples were analyzed in triplicates and repeated three times ($n = 3$).

2.4. FTIR spectroscopy

FTIR measurements of AuNPs, TB-bioconjugate, and TB-bioconjugate reacted with mycolic acid TB antigen were analyzed in transmission mode using a Perkin Elmer Spectrum 100 FTIR spectrometer equipped with a DTGS detector. The spectra were measured in the 4000 to 550 cm^{-1} wavenumber region. Before data acquisition, the spectrometer plate and crystal were thoroughly cleaned with tissue and

isopropanol and cleaned in between sample analyses. The spectrum of air was used as background before each sample analysis. The background and sample spectra were taken in a room with a temperature around 21–23 °C, at a spectral resolution of 4 cm^{-1}, and to each measurement, 32 scans were co-added and averaged to achieve an acceptable signal-to-noise ratio. In all cases, spectra resolution was maintained at 16 cm^{-1}. The original FTIR spectra were baseline-corrected using Perkin Elmer Spectrum software.

2.5. SEM and EDX spectroscopy

A gold-coated biosensor chip was developed using the HEX benchtop thin film deposition system (Korvus Technology Ltd., United Kingdom). A gold evaporation slug (Merck Millipore, 373,168–6.4G) was used to form the thin gold film. A 5 nm layer of titanium was sputtered on the SiO_2 substrate before Au deposition (≈ 40 nm) using e-beam evaporation. Titanium is usually deposited to strongly bind the substrate and the Au together [17]. The SEM and EDX data were acquired using the JSM-IT800 schottky field emission scanning electron microscope (JEOL Ltd., Japan). All samples were analyzed for SEM and EDX without coating. Three sample groups, including the bare Au-thin film sample, experiment, and control samples, were analyzed using SEM and EDX. The Experiment sample consisted of MA, anti-*Mycobacterium tuberculosis* antibody, and goat anti-rabbit IgG H&L secondary antibody bioconjugated to AuNPs (referred to as TB-bioconjugate). The control sample did not have an anti-*Mycobacterium tuberculosis* antibody on the surface. SEM was performed to study the surface morphology post immobilization of the TB-bioconjugate to the biosensor chip surface in the presence and absence of anti-*Mycobacterium tuberculosis* antibody linked to MA TB antigen. Subsequently, EDX spectroscopy was performed to study the different elements present on the biosensing surface, and both techniques were used to characterize the functionalized biosensing surface. To functionalize the biosensing surface as illustrated in Scheme 1, the gold thin layer was washed with absolute ethanol and blow-dried with N_2 gas before incubation with cysteamine (Cys) (10 mM) (Sigma-Aldrich, M9768) in absolute ethanol for 18 h at room temperature to form an Au-Cys monolayer (Fig. 2). NHS and EDC with similar molar ratios were used for covalent attachment of stearic acid using carbodiimide coupling chemistry to form an amide bond. After the formation of the Cys-STA monolayer, the modified gold-coated surface was washed thoroughly with ethanol and water to remove physically adsorbed stearic acid species. Mycolic acid TB antigens were immobilized on the STA monolayer by immersion the biosensor chip in MA solution overnight at room temperature. Post incubation, the biosensor chip was rinsed thoroughly with 1× PBS to remove physically adsorbed MA, and subsequently incubated in a solution of 1% BSA blocking agent for an hour before addition of primary anti-*Mycobacterium tuberculosis* antibody. To enhance the sensitivity of the biosensor chip, a goat anti-rabbit IgG H&L secondary antibody was conjugated to gold nanoparticles (AuNPs) (Sigma-Aldrich, 797,707) and herein called TB bioconjugate (AuNPs-IgG).

2.6. Atomic force microscopy

Atomic force microscopy (AFM) was used for surface morphology studies to characterize the biosensing surface of the custom-made biosensor chips at different stages of development. The AFM images were captured with a Vecco AFM system (Digital Instruments, USA) using a silicon cantilever tip. The tip has a curvature radius of 10 nm and is n-doped silicon, with a resonance frequency of 204–497 kHz and a force constant of approximately 10–130 N/m. Images acquired by the AFM instrument were analyzed using Nanoscope software.

2.7. LSPR biosensing

A custom-built transmission spectroscopy setup was used to perform LSPR biosensing. The setup was assembled using a 512 nm green light source with a power of 3.1 mW. The light was collimated using collimating lenses and focused on the biosensor chip sample placed on the sample stage. Transmitted light was collected through a 10× microscope objective, and a 50/50 beam splitter directed the light to the imaging system and the spectrometer through a fiber. The imaging system was formed by a charge-coupled device (CCD) camera connected to a computer and was used to visualize events taking place on the sample stage. Sample groups were prepared in triplicates under the same conditions and repeated three times ($n = 3$). During sample analysis, background measurements were taken at the same setting before each recording. Transmitted light was focused into the fiber using a focussing lens and directed to the USB 4000 portable spectrometer (Ocean Optics Inc., United States) connected to the computer for data acquisition and data analysis (Fig. 1). Further data analysis was performed using OriginPro software.

3. Results and discussion

3.1. Fluorescence microscopy

Fluorescence microscopy was performed to visualize the interaction between the SAM of mycolic acid TB antigen and the anti-*Mycobacterium tuberculosis* antibody. Two sample groups were prepared for fluorescence microscopy, an experiment, and a control sample. The experiment sample surface consisted of mycolic acid as the TB antigen, an anti-*Mycobacterium tuberculosis* primary antibody, and a fluorescent-labeled goat anti-rabbit IgG H&L (Alexa Fluor) secondary antibody. The control sample surface consisted of the components in the experimental samples except for the anti-*Mycobacterium tuberculosis* primary antibody. The goat anti-rabbit IgG H&L (Alexa Fluor) was specifically designed to interact with the anti-*Mycobacterium tuberculosis* antibody. In the

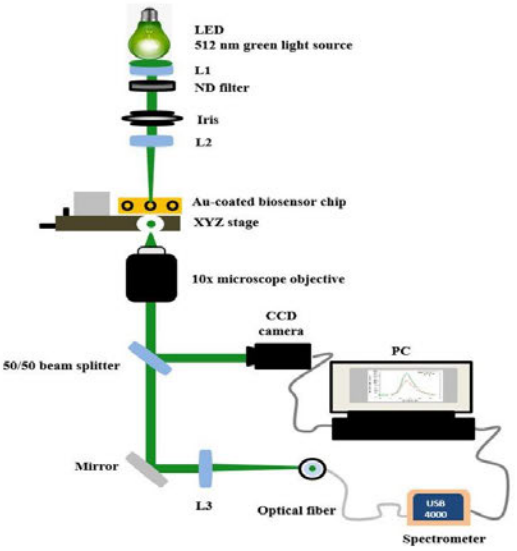

Fig. 1. Experimental setup of the transmission spectroscopy setup used for LSPR biosensing. The setup consists of a 512 nm green light source with a power of 3.1 mW, collimating lenses (L1 and 2), XYZ stage, a 10× microscope objective, and an imaging system consisting of a CCD camera and computer, focussing lens (L3), an optical fiber, and a portable USB spectrometer connected to a computer. (For interpretation of the references to colour in this figure legend, the reader is referred to the web version of this article.)

experiment sample, green fluorescence was detected after the addition of the goat anti-rabbit IgG H&L (Alexa Fluor) secondary antibody (Fig. 2A). In the control sample group (Fig. 2B), no fluorescence was detected because of a lack of anti-*Mycobacterium tuberculosis* antibody on the surface. This also suggests that the goat anti-rabbit IgG H&L (Alexa Fluor) antibody does not bind directly to mycolic acid TB antigen. These results confirm the successful binding and specificity of mycolic acid to anti-*Mycobacterium tuberculosis* antibody and specificity of the goat anti-rabbit IgG H&L (Alexa Fluor) to anti-*Mycobacterium tuberculosis* antibody.

3.2. UV–vis absorption spectroscopy

UV–vis absorption spectroscopy was used to characterize AuNPs before and after bioconjugated to goat anti-rabbit IgG H&L secondary antibody. The spectrophotometer can identify components in a solution mainly based on their unique absorbance characteristics [18]. Covalent conjugation chemistry was applied for the bioconjugation of AuNPs to the secondary antibody. EDC and NHS chemistry were used to link goat anti-rabbit IgG H&L secondary antibody to polyethylene glycol (SH-PEG-COOH). In this chemistry, EDC and NHS activate the carboxyl groups of the AuNP surface to form an intermediate that interacts with the amine group (NH_2) on the antibody [19]. Bioconjugation occurs upon successful binding of the antibody to the AuNPs surface, thus resulting in a redshift in absorption spectrum by a few nanometres [20]. Fig. 3 shows the UV–vis absorption spectrum of AuNPs before and after bioconjugation. After bioconjugation with the antibody, a reduction in absorption intensity in the TB-bioconjugate was observed indicating successful bioconjugation of the AuNPs with the antibody. Successful bioconjugation of AuNPs to the goat anti-rabbit IgG H&L secondary antibody plays a crucial role in enhancing the refractive index on the biosensing surface of the biosensor chip. Fig. 3 shows the absorption spectrum of AuNPs before bioconjugation (black spectrum) and the spectrum of AuNPs after bioconjugation (red spectrum). The AuNPs showed absorption peak intensity at 575 nm before bioconjugation and 585 nm after bioconjugation. Approximately 10 nm redshift was observed as confirmation of successful bioconjugation. AuNPs have unique optical properties that can be easily manipulated compared to bulk gold. These special characteristics provide a plethora of advantages, especially in biosensing and diagnostic imaging. One of the major attributes is the interchange of light with electrons on its exterior [9]. The resonance wavelength and bandwidth of the AuNPs are dependent on the shape, particle size, refractive index of the surrounding media, and temperature. The shift in the AuNPs-IgG bioconjugate spectra might be a result of the changes in the dielectric environment surrounding the AuNPs [18,21].

3.3. Dynamic light scattering

Further characterization of AuNPs was performed to determine the particle size distribution using DLS. The DLS measurements of changes in size distribution by intensity were used to study the AuNPs before and after bioconjugation with the secondary antibody. Each sample was measured in triplicates and repeated three times ($n = 3$) at 25 °C, and the dispersant refractive index was 1.330 with a viscosity of 0.8872 cP. Sample groups included AuNPs, TB-bioconjugate, and TB-bioconjugate in the presence of mycolic acid (Fig. 4). The *Z*-average value of the AuNPs before bioconjugation was 164 d.nm and increased to 190 d.nm after bioconjugation (Fig. 4B). This finding supports the UV–Vis absorption spectroscopy wavelength redshift observed after bioconjugation and indicates successful bioconjugation of AuNPs. There were no significant differences in hydrodynamic size when mycolic acid was introduced to the bioconjugate. The increase in the size of the neat nanoparticles to an average hydrodynamic size of 164 nm may be attributed to agglomeration [22]. The change in particle size between the TB-bioconjugate and the bioconjugate with mycolic acid was not significant (Fig. 4B). However, changes in average peak intensity were observed between the three sample groups (Fig. 4C). High peak intensity was observed in AuNPs before bioconjugation and a notable decline in intensity was observed after bioconjugation. The average peak intensity of the AuNPs, TB-bioconjugate, and TB-bioconjugate in the presence of mycolic acid was 11.3, 9.65, and 8.9 respectively.

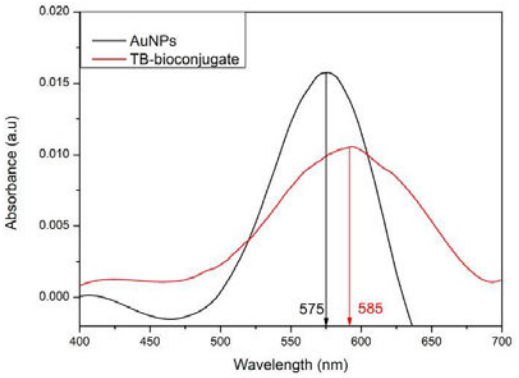

Fig. 3. A graphical representation of UV–vis absorption spectrograph for the bioconjugation of AuNPs to goat anti-rabbit IgG H&L secondary antibody. Measurements were taken before and after bioconjugation. The black line represents the spectrum of neat AuNPs before conjugation, and the red line represents the spectrum of AuNPs after bioconjugation with a secondary antibody. (For interpretation of the references to colour in this figure legend, the reader is referred to the web version of this article.)

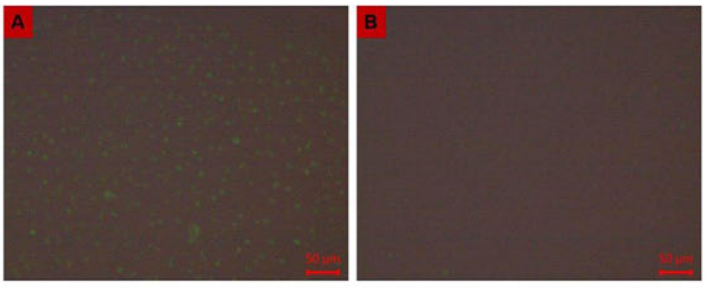

Fig. 2. Fluorescence images of mycolic acid TB antigen reaction with anti-*Mycobacterium tuberculosis* antibody used as primary antibody. Image A showing green fluorescence is the experiment sample consisting of SAM of mycolic acid, a primary antibody, and a fluorescent-labeled goat anti-rabbit IgG H&L (Alexa Fluor) secondary antibody. Image B shows the control sample with SAM of mycolic acid and the goat anti-rabbit IgG H&L (Alexa Fluor) antibody introduced on the surface in the absence of an anti-*Mycobacterium tuberculosis* antibody. No fluorescence was observed in the control sample. Images were captured with a CKX41 Olympus microscope, and the length of the scale bar is 50 μm. (For interpretation of the references to colour in this figure legend, the reader is referred to the web version of this article.)

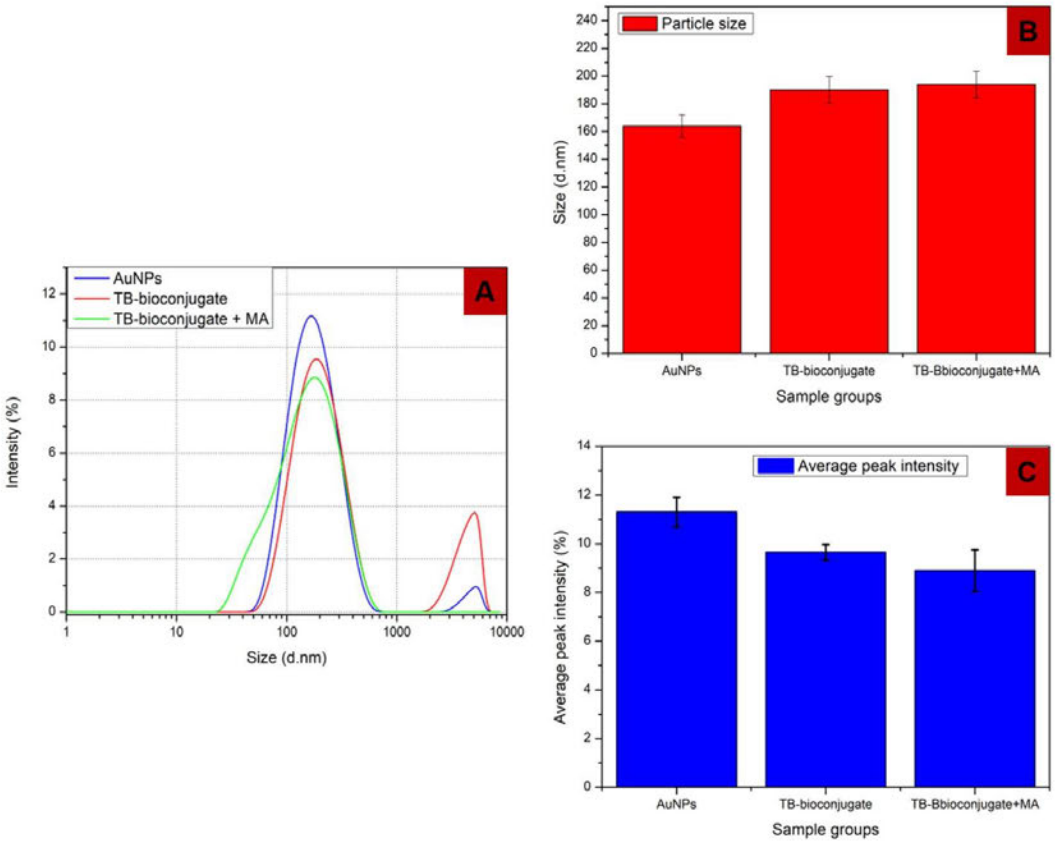

Fig. 4. DLS data of size distribution by intensity of AuNPs before and after bioconjugation (TB-Bioconjugate) and bioconjugate in the presence of mycolic acid (A). (B) particle size differences, and (C) average peak intensity differences. DLS was performed on a Zetasizer instrument using water as a dispersant at 25 °C. Samples were analyzed in triplicates and repeated three times ($n = 3$).

3.4. *FTIR spectroscopy*

FTIR spectroscopy analysis is a qualitative optical detection technique used to examine the existence of surface functional groups [19]. FTIR was carried out to identify the possible functional groups formed during the bioconjugation of AuNPs with anti-*Mycobacterium tuberculosis* antibody and monitor spectral changes due to the interaction between the anti-*Mycobacterium tuberculosis* antibody and mycolic acid TB antigen. A sample of neat AuNPs was used as a reference (Fig. 5A). FTIR was performed using a sample dry of AuNPs, TB-bioconjugate, and the TB-bioconjugate with mycolic acid TB antigen. This was done to determine the molecular bonds formed between the AuNPs, anti-*Mycobacterium tuberculosis* antibody, and mycolic acid. Mycolic acid used in this study is a long-chain fatty acid with carboxylic acid and hydroxyl functional groups. Fig. 5 shows the FTIR spectra of the three sample groups. The AuNPs (Fig. 5A) presented prominent peaks at 2983 cm^{-1}, 2923.2 cm^{-1}, 2830.4 cm^{-1} wavenumbers indicating alkane C—H stretching; 2287.8 cm^{-1} indicating the presence of O=C=O; 1558.6.6 cm^{-1} representing N—O stretching, and 1400.8 cm^{-1} representing C—H bending. The TB-bioconjugate (Fig. 5B) displayed a very similar spectra pattern to the AuNPs, however with reduced percentage transmittance and the introduction of very few new wavenumbers. The 2983 cm^{-1} also present in AuNPs spectra represents C—H stretching, 1980.7 cm^{-1} for C—H bending, 1656.6 cm^{-1}C=C stretching, and 1388 cm^{-1} for O—H bending. The reduction in percentage transmittance in the TB-bioconjugate supports the UV–vis absorption spectroscopy results from section 3.2 whereby a reduction in absorption intensity was observed when anti-*Mycobacterium tuberculosis* antibodies were bioconjugated to AuNPs. When mycolic acid was added to the bioconjugated AuNPs (Fig. 5C), strong bands were yielded at 3337 cm^{-1}, 2958 cm^{-1}, 2922 cm^{-1}, 2956 cm^{-1}, 1638 cm^{-1}, 1462 cm^{-1}, and 1378 cm^{-1}. The absorption band at 3337 cm^{-1} corresponds to carboxyl and hydroxyl functional groups [23,24]. In addition, the absorption bands at 2958 cm^{-1}, 2922 cm^{-1}, and 2956 cm^{-1} fall within the alkanes and carboxylic acid functional groups and therefore represent alkane (C—H) stretch and carboxylic acid (O—H stretch) [25]. In addition, the absorption band at 1638 cm^{-1} represents vibrational modes of C=C double bonds of the AuNP/antibody/mycolic acid complex. Lastly, the absorption peak at 1462 cm^{-1} shows the presence of an aromatic (C=C stretch). These findings indicate the presence of mycolic acid in the reaction mixture containing bioconjugated AuNPS, however, does not confirm direct binding without the support of other qualitative and quantitative characterization tests including SEM, EDX, AFM, and DLS.

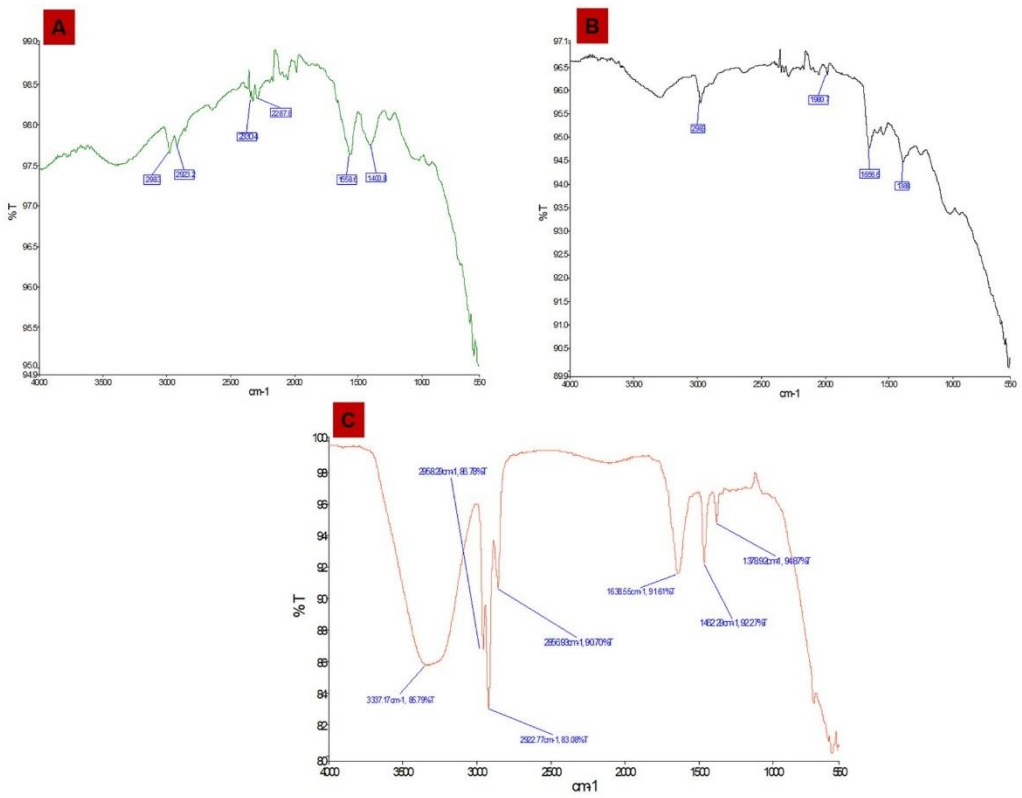

Fig. 5. FTIR spectra of AuNPs (A), TB-bioconjugate (B), and the TB-bioconjugate reacted with mycolic acid TB antigen (C) dissolved in hexane.

3.5. SEM and EDX spectroscopy

The presence of bioconjugated gold Nanourchins on the biosensing surface was studied using SEM analysis for end-point characterization. Gold NanoUrchins have unique optical properties as compared to spherical gold nanoparticles with the same diameter. NanoUrchins have a spiky uneven surface which causes a red shift in the surface plasmon peak and a larger enhancement of electromagnetic fields at the tips of the NanoUrchin spikes as compared to that of a spherical particles. The 60 nm nano-urchins used in this study were chosen because they have the same absorption wavelength as the gold deposited on the glass substrate. To perform SEM and EDX, three sample groups were prepared namely a thin gold film surface, the experiment sample, and the control sample. The experiment and control samples were prepared on a thin gold film surface. The thin gold sample with an approximately 40 nm Au layer was used as a reference to visualize the distribution of Au on the surface. The experiment sample surface consisted of mycolic acid TB antigen, anti-*Mycobacterium tuberculosis* primary antibody, and AuNPs bioconjugated with goat anti-rabbit IgG H&L secondary antibody. There was no anti-*Mycobacterium tuberculosis* antibody on the biosensing surface of the control sample. The control sample was used to test for the specificity of the biorecognition element (MA) to the primary antibody. SEM images were obtained without coating the samples. Observing the images in Fig. 6C and D of the Au thin film sample, it is evident that the gold is uniform, evenly distributed, closely, and densely packed. The film shows a columnar structure resembled by round-shaped structures. This is in agreement with what has been documented in literature [17]. The nano-interspaces between the columnar structures support what has been detected in other studies, and this is an indication that the film is robust and can be used to develop biosensing platforms [26]. The morphology of the Au nano-urchins used in this study is spherical and multi-branched. On the experiment sample, SEM was able to detect a substantial amount of the spherical multi-branched AuNPs (Fig. 6B). There were no agglomerations observed on the surface and the AuNPs were evenly dispersed. In the control sample, the addition of bioconjugated AuNPs was not expected to bind to the surface unless there was non-specific binding. The non-specific binding observed could result from the blocking agent (bovine serum albumin) immobilized on the biosensing surface, longer incubation time, or even inadequate wash steps. Fig. 6C shows the SEM results of the control sample where small traces of AuNPs were visualized. These traces of bioconjugated AuNPs detected on the biosensing surface of the control sample were confirmed by EDX to be insignificant. The percentage of Au for both the reference sample (Au thin film layer) and the control sample was 42.83 (Fig. 7A) and 42.50 (Fig. 7C), respectively. These results confirm the successful binding of bioconjugated AuNPs on surfaces containing immobilized anti-*Mycobacterium tuberculosis* antibodies and also support the specificity of mycolic acid reaction with anti-*Mycobacterium tuberculosis* antibodies.

To confirm the specific binding of bioconjugated AuNPs on the biosensing surface containing immobilized anti-*Mycobacterium tuberculosis*, EDX was performed. EDX was used to qualitatively determine the elemental composition between the reference sample (Au thin film), experiment, and control samples, with Au as the main element of interest. The biosensor chips used for SEM were also used to perform EDX spectroscopy. The biosensor chip design and development as seen in Scheme 1 consisted of a glass substrate (1 mm thick), a 40 nm Au thin layer deposited on a 5 nm thin layer of titanium. The elemental composition as per Fig. 7A - C shows that Au and Si dominate over all the other elements detected on the biosensor chip and are present in all

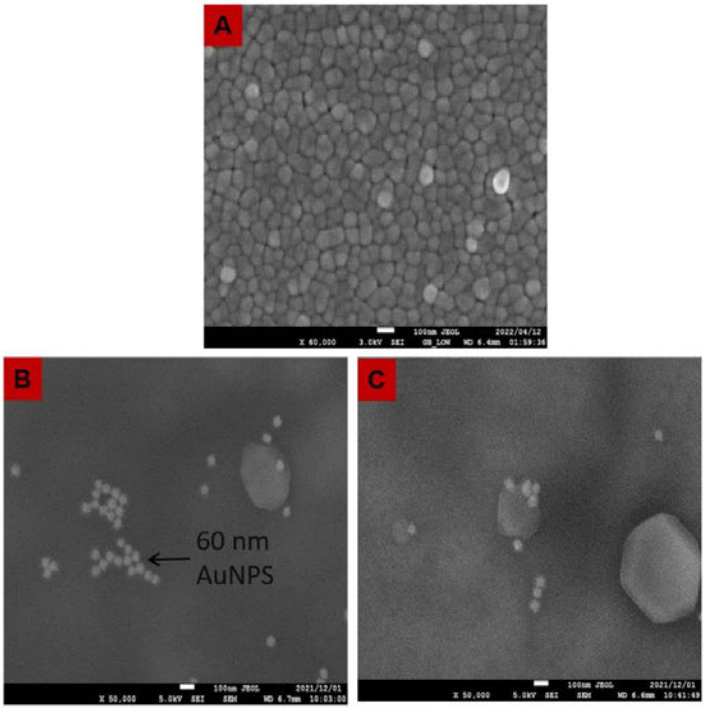

Fig. 6. SEM images of the biosensing surface of the thin bare gold surface (A), experiment sample (B)) and control sample (C). The experiment sample surface consists of SAM of mycolic acid TB antigen, anti-*Mycobacterium tuberculosis* antibody, and a secondary antibody bioconjugated to AuNPs. The control sample lacks an anti-*Mycobacterium tuberculosis* antibody on the surface. The AuNPs (nano-urchins) under SEM are visualized as tiny bright spots resembling stars. Minimal traces of bioconjugated AuNPs were spotted on the biosensing surface of the control sample. (For interpretation of the references to colour in this figure legend, the reader is referred to the web version of this article.)

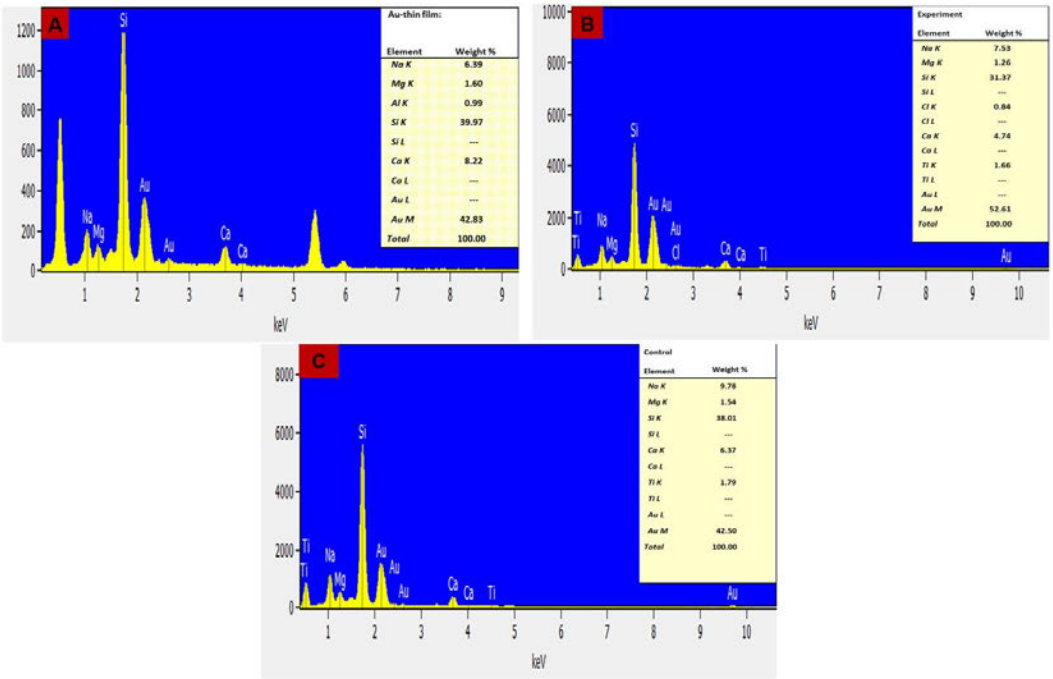

Fig. 7. EDX spectrographs of the bare gold-coated surface (A), the experiment sample (B), and the control sample (C). The same samples prepared for SEM were used to perform EDX. The biosensing surface of the experiment sample consisted of mycolic acid TB antigen, an anti-*Mycobacterium tuberculosis* primary antibody, and a goat anti-rabbit IgG H&L secondary antibody bioconjugated to AuNPs. The main elements obtained from all three samples are Au, Si, Ti, Na, Mg, Ca, and Cl. There were significant differences in the weight, and atomic percentage of Au detected between the experimental sample compared to the control and reference samples which had approximately similar percentages. (For interpretation of the references to colour in this figure legend, the reader is referred to the web version of this article.)

sample groups. Si is from the SiO_2 glass substrate, and Au is from the Au thin film and/or AuNPs. Si was detected at a weight percentage lower than Au in all sample groups, however, its atomic percentage was higher than Au in all the samples. The weight percentage of Au in the reference sample, experiment, and control sample were 42.83, 52.62, and 42.50, and the atomic percentage was 9.77, 13.77, and 9.57, respectively. The weight and atomic percentage of Au were higher on the experiment sample containing immobilized bioconjugated AuNPs as seen on SEM (Fig. 6B). This indicates that the additional Au percentage detected was contributed by the AuNPs on the surface. Approximately similar weights and atomic percentages of Au were detected on the Au thin film surface and the control sample. This indicates that the detected Au percentage was primarily from the Au layer. Common elements detected in all sample groups were magnesium (Mg), sodium (Na), and calcium (Ca). In addition, chlorine (Cl) was detected only in the experiment sample, and aluminium (Al) was detected at very low levels in the reference sample instead of Ti detected in both the experiment and control samples.

3.6. Atomic force microscopy

Atomic force microscopy was used to perform layer-by-layer characterization during the process of developing the biosensor chip. The AFM analysis is a quantitative technique and provides direct information on the height of the surface structures. This is a crucial technique in the process of developing a biosensor chip to confirm the surface binding of structures. Changes in height and surface roughness at various stages of biosensor chip development were studied. The images taken using AFM are shown in Fig. 8, and each of the scans represents a 5 μm × 5 μm lateral area that was scanned. AFM was used to characterize surfaces of the Au thin film layer, MA, MA + 1^0 Ab, MA + 1^0 Ab+2^0Ab, and MA + 2^0Ab. The Au-thin layer referred to as the background sample had nothing immobilized on the surface. The MA sample, referred to as the reference sample consisted of mycolic acid immobilized on a surface consisting of cysteamine (Cys). The Cys was used as a linker for MA which is the biorecognition element. Stearic acid was covalently attached to the Cys before the introduction of MA. The binding of MA to the Cys/stearic acid complex may be associated with the strong Van der Waal's hydrophobic attractive forces existing between the alkyl chains of the MA and stearic acid [27]. The MA + 1^0 Ab sample had an anti-*Mycobacterium tuberculosis* antibody introduced onto the MA surface. The MA + 1^0 Ab+2^0Ab referred to as the experiment sample, consisted of AuNPs bioconjugated with goat anti-rabbit IgG H&L secondary antibody and added to the surface containing the primary antibody. Lastly, the MA + 2^0Ab sample, referred to as the control sample, was introduced to test for non-specific binding and consisted of AuNPs bioconjugated with the goat anti-rabbit IgG H&L secondary antibody introduced on a MA surface in the absence of anti-*Mycobacterium tuberculosis* primary antibody. Homogenous and smooth coverage of the surface was observed in the Au thin film sample (Fig. 8A). Numerous islands were formed on the surface when MA was introduced (Fig. 8B). A similar pattern was observed when the bioconjugated antibody was introduced on the MA surface and subsequently washed. This may be due to the

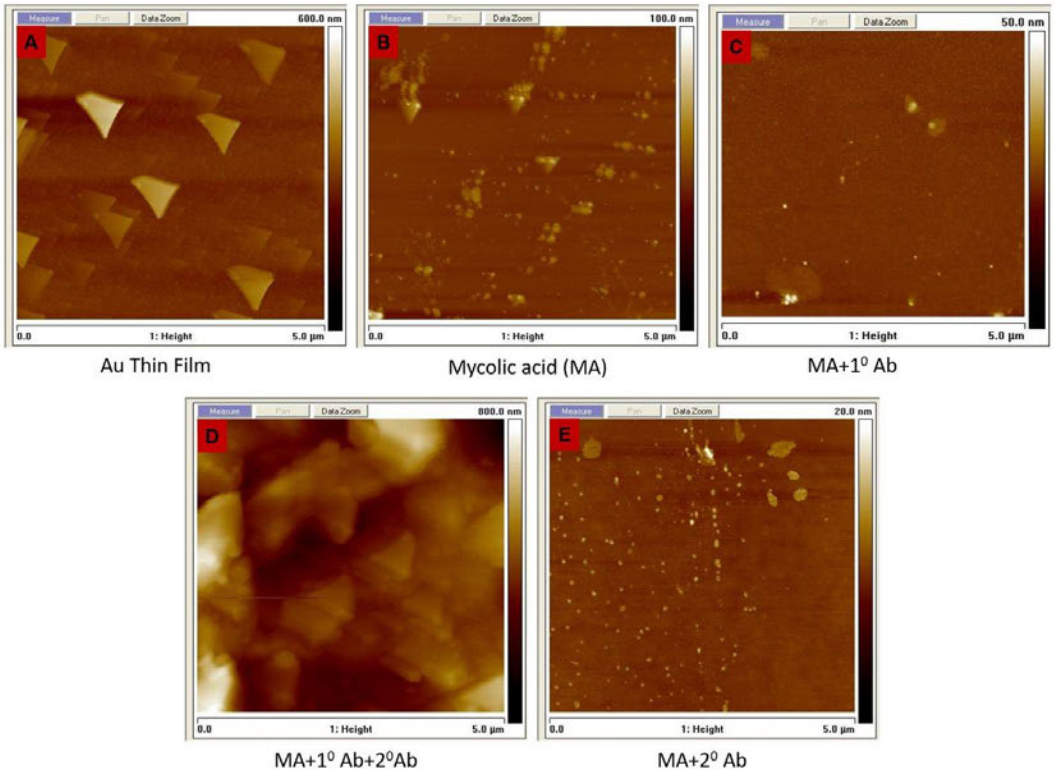

Fig. 8. Atomic force microscopy micrographs of the five sample groups captured at different stages of the biosensor chip development. Sample groups include Au thin film layer (A), MA (B), MA + 1^0Ab (C), MA + 1^0Ab + 2^0Ab (D), and MA + 2^0Ab (E). A sharp increase in height and surface roughness was observed in MA + 1^0 Ab+2^0Ab sample (D) confirming the successful binding of the bioconjugated AuNPs with the goat anti-rabbit IgG H&L secondary antibody added on a surface containing anti-*Mycobacterium tuberculosis* primary antibody. The binding of the bioconjugated AuNPs to the surface is critical for detection signal enhancement during optical biosensing.

absence of a primary antibody on the surface to react with the bioconjugated secondary antibody (Fig. 8E). Interestingly, when the primary antibody was introduced to react with mycolic acid, the islands disappeared and the surface displayed a smooth morphology (Fig. 8C). On the contrary, various large and rough structures were visualized in the MA + 1^0 Ab+2^0Ab sample (Fig. 8D). This may be the resemblance of AuNP-antibody complexes. This also supports findings by Lee et al., 2015 who demonstrated the possibility of visualizing AuNP-antibody complexes as a result of the presence of immobilized AuNPs. The roughness of the surface increased significantly on the surface containing AuNPs bioconjugated to goat anti-rabbit IgG H&L secondary antibody (Fig. 8D). The Z range increased from 289 nm in the Au thin film sample (Fig. 8A) to 681 nm in the MA + 1^0 Ab+2^0Ab sample containing immobilized bioconjugated AuNPs. This shows that immobilization of the secondary antibody to the AuNPs was achieved and the secondary antibody on the surface of the AuNPs was able to react with the primary antibody on the surface of the biosensor chip. This finding supports the UV–vis absorption spectroscopy findings in section 3.2, and the SEM and EDX spectroscopy results in section 3.5.

3.7. LSPR biosensing

The optimized biosensor chip with characterized bioconjugated AuNPs immobilized on the biosensing surface was analyzed using a custom-built transmission spectroscopy setup to perform LSPR biosensing. Samples were prepared in triplicates under the same conditions and repeated three times ($n = 3$). The transmitted intensity between the five sample groups was measured. Sample groups included Au-thin layer, MA, MA + 1^0 Ab, MA + 1^0 Ab+2^0Ab, and MA + 2^0Ab. Measurements of transmitted intensity of the five sample groups are depicted in Fig. 9A. The transmitted intensity measurements of the five sample groups demonstrated that there was more light transmitted in the Au-thin film sample used as the background. The MA sample transmitted less light compared to the Au. The MA + 2^0Ab sample used to test for non-specific binding transmitted less light compared to the MA. This shows that the bioconjugated secondary antibody could not bind directly to MA. The small traces of AuNPs seen on the SEM surface (Fig. 6C) may be a result of MA + 2^0Ab transmitting less light compared to the MA sample group. However, there were no significant differences between these two samples when comparing the average peak height (Fig. 9B) and the area under the graph (Fig. 9C). The MA + 1^0 Ab sample less light compared to the MA + 2^0Ab. This finding supports the successful binding of the primary antibody to the MA surface. A small shift in the wavelength from 516.25 to 516.67 nm was observed in sample groups containing the primary antibody. The MA + 1^0 Ab+2^0Ab sample reported the lowest transmitted intensity. From these results and the

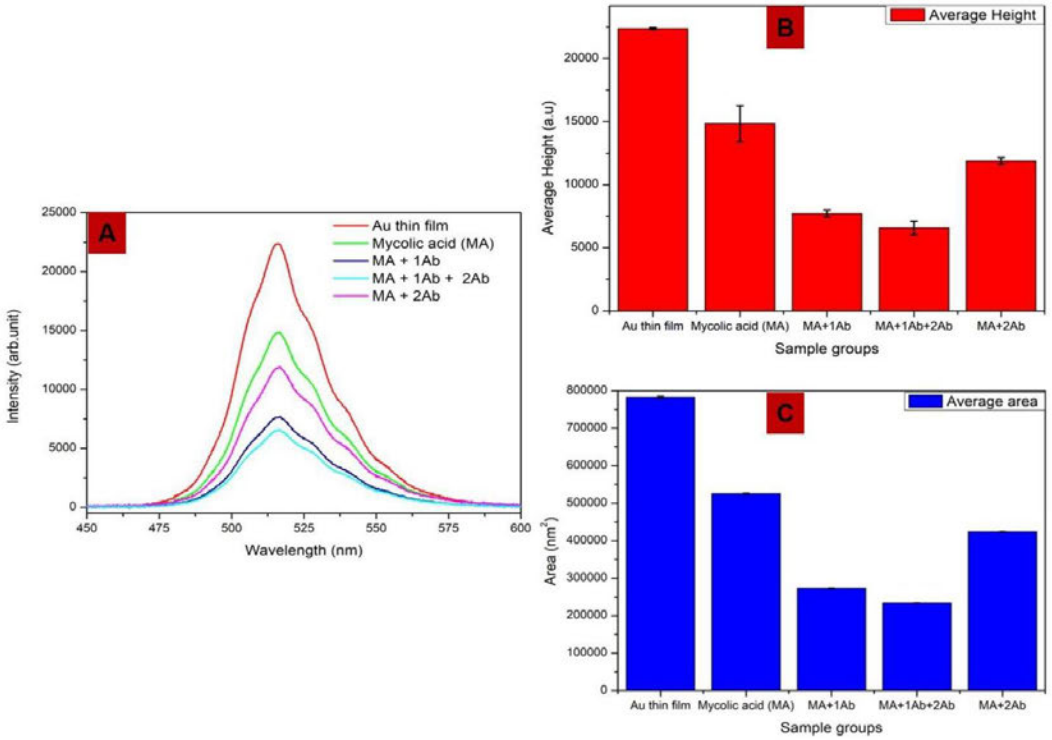

Fig. 9. The transmitted intensity between the Au thin film layer, MA, MA + 1^0Ab, MA + 1^0Ab + 2^0Ab, and MA + 2^0Ab. The Au-thin layer was used as the background sample since all the sample groups were developed from it. The MA sample was used as a reference sample since all the sample groups except the background sample have MA on the surface as the biorecognition element. (A) shows transmitted intensity peaks of the five sample groups, whereby the Au-thin layer transmitted more light, followed by MA, MA + 2^0Ab, MA + 1^0Ab, and the MA + 1^0Ab + 2^0Ab sample reported the lowest transmitted intensity. (B) shows differences in height (B) and area under the graph (C) for each sample group spectrum observed in (A). Sample groups were prepared in triplicates under the same conditions and repeated three times ($n = 3$).

AFM results, it is evident that immobilization of the biorecognition element on the biosensor chip was successful and enabled reaction with the targeted primary antibody which subsequently reacted with the secondary antibody on the surface of AuNPs, hence the increase in height and roughness detected on AFM which lead to less transmitted light on LSPR biosensing.

4. Conclusion

In summary, a custom-made optical biosensor chip consisting of a thin gold-coated layer deposited on a titanium layer on a glass substrate was developed using the Korvus Technology HEX benchtop thin film deposition system. The developed biosensor chip was subsequently functionalized with mycolic acid TB antigens for the detection of anti-*Mycobacterium tuberculosis* antibodies, and a custom-built localized surface plasmon resonance biosensing setup was successful in differentiating between experiment and control groups for the detection of anti-*Mycobacterium tuberculosis*. In this study, Mycolic acid TB antigens were realized as efficient biomarkers to specifically capture anti-*Mycobacterium tuberculosis* antibodies and produce a detectable signal for purposes of TB diagnosis. Based on data acquired using UV–vis absorption spectroscopy, DLS, and FTIR it was proven that the covalent bioconjugation of AuNPs with antibodies was successful. Furthermore, biosensing surface characterization using SEM showed the presence of the bioconjugated AuNPs on the biosensor chip surface, and the gold percentage on EDX spectroscopy was higher in the experiment group containing AuNPs than in the control group and the Au-coated chip used as reference. On AFM, surface roughness and height increased in the experiment group compared to the control and reference groups. And on LSPR biosensing, there was more light transmitted in the reference sample when analyzing peaks based on peak intensity and area under the peaks, followed by the control samples, and the experiment sample transmitted less light. Overall, it was proven that mycolic acid could be applied as an efficient biomarker to capture anti-*Mycobacterium tuberculosis* antibodies. It can be used for the development of biosensor chips for TB diagnosis. And also, biosensor chips can be successfully analyzed using optical detection techniques such as LSPR for diagnostic purposes.

Authors contribution

Charles Maphanga: Conceptualization, data curation, formal analysis, investigation, methodology, writing - original draft, writing - review and editing.

Sello Manoto: Literature search, acquisition of the information, and editing of the article.

Saturnin Ombinda Lemboumba: Literature search, acquisition of the

information, and editing of the article.

Yaseera Ismail: Revision of article for intellectual content, editing of the article.

Patience Mthunzi-Kufa: Revision of article for intellectual content, editing of the article.

Declaration of Competing Interest

The authors declare no conflict of interest.

Data availability

The data that has been used is confidential.

Acknowledgements

This work was made possible through support from the Council for Scientific and Industrial Research (CSIR), The University of KwaZulu Natal (UKZN), and the Department of Science and Innovation (DSI). I would like to thank Sharon Eggers and Bulelwa Mntanya, Characterization Testing, Material Characterization Testing and Analytical Facility (MCTAF), Centre for Nanostructured and Advanced Materials, CSIR for assisting with the FTIR, AFM, SEM, and EDX characterization.

References

[1] I. Barberis, N.L. Bragazzi, L. Galluzzo, M. Martini, The history of tuberculosis: from the first historical records to the isolation of Koch's bacillus, J. Prev. Med. Hyg. 58 (2017) E9–E12. http://www.ncbi.nlm.nih.gov/pubmed/28515626%0Ahttp://www.pubmedcentral.nih.gov/articlerender.fcgi?artid=PMC5432783.

[2] W. Sun, S. Yuan, H. Huang, N. Liu, Y. Tan, A label-free biosensor based on localized surface plasmon resonance for diagnosis of tuberculosis, J. Microbiol. Methods 142 (2017) 41–45, https://doi.org/10.1016/j.mimet.2017.09.007.

[3] A.R. Hinman, M. Director, D.M. James Hughes, H. Linda Rosenstock, E.B. Program Office Stephen Thacker, D.A. Richard Goodman, M. Editor, R.J. Wilson, P.C. Bourque Sandra L Ford Morie M Higgins Peter M Jenkins, Guidelines for Preventing the Transmission of *Mycobacterium tuberculosis* in Health-Care Facilities, 1994 Writer-Editor Visual Information Specialists 43, 1994. https://www.cdc.gov/mmwr/pdf/rr/rr4313.pdf.

[4] N.A. Knechel, Tuberculosis: pathophysiology, clinical features, and diagnosis, Crit. Care Nurse 29 (2009) 34–43, https://doi.org/10.4037/ccn2009968.

[5] S. Ahmad, Pathogenesis, immunology, and diagnosis of latent *Mycobacterium tuberculosis* infection, Clin. Dev. Immunol. 2011 (2011), https://doi.org/10.1155/2011/814943.

[6] T. Tsai, C. Huang, C. Chen, S. Shen, M. Wang, C. Cheng, C. Chen, Diagnosis of Tuberculosis Using Colorimetric Gold Nanoparticles on a Paper-Based Analytical Device, 2017, https://doi.org/10.1021/acssensors.7b00450.

[7] J. Frith, History of tuberculosis. Part 1 – phthisis, consumption and the white plague, J. Mil. Vet. Health 22 (2014) 29–35. http://www.atsjournals.org/doi/abs/10.1164/ajrccm/140.6.1788.

[8] H.Y. Highsmith, J.R. Starke, A.M. Mandalakas, Tuberculosis, Kendig's Disord. Respir. Tract Child (2018) 475–497.e5, https://doi.org/10.1016/B978-0-323-44887-1.00029-8.

[9] L. King, S. Ahuja, TB and HIV Coinfection: Current Trends, Diagnosis and Treatment Update 11, 2006, pp. 17–23.

[10] S. Singh, P. Sharma, V. Chaudhary, K. Chopra, B. Dey, K. Sachdeva, S. Kabra, V. Katoch, Challenges in tuberculosis diagnosis and management: recommendations of the expert panel, J. Lab. Phys. 7 (2015) 1, https://doi.org/10.4103/0974-2727.154778.

[11] B. Golichenari, R. Nosrati, A. Farokhi-fard, M.F. Maleki, S. Mohammad, G. Hayat, K. Ghazvini, F. Vaziri, Critical reviews in biotechnology electrochemical-based biosensors for detection of *Mycobacterium tuberculosis* and tuberculosis biomarkers tuberculosis and tuberculosis biomarkers, Crit. Rev. Biotechnol. 0 (2019) 1–22, https://doi.org/10.1080/07388551.2019.1668348.

[12] E.C. Pelaez, M.C. Estévez, A. Mongui, M. Menendez, C. Toro, O.L. Herrera-sandoval, J. Robledo, M.J. Garcia, P. Portillo, L.M. Lechuga, Detection and Quantification of HspX Antigen in Sputum Samples Using Plasmonic Biosensing: Toward a Real Point-of-Care (POC) for Tuberculosis Diagnosis, 2020, https://doi.org/10.1021/acsinfecdis.9b00502.

[13] N.D. Samsuri, W.M. Mukhtar, A. Rozana, A. Rashid, K.A. Dasuki, A. Rahman, H. Awangku, Synthesis methods of gold nanoparticles for localized surface Plasmon resonance (LSPR), Sens. Appl. 01002 (2017) 1–5, https://doi.org/10.1051/epjconf/201716201002.

[14] Z. Li, L. Leustean, F. Inci, M. Zheng, U. Demirci, S. Wang, Plasmonic-based platforms for diagnosis of infectious diseases at the point- of-care, Biotechnol. Adv. 37 (2019), 107440, https://doi.org/10.1016/j.biotechadv.2019.107440.

[15] J.L. Hammond, N. Bhalla, S.D. Rafiee, P. Estrela, Localized surface plasmon resonance as a biosensing platform for developing countries, Biosensors 4 (2014) 172–188, https://doi.org/10.3390/bios4020172.

[16] S.H. Baek, H.W. Song, S. Lee, J.E. Kim, Y.H. Kim, J.S. Wi, J.G. Ok, J.S. Park, S. Hong, M.K. Kwak, H.J. Lee, S.W. Nam, Gold nanoparticle-enhanced and roll-to-roll nanoimprinted LSPR platform for detecting Interleukin-10, Front. Chem. 8 (2020), https://doi.org/10.3389/fchem.2020.00285.

[17] F. Ruffino, M.G. Grimaldi, Morphological characteristics of au films deposited on Ti: a combined SEM-AFM study, Coatings 8 (2018), https://doi.org/10.3390/coatings8040121.

[18] S.L. Manoto, A. El-Hussein, R. Malabi, L. Thobakgale, S. Ombinda-Lemboumba, Y. A. Attia, M.A. Kasem, P. Mthunzi-Kufa, Exploring optical spectroscopic techniques and nanomaterials for virus detection, Saudi, J. Biol. Sci. 28 (2021) 78–89, https://doi.org/10.1016/j.sjbs.2020.08.034.

[19] P.S. Parsamehr, M. Zahed, M.A. Tofighy, T. Mohammadi, M. Rezakazemi, Preparation of novel cross-linked graphene oxide membrane for desalination applications using (EDC and NHS)-activated graphene oxide and PEI, Desalination 468 (2019), 114079, https://doi.org/10.1016/j.desal.2019.114079.

[20] X. Zhang, Plasmon extinguishment by bandedge shift identified as a second-order spectroscopic differentiation, Nanophotonics 10 (2021) 1329–1335, https://doi.org/10.1515/nanoph-2020-0603.

[21] S. Link, M.A. El-Sayed, Optical properties and ultrafast dynamics of metallic nanocrystals, Annu. Rev. Phys. Chem. 54 (2003) 331–366, https://doi.org/10.1146/annurev.physchem.54.011002.103759.

[22] A. Husen, M. Iqbal, Nanomaterials and Plant Potential, 2019, https://doi.org/10.1007/978-3-030-05569-1.

[23] S. Gurunathan, J.W. Han, J.H. Park, J.H. Kim, A green chemistry approach for synthesizing biocompatible gold nanoparticles, Nanoscale Res. Lett. 9 (2014) 1–11, https://doi.org/10.1186/1556-276X-9-248.

[24] M. Lee, H.S. Gwak, B.D. Park, S.T. Lee, Synthesis of mycolic acid biosurfactants and their physical and surface-active properties, JAOCS, J. Am. Oil Chem. Soc. 82 (2005) 181–188, https://doi.org/10.1007/s11746-005-5170-8.

[25] N. Hari, V.P. Nair, FTIR spectroscopic analysis of leaf extract in hexane in Jasminum azoricum L, Int. J. Sci. Res. Technol. 4 (2018) 170–172. www.ijsrst.com.

[26] Q. Yu, H. Huang, X. Peng, Z. Ye, Ultrathin free-standing close-packed gold nanoparticle films: conductivity and Raman scattering enhancement, Nanoscale. 3 (2011) 3868–3875, https://doi.org/10.1039/c1nr10578g.

[27] N.S. Mathebula, J. Pillay, G. Toschi, J.A. Verschoor, K.I. Ozoemena, Recognition of anti-mycolic acid antibody at self-assembled mycolic acid antigens on a gold electrode: a potential impedimetric immunosensing platform for active tuberculosis, Chem. Commun. (2009) 3345–3347, https://doi.org/10.1039/b905192a.

INDIAN JOURNAL OF TUBERCULOSIS 70 (2023) 468–474

Available online at www.sciencedirect.com

ScienceDirect

journal homepage: http://www.journals.elsevier.com/indian-journal-of-tuberculosis/

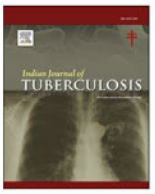

Review article

TB diagnostic insights, progress made on point of care diagnostics and bioinformatics as an additional tool for improvement

Mabotse A. Tjale [a,*], *Saturnin Ombinda-Lemboumba* [a], *Charles Maphanga* [a,b], *Patience Mthunzi-Kufa* [a,b]

[a] *Biophotonics, National Laser Centre, Council for Scientific and Industrial Research, P/O Box 395, Meiring Naudé Road Brummeria, Pretoria, South Africa*

[b] *College of Agriculture, Engineering and Science, School of Chemistry and Physics, University of KwaZulu-Natal, Pietermaritzburg Campus, King Edward Avenue, Pietermaritzburg, South Africa*

ARTICLE INFO

Article history:
Received 26 July 2022
Received in revised form
19 August 2022
Accepted 31 March 2023
Available online 5 April 2023

Keywords:
Tuberculosis (TB)
Mycobacterium tuberculosis
Point of care (POC)

ABSTRACT

Despite major efforts made to control tuberculosis disease (TB), this disease continues to present a major global health challenge and drug resistance is continuously growing. TB is caused by *Mycobacterium tuberculosis* and spreads exclusively via human-to-human contact transmission. Therefore, early detection and diagnosis for proper treatment with active TB have a great impact on public health. Regardless, most people in developing countries with TB or TB-associated symptoms do not have access to an adequate initial diagnosis. Available bacteriologic-based techniques are either inefficient or may require a longer turnaround time from the laboratory. Contemporarily, non-bacteriologic based methods have both questionable sensitivity and specificity and while others cannot distinguish between active and latent TB. Thus, additional efforts have been made to find accurate diagnostic tests for TB. Herein, we review the available methods used for TB diagnosis, and in addition, we explore point of care (POC) diagnostics as an alternative way to develop TB diagnostic tests and further evaluate whether bioinformatics can be used as an additional screening tool for identification of possible TB biomarkers for the development of POC TB diagnostics, which is part of our research focus.

© 2023 Tuberculosis Association of India. Published by Elsevier B.V. All rights reserved.

1. Introduction

Tuberculosis (TB) is a contagious, chronic infectious disease that is caused by a bacterium, *Mycobacterium tuberculosis*, and can infect a variety of organs including the lungs (pulmonary TB) or organs other than the lungs (extrapulmonary TB).[1] The Global Tuberculosis report of 2020 reported that almost 10.4 million people were infected with TB in 2019 and approximately 1.2 million TB-related deaths were reported in HIV-negative individuals, while an estimated 250 000 accounted for HIV-positive individuals. The majority of these cases were reported in the developing world including Asia (44%), Africa (25%), Western Pacific (18%), and Eastern Mediterranean

* *Corresponding author*. Council for Scientific and Industrial Research, Meiring Naudé Road Brummeria, Pretoria, South Africa.
E-mail address: mtjale@csir.co.za (M.A. Tjale).

https://doi.org/10.1016/j.ijtb.2023.03.023
0019-5707/© 2023 Tuberculosis Association of India. Published by Elsevier B.V. All rights reserved.

Downloaded for Anonymous User (n/a) at University of Pretoria from ClinicalKey.com by Elsevier on December 11, 2023. For personal use only. No other uses without permission. Copyright ©2023. Elsevier Inc. All rights reserved.

(8.2%), while the developed regions accounted for a minority of the cases, Americas (2.9%), and finally Europe (2.5%).[2]

TB is curable and preventable under the right conditions.[3,4] People who develop TB disease can be successfully treated with a 6-month antibiotic regimen. Although the cost of treatment is reasonably cheap and highly effective, this disease has remained the leading cause of illness and death for many years before the COVID-19 pandemic. TB is mostly associated with poverty, with the majority of cases (95%) and deaths (98%) reported in developing countries.[5] Moreover, the HIV/AIDS pandemic in the majority of these regions has been shown to increase the risk of infection proceeding to overt disease.[5]

TB is primarily spread through human-to-human transmission and thus the disease must be diagnosed early and followed by appropriate treatment in individuals with active TB.[6] Several issues have been associated with the elimination of TB globally. One of the major aspects of the hindrance is the availability of better diagnostic tools to enhance early detection.[7] Many developing countries still employ traditional methods such as Tuberculin skin testing (TST), sputum smear microscopy (SSM), and evaluation of clinical symptoms as a way of early detection.[8,9] The sensitivity and specificity of these tests have been questionable, particularly in patients with HIV and extrapulmonary infection.[10,11] Thus, there is a need to improve current diagnostics which will ultimately improve cure rates, and to achieve this relies primarily on the implementation of point of care (POC) diagnostics.[11]

Almost two-thirds of TB cases remain undiagnosed or reported to health authorities.[12] Thus, if the goal is to eliminate TB, several tools must be put in place. For example, new vaccines against TB, the development of new treatment regimens that can be administered for a shorter period, and lastly, new diagnostic tools that are easier to use and do not require specialized infrastructure.[12] Central to TB control and possibly elimination is the development of rapid diagnosis. Improved diagnosis does not rely entirely on sensitivity or specificity and drug resistance, but the test should be cost-effective, and user-friendly, i.e., useable in remote areas with no or lack of infrastructure development and can be used by health workers with minimal training.

Advancements in TB POC diagnostics have been made in recent years. For example, molecular tests such as the Xpert MTB, loop-mediated isothermal amplification (LAMP) assays, lipoarabinomannan (LAM) urine strip test, and molecular line-probe assay have been used and shown improvements in early TB diagnosis.[13] However, these are costly and there is still limited access to these diagnostic tools in most developing countries, thus a need for improvement and accessibility. This review aims to provide insights on POC diagnostics and highlight other technologies that can be used to further improve this diagnostic test for better use and improved sensitivity and specificity.

2. Current TB diagnostic methods

There are numerous methods used for screening and diagnosing TB. Diagnosis is primarily dependent on initial clinical assessment, chest radiography or chest x-ray (CXR), and subsequent laboratory confirmation by various bacteriologic studies. The most commonly used TB screening and diagnostic methods include purified protein derivative (PPD), TST or Mantoux test, SSM, TB culture, and various nucleic acid amplification tests (NAATs).[14,15]

2.1. *Rapid tests*

The TST is a subcutaneous delivery/injection of a purified protein derivative protein. This test has been successfully used for rapid TB screening, but it has since failed to discriminate between active and latent TB infection. Moreover, a high percentage of false positive results have been reported in individuals with preceding Bacillus Calmette–Guérin (BCG) vaccination.[14] It is used as a standard test to diagnose latent TB but has the potential for a high number of false positives. The high percentage of false positives cannot only be not limited to previous BCG vaccination but infection with non-tuberculosis mycobacteria and incorrect interpretation of the results[15,16]

2.2. *Microscopy*

The SSM is a simple test used to identify MTB acid-fast bacilli and remains the primary method for diagnosis of pulmonary TB in low- and middle-income countries with limited settings. It is affordable and can be performed in basic laboratories at primary healthcare clinics.[17] It has low sensitivity and requires a minimum of 5000 acid-fast bacilli per milliliter (AFB/ml) for detection which is a challenge to pulmonary TB diagnosis in children and immunocompromised individuals with HIV/AIDS comorbidities that have low bacilli count and those with extrapulmonary TB.[18] Furthermore, it cannot distinguish between dead or live bacilli. Since all mycobacteria are acid-fast, the SSM cannot distinguish between tuberculous and non-tuberculous mycobacteria, hence it cannot be used for species differentiation and drug sensitivity testing (DST).[19]

TB culture is the gold standard for diagnosing TB and has high sensitivity and specificity and can also be used for DST. MTB is a slow-growing and fastidious bacterium that requires specialized media and approximately 2–6 weeks to detect growth on culture media, and these cultures are kept for up to 12 weeks before they can be reported negative.[15] TB culture has its limitations, for instance, it requires specialized infrastructure such as Biosafety level 4 (BSL4) laboratories which may not be always available in resource-limited settings, poses a high risk to laboratory personnel, and therefore requires highly trained staff to perform tests, and the turn-around time for results is long.[20]

2.3. *Point of care diagnostics*

Recent innovations in POC diagnostic technologies for TB have resulted in early treatment initiation. For instance, the roll-out of GeneXpert MTB/RIF devices offers the potential for rapid and effective diagnosis of TB, especially in resource-limited countries with a high burden for TB/HIV co-infection.[21–23] Currently, Xpert MTB/RIF assay (Cepheid, Inc., Sunnyvale, CA, USA) is the recommended NAAT for rapid detection of TB and rifampicin resistance by WHO in people with suspected pulmonary TB[24–26] The NAAT can rapidly detect the genetic

Downloaded for Anonymous User (n/a) at University of Pretoria from ClinicalKey.com by Elsevier on December 11, 2023. For personal use only. No other uses without permission. Copyright ©2023. Elsevier Inc. All rights reserved.

material of MTB from the respiratory specimen; however, it cannot be used to monitor treatment response because it detects both viable and non-viable tuberculous mycobacteria.[15] The Xpert MTB/RIF also has limitations associated with it, for example, resistance to rifampicin (RIF) is used as a marker for multi-drug resistance TB (MDR-TB), however, other bacterial strains may exhibit only mono-resistance to RIF which may not necessitate full line MDR therapy, thus resulting in false positive RIF diagnosis. Other drawbacks include high costs for testing, appropriate infrastructure, and annual calibration of the instrument.[27] Ensuring an uninterrupted supply of cartridges remains a challenge as the global demand for Xpert cartridges increases.[24]

3. Bioinformatics

The introduction of high throughput sequencing technologies has allowed clinical laboratories to extract a large amount of data about the genome, transcriptome, metabolome, and phenome of various patients.[28] This information allows screening and early detection of diseases as well as therapeutic targets in drug discovery. Bioinformatics is a discipline in the field of biology that uses computational techniques for analysis and extracting information from biomolecules.[28] This review will be mainly focused on the role of transcriptomics in the identification of possible biomarkers for TB diagnosis.

3.1. *Transcriptomics*

In recent years transcriptomic analysis of human samples has provided insights into understanding genes that are expressed in different patient samples. Thus, comparisons of gene expression profiles from test samples (i.e. those with disease) to those without, have made it possible to identify genes that differ in their expression between groups, thus giving a disease signature. Identification of disease signatures is beneficial for diagnostic tool development and drug discovery, thus understanding pathways that are affected during the disease.[29] For example, de Araujo et al. (2019) showed differential expression of four major classes of small non-coding RNAs in peripheral blood from patients with different stages of TB infection. This study reported that in addition to microRNA (miRNAs), which are known to be highly regulated in blood cells of TB patients, there was a significant expression of PIWI-interacting RNA (piRNA) and small nucleolar RNA (snoRNA) in both latent and active TB, thus yielding promising biomarkers. While the functions of small nuclear RNA (sncRNA) have not been fully elucidated, their results strongly suggested that at least piRNA and snoRNA populations may represent potential biomarkers of TB diagnosis in the different stages of TB infection.[30] Currently, there is a plethora of data generated for biomarker development using microarray platforms. In another study, bioinformatic tools including gene ontology (GO) analysis, and KEGG pathway analysis for gene function, and enrichment was used to analyze differentially expressed genes from pulmonary TB from the Gene expression Omnibus (GEO) database. Overall, 7 genes namely C–C motif chemokine ligand 20 (*CCL20*), prostaglandin-endoperoxide synthase 2 (*PTGS2*), Intercellular adhesion molecule 1 (*ICAM1*), TIMP metallopeptidase inhibitor 1 (*TIMP1*), matrix metalloproteinase 9 (*MMP9*), C-X-C motif chemokine ligand 8 (*CXCL8*) and Interleukin-6 (*IL6*) were associated.[31] Using a similar approach, a transcriptional regulator factor 1 (IRF1) was up-regulated in TB-infected individuals when compared to healthy controls and thus making it a potential biomarker for TB.[32] Another study investigating host-blood derived biomarkers using blood-derived transcriptomes for the GEO database has revealed that Ubiquitin/ISG15-conjugating enzyme E2 L6 (UBE2L6), Basic leucine zipper transcriptional factor ATF-like (BATF2), Plasma protease C1 inhibitor (C1-IMH), and vesicle-associated membrane protein 5 (VAMP5) could potentially be used for diagnosis of active TB and possibly be used to differentiate active and latent TB.[33] Another study showed that a protein marker, C-X-C motif chemokine ligand 1 (CXCL1) was successfully used in discriminating between active pulmonary TB from non-pulmonary TB, latent TB, and healthy controls.[34] A recent study was conducted using whole-blood transcriptome data obtained from the GEO database. This data was collected from children with active and latent TB. The data revealed that genes associated with neutrophil activation and degranulation, neutrophil-mediated immunity, and defense response were significantly differentially expressed. Amongst the cohort was Toll-like receptor 2 (TLR2), Formyl peptide receptor 2 (FPR2), Matrix metallopeptidase 9 (MMP9), Myeloperoxidase (MPO), carcinoembryonic antigen-related cell adhesion molecule 8(CEACAM8), Elastase, neutrophil Expressed ELANE (Fc fragment of IgG receptor 1A), Fc fragment of IgG receptor 1A (FCGR1A), Selectin (SELP), Arginase 1 (ARG1), G protein subunit gamma 10 (GNG10), Haptoglobin (HP), Lipocalin 2 (LCN2), Lactotransferrin (LTF), Adenylate cyclase 3 (ADCY3) were able to differentiate between latent and active TB in children, thus, presenting potential gene markers for developing non-sputum diagnostic tools for childhood tuberculosis.[35] These are just a few examples of studies performed on host transcriptomics to search for potential biomarkers for the diagnosis of different stages of TB. Many studies available on biomarker development for diagnosis and treatment have mainly focused on the host transcriptome and little has been reported on the pathogen differential expression at different stages of the disease. Perhaps, future studies should also consider the differential expression of the TB pathogen in the host in conjugation with the host immune response to better understand the host-pathogen interaction. These findings may be useful in searching for additional biomarkers for TB diagnostics.

4. The application of photonics in TB diagnostic test development

Photonics-based diagnostic platforms have shown a great potential to be adapted for rapid and accurate diagnosis of TB, nonetheless, these have not been extensively explored and thus, have since emerged as a promising technology for diagnosis. For example, more advanced biophotonics-based methods such as Raman spectroscopy (RS), surface plasmon resonance (SPR), and biosensors-based approaches for TB diagnosis will be discussed in more detail in this review.

Downloaded for Anonymous User (n/a) at University of Pretoria from ClinicalKey.com by Elsevier on December 11, 2023. For personal use only. No other uses without permission. Copyright ©2023. Elsevier Inc. All rights reserved.

4.1. *Surface plasmon resonance*

Surface plasmon resonance (SPR) is defined as a label-free, high-throughput, optical test that can be used to analyze protein-protein interactions. It is highly sensitive and uses small numbers of samples for real-time measurement of biomolecular interactions. In addition to studying the thermodynamics of biomolecular interactions, it can also be used to determine study binding kinetics, specificity, and affinity. The phenomenon of SPR occurs when photons of an incident light source hit a thin metal surface (for example, gold, and silver) at a specific angle, these metal surface electrons get excited and start resonating. These resonating electrons generated at the boundary of the metal surface are referred to as surface plasmons.[36] A study by Malabi et al. (2019) showed that SPR can be used to detect biological analyte.[37] Other studies showed that SPR was able to detect TB-specific antigens or antibodies. For example, Hong et al. (2010) showed that a tissue-specific antigen found in most TB patients, CF10 could be detected using SPR. In this study monoclonal antibodies (anti-CF10) were immobilized on a gold surface to specifically bind to CF10 antigen. This assay was able to detect up to 100 ng/μl of TB antigen (CFP-10 antigen) in tissue fluid.[38] The sensitivity of the SPR system was further enhanced by using TB antigen CFP-10 in sandwich assay and coupling the secondary sandwich antibodies with nanoparticles ([39]). Another study by Sun et al. (2017) showed that a localized SPR was able to detect TB- specific antibodies. In this study, a fusion protein CFP10-ESAT6 antigen was immobilized to gold nano-rods by using chemical modification. The functionalized gold nanorods-antigen complex was incubated with serum collected from patients with active TB, non-tuberculous pulmonary disease, and their healthy controls. The test successfully detected TB CFP10-ESAT6 with a specificity and sensitivity of 79% and 92%, respectively.[40] Kimuda et al. (2018) showed that SPR can also be used to characterize antibody avidity in patients with active pulmonary TB, and latent TB when compared to the healthy controls.[41] SPR has also been used to detect TB-specific sequences, for example, Duman et al. (2010) showed that the *M. tuberculosis* complex (MTBC) was successfully detected using SPR based multichannel system. Herein the probe was designed to have a spacer that would bind directly to the target sequence. The sensor was prepared by direct coupling of the thiolated probe with a gold surface and blocked with mercapto-1-hexanol to prevent non-specific binding. This assay was able to detect up to 30 ng/μl of the target.

4.2. *Raman Spectroscopy*

Raman Spectroscopy has been used as a preferred method for qualitative analysis and it is often used for the characterization of biological samples owing to its high specificity in determining and differentiating chemical bonds in molecules.[42] It has become a powerful non-invasive and non-destructive molecular identification tool.[42] RS has been used for TB detection using sputum sample.[43] The analysis done on Raman spectra showed the presence of a TB biomarker compound in the sputum sample and this biomarker created variations of Raman peaks. These variations included intensity fluctuation and wavenumber shift of coinciding peaks, furthermore, the signal detected was weak. As a result, RS was coupled to a machine learning algorithm, Principal component analysis (PCA) to accurately differentiate TB-negative and TB-positive specimens using cell-free supernatant of sputum samples. Thus, the inclusion of PCA on the acquired Raman data resulted in a more rapid and accurate detection system for TB.

5. Biomarkers and biosensors

Studies on the identification of TB biomarkers for the development of biosensors that can be used for effective TB diagnosis have been described. For example, Liu et al. (2018) developed a multiplex TB biomarkers detector coupled with an optical sensor. This optical diagnostic platform was based on silicon photonic microring sensors and asymmetric isothermal amplification technique (SPMS-AIA). These biphotonic sensors did not require labeling and were successfully used for the detection of a single MTBC biomarker (IS6110) and as a multiplex for the detection of two biomarkers (IS6110 and IS1081) in clinical sputum specimens. The assay was rapid and label-free, and results were obtained in real-time.[44] In another study, Crawford et al. (2017) used a Surface-enhanced Raman scattering (SERS)-based immunoassay approach for the detection of mannose-capped Lipoarabinomannan (ManLAM), an antigenic marker for active tuberculosis infection in human serum. The platform used a combination of gold nanoparticle (AuNP) labels, ManLAM monoclonal antibodies (mAbs), and surface-enhanced Raman scattering (SERS) detection. The limit of detection was also evaluated in human serum samples that were spiked with ManLAM antigen. Furthermore, the sensitivity was further enhanced by adding a layer of Cyanine 5 to a layer of gold capture surface, thus this complex chemically interacts with the substrate to form the Surface-enhanced Resonance Raman Scattering (SERRS).[45] Other studies showed that the fabrication of biosensors has improved with the coupling of photonic sensor chips into polymer microfluidic cartridges. For instance, Gonzalez-Guerrero et al. (2016) developed a novel photonics-based platform for the detection of TB in human urine samples.[46] This platform consists of the label-free detection of Lipoarabinomannan (LAM) in unprocessed urine. The photonic sensor chip is based on a Mach–Zehnder Interferometer (MZI) transducer which was combined with an on-chip spectral filter.[46,47] A broadband light source was used as a light source whereas a complementary metal oxide semiconductor (CMOS) sensor was employed as a signal detector. The sensor chip surface was functionalized with specific monoclonal antibodies against LAM. The shift in the wavelength induced by the refractive index changes on the surface of the sensor was used to evaluate the sample diagnosis in real-time. TB has detected in human urine samples in less than 15 min and the limit of detection was as low as 475 pg/mL for the direct detection in spiked urine samples. The results obtained using the Mach-Zehnder interferometer biosensor correlated to those obtained with GeneXpert. The platform showed up to 100% sensitivity and specificity when compared to rapid tests commercially available for TB detection.[47]

Downloaded for Anonymous User (n/a) at University of Pretoria from ClinicalKey.com by Elsevier on December 11, 2023. For personal use only. No other uses without permission. Copyright ©2023. Elsevier Inc. All rights reserved.

Novel devices that utilize immunosensor and bio-opticals have been developed to diagnose pulmonary Tuberculosis (TB) in patients.[39,48] These devices use prisms whereby the surfaces are coated with *Mycobacterium* tuberculosis-specific antibody and fluorescent peptide determinants.[48] In the presence of TB bacterium, the fluorescent-coated determinants are displaced by TB bacterium and the diode laser of the measuring device interrogates this biochemical process. The amount of the antigen present on the surface of the prism is determined by evanescent wave fluorimetry on the device.[39,48] Results are obtained within a few minutes and the assay was able to detect up to 50–75 CFU/mL of Mycobacterium tuberculosis cells[48]

All these studies show that POC diagnostics offers more advantage in TB diagnosis as they are rapid, easy to handle, and operate. In particular, biosensors are portable, rapid, and sensitive and they can be used even in clinical settings outside the laboratory which is advantageous, especially in the developing world where there is limited access to specialized laboratories.[39]

6. Conclusions

TB disease still affects millions of people globally and achieving complete eradication will depend primarily on the availability of proper diagnostic tools for early detection. Herein, we reviewed POC diagnostic tools that are reliable, robust, and easily accessible even in the most decentralized areas that offer a better alternative. Most of these tests are performed on samples that are easily accessible and results are usually obtained in real-time. Thus, the availability of these tests will increase treatment turnaround time and consequently reduce the risk of patient loss-to-follow-up. Although many of these tests including the Xpert MTB/RIF, LAM, and NAAT have been proven effective in recent years, there is also a major drawback associated with them, thus a need for improvement. Biophotonics-based techniques have somewhat shown increased sensitivity and specificity in TB diagnostics and thus can ultimately be used to complement available diagnostic tools. Regardless, there is still limited data available on the biomarkers that can be effectively used for the definitive diagnosis of TB in different stages of infection (active vs latent), different patient samples (healthy vs immunocompromised), and in adults vs children. The advancement of next-generation sequencing technology or bioinformatic tools has enabled the identification of possible TB biomarkers in the host. Similarly, these technologies can also be used for searching for additional biomarkers of TB *ex vivo* in different stages of TB infection, which is our research focus. These biomarkers can be effectively used for the development of biphotonic-based POC diagnostics tools.

Author's contribution

Dr. Mabotse A Tjale: Concept of the paper, literature search, acquisition of the information, and drafting of the article.

Dr. Saturnin Ombinda-Lemboumba: Literature search, acquisition of the information, and editing of the article.

Mr. Charles Maphanga: Literature search, acquisition of the information, and editing of the article.

Dr. Patience Mthunzi-Kufa: Revision of article for intellectual content, editing of the article.

Conflicts of interest

The authors have none to declare.

Acknowledgments

We would like to thank the Council for Scientific and Industrial Research (CSIR) and the Department of Science and Innovation (DSI) for providing funding.

REFERENCES

1. Yu G, Shen Y, Ye B, Shi Y. Diagnostic accuracy of Mycobacterium tuberculosis cell-free DNA for tuberculosis: a systematic review and meta-analysis. *PLoS One*. 2021;16(6 June):1–16. https://doi.org/10.1371/journal.pone.0253658.
2. Chakaya J, Khan M, Ntoumi F, et al. Global tuberculosis report 2020 – reflections on the global TB burden, treatment and prevention efforts. *Int J Infect Dis*. 2021;113:S7–S12. https://doi.org/10.1016/j.ijid.2021.02.107.
3. Bhargava A, Bhargava M. Tuberculosis deaths are predictable and preventable: comprehensive assessment and clinical care is the key. *J Clin Tuberc Other Mycobact Dis*. 2020;19, 100155. https://doi.org/10.1016/j.jctube.2020.100155.
4. Wu Y, Huang M, Wang X, Li Y, Jiang L, Yuan Y. The prevention and control of tuberculosis: an analysis based on a tuberculosis dynamic model derived from the cases of Americans. *BMC Publ Health*. 2020;20(1):1–16. https://doi.org/10.1186/s12889-020-09260-w.
5. Grange JM, Zumla A. The global emergency of tuberculosis: what is the cause? *J R Soc Promot Health*. 2002;122(2):78–81. https://doi.org/10.1177/146642400212200206.
6. Chan ED, Heifets L, Iseman MD. Immunologic diagnosis of tuberculosis: a review. *Tuber Lung Dis*. 2000;80(3):131–140. https://doi.org/10.1054/tuld.2000.0243.
7. Jassal MS, Bishai WR. Epidemiology and challenges to the elimination of global tuberculosis. *Clin Infect Dis*. 2010;50(SUPPL. 3):0–8. https://doi.org/10.1086/651486.
8. Pai M, Nicol MP, Boehme CC. *Tuberculosis Diagnostics: State of the Art and Future Directions*. second ed. Tuberc Tuber Bacillus; 2017:363–378. https://doi.org/10.1128/9781555819569.ch16. Published online.
9. Siddiqi K, Lambert ML, Walley J. Clinical diagnosis of smear-negative pulmonary tuberculosis in low-income countries: the current evidence. *Lancet Infect Dis*. 2003;3(5):288–296. https://doi.org/10.1016/S1473-3099(03)00609-1.
10. Millen SJ, Uys PW, Hargrove J, van Helden PD, Williams BG. The effect of diagnostic delays on the drop-out rate and the total delay to diagnosis of tuberculosis. *PLoS One*. 2008;3(4). https://doi.org/10.1371/journal.pone.0001933.
11. Getahun H, Harrington M, O'Brien R, Nunn P. Diagnosis of smear-negative pulmonary tuberculosis in people with HIV infection or AIDS in resource-constrained settings: informing urgent policy changes. *Lancet*. 2007;369(9578):2042–2049. https://doi.org/10.1016/S0140-6736(07)60284-0.

Downloaded for Anonymous User (n/a) at University of Pretoria from ClinicalKey.com by Elsevier on December 11, 2023. For personal use only. No other uses without permission. Copyright ©2023. Elsevier Inc. All rights reserved.

12. García-Basteiro AL, DiNardo A, Saavedra B, et al. Point of care diagnostics for tuberculosis. *Rev Port Pneumol (English Ed.* 2018;24(2):73–85. https://doi.org/10.1016/j.rppnen.2017.12.002.
13. Masawa N, Bani F, Ndege R. Tuberculosis: diagnostic challenges in rural Africa. *Praxis*. 2019;108(15):991–996. https://doi.org/10.1024/1661-8157/a003355.
14. Huddart S, Nash M, Pai M. Tuberculosis diagnosis: challenges and solutions. *J Heal Spec*. 2017;4(4):230. https://doi.org/10.4103/2468-6360.191903.
15. Nachiappan AC, Rahbar K, Shi X, et al. Pulmonary tuberculosis: role of radiology in diagnosis and management. *Radiographics*. 2017;37(1):52–72. https://doi.org/10.1148/rg.2017160032.
16. Nayak S, Acharjya B. Mantoux test and its interpretation. *Indian J Dermatol*. 2012;57(1):3–8. https://doi.org/10.4103/0019-5154.92666.
17. Walzl G, McNerney R, du Plessis N, et al. Tuberculosis: advances and challenges in the development of new diagnostics and biomarkers. *Lancet Infect Dis*. 2018;18(7):e199–e210. https://doi.org/10.1016/S1473-3099(18)30111-7.
18. *Department of Heath Republic of South Africa. South Africa TB Guidelines*. 2014.
19. Suleiman Khairunisa, Lessem Erica, Bryn Gay DW van G. *An Activist's Guide to Tuberculosis Diagnostic Tools*. Treat Action Gr.; 2017:978 (February 2017).
20. Singh S, Sharma P, Chaudhary V, et al. Challenges in tuberculosis diagnosis and management: recommendations of the expert panel. *J Lab Physicians*. 2015;7(1):1. https://doi.org/10.4103/0974-2727.154778.
21. S K, M-R G, L L, S WS, S I, R S. Diagnosing Xpert MTB/RIF-negative TB: impact and cost of alternative algorithms for South Africa. *SAMJ (S Afr Med J)*. 2013;103(2):101–106. https://doi.org/10.7196/SAMJ.6182.
22. Schnippel K, Meyer-Rath G, Long L, Stevens WS, Sanne I, Rosen S. Diagnosing Xpert MTB/RIF-negative TB: impact and cost of alternative algorithms for South Africa. *SAMJ (S Afr Med J)*. 2013;103(2):101–106. https://doi.org/10.7196/SAMJ.6182.
23. Schnippel K, Long L, Stevens WS, Sanne I. Diagnosing Xpert MTB/RIF-negative TB. *Impact and cost of alternative algorithms for South Africa*. 2019;103(2):1–14. https://doi.org/10.7196/SAMJ.61823.
24. Churchyard GJ, Mametja LD, Mvusi L, et al. Tuberculosis control in South Africa: successes, challenges, and recommendations. *SAMJ (S Afr Med J)*. 2014;104(3):244–248. https://doi.org/10.7196/SAMJ.7689.
25. Vassall A, Siapka M, Foster N, et al. Cost-effectiveness of Xpert MTB/RIF for tuberculosis diagnosis in South Africa: a real-world cost analysis and economic evaluation. *Lancet Global Health*. 2017;5(7):e710–e719. https://doi.org/10.1016/S2214-109X(17)30205-X.
26. Phillips JA. *Global Tuberculosis*. 2015;63. https://doi.org/10.1177/2165079915607875.
27. Theron G, Peter J, Van Zyl-Smit R, et al. Evaluation of the Xpert MTB/RIF assay for the diagnosis of pulmonary tuberculosis in a high HIV prevalence setting. *Am J Respir Crit Care Med*. 2011;184(1):132–140. https://doi.org/10.1164/rccm.201101-0056OC.
28. Xia X. Bioinformatics and drug discovery. *Curr Top Med Chem*. 2017;17(15):1709–1726. https://doi.org/10.2174/1568026617666161116143440.
29. Burel JG, Babor M, Pomaznoy M, et al. Host transcriptomics as a tool to identify diagnostic and mechanistic immune signatures of tuberculosis. *Front Immunol*. 2019;10(FEB):1–12. https://doi.org/10.3389/fimmu.2019.00221.
30. de Araujo LS, Ribeiro-Alves M, Leal-Calvo T, et al. Reprogramming of small noncoding RNA populations in peripheral blood reveals host biomarkers for latent and active mycobacterium tuberculosis infection. *mBio*. 2019;10(6). https://doi.org/10.1128/mBio.01037-19.
31. Sun Y, Chen G, Liu Z, Yu L, Shang Y. A bioinformatics analysis to identify novel biomarkers for prognosis of pulmonary tuberculosis. *BMC Pulm Med*. 2020;20(1):1–7. https://doi.org/10.1186/s12890-020-01316-2.
32. Xie C, Mao X, Huang J, et al. Kobas 2.0: a web server for annotation and identification of enriched pathways and diseases. *Nucleic Acids Res*. 2011;39(SUPPL. 2):316–322. https://doi.org/10.1093/nar/gkr483.
33. Gong Z, Gu Y, Xiong K, et al. The evaluation and validation of blood-derived novel biomarkers for precise and rapid diagnosis of tuberculosis in areas with high-TB burden. *Front Microbiol*. 2021;12 June:1–11. https://doi.org/10.3389/fmicb.2021.650567.
34. Koyuncu D, Niazi MKK, Tavolara T, et al. CXCL1: a new diagnostic biomarker for human tuberculosis discovered using Diversity Outbred mice. *PLoS Pathog*. 2021;17(8):1–22. https://doi.org/10.1371/journal.ppat.1009773.
35. Shao M, Wu F, Zhang J, et al. Screening of potential biomarkers for distinguishing between latent and active tuberculosis in children using bioinformatics analysis. *Medicine (Baltim)*. 2021;100(5), e23207. https://doi.org/10.1097/MD.0000000000023207.
36. Englebienne P, Van Hoonacker A, Verhas M. Surface plasmon resonance: principles, methods, and applications in biomedical sciences. *Spectroscopy*. 2003;17(2-3):255–273. https://doi.org/10.1155/2003/372913.
37. Malabi R, Manoto SL, Ombinda-Lemboumba S, Maaza M, Mthunzi-Kufa P. *Detection of Biological Analytes Using Surface Plasmon Resonance as a Biosensing Technique for Possible Development of a Point of Care Diagnostic Tool*. 2019:24. https://doi.org/10.1117/12.2509850. March 2019.
38. Hong SC, Chen H, Lee J, et al. Ultrasensitive immunosensing of tuberculosis CFP-10 based on SPR spectroscopy. *Sensor Actuator B Chem*. 2011;156(1):271–275. https://doi.org/10.1016/j.snb.2011.04.032.
39. Srivastava SK, Van Rijn CJM, Jongsma MA. Biosensor-based detection of tuberculosis. *RSC Adv*. 2016;6(22):17759–17771. https://doi.org/10.1039/c5ra15269k.
40. Sun W, Yuan S, Huang H, Liu N, Tan Y. A label-free biosensor based on localized surface plasmon resonance for diagnosis of tuberculosis. *J Microbiol Methods*. 2017;142:41–45. https://doi.org/10.1016/j.mimet.2017.09.007. September.
41. Cose S, Kimuda SG, Biraro IA, Bagaya BS, Raynes JG. Characterizing antibody avidity in individuals of varied Mycobacterium tuberculosis infection status using surface plasmon resonance. *PLoS One*. 2018;13(10):1–18. https://doi.org/10.1371/journal.pone.0205102.
42. Ichimura T, Chiu L Da, Fujita K, et al. Visualizing cell state transition using Raman spectroscopy. *PLoS One*. 2014;9(1). https://doi.org/10.1371/journal.pone.0084478.
43. Ullah U, Tahir Z, Qazi O, Mirza S, Cheema MI. *Raman Spectroscopy and Machine Learning-Based Optical Sensor for Rapid Tuberculosis Diagnosis via Sputum*; 2022. Published online https://arxiv.org/abs/2204.12157v1.
44. Liu Q, Lim BKL, Lim SY, et al. Label-free, real-time and multiplex detection of Mycobacterium tuberculosis based on silicon photonic microring sensors and asymmetric isothermal amplification technique (SPMS-AIA). *Sensor Actuator B Chem*. 2018;255:1595–1603. https://doi.org/10.1016/j.snb.2017.08.181.
45. Owens NA, Pinter A, Porter MD. Surface-enhanced resonance Raman scattering for the sensitive detection of a tuberculosis biomarker in human serum. *J Raman Spectrosc*. 2019;50(1):15–25. https://doi.org/10.1002/jrs.5500.
46. González-Guerrero AB, Maldonado J, Herranz S, Lechuga LM. Trends in photonic lab-on-chip interferometric biosensors for point-of-care diagnostics. *Anal Methods*. 2016;8(48):8380–8394. https://doi.org/10.1039/c6ay02972h.

Downloaded for Anonymous User (n/a) at University of Pretoria from ClinicalKey.com by Elsevier on December 11, 2023. For personal use only. No other uses without permission. Copyright ©2023. Elsevier Inc. All rights reserved.

47. Ramirez-Priego P, Martens D, Elamin AA, et al. Label-free and real-time detection of tuberculosis in human urine samples using a nanophotonic point-of-care platform. *ACS Sens*. 2018;3(10):2079–2086. https://doi.org/10.1021/acssensors.8b00393.

48. McNerney R, Wondafrash BA, Amena K, Tesfaye A, McCash EM, Murray NJ. Field test of a novel detection device for Mycobacterium tuberculosis antigen in cough. *BMC Infect Dis*. 2010;10. https://doi.org/10.1186/1471-2334-10-161.

Downloaded for Anonymous User (n/a) at University of Pretoria from ClinicalKey.com by Elsevier on December 11, 2023. For personal use only. No other uses without permission. Copyright ©2023. Elsevier Inc. All rights reserved.

6.2. Appendix B: Published peer-reviewed conference proceedings

Optical biosensing of mycolic acid biomarker for TB diagnosis

Charles Maphanga, Sello Manoto, Saturnin Ombinda-Lemboumba, Yaseera Ismail, Patience Mthunzi-Kufa

Charles Maphanga, Sello Manoto, Saturnin Ombinda-Lemboumba, Yaseera Ismail, Patience Mthunzi-Kufa, "Optical biosensing of mycolic acid biomarker for TB diagnosis," Proc. SPIE 12387, Optical Diagnostics and Sensing XXIII: Toward Point-of-Care Diagnostics, 123870E (16 March 2023); doi: 10.1117/12.2650013

SPIE.

Event: SPIE BiOS, 2023, San Francisco, California, United States

Downloaded From: https://www.spiedigitallibrary.org/conference-proceedings-of-spie on 22 Mar 2023 Terms of Use: https://www.spiedigitallibrary.org/terms-of-use

Optical biosensing of mycolic acid biomarker for TB diagnosis

Charles Maphanga [1, 2*], Sello Manoto [3], Saturnin Ombinda-Lemboumba [1], Yaseera Ismail [2], Patience Mthunzi-Kufa [1, 2]

[1]Council for Scientific and Industrial Research, National Laser Centre, P O BOX 395, Pretoria, 0001, South Africa

[2]School of Chemistry and Physics, University of KwaZulu-Natal, Westville Campus, University Road, Durban, South Africa

[3]National Research Foundation, CSIR Complex, Meiring Naude Road, Brummeria, Pretoria, Gauteng, 0184, South Africa

ABSTRACT

When it comes to diagnostics for various microorganisms, biosensors offer great advantages over conventional analytical techniques. Specifically, they can provide multiple capabilities such as user-friendly operation, real-time analysis, rapid response, high sensitivity and specificity, portability, label-free detection, and cost-effectiveness. As a result, this diagnostic approach possesses suitable features to develop point-of-care (POC) diagnostics and monitoring technologies. In this study, for the first time, an optical biosensor chip was developed and analysed using a localised surface plasmon resonance (LSPR) optical biosensing technique to monitor biomolecular interactions between mycolic acid TB antigen and anti-mycobacterium tuberculosis antibody. Mycolic acid was successfully immobilised on a gold-coated biosensor chip and allowed to react with an anti-mycobacterium tuberculosis antibody. To enhance the detection signal from biomolecular binding events, AuNPs were used and successfully bioconjugated with goat anti-rabbit IgG H&L secondary antibody and characterised using ultraviolet-visible (UV-vis) spectroscopy and subsequently introduced on the biosensing layer. Scanning electron microscopy (SEM) and energy-dispersive X-ray (EDX) spectroscopy were used to characterise the biosensing surface. The optimised biosensor chip was analysed using a custom-built biosensing transmission spectroscopy setup to perform LSPR biosensing. From our findings, it was realised that mycolic acid was successfully immobilised on the biosensing surface and made it possible to capture anti-mycobacterium tuberculosis antibodies. The LSPR optical biosensing technique was indeed successful in the detection of anti-mycobacterium tuberculosis antibodies.

Keywords: Localised surface plasmon resonance, optical biosensing, transmission spectroscopy, scanning electron microscopy, energy dispersive X-ray, atomic force microscopy, mycolic acid, *mycobacterium tuberculosis*

*Corresponding author: CMaphanga@csir.co.za

Optical Diagnostics and Sensing XXIII: Toward Point-of-Care Diagnostics,
edited by Gerard L. Coté, Proc. of SPIE Vol. 12387, 123870E
© 2023 SPIE · 1605-7422 · doi: 10.1117/12.2650013

Downloaded From: https://www.spiedigitallibrary.org/conference-proceedings-of-spie on 22 Mar 2023
Terms of Use: https://www.spiedigitallibrary.org/terms-of-use

1. INTRODUCTION

Tuberculosis (TB) is an airborne infection caused by *mycobacterium tuberculosis* (MTB). Until the coronavirus (COVID-19) pandemic, TB was the leading cause of death from a single infectious agent, ranking above human immunodeficiency virus, an acquired immunodeficiency syndrome (HIV/AIDS) [1]. TB primarily affects the lungs as Pulmonary tuberculosis (PTB) and constitutes about 80% of total TB cases [2,3]. Pulmonary TB should be suspected when patients present with a persistent cough, haemoptysis, night sweat, weight loss, and fever [4]. TB can affect other sites of the body and is referred to as extra-pulmonary tuberculosis (EPTB). It can affect the bones, joints, meninges, lymph nodes, kidneys, intestines, and skin [3]. Transmission of MTB occurs after inhalation of aerosol droplets containing live bacteria expelled by patients with pulmonary TB and inhaled by exposed individuals. The size of infectious aerosol droplets ranges from as little as 0.65 to 7µm [5]. After inhalation, the small droplets may transit the nasopharyngeal or tracheobronchial region to be deposited into the lungs. The larger particles can be trapped in the upper airway or oropharynx, where they can potentially cause TB of the oropharynx or cervical lymph nodes [5]. Approximately one in four people worldwide demonstrate an immunological response to MTB infection, which can remain dormant (TB infection) or later progress into active TB disease. Patients with TB infection may present with no signs or symptoms of TB disease and have a 5-10% lifetime risk of developing TB disease, which increases in varying states of immunodeficiency up to 16% annual risk in HIV patients [4]. According to the global report released by the World Health Organization (WHO) (2022), there were an estimated 1.4 million deaths among HIV-negative people and 187 000 deaths among HIV-positive people in 2021, for a combined total of 1.6 million. This represents an increase from 1.5 million in 2020 and 1.4 million in 2019. This reported increase in TB mortality has been severely impacted by the COVID-19 pandemic [1].

The main health care intervention available to reduce the risk of TB infection progressing to active TB disease is TB preventive treatment. The *Mycobacterium bovis* bacillus Calmette-Guerin (BCG), an attenuated strain of *M. bovis* remains the only licensed vaccine against TB. Vaccination with BCG can provide protection, especially from severe forms of TB in children, but has variable efficiency in preventing pulmonary disease in children and adults [1,2]. Individuals who develop active pulmonary TB disease can be treated; however, rapid diagnosis, especially at the point-of-care (POC) setting, is required for early treatment initiation. Difficulty in TB diagnosis is one of the main contributing factors in the struggle to control TB [6]. Therefore, TB diagnostics need to provide timely, accurate, cost-effective results in settings where access to electricity, equipment, and technical expertise remains a challenge. Currently, there are numerous methods used for screening and diagnosing TB. The WHO recommends eight diagnostic tools, which include light emitting diode microscopy, commercial liquid culture and drug susceptibility testing, rapid speciation strip technology for identification of MTB, Xpert MTB/RIF, lateral flow urine lipoarabinomannan assay to detect TB in severely ill HIV patients or those with CD4 count $\leq$ 100 cells/µL, loop-mediated isothermal amplification (LAMP), line probe assay to detect resistance to isoniazid (INH) and rifampicin (RIF) in the smear-positive specimen or cultured colonies, and second-line line probe assays (SL-LPA) to detect fluoroquinolone and second-line injectable drug (SLID) resistance [3]. The availability of these advanced tools comes with limitations, especially where the TB burden is high, and most of them require specialised infrastructure, power, and trained personnel, are costly, and cannot be performed in a POC setting [3,4,7,8]. Hence this study focuses on the application of the plasmonic optical biosensing technique for the detection of anti-mycobacterium tuberculosis antibodies.

A biosensor is an analytical device incorporating a biorecognition element (receptor), an optical transducer system, and a signal output detector [9–11]. Biosensors are used as tools for detecting and measuring analytes of interest. The biorecognition element may be a biological material such as antibodies, nucleic acids, cell receptors, microorganisms, and enzymes; or a biologically derived material such as engineered proteins, functional nucleic acids, and functional nucleic acids [10,11]. These materials are immobilised on the biosensor surface to recognise and capture the analyte (target molecule), thus providing biochemical specificity and sensitivity to the biosensor [12]. The immobilisation of biorecognition elements on the biosensing surface is a very crucial step in the design and development of biosensors. The applied surface chemistry used to functionalise the biosensor chip is critical in obtaining sensitive detection signals. To date, there are different and well-described techniques used for surface functionalisation, such as covalent binding, non-covalent binding, and physical adsorption [11]. Besides receptor-analyte biorecognition and binding, a fundamental part of biosensing is the signal transduction mechanism, through which binding events are converted into a detectable output signal. This requires a transducer system which may be optical, electrochemical, magnetic, thermometric, or micromechanical [10]. Among the various transduction approaches, optical biosensors have attained great attention in the past decades as powerful analysis and detection tools with vast applications in healthcare (e.g. diagnosis and monitoring of diseases and drug discovery), environmental applications (e.g. environmental detection of pollutants and/or biological agents), and in biotechnology

Downloaded From: https://www.spiedigitallibrary.org/conference-proceedings-of-spie on 22 Mar 2023
Terms of Use: https://www.spiedigitallibrary.org/terms-of-use

[11,13,14]. Optical biosensors offer significant advantages over conventional analytical techniques because they enable direct, real-time, label-free detection, and multiplexing capabilities. They also have the potential for miniaturisation into portable, robust, user-friendly, and cost-effective point-of-care devices [10,11,13,15]. In this study, a biosensor chip was developed and analysed using a custom-built optical biosensing setup, by measuring transmitted intensity. To functionalise the biosensor chip, mycolic acid TB antigen was immobilised on the biosensing surface as the biorecognition element to specifically capture the anti-mycobacterium tuberculosis antibody. For signal enhancement, gold nanoparticles (AuNPs) were covalently conjugated with a secondary antibody, characterised before and after bioconjugation, and subsequently introduced on the biosensing surface. Furthermore, the biosensing surface was characterised using scanning electron microscopy (SEM) and energy-dispersive X-ray (EDX) spectroscopy. The acquired transmission spectroscopy optical biosensing data was analysed using OriginPro software.

2. MATERIALS AND METHODS

2.1 Characterisation of AuNPs

2.1.1. UV-vis absorption spectroscopy

UV-vis absorption spectroscopy was used in this study to characterise the gold nanoparticles (AuNPs) before and after covalent bioconjugation with secondary goat anti-rabbit IgG H&L antibody (Abcam, ab6702). To perform bioconjugation of AuNPs, 60nm gold NanoUrchins (Cytodiagnostics, 2459298_60U), N-hydroxysuccinimide (NHS) (Sigma-Aldrich, 56480), and 1-Ethyl-3-(3-dimethylaminopropyl)-carbodiimide) (EDC) (Sigma-Aldrich, E7750) with similar molar ratio were added to heterobifunctional polyethylene glycol (SH-PEG-COOH) (Sigma-Aldrich, 757845) in ultrapure water and shaken for an hour. The pH of this reaction mixture was adjusted to 7.4 using 10x PBS, and the antibody was added to the solution. The reaction mixture was incubated for 2 hours before filtering with a 50kDA filter to remove impurities. The final SH-PEG-IgG solution was obtained after washing twice with 1x PBS. The SH-PEG-IgG conjugate was added to AuNPs and incubated for an hour to form the TB-bioconjugate (AuNPs-IgG). A NanoDrop 8000 spectrophotometer (Thermo Fisher Scientific, United States) was used to measure wavelength shift before and after bioconjugation. The bioconjugated AuNPs were subsequently introduced to the biosensing surface containing immobilised anti-mycobacterium tuberculosis antibody (Abcam, ab905).

2.2 Characterisation of the biosensing surface

2.2.1. Scanning Electron Microscopy (SEM)

SEM end-point analysis was performed to study the biosensing surface morphology. A gold-coated biosensor chip was developed using the HEX benchtop thin film deposition system (Korvus Technology Ltd, United Kingdom). A gold evaporation slug (Merck Millipore, 373168-6.4G) was used to form the gold thin film on a glass substrate. A 5 nm layer of titanium was sputtered on the SiO_2 substrate before Au deposition (~40nm) using e-beam evaporation. To functionalise the biosensing surface as illustrated in Scheme 1, the gold thin film layer was first washed with absolute ethanol and blow-dried with N_2 gas. Cysteamine (Cys) (10mM) (Sigma-Aldrich, M9768) dissolved in absolute ethanol was introduced on the Au surface and incubated for 18 hours at room temperature to form an Au-Cys monolayer. NHS and EDC with similar molar ratios were used for covalent attachment of stearic acid (STA) (Sigma-Aldrich, S4751) to Cys using carbodiimide coupling chemistry, forming an amide bond. After the formation of the Cys-STA monolayer, the surface was washed thoroughly with ethanol and water to remove physically adsorbed stearic acid species. Mycolic acid (MA) from mycobacterium tuberculosis (bovine strain) (0.5 mg/ml) (Sigma-Aldrich, M4537) TB antigen dissolved in hexane was immobilised on STA monolayer through Van der Waals intermolecular by immersion the biosensor chip in MA overnight at room temperature. After incubation, the biosensor chip was rinsed thoroughly with 1x PBS (Sigma-Aldrich, D1283) to remove physically adsorbed MA, and subsequently incubated in a solution of 1% bovine serum albumin (BSA) (Roche Diagnostics, 10711454001) blocking agent for an hour. Anti-mycobacterium tuberculosis antibody (Abcam, ab905) was added to the surface and incubated at 4 ℃ overnight. The AuNPs bioconjugated with secondary goat anti-rabbit IgG H&L

Downloaded From: https://www.spiedigitallibrary.org/conference-proceedings-of-spie on 22 Mar 2023
Terms of Use: https://www.spiedigitallibrary.org/terms-of-use

antibody from section 2.1.1. were subsequently introduced on the surface and incubated for an hour before analysis. The chip was used to perform SEM and EDX analysis.

2.2.2. Energy-dispersive X-ray (EDX) spectroscopy

EDX spectroscopy was performed to identify the different elements present on the biosensing surface. The SEM and EDX data were acquired using the JSM-IT800 schottky field emission scanning electron microscope (JEOL Ltd, Japan). Three sample groups, including the bare Au-thin film, experiment, and control samples, were analysed for SEM and EDX. The experiment sample consisted of MA, anti-mycobacterium tuberculosis antibody, and goat anti-rabbit IgG H&L secondary antibody bioconjugated to AuNPs (referred to as TB-bioconjugate). Anti-mycobacterium tuberculosis antibody was not introduced on the biosensing surface in the control sample. The bioconjugated AuNPs were introduced on the surface of the control sample, incubated for an hour, and washed before sample analysis.

2.3. Optical biosensing

A custom-built transmission spectroscopy setup was used to measure transmitted light between the different sample groups. Sample groups included Au thin film, immobilised MA, primary antibody immobilised on MA monolayer (MA + 1° Ab), secondary antibody bioconjugated with AuNPs immobilised on a surface containing primary antibody (MA + 1° Ab + 2° Ab), and bioconjugated secondary antibody immobilised on a surface containing MA (MA + 2° Ab). The setup was assembled using a 512 nm green light source with a power of 3.1 mW. A combination of lenses was used to collimate the light and focused it on the biosensor chip sample placed on the sample stage. Transmitted light was collected through a 10x microscope objective, and a 50/50 beam splitter directed the light to the imaging system and the spectrometer through a fibre. The imaging system was formed by a charge-coupled device (CCD) camera connected to a computer. Sample groups were prepared in duplicates under the same conditions, and the analysis was repeated three times ($n=3$). Transmitted light was collected using fibre and directed to the USB 4000 portable spectrometer (Ocean Optics Inc, United States) connected to the computer for data acquisition (Figure 1). Further data analysis was performed using OriginPro software.

Downloaded From: https://www.spiedigitallibrary.org/conference-proceedings-of-spie on 22 Mar 2023
Terms of Use: https://www.spiedigitallibrary.org/terms-of-use

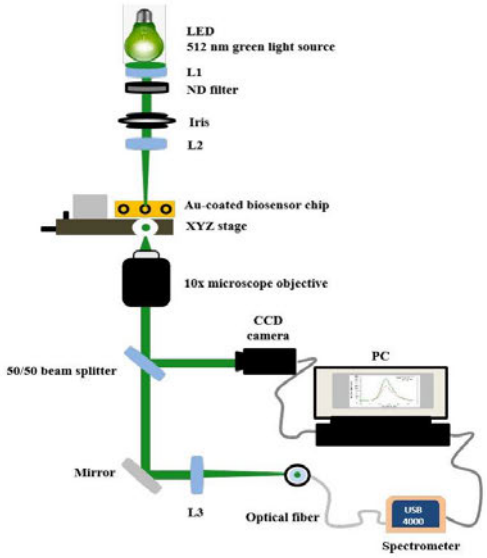

Figure 1: A custom-built optical biosensing setup used to measure transmitted light. The setup consists of a 512nm green light source with a power of 3.1 mW, collimating lenses (L1 and 2), XYZ stage, a 10x microscope objective, and an imaging system consisting of a CCD camera and computer, focussing lens (L3), an optical fiber, and a portable USB spectrometer connected to a computer.

3. RESULTS AND DISCUSSION

3.1. UV-vis absorption spectroscopy

UV-vis absorption spectroscopy was used in this study to characterise the 60 nm Au Nanourchins before and after bioconjugation to goat anti-rabbit IgG H&L secondary antibody. The bioconjugated AuNPs play a significant role in enhancing the detection signal when introduced on the biosensing surface containing the complementary primary antibody. A spectrophotometer can be used to identify components in a solution mainly based on their unique absorbance characteristics [16]. Covalent conjugation chemistry was used to functionalise AuNPs with the secondary antibody. Specifically, EDC and NHS chemistry was used to link the goat anti-rabbit IgG H&L secondary antibody to polyethylene glycol (SH-PEG-COOH). In this chemistry, EDC and NHS activate the carboxyl groups of the AuNP surface to form an intermediate that interacts with the amine group (NH_2) on the antibody [17]. Successful bioconjugation occurs when the secondary antibody binds to the AuNPs surface and is confirmed by observing a wavelength redshift in the absorption spectrum by a few nanometres [18]. Figure 3 shows the UV-vis absorption spectrum of AuNPs before and after bioconjugation.

Downloaded From: https://www.spiedigitallibrary.org/conference-proceedings-of-spie on 22 Mar 2023
Terms of Use: https://www.spiedigitallibrary.org/terms-of-use

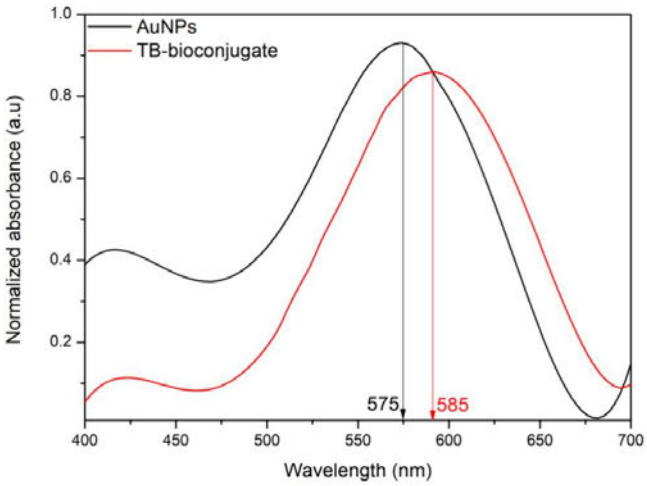

Figure 2: UV-vis absorption spectrograph of the AuNPs recorded before and after bioconjugation to goat anti-rabbit IgG H&L secondary antibody. The black line represents the spectrum of neat AuNPs before bioconjugation, and the red spectrum represents AuNPs after bioconjugation with a secondary antibody. A redshift of 10 nm was detected to confirm successful conjugation.

The reduction in absorption intensity and the redshift in the wavelength observed after AuNPs bioconjugation with the secondary antibody was an indication of successful covalent bioconjugation. The use of this bioconjugated AuNPS plays a significant role in signal enhancement by changing the refractive index when introduced on the biosensing surface. Figure 3 shows the absorption spectrum of AuNPs before bioconjugation (black line spectrum) and the spectrum of AuNPs after bioconjugation (red line spectrum). An absorption peak intensity of 575 nm was detected before bioconjugation, and 585 nm after bioconjugation was observed, thus resulting in a redshift of 10 nm. The NanoUrchins used in this study have a spiky uneven surface morphology which causes a red shift in the surface plasmon peak and a larger enhancement of electromagnetic fields at the tips of the NanoUrchin spikes as compared to that of spherical particles [19]. The unique optical properties of the Nanourchins allow them to be easily manipulated compared to bulk gold. These special characteristics provide vast advantages, especially in biosensing and diagnostic imaging. One of the major attributes is the interchange of light with electrons on the exterior [20]. The resonance wavelength and bandwidth of the AuNPs are dependent on the shape, particle size, refractive index of the surrounding media, and temperature. The shift in the AuNPs-IgG bioconjugate spectra might be a result of the changes in the dielectric environment surrounding the AuNPs [16,21].

3.2. Scanning Electron Microscopy (SEM)

The SEM analysis was used for end-point characterisation of the biosensing surface. To perform SEM and EDX, three sample groups were prepared, namely a gold thin film surface as the background sample, the experiment sample, and the control sample. The Au thin film was used to prepare the experiment and control samples consisting of the MA biorecognition element on the surface. The Au thin film sample consisted of approximately 40nm of Au, and SEM was able to produce images of the distribution pattern on the surface (Figure 3A). The experiment sample surface consisted of mycolic acid TB antigen, anti-mycobacterium tuberculosis primary antibody, and AuNPs bioconjugated with goat anti-rabbit IgG H&L secondary antibody. The control sample consisted of everything else except the anti-mycobacterium tuberculosis antibody. This was done to test the specificity of the biorecognition element (MA) to the primary antibody and other antibodies. Images of the three sample groups are depicted in figure 3.

Downloaded From: https://www.spiedigitallibrary.org/conference-proceedings-of-spie on 22 Mar 2023
Terms of Use: https://www.spiedigitallibrary.org/terms-of-use

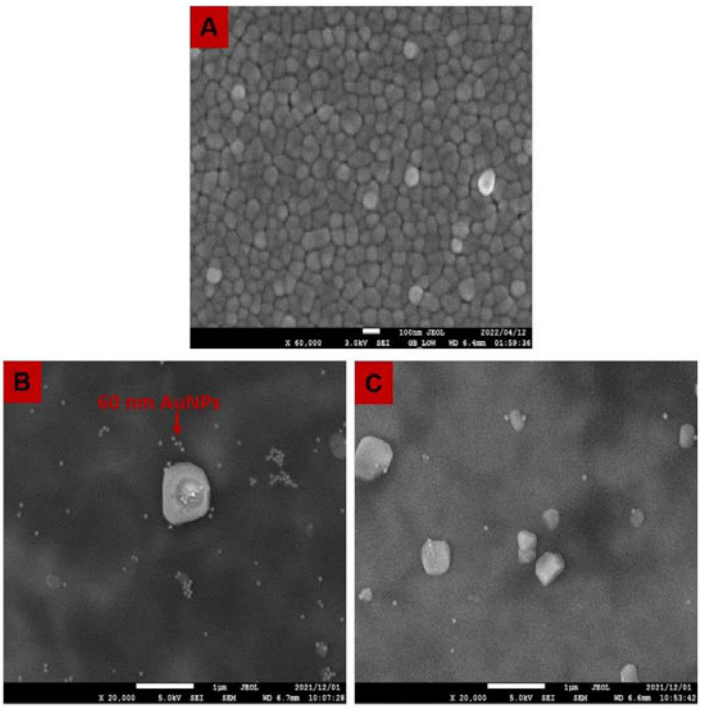

Figure 3: SEM images of the biosensing surface of the Au thin film deposited on a glass substrate (A), experiment sample consisting of SAM of mycolic acid TB antigen, anti-mycobacterium tuberculosis antibody, and a secondary antibody bioconjugated to AuNPs. (B), and the control sample which lacks an anti-mycobacterium tuberculosis antibody. The AuNPs (Nano-urchins) under SEM are visualised as tiny bright spots resembling stars. Minimal traces of bioconjugated AuNPs were spotted on the biosensing surface of the control sample.

Figure 3A displays how Au was deposited on the glass substrate using titanium for attachment. It is evident that the distribution is uniform, closely, and densely packed. They are columnar structures that resembled round-shaped structures, and this is in agreement with what has been documented in the literature [22]. The nano-interspaces between the columnar structures support what has been detected in other studies, and this is an indication that the film is robust and can be used to develop biosensing platforms [23]. On the experiment sample, SEM was able to detect a substantial amount of the spherical multi-branched AuNPs (Figure 3B). Agglomeration of AuNPs was not observed on the surface, and the AuNPs were evenly dispersed. The secondary antibody bioconjugated to the AuNPs is specifically designed to bind the primary antibody and not MA; hence in the control sample, the addition of bioconjugated AuNPs on the surface resulted in a negative outcome following the wash step before sample analysis. The non-specific binding observed could result from the blocking agent (bovine serum albumin) immobilised on the biosensing surface, longer incubation time, or even inadequate wash steps. Figure 3C shows the SEM results of the control sample where small traces of AuNPs were visualised. These traces of bioconjugated AuNPs detected on the biosensing surface of the control sample were confirmed by EDX to be insignificant.

Downloaded From: https://www.spiedigitallibrary.org/conference-proceedings-of-spie on 22 Mar 2023
Terms of Use: https://www.spiedigitallibrary.org/terms-of-use

3.3. Energy-dispersive X-ray (EDX) spectroscopy

EDX spectroscopy was used to detect the elements present on the surface of the three samples described in section 3.2. EDX was able to qualitatively determine the elemental composition between the reference sample (Au thin film), experiment, and control samples, primarily focusing on the quantity of Au as the main element of interest. The biosensor chips used for SEM were also used to perform EDX spectroscopy. The elemental composition, as per figure 4A - C shows that Au and Si dominate over all the other elements detected between the three sample groups. Since the glass was used as the substrate, Si is present in all the samples in approximately equal quantities. The quantity of Au between the different samples is per contribution from the Au thin film and the amount of AuNPs on the surface.

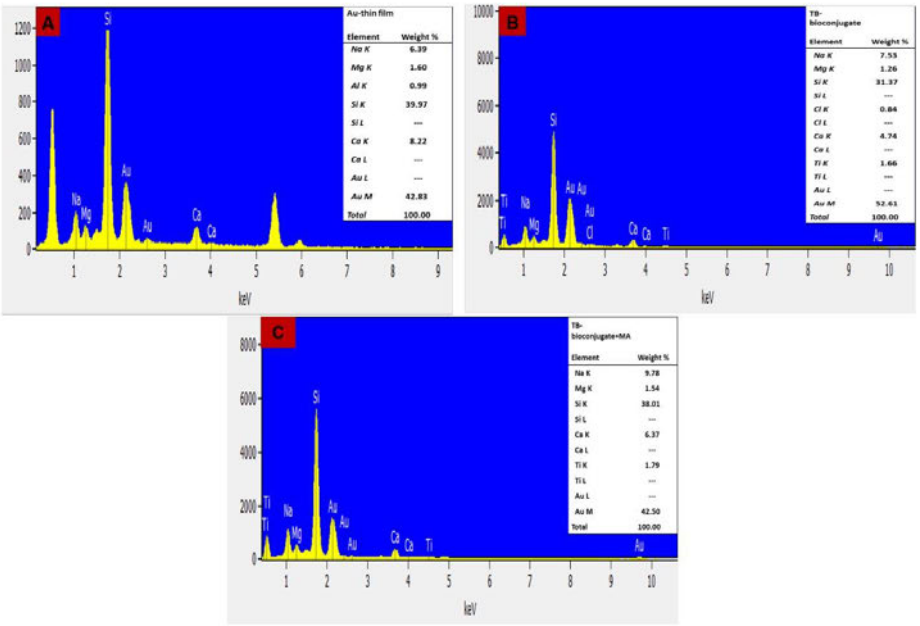

Figure 4: EDX spectrographs of the Au thin film deposited on a glass substrate (A); the experiment sample consisted of mycolic acid TB antigen, an anti-mycobacterium tuberculosis primary antibody, and a goat anti-rabbit IgG H&L secondary antibody bioconjugated to AuNPs. (B), and the control sample consists of the biorecognition element (MA) and the bioconjugated secondary antibody which is not designed to bind to MA (C). The main elements obtained from all three samples are Au, Si, Ti, Na, Mg, Ca, and Cl. Significant differences in Au quantity were observed when the experiment sample was compared to the control and reference samples.

The quantity of Au in the reference sample, experiment, and control sample were 42.83, 52.62, and 42.50. This observation supports the SEM data whereby AuNPs were dominant on the surface of the experiment sample (Figure 3B) compared to the control. The additional Au percentage detected in the experiment sample was contributed by the presence of AuNPs on the surface. Approximately similar quantities of Au were detected on the Au thin film sample and the control as an indication that the detected quantity was mainly from the surface deposited Au.

Downloaded From: https://www.spiedigitallibrary.org/conference-proceedings-of-spie on 22 Mar 2023
Terms of Use: https://www.spiedigitallibrary.org/terms-of-use

3.4. Optical biosensing

The optimised biosensor chip with immobilised biorecognition element was analysed using the custom-built nanoplasmonic biosensing setup to measure transmitted light intensity between the five sample groups. Samples were prepared in duplicates under the same conditions, and analysis was performed three times (*n=3*) for reproducibility. Optical biosensing was performed on five sample groups obtained at different stages of the biosensor chip development. This is significant to confirm the surface immobilisation integrity of the biosensor chip. Sample groups included Au-thin film immobilised on a glass substrate, MA monolayer (MA + 1° Ab), secondary antibody bioconjugated with AuNPs immobilised on a surface containing primary antibody (MA + 1° Ab + 2° Ab), and bioconjugated secondary antibody immobilised on a surface containing MA (MA + 2° Ab). Measurements of transmitted intensities between the five sample groups are depicted in figure 5A. From the analysis, it was realised that there was more light transmitted in the Au-thin film sample used as a reference.

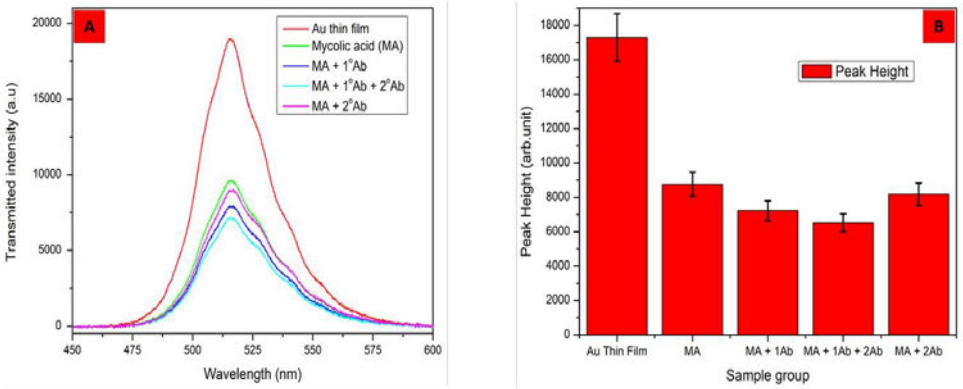

Figure 5: Transmitted intensity between the Au thin film layer, MA, MA+1^0Ab, MA+1^0Ab+2^0Ab, and MA+2^0Ab. Figure (A) shows the transmitted intensity peaks of the five sample groups, whereby the Au-thin layer transmitted more light, followed by MA, MA+2^0Ab, MA+1^0Ab, and the MA+1^0Ab+2^0Ab sample reported the lowest transmitted intensity. Figure (B) shows the difference in peak height between the five sample groups.

The MA sample transmitted less light compared to the Au. The MA+2^0Ab (referred to as control in sections 3.2 and 3.3) sample was used to test for non-specific binding transmitted less light compared to the MA. This may have been due to the small traces of AuNPs observed under SEM in figure 3C. This shows that the bioconjugated secondary antibody could not bind directly to MA; however, there was still non-specific binding detailed in section 3.2. There were no significant differences between these two samples when comparing the average peak height (Figure 5B). The MA+1^0 Ab sample transmitted less light compared to the MA+2^0Ab. This finding supports the successful binding of the primary antibody to the MA surface. The MA+1^0 Ab+2^0Ab (referred to as the experiment sample in sections 3.2 and 3.3) sample reported the lowest transmitted intensity. From these findings, it is proven that immobilisation of the biorecognition element on the biosensor chip was successful, and binding to the primary antibody was successful. It was also evident that the biorecognition element specifically binds to anti-mycobacterium tuberculosis and not any other antibody.

4. CONCLUSION

In conclusion, a custom-made gold-coated optical biosensor chip was designed and successfully developed for the optical detection of anti-mycobacterium tuberculosis. The developed biosensor chip was efficiently functionalised with mycolic acid TB antigen as the biorecognition element to react specifically to the anti-mycobacterium tuberculosis antibody. The biorecognition element's specificity was proven by introducing a goat anti-rabbit IgG H&L antibody bioconjugated with

Downloaded From: https://www.spiedigitallibrary.org/conference-proceedings-of-spie on 22 Mar 2023
Terms of Use: https://www.spiedigitallibrary.org/terms-of-use

AuNPs and was unable to bind to MA. AuNPs were also functionalised with the goat anti-rabbit IgG H&L secondary antibody and introduced on the surface of the biosensor chip. Based on data acquired from UV-vis absorption spectroscopy, it was proven that the covalent bioconjugation of AuNPs with antibodies was successful, and a 10 nm redshift was noted when comparing AuNPs before and after bioconjugation. Furthermore, biosensing surface characterisation using SEM showed the presence of the bioconjugated AuNPs on the biosensor chip surface. EDX spectroscopy analysis of elements present on the biosensor chip showed high gold percentage in the experiment group containing AuNPs than in the control group, further supporting the significance of introducing AuNPs on the biosensing surface. A transmission spectroscopy configuration custom-built optical setup was successful in detecting transmitted light differences between different sample groups obtained at various steps of the biosensor chip development process. There was more light transmitted in the reference sample when analysing peaks based on peak intensity, and the experiment sample transmitted the lowest light. Overall, it was proven that mycolic acid could be applied as an efficient biomarker to capture anti-mycobacterium tuberculosis antibodies. It can be used for the development of biosensor chips for TB diagnosis. And also, biosensor chips can be successfully analysed using optical detection techniques, which have the capability of miniaturisation.

5. REFERENCES

[1] World Health Organisation, WHO Global Tuberculosis Report, 2022.

[2] J.K. Sia, J. Rengarajan, Immunology of mycobacterium tuberculosis infections, Gram-Positive Pathog. (2019) 1056–1086. https://doi.org/10.1128/9781683670131.ch64.

[3] B. Acharya, A. Acharya, S. Gautam, S.P. Ghimire, G. Mishra, N. Parajuli, B. Sapkota, Advances in diagnosis of Tuberculosis: an update into molecular diagnosis of Mycobacterium tuberculosis, Mol. Biol. Rep. 47 (2020) 4065–4075. https://doi.org/10.1007/s11033-020-05413-7.

[4] C.M. Gill, L. Dolan, L.M. Piggott, A.M. McLaughlin, New developments in tuberculosis diagnosis and treatment, Breathe. 18 (2022) 1–15. https://doi.org/10.1183/20734735.0149-2021.

[5] C. Bussi, M.G. Gutierrez, Mycobacterium tuberculosis infection of host cells in space and time, FEMS Microbiol. Rev. 43 (2019) 341–361. https://doi.org/10.1093/femsre/fuz006.

[6] L. Fan, D. Li, S. Zhang, L. Yao, X. Hao, J. Gu, H. Li, J. Niu, Z. Zhang, C. Zhu, Parallel tests using culture, Xpert MTB/RIF, and SAT-TB in sputum plus bronchial alveolar lavage fluid significantly increase diagnostic performance of smear-negative pulmonary tuberculosis, Front. Microbiol. 9 (2018) 1–7. https://doi.org/10.3389/fmicb.2018.01107.

[7] E. Maclean, M. Kohli, S.F. Weber, A. Suresh, Advances in Molecular Diagnosis of Tuberculosis, J. Clin. Microbiol. 58 (2020).

[8] A.Y. Vittor, J.M. Garland, R.H. Gilman, Molecular diagnosis of TB in the HIV positive population, Ann. Glob. Heal. 80 (2014) 476–485. https://doi.org/10.1016/j.aogh.2015.01.001.

[9] L.M. Lechuga, Chapter 5 Optical biosensors, Compr. Anal. Chem. 44 (2005) 209–250. https://doi.org/10.1016/S0166-526X(05)44005-2.

[10] Y. Chen, J. Liu, Z. Yang, J.S. Wilkinson, X. Zhou, Optical biosensors based on refractometric sensing schemes: A review, Biosens. Bioelectron. 144 (2019) 111693. https://doi.org/10.1016/j.bios.2019.111693.

[11] S. Akgönüllü, A. Denizli, Recent advances in optical biosensing approaches for biomarkers detection, Biosens. Bioelectron. X. 12 (2022). https://doi.org/10.1016/j.biosx.2022.100269.

[12] X. Fan, I.M. White, S.I. Shopova, H. Zhu, J.D. Suter, Y. Sun, Sensitive optical biosensors for unlabeled targets: A review, Anal. Chim. Acta. 620 (2008) 8–26. https://doi.org/10.1016/j.aca.2008.05.022.

[13] P. Damborský, J. Švitel, J. Katrlík, Optical biosensors, Essays Biochem. 60 (2016) 91–100. https://doi.org/10.1042/EBC20150010.

[14] I. Abdulhalim, M. Zourob, A. Lakhtakia, Overview of Optical Biosensing Techniques, 2008. https://doi.org/10.1002/9780470061565.hbb040.

[15] G. Zanchetta, R. Lanfranco, F. Giavazzi, T. Bellini, M. Buscaglia, Emerging applications of label-free optical biosensors, Nanophotonics. 6 (2017) 627–645. https://doi.org/10.1515/nanoph-2016-0158.

[16] S.L. Manoto, A. El-Hussein, R. Malabi, L. Thobakgale, S. Ombinda-Lemboumba, Y.A. Attia, M.A. Kasem, P. Mthunzi-Kufa, Exploring optical spectroscopic techniques and nanomaterials for virus detection, Saudi J. Biol. Sci. 28 (2021) 78–89. https://doi.org/10.1016/j.sjbs.2020.08.034.

[17] P.S. Parsamehr, M. Zahed, M.A. Tofighy, T. Mohammadi, M. Rezakazemi, Preparation of novel cross-linked graphene oxide membrane for desalination applications using (EDC and NHS)-activated graphene oxide and PEI, Desalination. 468 (2019) 114079. https://doi.org/10.1016/j.desal.2019.114079.

Downloaded From: https://www.spiedigitallibrary.org/conference-proceedings-of-spie on 22 Mar 2023
Terms of Use: https://www.spiedigitallibrary.org/terms-of-use

[18] X. Zhang, Plasmon extinguishment by bandedge shift identified as a second-order spectroscopic differentiation, Nanophotonics. 10 (2021) 1329–1335. https://doi.org/10.1515/nanoph-2020-0603.
[19] J. Langer, D.J. de Aberasturi, J. Aizpurua, R.A. Alvarez-Puebla, B. Auguié, J.J. Baumberg, G.C. Bazan, S.E.J. Bell, A. Boisen, A.G. Brolo, J. Choo, D. Cialla-May, V. Deckert, L. Fabris, K. Faulds, F. Javier García de Abajo, R. Goodacre, D. Graham, A.J. Haes, C.L. Haynes, C. Huck, T. Itoh, M. Käll, J. Kneipp, N.A. Kotov, H. Kuang, E.C. Le Ru, H.K. Lee, J.F. Li, X.Y. Ling, S.A. Maier, T. Mayerhöfer, M. Moskovits, K. Murakoshi, J.M. Nam, S. Nie, Y. Ozaki, I. Pastoriza-Santos, J. Perez-Juste, J. Popp, A. Pucci, S. Reich, B. Ren, G.C. Schatz, T. Shegai, S. Schlücker, L.L. Tay, K. George Thomas, Z.Q. Tian, R.P. van Duyne, T. Vo-Dinh, Y. Wang, K.A. Willets, C. Xu, H. Xu, Y. Xu, Y.S. Yamamoto, B. Zhao, L.M. Liz-Marzán, Present and future of surface-enhanced Raman scattering, ACS Nano. 14 (2020) 28–117. https://doi.org/10.1021/acsnano.9b04224.
[20] A.R. Shafiqa, A. Abdul Aziz, B. Mehrdel, Nanoparticle Optical Properties: Size Dependence of a Single Gold Spherical Nanoparticle, J. Phys. Conf. Ser. 1083 (2018). https://doi.org/10.1088/1742-6596/1083/1/012040.
[21] S. Link, M.A. El-Sayed, Optical Properties and Ultrafast Dynamics of Metallic Nanocrystals, Annu. Rev. Phys. Chem. 54 (2003) 331–366. https://doi.org/10.1146/annurev.physchem.54.011002.103759.
[22] F. Ruffino, M.G. Grimaldi, Morphological characteristics of Au films deposited on Ti: A combined SEM-AFM study, Coatings. 8 (2018). https://doi.org/10.3390/coatings8040121.
[23] Q. Yu, H. Huang, X. Peng, Z. Ye, Ultrathin free-standing close-packed gold nanoparticle films: Conductivity and Raman scattering enhancement, Nanoscale. 3 (2011) 3868–3875. https://doi.org/10.1039/c1nr10578g.

Downloaded From: https://www.spiedigitallibrary.org/conference-proceedings-of-spie on 22 Mar 2023
Terms of Use: https://www.spiedigitallibrary.org/terms-of-use

PROCEEDINGS OF SPIE

SPIEDigitalLibrary.org/conference-proceedings-of-spie

Photonic crystal-based biosensor chip development for TB diagnosis

Charles Maphanga, Saturnin Ombinda-Lemboumba, Yaseera Ismail, Patience Mthunzi-Kufa

Charles Maphanga, Saturnin Ombinda-Lemboumba, Yaseera Ismail, Patience Mthunzi-Kufa, "Photonic crystal-based biosensor chip development for TB diagnosis," Proc. SPIE 12387, Optical Diagnostics and Sensing XXIII: Toward Point-of-Care Diagnostics, 123870K (16 March 2023); doi: 10.1117/12.2650057

SPIE.

Event: SPIE BiOS, 2023, San Francisco, California, United States

Downloaded From: https://www.spiedigitallibrary.org/conference-proceedings-of-spie on 22 Mar 2023 Terms of Use: https://www.spiedigitallibrary.org/terms-of-use

Photonic crystal-based biosensor chip development for TB diagnosis

Charles Maphanga [1, 2*], Saturnin Ombinda-Lemboumba [1], Yaseera Ismail [2], Patience Mthunzi-Kufa [1, 2]

[1]Council for Scientific and Industrial Research, National Laser Centre, P O BOX 395, Pretoria, 0001, South Africa

[2]University of KwaZulu-Natal, School of Chemistry and Physics, Westville Campus, University Road, Durban, South Africa

ABSTRACT

Tuberculosis (TB) is one of the world's largest infectious diseases. It causes high mortality in humans and leads to about three million deaths worldwide annually, hence early detection is crucial, especially in a point-of-care (POC) setting to prevent the spreading of the pathogen by undiagnosed individuals. In the current work, a photonic crystal (PhC)-based optical biosensor chip was developed for diagnosing TB using mycolic acid TB antigen as a biorecognition element to capture anti-mycobacterium tuberculosis antibodies. Mycolic acid was successfully immobilized on the PhC biosensor chip to react with anti- mycobacterium tuberculosis antibody, and the white light-based transmission setup was used for optical biosensing to monitor biomolecular interactions between the antigen and antibody. Gold nanoparticles (AuNPs) before and after bioconjugation with goat anti-rabbit IgG H&L secondary antibody were characterised using ultraviolet-visible (UV-vis) spectroscopy. Bioconjugated AuNPs were subsequently bound to the biosensing surface to enhance the detection signal of biomolecular binding events. The biosensing surface was further characterised using atomic force microscopy (AFM). Analysis of biomolecular binding events on the biosensing surface was achieved using a custom-built PhC optical biosensing setup which successfully distinguished between experiment and control samples. From our findings, it was realised for the first time that mycolic acid antigen could be immobilised on a biosensing surface to capture anti-mycobacterium tuberculosis antibodies. From this result, it was concluded that the PhC optical biosensing technique was successful in detecting small refractive index changes on the biosensing surface for the diagnosis of TB. These results pave the way for the development of a photonics-based POC diagnostic device for TB.

Keywords: Optical biosensing, photonic crystal, gold nanoparticles, atomic force microscopy, mycolic acid, *mycobacterium tuberculosis*

*Corresponding author: CMaphanga@csir.co.za

Optical Diagnostics and Sensing XXIII: Toward Point-of-Care Diagnostics,
edited by Gerard L. Coté, Proc. of SPIE Vol. 12387, 123870K
© 2023 SPIE · 1605-7422 · doi: 10.1117/12.2650057

Proc. of SPIE Vol. 12387 123870K-1

Downloaded From: https://www.spiedigitallibrary.org/conference-proceedings-of-spie on 22 Mar 2023
Terms of Use: https://www.spiedigitallibrary.org/terms-of-use

1. INTRODUCTION

Biosensing is an emerging analytical field for the detection and analysis of biomolecular or biochemical interactions of various analytes using optical, electrical, calorimetric, and electrochemical transduction systems [1]. These transduction mechanisms are used to translate changes or detectable variations on the transducer surface into readable and quantifiable signals [1]. Biosensing has rapidly advanced over the last few decades due to applications in various disciplines such as health diagnostics, environmental monitoring, and food quality [2]. A biosensor is an analytical device that consists of a biosensing recognition element to detect the analyte, a transducer that translates or converts the biological information into a detectable signal, and a signal processing unit that processes the signal into a readable outcome [3–6]. Biosensors can be easily miniaturised for applications at point-of-care (POC). In particular, optical biosensors have been developed and can operate in different modes including transmission, absorption, and reflection of light waves. Unlike biochemical methods, detection is label-free, making them environmentally friendly [7]. Label-free optical biosensing is a rapidly emerging research focus area with potential applications in clinical diagnostics, pharmaceutical screening, and fundamental research toward the development of portable and easy-to-use POC devices [8]. Over the last three decades, biosensors based on photonic crystals (PhCs) have been developed and continue to receive significant recognition owing to their distinctive electromagnetic properties and broad applications domain [9]. PhCs are spatially arranged periodic structures made of low and high-refractive index materials, providing high-efficiency reflection at specific wavelengths [1,10]. The existence of a forbidden frequency range called a photonic band gap (PBG) is one of the most significant and special properties of PhCs. In this frequency range, the propagation of electromagnetic waves (EMWs) is prohibited [11]. In practice, this means if the radiation with a wavelength inside the PBG is incident on the PhC it experiences a strong reflection from the PhC, hence a PhC can act as an optical filter [7,11]. This can be designed in one-dimensional (1-D), two-dimensional (2-D), or three-dimensional (3-D) depending on the number of directions with a periodic repetition [3,4,12,13]. The 1-D PhCs also known as dielectric mirrors or Bragg mirrors are simple multilayer stacks commonly used as biosensors [3,4]. In this work, a 1-D PhC surface was modified and used as the biosensor chip.

Like other optical biosensors, PhC biosensors have been utilised as label-free biosensors for a wide variety of biomolecular assays. They can detect biomolecular interactions on the surface of a transducer [14]. In contrast to other optical detection techniques which measure layer thickness for detection, PhC biosensing and detection is primarily based on refractive index change induced by the adsorption of biomolecules and allows direct measurement of the binding affinities and binding kinetics to characterise biomolecular interactions in real-time [4,14–17]. With variations in refractive index on the biosensing surface, the resonant wavelength shifts. This resonant wavelength shift is preferred in biosensing as an indication and measure of sensitivity which forms the basis of detection in label-free PhC biosensing [16]. Studies that have used refractive index as a parameter to design optical biosensing devices based on PhCs have resulted in optical devices that are sensitive with quick response time for small variations in samples [18]. In this study, PhC biosensing towards the diagnosis of tuberculosis (TB) was based on the detection of refractive index changes on the functionalised biosensing surface.

A PhC biosensor chip was developed in this study by immobilizing the mycolic acid TB antigen surface of the PhC. Mycolic acid was used as a biorecognition element to specifically bind the anti-mycobacterium tuberculosis antibody as the analyte. Furthermore, gold nanoparticles (AuNPs) were covalently conjugated with a secondary antibody and introduced on the biosensing surface to enhance the detection signal. The AuNPs were characterised before and after bioconjugation using ultraviolet-visible (UV-vis) spectroscopy before introducing them on the biosensing surface. The biosensing surface was also characterised layer-by-layer during the development process of the biosensor chip using atomic force microscopy (AFM). The biosensor chip was analysed using a custom-built PhC setup, transmitted light intensity was measured, and a shift in the wavelength due to refractive index changes was detected using a spectrometer. The acquired data were analysed using OriginPro software to visualise the transmission spectra between the neat PhC, experiment, and control samples.

Downloaded From: https://www.spiedigitallibrary.org/conference-proceedings-of-spie on 22 Mar 2023
Terms of Use: https://www.spiedigitallibrary.org/terms-of-use

2. MATERIALS AND METHODS

2.1 Characterisation of the biosensing surface using AFM

Atomic force microscopy (AFM) was used to perform layer-by-layer characterisation of the biosensing surface for surface morphology studies of the PhC biosensor chips at different stages of the development process. A 1-D PhC biosensor chip was washed with absolute ethanol and blow-dried with nitrogen gas. The chip was subsequently placed in the oxygen plasma treatment oven to make the surface hydrophilic. After the surface activation procedure, the PhC was immersed in (3-Aminopropyl) triethoxysilane (APTES) (1%, v/v) (Sigma-Aldrich, A3648) in a vertical Coplin jar and incubated at room temperature overnight. Post incubation, the PhC was washed thoroughly by sonication in absolute ethanol for 5 minutes and followed by sonication in ultrapure water (resistivity of 18 MΩ) for 5 minutes. The clean PhC was blow-dried with nitrogen (N2) gas and placed in the incubator at 90°C for 1 hour. The silanized PhC surface was functionalised with stearic acid (STA) (141 mM) (Sigma-Aldrich, S4745) using carbodiimide coupling chemistry to form an amide bond. Mycolic acid (MA) from *mycobacterium tuberculosis* (bovine strain) (0.5 mg/mL) (Sigma-Aldrich, M4537) was used as the biorecognition element. MA dissolved in hexane (1mg MA, 2mL hexane: MW 86,18 g/mol) (Sigma-Aldrich, 34859) was immobilised on the STA monolayer by incubating the chip in a solution of MA overnight at room temperature. Post incubation the chip was rinsed thoroughly with 1x phosphate buffered saline (PBS) (Sigma-Aldrich, D1283) to remove physically adsorbed MA. A solution of bovine serum albumin (BSA) (1%, v/v) (Roche Diagnostics, 10711454001) prepared in 1x PBS was used as the blocking agent and added to the chip for an hour. Anti-mycobacterium tuberculosis primary antibody (8.8 mg/ml) (Abcam, ab905) prepared in 1x PBS was added to the MA monolayer and incubated overnight. In the experiment sample, a goat anti-rabbit IgG H&L secondary antibody (2.1 mg/ml) (Abcam, ab6702) was conjugated to gold nanoparticles (AuNPs) (Sigma-Aldrich, 797707) and herein called TB bioconjugate (AuNPs-IgG) and introduced on the surface containing primary antibody. In the control sample, the primary antibody was not introduced on the surface; however, the TB bioconjugate was introduced on the surface containing MA. AFM images of the neat PhC biosensor chip, experiment, and control samples were captured with a Vecco AFM system (Digital Instruments, USA) using a silicon cantilever tip. The tip has a curvature radius of 10 nm and is n-doped silicon; with a resonance frequency of 204-497 kHz and a force constant of approximately 10-130 N/m. Images acquired by the AFM instrument were analysed using Nanoscope software.

2.2 Characterisation of AuNPs using UV-vis absorption spectroscopy

UV-vis absorption spectroscopy was performed to characterise the gold nanoparticles (AuNPs) before and after bioconjugation. Covalent bioconjugation chemistry was adopted to conjugate the 60 nm gold NanoUrchins (Cytodiagnostics, 2459298_60U) to the secondary antibody mentioned in section 2.1. To perform bioconjugation, N-hydroxysuccinimide (NHS) (13 mM) (Sigma-Aldrich, 56480) and 1-Ethyl-3-(3-dimethylaminopropyl)-carbodiimide) (EDC) (5 mM) (Sigma-Aldrich, E7750) with similar molar ratio were added to heterobifunctional polyethylene glycol (PEG) (SH-PEG-COOH) (10 mg diluted in 10 mL ultrapure water) (Sigma-Aldrich, 757845) in ultrapure water and shaken for an hour on an orbital shaker. 10x PBS was added to the solution to adjust the pH of the reaction mixture to 7.4. The secondary antibody was introduced to the reaction mixture and incubated for 2 hours before filtering the solution with a 50 kDa filter to remove any by-products. The final SH-PEG-IgG bioconjugated solution was obtained after washing with 1x PBS twice. Then, 12µL of the SH-PEG-IgG complex was added to 200 µL of AuNPs and incubated for an hour on an orbital shaker to form the TB-bioconjugate complex (AuNPs-IgG). Successful bioconjugation was confirmed using NanoDrop 8000 spectrophotometer (Thermo Fisher Scientific, United States) measuring UV-vis absorption. Several absorption spectra (~4) of the AuNPs were recorded to determine the redshift before and after bioconjugation.

2.3 Photonic crystal biosensing

A custom-built optical biosensing setup with a transmission spectroscopy conformation was used to perform PhC biosensing. The setup was assembled using a broadband light-emitting diode (LED) light source. The light was collimated using a combination of collimating lenses and focused on the sample stage. Light transmitted through the PhC biosensor chip on the stage was collected using a 10x microscope objective. A 50/50 beam splitter directed the light to the imaging

Downloaded From: https://www.spiedigitallibrary.org/conference-proceedings-of-spie on 22 Mar 2023
Terms of Use: https://www.spiedigitallibrary.org/terms-of-use

system and the spectrometer using a fiber. Transmitted light was focused into the fiber using a focussing lens and directed to the USB 4000 portable spectrometer (Ocean Optics Inc, United States) connected to the computer. The imaging system enabled the visualisation of biosensing activities on the sample stage and was formed by a charge-coupled device (CCD) camera connected to a computer. SpectraSuit software was used to perform spectroscopic analysis of the different sample groups. Sample groups were prepared in triplicates under the same conditions and the analysis was repeated three times ($n=3$). During sample analysis, background measurements were taken before each recording. The acquired data were further analysed using OriginPro software to plot wavelength-shift differences between the sample groups.

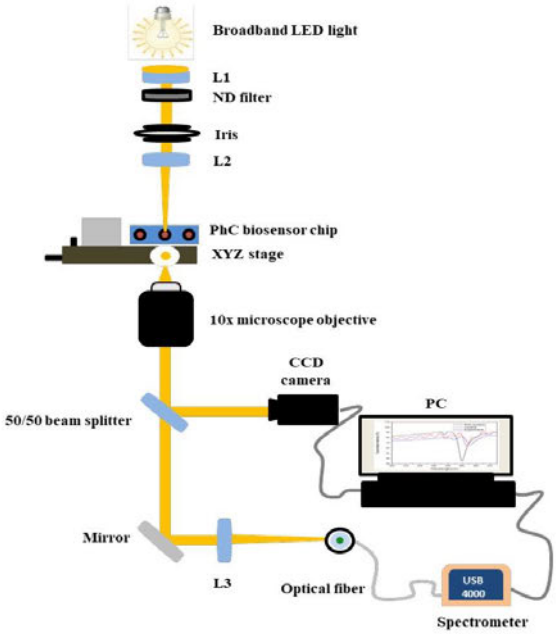

Figure 1: A custom-built photonic crystal biosensing setup used to measure transmitted light. The setup consists of a broadband LED light source, collimating lenses (L1 and 2), XYZ stage, a 10x microscope objective, and an imaging system consisting of a CCD camera and computer. The focusing lens (L3) was used to focus the light into the optical fiber, and the portable USB spectrometer connected to a computer was used for data acquisition.

2. RESULTS AND DISCUSSION

3.1. Atomic force microscopy

Atomic force microscopy was used in this study to perform layer-by-layer characterisation of the PhC biosensor chip surface during the chip development process. As different elements were covalently and physically adsorbed on the biosensor chip surface to distinguish the experiment from the control sample, it was crucial to study the changes in height and surface roughness between the different sample groups. Sample groups included neat PhC, control, and experiment sample. The control sample consisted of mycolic acid immobilised on the biosensing surface as the biorecognition element, and the goat anti-rabbit IgG H&L secondary antibody bioconjugated to AuNPs (TB-bioconjugate). The introduction of the TB bioconjugate on the surface containing mycolic acid was used to test for the specificity of mycolic acid to antibodies.

Downloaded From: https://www.spiedigitallibrary.org/conference-proceedings-of-spie on 22 Mar 2023
Terms of Use: https://www.spiedigitallibrary.org/terms-of-use

There was no primary antibody on the surface of the control sample. Mycolic acid used in this study should only bind to the anti-mycobacterium tuberculosis antibody, and the secondary antibody is designed to bind to the primary antibody. The experiment sample consisted of mycolic acid, anti-mycobacterium tuberculosis primary antibody, and the TB bioconjugate. The images taken using AFM are shown in figure 2, and each of the scans represents a 5µm X 5µm lateral area that was scanned.

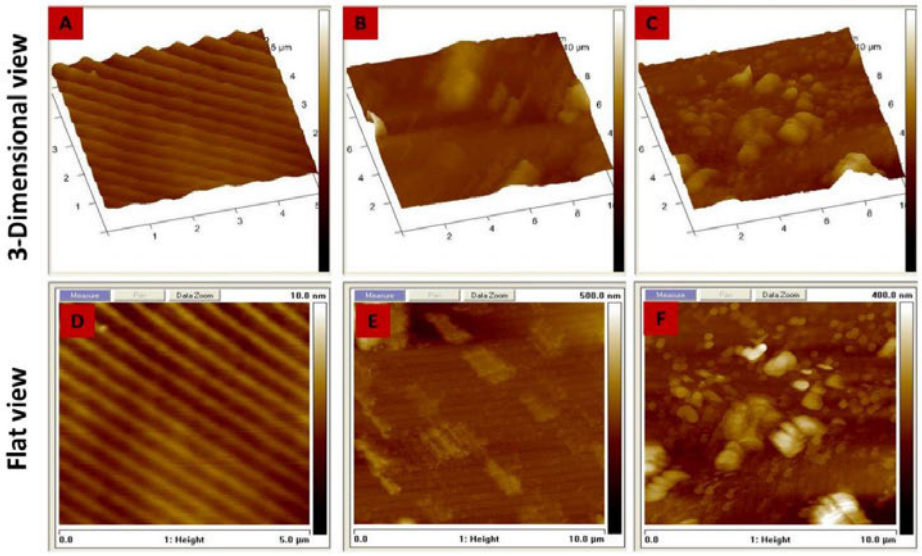

Figure 2: Atomic force microscopy micrographs of the PhC, control, and experiment group displayed in 3-dimensional and flat view projection. Figure A and D show the 1-D PhC used as the reference sample displayed in 3D and flat view. Figures B and E show the control sample in 3D and flat view projection. Figures C and F show the experiment sample in 3D and flat view. The PhC surface was smooth with no debris detected on it. The experiment sample displayed much more surface roughness compared to the control sample.

In the absence of a primary antibody on the surface of the control sample, the TB-bioconjugate was not expected to bind to the surface, hence the intense surface roughness observed in the experimental sample was not detected in the control sample (Figure 2B and E). Various structures resembling AuNP-antibody complexes were visualised on the surface containing bioconjugated AuNPs in figures 2C and F of the experiment sample. This also supports findings by Lee et al., 2015 who demonstrated the possibility of visualising AuNP-antibody complexes as a result of the presence of immobilised AuNPs. The increased surface roughness in the experiment sample could be attributed to the immobilisation of the AuNPs contained in the TB-bioconjugate bound to the surface of the experiment sample. The Z-range increased from 150 nm in the neat 1D PhC sample used as a reference to 344 nm in the control sample. The experiment sample containing immobilised bioconjugated AuNPs displayed a z-range of 473 nm. This shows that the immobilisation of the secondary antibody to the AuNPs was successful, and the secondary antibody was subsequently attached to the primary antibody on the surface of the biosensor chip. This finding supports the UV-vis absorption spectroscopy findings in section 3.2 below.

3.2. UV-vis absorption spectroscopy

UV-vis absorption spectroscopy was performed to characterise AuNPs before and after bioconjugated to goat anti-rabbit IgG H&L secondary antibody. The spectrophotometer can identify components in a solution mainly based on their unique

Downloaded From: https://www.spiedigitallibrary.org/conference-proceedings-of-spie on 22 Mar 2023
Terms of Use: https://www.spiedigitallibrary.org/terms-of-use

absorbance characteristics [20,21]. Covalent bioconjugation chemistry was used for the bioconjugation of AuNPs to the secondary antibody. NHS and EDC chemistry was used to bind the secondary antibody to PEG. In this chemistry, NHS and EDC activate the carboxyl groups of the AuNP surface to form an intermediate that reacts with primary amine groups on the antibody [22]. Bioconjugation occurs upon successful binding of the antibody to the AuNPs surface, thus resulting in a wavelength redshift in the absorption spectrum by a few nanometres [23]. The UV-vis absorption spectrum of AuNPs before and after bioconjugation is shown in figure 3. After successful bioconjugation of the AuNPs with the antibody, a reduction in absorption intensity in the TB-bioconjugate was observed. Successful bioconjugation of AuNPs with the secondary antibody plays a crucial role in changing the refractive index when introduced on the biosensing surface of the biosensor chip. As a result, the sensitivity of the detection system during optical biosensing is enhanced.

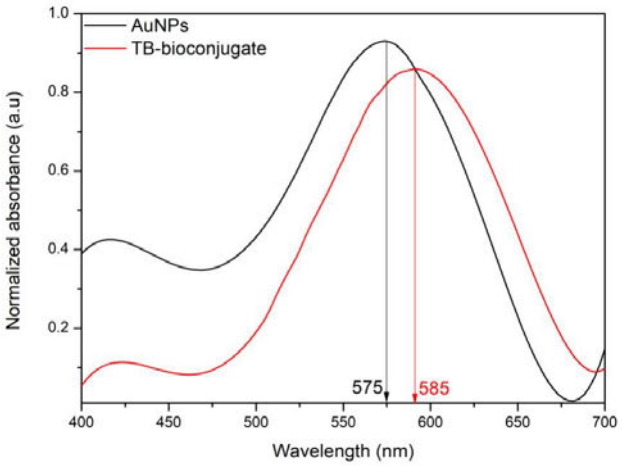

Figure 3: UV-vis absorption spectrograph of AuNPs before and after bioconjugation to goat anti-rabbit IgG H&L secondary antibody (TB-bioconjugate). The black line represents the spectrum of neat AuNPs before bioconjugation, and the red line represents the spectrum of AuNPs after bioconjugation with the secondary antibody. A reduction in absorption intensity and a redshift in the wavelength were observed between the AuNPs and the TB-bioconjugate.

The absorption spectrum of AuNPs before bioconjugation (black spectrum) and the spectrum of AuNPs after bioconjugation (red spectrum) with goat anti-rabbit IgG H&L secondary antibody is represented in figure 3. Before bioconjugation, the AuNPs displayed an absorption peak intensity of 575 nm, and a 585 nm peak intensity was observed after bioconjugation in the TB-bioconjugate. A 10nm redshift in the wavelength was observed as confirmation of successful bioconjugation. The resonance wavelength and bandwidth of the AuNPs are dependent on the shape, particle size, refractive index of the surrounding media, and temperature. The shift in the AuNPs-IgG bioconjugate spectra might be a result of the changes in the dielectric environment surrounding the AuNPs [20,24].

3.3. Photonic crystal biosensing

A custom-built PhC biosensing setup was used to differentiate and detect differences between the neat PhC sample, the control, and the experiment sample. Transmitted light intensity was measured between the three sample groups. During data acquisition, the samples were placed flat (0° angle) on the sample stage, enabling light to pass directly vertically through the sample. Based on the manufacturer's instruction, the 1D PhC used in this study provides optimum results at 0° to 10° angles. In this study, 0° angle provided optimum results. There were clear wavelength-shift differences between the three samples (Figure 4). The neat PhC sample was detected at a wavelength of 650.08 nm, and the control sample with

Downloaded From: https://www.spiedigitallibrary.org/conference-proceedings-of-spie on 22 Mar 2023
Terms of Use: https://www.spiedigitallibrary.org/terms-of-use

mycolic acid biorecognition element on the surface was detected at a wavelength of 653.48 nm. There was a redshift of 3.4 nm in the wavelength detected between the reference sample and the control. The redshift detection is due to changes in the refractive index between the two samples [21]. There was also a significant reduction in transmitted intensity between the neat PhC and the control, and this is attributed to the successful immobilisation of the biorecognition element in the control sample. The experiment sample was detected at a wavelength of 655.88 nm, and a redshift of 2.4 nm was detected between the control and the experiment. A further reduction in transmitted intensity was detected between the control and the experiment, suggestive of successful binding of anti-mycobacterium tuberculosis to the biosensing surface containing immobilised biorecognition element, and the binding of the TB-bioconjugate containing AuNPs may also have contributed. These results fully support the AFM results in section 3.1. When the experiment sample was compared to the reference sample, a redshift of 5.8 nm was recorded. From these findings, it is evident that the introduction of elements on the PhC changes the refractive index of the material, which contributes directly to changes in detectable wavelength between various sample groups. These findings suggest a possible diagnosis of TB using label-free PhC optical biosensing and provide a platform for the possible development of photonics-based POC TB diagnostic devices.

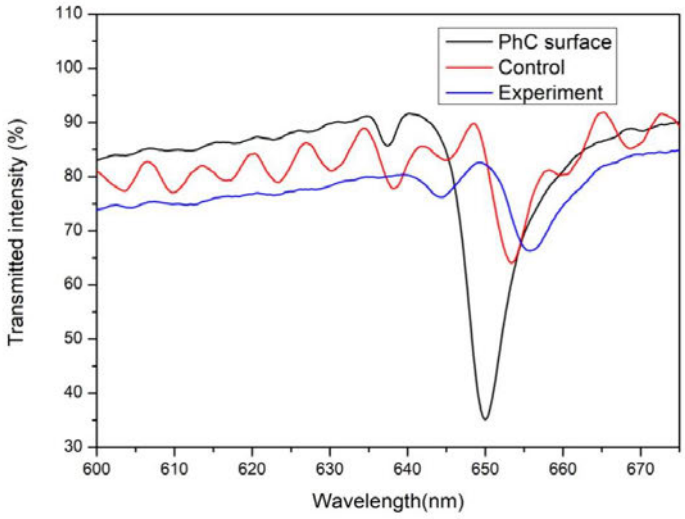

Figure 4: Photonic crystal spectrograph for the detection of anti-mycobacterium tuberculosis antibodies. The neat PhC spectrum is represented by the black line, the control is represented by the red spectrum, and the experiment is represented by the blue spectrum. There were clear detectable wavelength differences between the three sample groups, and a reduction in transmitted intensity was also recorded.

4. CONCLUSION

In conclusion, anti-mycobacterium tuberculosis antibodies were successfully detected using a 1D photonic crystal-based biosensor chip. Mycolic acid was successfully immobilised on the biosensor chip for purposes of specific binding to anti-mycobacterium tuberculosis. Non-specific binding was successfully ruled out by introducing a bioconjugated secondary antibody to the surface of the biosensor chip containing the biorecognition element. The secondary antibody was unable to bind to the biorecognition element and was confirmed using atomic force microscopy. The AFM further provided clear height and surface roughness differences between the three samples. The bioconjugated secondary antibody was able to bind to the primary antibody on the biosensing surface, and further changed the refractive index of the surface. This resulted

Downloaded From: https://www.spiedigitallibrary.org/conference-proceedings-of-spie on 22 Mar 2023
Terms of Use: https://www.spiedigitallibrary.org/terms-of-use

in a redshift in the wavelength which enabled the distinction between the experiment, control, and reference samples. These findings pave a way for the future development of POC photonics-based biosensing platforms for TB diagnosis.

5. REFERENCES

[1] H. Inan, M. Poyraz, F. Inci, M.A. Lifson, M. Baday, B.T. Cunningham, U. Demirci, Photonic crystals: Emerging biosensors and their promise for point-of-care applications, Chem. Soc. Rev. 46 (2017) 366–388. https://doi.org/10.1039/c6cs00206d.

[2] S. Mittal, T. Sharma, M. Tiwari, Surface plasmon resonance based photonic crystal fiber biosensors: A review, Mater. Today Proc. 43 (2021) 3071–3074. https://doi.org/10.1016/j.matpr.2021.01.405.

[3] D. Gowdhami, V.R. Balaji, M. Murugan, S. Robinson, G. Hegde, Photonic crystal based biosensors: an overview, ISSS J. Micro Smart Syst. 11 (2022) 147–167. https://doi.org/10.1007/s41683-022-00092-x.

[4] D. Threm, Y. Nazirizadeh, M. Gerken, Photonic crystal biosensors towards on-chip integration, J. Biophotonics. 5 (2012) 601–616. https://doi.org/10.1002/jbio.201200039.

[5] G. Pitruzzello, T.F. Krauss, Photonic crystal resonances for sensing and imaging, J. Opt. (United Kingdom). 20 (2018). https://doi.org/10.1088/2040-8986/aac75b.

[6] Y. Zhao, X. Zhao, Z. Gu, Photonic crystals in bioassays, Adv. Funct. Mater. 20 (2010) 2970–2988. https://doi.org/10.1002/adfm.201000098.

[7] I.M. Efimov, N.A. Vanyushkin, A.H. Gevorgyan, Defected photonic crystal-based sensor with enhanced performance, (n.d.).

[8] D. Dorfner, T. Zabel, T. Hürlimann, N. Hauke, L. Frandsen, U. Rant, G. Abstreiter, J. Finley, Photonic crystal nanostructures for optical biosensing applications, Biosens. Bioelectron. 24 (2009) 3688–3692. https://doi.org/10.1016/j.bios.2009.05.014.

[9] A. Panda, P. Devi, N. Ayyanar, Investigation of transmission properties in defective one dimensional superconductive photonic crystal for ultralow level bioethanol detection, Optik (Stuttg). 245 (2021) 167733. https://doi.org/10.1016/j.ijleo.2021.167733.

[10] F. Bayat, S.A. Kandjani, H. Tajalli, Designing Real Time Biosensors and Chemical Sensors Based on Defective 1D Photonic Crystals, IEEE PHOTONICS Technol. 6 (2016). https://doi.org/10.1109/LPT.2016.2573852.

[11] N.R. Ramanujam, S.K. Patel, N.M. Reddy, S.A. Taya, D. Vigneswaran, M.S.M. Rajan, One-dimensional ring mirror-defect photonic crystal for detection of mycobacterium tuberculosis bacteria, Opt. - Int. J. Light Electron Opt. 219 (2020) 165097. https://doi.org/10.1016/j.ijleo.2020.165097.

[12] V.N. Konopsky, E. V. Alieva, Photonic crystal surface waves for optical biosensing, 2011 Int. Work. Biophotonics, BIOPHOTONICS 2011. 79 (2011) 4729–4735. https://doi.org/10.1109/IWBP.2011.5954807.

[13] E. Ozbay, I. Bulu, K. Aydin, Physics and applications of photonic crystals, 2 (2004) 87–95. https://doi.org/10.1016/j.photonics.2004.08.001.

[14] S.M. Shamah, B.T. Cunningham, Label-free cell-based assays using photonic crystal optical biosensors, Analyst. 136 (2011) 1090–1102. https://doi.org/10.1039/c0an00899k.

[15] S. Romano, A. Lamberti, M. Masullo, E. Penzo, S. Cabrini, I. Rendina, V. Mocella, Optical biosensors based on photonic crystals supporting bound states in the continuum, Materials (Basel). 11 (2018) 1–11. https://doi.org/10.3390/ma11040526.

[16] J. Divya, S. Selvendran, A. Sivanantha Raja, Photonic crystal-based optical biosensor: A brief investigation, Laser Phys. 28 (2018). https://doi.org/10.1088/1555-6611/aab7d2.

[17] B.T. Cunningham, M. Zhang, Y. Zhuo, L. Kwon, C. Race, Recent Advances in Biosensing with Photonic Crystal Surfaces: A Review, IEEE Sens. J. 16 (2016) 3349–3366. https://doi.org/10.1109/JSEN.2015.2429738.

Downloaded From: https://www.spiedigitallibrary.org/conference-proceedings-of-spie on 22 Mar 2023
Terms of Use: https://www.spiedigitallibrary.org/terms-of-use

[18] B. Suthar, Biosensor Application of One-Dimensional Photonic Crystal for Malaria Diagnosis, Plasmonics. (2020).

[19] J.H. Lee, B.C. Kim, B.K. Oh, J.W. Choi, Highly sensitive electrical detection of HIV-1 virus based on scanning tunneling microscopy, J. Nanosci. Nanotechnol. 15 (2015) 1117–1122. https://doi.org/10.1166/jnn.2015.9336.

[20] S.L. Manoto, A. El-Hussein, R. Malabi, L. Thobakgale, S. Ombinda-Lemboumba, Y.A. Attia, M.A. Kasem, P. Mthunzi-Kufa, Exploring optical spectroscopic techniques and nanomaterials for virus detection, Saudi J. Biol. Sci. 28 (2021) 78–89. https://doi.org/10.1016/j.sjbs.2020.08.034.

[21] C. Maphanga, S. Manoto, S. Ombinda-lemboumba, Y. Ismail, Localized surface plasmon resonance biosensing of Mycobacterium tuberculosis biomarker for TB diagnosis, Sens. Bio-Sensing Res. 39 (2023) 100545. https://doi.org/10.1016/j.sbsr.2022.100545.

[22] P.S. Parsamehr, M. Zahed, M.A. Tofighy, T. Mohammadi, M. Rezakazemi, Preparation of novel cross-linked graphene oxide membrane for desalination applications using (EDC and NHS)-activated graphene oxide and PEI, Desalination. 468 (2019) 114079. https://doi.org/10.1016/j.desal.2019.114079.

[23] X. Zhang, Plasmon extinguishment by bandedge shift identified as a second-order spectroscopic differentiation, Nanophotonics. 10 (2021) 1329–1335. https://doi.org/10.1515/nanoph-2020-0603.

[24] S. Link, M.A. El-Sayed, Optical Properties and Ultrafast Dynamics of Metallic Nanocrystals, Annu. Rev. Phys. Chem. 54 (2003) 331–366. https://doi.org/10.1146/annurev.physchem.54.011002.103759.

Downloaded From: https://www.spiedigitallibrary.org/conference-proceedings-of-spie on 22 Mar 2023
Terms of Use: https://www.spiedigitallibrary.org/terms-of-use

PROCEEDINGS OF SPIE

SPIEDigitalLibrary.org/conference-proceedings-of-spie

Surface plasmon resonance (SPR) based biosensor for mycobacterium tuberculosis diagnosis

Maphanga, Charles, Ombinda-Lemboumba, Saturnin, Manoto, Sello, Mthunzi-Kufa, Patience

Charles Maphanga, Saturnin Ombinda-Lemboumba, Sello Manoto, Patience Mthunzi-Kufa, "Surface plasmon resonance (SPR) based biosensor for mycobacterium tuberculosis diagnosis," Proc. SPIE 11651, Optical Diagnostics and Sensing XXI: Toward Point-of-Care Diagnostics, 1165103 (5 March 2021); doi: 10.1117/12.2578728

SPIE.

Event: SPIE BiOS, 2021, Online Only

Downloaded From: https://www.spiedigitallibrary.org/conference-proceedings-of-spie on 11 May 2021 Terms of Use: https://www.spiedigitallibrary.org/terms-of-use

Surface plasmon resonance (SPR) based biosensor for mycobacterium tuberculosis diagnosis

Charles Maphanga [1*], Saturnin Ombinda-Lemboumba [1,2], Sello Manoto [1], Patience Mthunzi-Kufa [1]

[1]Council for Scientific and Industrial Research, National Laser Centre, P O BOX 395, Pretoria, 0001, South Africa

[2]University of KwaZulu-Natal, H Block, Westville Campus, University Road, Westville, Durban, 3209

ABSTRACT

Recently, various nanomaterials have been used to develop nanotechnology-based rapid diagnostic tests. Due to their unique optical properties, gold nanoparticles (AuNPs) have been employed to design and develop modern biosensors for the rapid and real-time detection of various diseases or pathogen-specific biomolecules/markers, such as DNA, RNA, proteins, and whole cells. Optical biosensors offer great advantages over conventional analytical techniques. Specifically, they can provide multiple capabilities such as user-friendly operation, real-time analysis, rapid response, high sensitivity and specificity, portability, label-free detection and cost-effectiveness. As a result, this diagnostic approach possesses suitable features to develop point-of-care (POC) diagnostics and monitoring technologies. This study implemented the use of surface plasmon resonance (SPR) biosensing to monitor biomolecular interaction between biorecognition element covalently immobilized on a gold-coated glass substrate and an analyte. A custom-built Kretschmann configuration SPR optical biosensing setup was used to measure angle shift to monitor the biomolecular interaction events on the biosensing layer. To amplify the differences in SPR biosensing due to biomolecular binding events, AuNPs were used and successfully conjugated to the anti-TB antibodies and confirmed using ultraviolet–visible (UV-vis) spectroscopy. Mycolic acids were successfully immobilized on gold-coated substrates and were able to bind to the anti-TB antibodies that were introduced on the substrates, therefore enabling the detection of the captured anti-TB antibodies. As a result, mycolic acids have been realized to be efficient biomarkers to specifically react with anti-TB antibodies and produce a detectable signal for the purpose of TB diagnosis.

Keywords: Surface plasmon resonance (SPR), optical biosensing, gold nanoparticles, mycolic acid, *mycobacterium tuberculosis*, point-of-care.

*Corresponding author: CMaphanga@csir.co.za

Optical Diagnostics and Sensing XXI: Toward Point-of-Care Diagnostics, edited by Gerard L. Coté, Proc. of SPIE
Vol. 11651, 1165103 · © 2021 SPIE · CCC code: 1605-7422/21/$21 · doi: 10.1117/12.2578728

Downloaded From: https://www.spiedigitallibrary.org/conference-proceedings-of-spie on 11 May 2021
Terms of Use: https://www.spiedigitallibrary.org/terms-of-use

1. INTRODUCTION

Tuberculosis (TB) is the ninth global leading cause of death and a leading cause from a single infectious agent called *mycobacterium tuberculosis* (MTB), and is ranking above HIV/AIDS infections [1]. In 2016, there were an estimated 1.3 million TB deaths among HIV-positive co-infected people; an estimated 10.4 million people fell ill with TB [2]. Despite a slow decline in global TB rates, the progress in closing detection/diagnosis and treatment gaps is slow and big gaps still remain especially in Africa [1]. Regardless of the improvements in TB control program performance, active tuberculosis case detection rates in many regions remain at unacceptable levels [3]. Advances occurring during the last years in the diagnosis of TB have contributed to increased survival rates of patients, however limitations related to inefficiency of an early diagnosis still remains [4]. The general impact of any new diagnostic test for active TB disease or latent TB infection primarily depends on the extent of their uptake into national TB programs, affordability for the patient and the health system, the quality and durability of the diagnostic devices [3].

Currently, several TB diagnostic methods have been implemented and endorsed by the WHO for the diagnosis of TB, such as the tuberculin skin test (TST), sputum spear microscopy (SSM), TB culture, and various nucleic acid amplification tests (NAATs) [4,5]. The major limitations with these tests is they are expensive, requires specialised infrastructure and sophisticated equipment, trained personnel and therefore hinders TB diagnosis in low-resource settings [4,6]. For example, the TST is used for rapid TB screening; however it has high false positive results especially in individuals with prior Bacillus Calmette–Guérin (BCG) vaccination [5]. The SSM is a simple direct microscopy test used to identify MTB acid-fast bacilli and still remains the most commonly used test for TB diagnosis in resource-limited settings. It is affordable and can be done in basic laboratories at primary health-care clinics [7]. Unfortunately the SSM test lacks adequate sensitivity, cannot provide information on drug sensitivity testing (DST), and performs poorly in many TB patient subgroups, such as those who are unable to produce sputum or have low bacterial loads (i.e., children, HIV co-infected persons, and those with extrapulmonary disease) [5,8-9]. TB culture is considered the gold standard of diagnosing TB with relatively high sensitivity, and specificity. Although TB culture has reasonably acceptable detection rate, it requires specialised infrastructure, poses high risk on laboratory personnel and therefore requires highly trained staff to perform tests, and its major setback is turnaround time which may take 2 to 6 weeks to grow the mycobacteria [10]. To date, the recommended NAAT for rapid detection of TB and rifampicin resistance by WHO for all people suspected of having pulmonary TB is the Xpert MTB/RIF assay (Cepheid, Inc., Sunnyvale, CA, USA), nevertheless these test is costly [1,11-13].

For these reasons, WHO recognizes the need for new and more sensitive and specific techniques to improve early TB diagnosis such as point-of-care (POC) devices as an alternative to the conventional methods by offering significant advantages of portability, simplicity, and affordability [4]. Therefore, this study investigated the use of optical biosensors in particular surface plasmon resonance (SPR) for the diagnosis of TB through the detection of anti-TB antibodies using mycolic acid TB antigens immobilized on the biosensing surface gold-coated detection chip. SPR can be used to determine the presence biomolecular interactions and this relies on the evanescent field which is generated at the interface of the gold metal layer and a dielectric when a polarized light strikes under proper angle conditions [4,14]. This evanescent field is primarily dependent on the external media properties and its refractive index, hence small interactions occurring on the sensor surface resulting in a change in refractive index can be measured in real-time and makes it ideal for the development of POC devices [4].

Downloaded From: https://www.spiedigitallibrary.org/conference-proceedings-of-spie on 11 May 2021
Terms of Use: https://www.spiedigitallibrary.org/terms-of-use

2. MATERIALS AND METHODS

2.1 UV-vis absorption spectroscopy

The absorption spectra of the AuNPs before and after conjugation (TB bioconjugate) were recorded using the NanoDrop ND-1000 spectrophotometer. Several UV-vis spectra were recorded before and after conjugation.

2.2 SPR biosensing

2.2.1 The SPR setup

The custom-built Kretschmann configuration SPR setup (figure 1) used in this study consisted of a 627 nm light emitting diode (LED) with 5.8 mW total optical power as light source. The incident beam was passed through a neutral density (ND) filter, a half-wave plate and a polarizing beam splitter in order to control the power and also enable selection of the *p*-polarisation of the laser beam. The incident light from the LED was set to *p*-polarization. The light propagating from the polarizer was then focused and used to illuminate the gold-coated biosensing layer containing immobilised bio-recognition element and an analyte through the BK7 equilateral glass prism with a refractive index n = 1.517 to excite surface plasmons. The reflected beam was collected using a Watec charge-coupled device (CCD) camera attached to a computer for image acquisition. The CCD camera was used as a photodetector. The obtained images were analysed for mean intensity using ImageJ software.

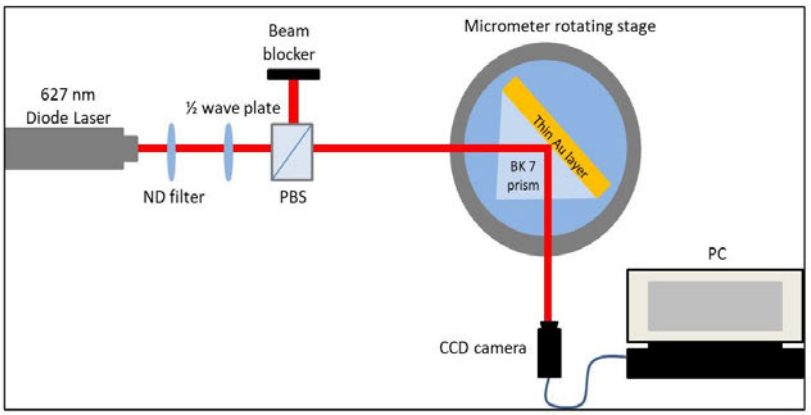

Figure 1: A schematic representation of the custom-built Kretschmann configuration surface plasmon resonance (SPR) optical biosensing setup using a CCD camera as a detector for intensity variation image analysis using ImageJ software.

2.2.2 Functionalization of the gold-coated biosensor chip

The gold-coated biosensor chip surface was washed with absolute ethanol and blow dried with N_2 gas prior to incubation with 10 mM cysteamine (Cys) (Sigma-Aldrich, M9768) in absolute ethanol for 18 hours at room temperature to form an Au-Cys monolayer (figure 2). NHS (N-hydroxysuccinimide) (Sigma-Aldrich, 56480) and EDC (1-Ethyl-3-(3-dimethylaminopropyl)-carbodiimide) (Sigma-Aldrich, E7750) with similar molar ratio were used for covalent attachment of stearic acid (STA) (Sigma-Aldrich, S4751) using carbodiimide coupling chemistry to form an amide bond. After the formation of the Cys-STA monolayer, the modified gold-coated surface was washed thoroughly with ethanol and water to remove physically adsorbed stearic acid species. Mycolic acid (MA) from *mycobacterium tuberculosis* (bovine strain)

Downloaded From: https://www.spiedigitallibrary.org/conference-proceedings-of-spie on 11 May 2021
Terms of Use: https://www.spiedigitallibrary.org/terms-of-use

(Sigma-Aldrich, M4537) TB antigens were immobilised on STA monolayer by incubating the biosensor chip in a solution of 0.5 mg/ml of MAs in hexane over night at room temperature. Post incubation the biosensor chip was rinsed thoroughly with 1x phosphate buffered saline (PBS) (Sigma-Aldrich, D1283) to remove physically adsorbed MA, and subsequently incubated in a solution of 1% bovine serum albumin (BSA) (Roche Diagnostics, 10711454001) blocking agent for an hour prior to addition of primary a*nti-mycobacterium tuberculosis antibody* (Abcam, ab905). To enhance the sensitivity of the biosensor chip, a secondary *goat anti-rabbit IgG H&L* antibody (Abcam, ab6702) was conjugated to gold nanoparticles (AuNPs) (Sigma-Aldrich, 797707) and herein called TB bioconjugate.

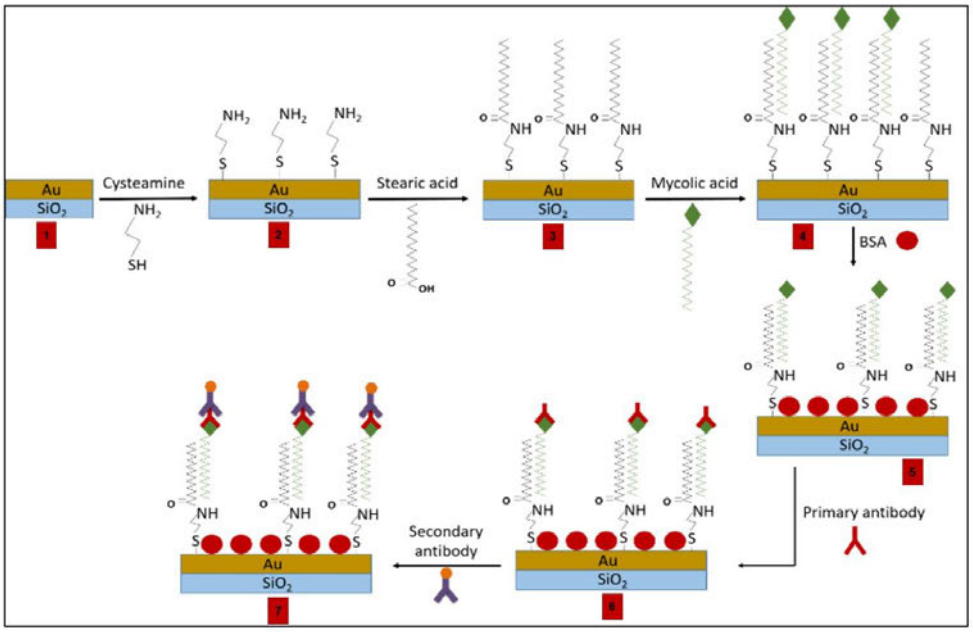

Figure 2: Schematic representation of the gold-coated biosensor chip developed in-house for TB diagnosis using immobilised mycolic acid antigens to capture anti-TB antibodies. Schematic key steps include the following: (1) thin gold coated slide, (2) immobilization of cysteamine monolayer on the gold coated surface, (3) covalent attachment of STA (stearic acid) to cysteamine and formation of amide bonds using NHS and EDC, (4) development of a self-assembled monolayer (SAM) of mycolic acid (MA) through inter-molecular forces existing between STA and MA, (5) introduction of 1% bovine serum albumin (BSA) to prevent non-specific binding of molecules, (6) binding of anti-TB primary antibody to MA, (7) binding of gold-conjugated secondary antibody to primary antibody.

NHS (N-hydroxysuccinimide) (Sigma-Aldrich, 56480) and EDC (1-Ethyl-3-(3-dimethylaminopropyl)-carbodiimide) (Sigma-Aldrich, E7750) with similar molar ratio were added to a heterobifunctional polyethylene glycol (SH-PEG-COOH) (Sigma-Aldrich, 757845) in ultrapure water and shaken for an hour on an orbital shaker. The pH of this reaction mixture was adjusted to 7.4 using 10x PBS and the *goat anti-rabbit IgG H&L* secondary antibody was added to the solution. The reaction mixture was incubated for an additional 2 hours before filtering with a 50kDA filter to remove any by-products. The final SH-PEG-IgG conjugated solution was obtained after washing with 1x PBS twice. From the SH-PEG-IgG mixture, 12µL was added to 200µL of AuNPs and incubated for an hour to form the TB bioconjugate confirmed using UV-vis spectroscopy.

Downloaded From: https://www.spiedigitallibrary.org/conference-proceedings-of-spie on 11 May 2021
Terms of Use: https://www.spiedigitallibrary.org/terms-of-use

3 RESULTS AND DISCUSSION

3.1 UV-vis absorption spectroscopy

UV-vis absorption spectroscopy was used to characterize AuNPs conjugated to the secondary antibody using covalent conjugation method (figure 3). EDC and NHS chemistry were used for covalent conjugation of the secondary antibody to polyethylene glycol (SH-PEG-COOH). EDC and NHS activate the carboxyl groups on the particle surface to form an intermediate that can subsequently react with primary amine groups on the antibody. Figure 3 shows UV-vis spectra of AuNPs before and after conjugation. The LSPR of the AuNPs was observed at 645.5 nm wavelength and the TB bioconjugate at 652 nm. The spectra show a 6.5 nm red shift and a reduction in the absorption intensity after conjugation of AuNPs to the secondary antibody. Bioconjugation occurs upon successful binding of the antibody to the AuNPs surface, thus resulting in localized surface plasmon resonance (LSPR) red-shift in the spectrum which is an increase in wavelength by a few nanometres [15].

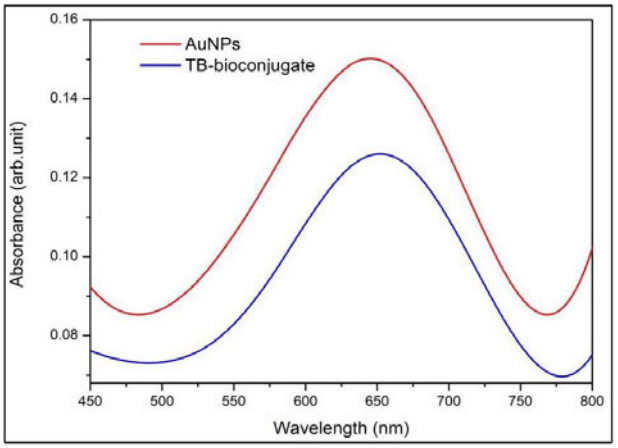

Figure 3: UV-vis absorption spectra of AuNPs before and after covalent conjugation with secondary antibody. The TB bioconjugate consists of AuNPs covalently attached to secondary antibody through PEG, NHS and EDC.

AuNPs have unique optical properties that can be easily manipulated compared to bulk gold. These special characteristics provide a variety of advantages especially in biosensing. One of the major attributes is the interchange of light with electrons on its exterior [10]. AuNPs optical properties also depend on the refractive index near the nanoparticle surface. As the refractive index near the nanoparticle surface increases, the AuNPs spectrum shifts to longer wavelengths known as a red shift. A shift to longer wavelengths and broadening of the LSPR peak is observed as the size of NPs increases and as the distance between particles decreases due to aggregation [17].

3.2 SPR biosensing

SPR was used to study the molecular binding interactions on the biosensing surface of the biosensor chip between immobilised MA TB antigens and anti-TB antibodies. SPR biosensing was successfully performed on the Kretschmann configuration custom-built setup. Figure 4 show images of PBS, AuNPs, TB bioconjugate, first (D1) and second (D2) serial dilutions of the TB bioconjugate as analytes on the biosensor chip taken at various incident angle (45° - 60°). Each picture indicates the intensity of the sample surface at a specified incident angle. A CCD camera was able to capture images at the various incident angles. The images we processed with ImageJ software for mean intensity. The SPR

Downloaded From: https://www.spiedigitallibrary.org/conference-proceedings-of-spie on 11 May 2021
Terms of Use: https://www.spiedigitallibrary.org/terms-of-use

biosensing spectra were represented as the intensity variation of the reflected light at various incident angles for each analyte (figure 5).

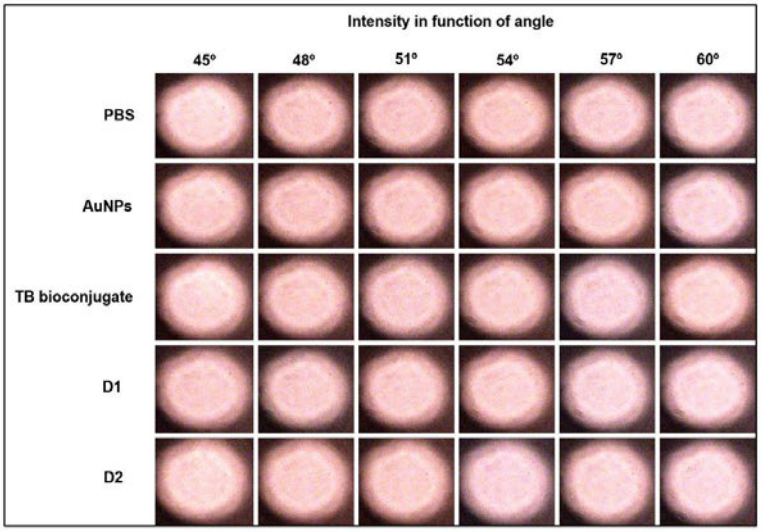

Figure 4: SPR images of the biosensor chip for TB detection as seen from the CCD camera. The biosensing layer consisted of SAM of mycolic acid TB antigens and primary anti-TB antibodies. Analytes included PBS, AuNPs, TB bioconjugate which consisted of conjugated AuNPs with secondary antibody, first (D1) and second (D2) serial dilutions of the TB bioconjugate. The analytes were washed off and the biosensor chip was dried with N_2 gas prior to SPR biosensing image acquisition.

Figure 5 shows the results of SPR biosensing using the custom-built Kretschmann configuration optical setup. Five sample reactions as analytes where prepared on a biosensor chip coated with primary anti-TB antibodies immobilised on a MA SAM monolayer. Analytes included PBS, AuNPs, TB bioconjugate, serial dilution 1 (D1) and 2 (D2) of the bioconjugate.

Downloaded From: https://www.spiedigitallibrary.org/conference-proceedings-of-spie on 11 May 2021
Terms of Use: https://www.spiedigitallibrary.org/terms-of-use

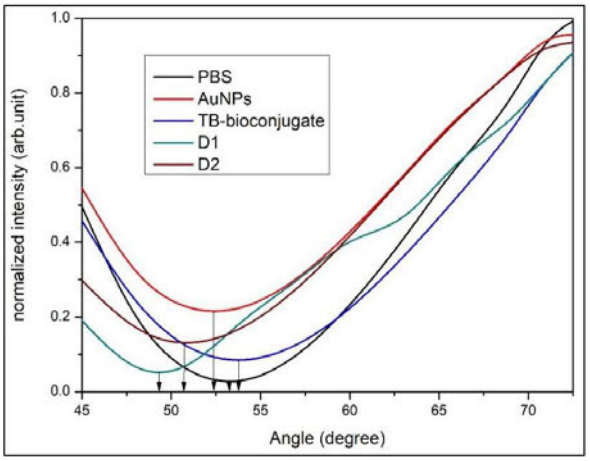

Figure 5: SPR biosensing spectra of PBS, AuNPs, TB bioconjugate, D1 and D2 analytes. The spectra are a representation of the recorded data images processed by ImageJ software as intensity variation of the reflected light at various incident angles for each analyte.

The SPR resonance angle for PBS or AuNPs could both serve as the background. PBS and AuNPs are the only two analytes which had no complementary binding species on the biosensing surface; however the TB bioconjugate and its serial dilutions (D1 and D2) chemically reacted to the primary antibody on the biosensing surface. Therefore Resonance angle of the TB bioconjugate, D1 and D2 could be subtracted from either PBS or AuNPs as background on the spectra. There were significant angular shifts observed between the five analytes. PBS was detected at SPR resonance angle of 53.23°, AuNPs at 52.38°, TB bioconjugate at 53.77°, D1 at 49.31, and D2 at 50.74°. A 0.54° shift was observed between PBS and TB bioconjugate, 3.92° between PBS and D1, and 2.49° angle shift between PBS and D2. The detected angular shifts are a result of changes in the refractive index on the biosensing surface and are of diagnostic significance for TB. However, the shifts were not consistent and further optimization of the biosensor chip and/or data analysis will be explored.

4 CONCLUSION

In conclusion, the biosensor chip was successfully fabricated and MA TB antigens SAM was formed on the biosensing surface and used to detect anti-TB antibodies. To enhance the sensitivity on the biosensing surface, AuNPs were covalently conjugated to secondary antibody and a red shift was detected using UV-vis absorbance spectroscopy. SPR was successful in detecting angular shifts between various analytes while varying the incident angle at a fixed wavelength of 627 nm. The shifts were not consistent and therefore further optimization of the system and/or data analysis will be explored in future studies.

5 REFERENCES

[1] WHO. (2017). *TB Report 2017*. https://doi.org/10.1001/jama.2014.11450
[2] WHO. (2018). *Global WHO report on tuberculosis 2018*.
[3] McNerney, R., Maeurer, M., Abubakar, I., Marais, B., McHugh, T. D., Ford, N., Zumla, A. (2012). Tuberculosis diagnostics and biomarkers: Needs, challenges, recent advances, and opportunities. *Journal of*

Downloaded From: https://www.spiedigitallibrary.org/conference-proceedings-of-spie on 11 May 2021
Terms of Use: https://www.spiedigitallibrary.org/terms-of-use

Infectious Diseases, *205*(SUPPL. 2), 147–158. https://doi.org/10.1093/infdis/jir860
[4] Pelaez, E. C., Estévez, M. C., Mongui, A., Menendez, M., Toro, C., Herrera-sandoval, O. L., Lechuga, L. M. (2020). *Detection and quantification of HspX antigen in sputum samples using plasmonic biosensing : toward a real Point-of-Care (POC) for tuberculosis diagnosis*. https://doi.org/10.1021/acsinfecdis.9b00502
[5] Huddart, S., Nash, M., & Pai, M. (2017). Tuberculosis diagnosis: Challenges and solutions. *Journal of Health Specialties*, *4*(4), 230. https://doi.org/10.4103/2468-6360.191903
[6] Hsieh, S., Chang, C., Lu, C., Wei, C., Lin, C., Lai, H., & Lin, C. (2012). Rapid identification of Mycobacterium tuberculosis infection by a new array format-based surface plasmon resonance method. *Nanoscale Research Letters*, *7*(1), 180. https://doi.org/10.1186/1556-276X-7-180
[7] Walzl, G., McNerney, R., du Plessis, N., Bates, M., McHugh, T. D., Chegou, N. N., & Zumla, A. (2018). Tuberculosis: advances and challenges in development of new diagnostics and biomarkers. *The Lancet Infectious Diseases*, *18*(7), e199–e210. https://doi.org/10.1016/S1473-3099(18)30111-7
[8] Ciach, T. (2018). *Sensors and Actuators B : Chemical Detection of tuberculosis in patients with the use of portable SPR device*. *260*, 786–792. https://doi.org/10.1016/j.snb.2017.12.183
[9] Wood, A., Barizuddin, S., Darr, C. M., Mathai, C. J., Ball, A., Minch, K., Gangopadhyay, S. (2019). *Ultrasensitive detection of lipoarabinomannan with plasmonic grating biosensors in clinical samples of HIV negative patients with tuberculosis*. 1–12.
[10] Singh, S., Sharma, P., Chaudhary, V., Chopra, K., Dey, B., Sachdeva, K., … Katoch, V. (2015). Challenges in tuberculosis diagnosis and management: Recommendations of the expert panel. *Journal of Laboratory Physicians*, *7*(1), 1. https://doi.org/10.4103/0974-2727.154778
[11] Churchyard, G. J., Mametja, L. D., Mvusi, L., Ndjeka, N., Hesseling, A. C., Reid, A., Pillay, Y. (2014). Tuberculosis control in South Africa: Successes, challenges and recommendations. *South African Medical Journal*, *104*(3), 244–248. https://doi.org/10.7196/SAMJ.7689
[12] Erasmus, L. K., Ndjeka, N. O., Vassall, A., Fielding, K. L., Mametja, L. D., Stevens, W. S., Nicol, M. P. (2015). Xpert MTB/RIF versus sputum microscopy as the initial diagnostic test for tuberculosis: a cluster-randomised trial embedded in South African roll-out of Xpert MTB/RIF. *The Lancet Global Health*, *3*(8), e450–e457. https://doi.org/10.1016/s2214-109x(15)00100-x
[13] Vassall, A., Siapka, M., Foster, N., Cunnama, L., Ramma, L., Fielding, K., Sinanovic, E. (2017). Cost-effectiveness of Xpert MTB/RIF for tuberculosis diagnosis in South Africa: a real-world cost analysis and economic evaluation. *The Lancet Global Health*, *5*(7), e710–e719. https://doi.org/10.1016/S2214-109X(17)30205-X
[14] He, X., Zhou, L., He, D., Wang, K., & Qin, D. (2011). Biosensing technologies for mycobacterium tuberculosis detection: Status and new developments. *Clinical and Developmental Immunology*, *2011*. https://doi.org/10.1155/2011/193963
[15] Oliveira, J. P., Prado, A. R., Keijok, W. J., Wagnner, P., Antunes, P., Yapuchura, E. R., Guimarães, C. (2019). *Impact of conjugation strategies for targeting of antibodies in gold nanoparticles for ultrasensitive detection of 17 β -estradiol*. (September), 1–8. https://doi.org/10.1038/s41598-019-50424-5
[16] Huang, X., El-sayed, M. A. (2010). *Gold nanoparticles : Optical properties and implementations in cancer diagnosis and photothermal therapy*. 13–28. https://doi.org/10.1016/j.jare.2010.02.002
[17] Zuber, A., Purdey, M., Schartner, E., Forbes, C., Hoek, B. Van Der, Giles, D., Monro, T. (2016). Sensors and Actuators B : Chemical Detection of gold nanoparticles with different sizes using absorption and fluorescence based method. *Sensors & Actuators: B. Chemical*, *227*, 117–127. https://doi.org/10.1016/j.snb.2015.12.044

Downloaded From: https://www.spiedigitallibrary.org/conference-proceedings-of-spie on 11 May 2021
Terms of Use: https://www.spiedigitallibrary.org/terms-of-use

PROCEEDINGS OF SPIE

SPIEDigitalLibrary.org/conference-proceedings-of-spie

Detection of mycobacterium tuberculosis using gold nanoparticles conjugated to TB antibodies

Maphanga, Charles, Manoto, Sello, Ombinda-Lemboumba, Saturnin, Mthunzi-Kufa, Patience

Charles Maphanga, Sello Manoto, Saturnin Ombinda-Lemboumba, Patience Mthunzi-Kufa, "Detection of mycobacterium tuberculosis using gold nanoparticles conjugated to TB antibodies," Proc. SPIE 11651, Optical Diagnostics and Sensing XXI: Toward Point-of-Care Diagnostics, 116510X (5 March 2021); doi: 10.1117/12.2578789

SPIE.

Event: SPIE BiOS, 2021, Online Only

Downloaded From: https://www.spiedigitallibrary.org/conference-proceedings-of-spie on 11 May 2021 Terms of Use: https://www.spiedigitallibrary.org/terms-of-use

Detection of mycobacterium tuberculosis using gold nanoparticles conjugated to TB antibodies

Charles Maphanga [1*], Sello Manoto [1], Saturnin Ombinda-Lemboumba [1], Patience Mthunzi-Kufa [1,2]

[1]Council for Scientific and Industrial Research, National Laser Centre, P O BOX 395, Pretoria, 0001, South Africa

[2]University of KwaZulu-Natal, H Block, Westville Campus, University Road, Westville, Durban, 3209

ABSTRACT

In recent years, conjugated nanoparticles have gained significant applications in diagnostics, particularly gold nanoparticles (AuNPs). When functionalized with antibodies, AuNPs can selectively interact with cells and biomolecules. The conjugation of biomolecules to AuNPs has been achieved using a variety of techniques, one such approach is the covalent coupling method used in the current study. Generally, in diagnostics, the conjugation of different moieties such as antibodies to the AuNPs widens their applications and provides them with new or enhanced properties. Due to their high specificity and diversity, antibodies are widely used to provide specificity and bioactivity to AuNPs, particularly for biosensor applications. Localized surface plasmon resonance (LSPR) has emerged as a leader among label-free biosensing techniques because it offers sensitive, robust, and rapid detection of biological analytes. Biomolecular adsorptions on AuNPs surface increases the dielectric constant and change the intensities and the wavelengths of the LSPR band associated with AuNPs. As a result, the adsorptions of biomolecules onto surfaces of this AuNPs can be monitored by measuring the absorption spectra of the AuNPs. In this study, TB antibodies were covalently conjugated to AuNPs and used to detect mycolic acid TB antigens at various concentrations. Characterization of the AuNPs was done using transmission electron microscopy (TEM) while the biomolecular interaction between TB antibodies and the antigen was measured using LSPR. From our findings, it was realised that the use of antibody-conjugated AuNPs enhanced the detection of the analyte even at low concentrations of the analyte.

Keywords: Localized surface plasmon resonance (LSPR), gold nanoparticles (AuNPs), biosensing, mycolic acid, *mycobacterium tuberculosis.*

*Corresponding author: CMaphanga@csir.co.za

Optical Diagnostics and Sensing XXI: Toward Point-of-Care Diagnostics, edited by Gerard L. Coté, Proc. of SPIE
Vol. 11651, 116510X · © 2021 SPIE · CCC code: 1605-7422/21/$21 · doi: 10.1117/12.2578789

Downloaded From: https://www.spiedigitallibrary.org/conference-proceedings-of-spie on 11 May 2021
Terms of Use: https://www.spiedigitallibrary.org/terms-of-use

1. INTRODUCTION

Tuberculosis (TB) is one of the world's deadliest infectious diseases caused by infection with *mycobacterium tuberculosis* (MTB) [1]. It is a bacterial disease and typically affects the lungs as pulmonary TB; however it can also cause severe meningitis and extrapulmonary infections such as disseminated acute TB, spinal, abdominal, and pericardial forms of the illness [2]. TB infections remain a worldwide major public health problem especially in developing and some industrialized countries associated with high rates of morbidity and mortality. According to the World Health Organisation (WHO), one-third (~2 billion) of the world population is latently infected with TB with more than 9 million new infections annually [1]. TB is transmitted by aerosols released from the upper respiratory tract of an infected individual to a healthy one, hence early detection of the pathogen is crucial and will subsequently reduce the interval between active infection and treatment initiation [3]. When TB occurs in combination with other serious infections such as HIV it can severely compromise the host immune system and complicate effective forms of therapy [2]. Currently, TB can be diagnosed in several ways including tuberculin skin test, sputum smear microscopy, culture-based techniques, immunological methods, rapid molecular tests, as well as the use of chest X-ray and CT scans [2]. All of these tests have limitations, for instance tuberculin skin test is one of the most used TB screening test but has low specificity. Culture-based techniques considered the gold standard method for TB diagnosis is time consuming, taking up to 4 – 8 weeks [4]. Although more recently developed nucleic acid amplification tests (NAATs) such as the Xpert MTB/RIF assay and line probe assays (LPAs) as well as MIRU-VNTR genotyping methods have been able to provide rapid and sensitive diagnosis and accuracy of approximately 92 – 95%. However, they are costly, require bulky instruments and specialised infrastructure with skilled technicians [3]. It is therefore important to develop new methods of diagnosing TB, and ideally the test should be sensitive, accurate, cost-effective, and built on an analytical platform that is easy to use [2].

Localized surface plasmon resonance (LSPR) method has emerged as a leader among label-free biosensing techniques offering real-time, robust, precise and high-sensitivity detection [5,6]. It is an optical phenomenon caused by the interaction of incident photons and metallic nanoparticles [7]. It is also a surface plasmon resonance (SPR) phenomenon existing in metallic nanoparticles instead of thin film metals [8]. During LSPR biosensing, the incident light induces collective oscillations of valence electrons, subsequently increasing the intensity of the electric field at the sensor and creating a characteristic extinction peak at the plasmonic resonance frequency. LSPR biosensors differ from SPR-based biosensors as the induced plasmons oscillate locally around the metallic nanoparticle instead of propagating along the metal-dielectric interface [7,9]. Upon analyte attachment to the nanoparticle, the refractive index change causes a wavelength shift in the extinction spectrum, thus making LSPR platform suitable for label-free detection and quantification of biorecognition events [9]. During LSPR biosensing, changes in refractive index of the surrounding media enables application of this method in biosensing, chemical sensing and gas sensing [10]. In biosensing, LSPR sensors can monitor a variety of binding events including protein-ligand interactions, deoxyribonucleic acid (DNA) hybridizations, and biomarker interactions [11]. When binding events occur, changes in LSPR properties manifesting as a shift in the extinction peak can be easily measured by ultraviolet-visible (UV-vis) spectroscopy [11].

The use of noble metal nanoparticles in biosensing has grown immensely in recent years. Several elements have been demonstrated to support localized surface plasmons, including palladium (Pd), platinum (Pt), silver (Ag) and gold (Au). Both Ag and Au nanostructures are intensely researched for their role in biosensing, with their popularity stemming from their high refractive index sensitivity values. Gold is 44 nm/refractive index units (RIU) and Ag is 161 nm/RIU, and although Au has a lower sensitivity than Ag nanostructures they are mostly preferred for biosensing applications due to their lower toxicity to biological material and being prone to less oxidation [7].

FTIR spectroscopy is one of the most powerful techniques used for structural and spectral recognition of biological materials and their interactions [12]. It is a technique used to obtain an infrared spectrum of absorption or emission of a solid, liquid or gas. It detects biochemical compositions including proteins, lipids, nucleic acids and carbohydrates within biological samples by specifically identifying molecular conformations, bonding types, functional groups and intermolecular interactions of the sample under study [13,14]. FTIR Spectroscopy relies on the fact that the most biological material absorb light in the mid infra-red (IR) region (4000 – 400 cm^{-1}) of the electromagnetic spectrum [14-16]. The region of significant interest is between 1800 and 900 cm^{-1} and is called the biofingerprint region because it provides a large amount of information and representation of the composition of samples under study based on the vibrational modes of chemical bonds [16]. Other spectral regions of interest include amide I and II region (1700 – 1500 cm^{-1}), higher-wavenumber regions (3500 – 2550 cm^{-1}) associated with stretching vibrations including C-H, O-H, N-H, and S-H, while lower-wavenumber regions are associated with bending and skeletal fingerprint vibrations [14].

Downloaded From: https://www.spiedigitallibrary.org/conference-proceedings-of-spie on 11 May 2021
Terms of Use: https://www.spiedigitallibrary.org/terms-of-use

In this study, gold nanoparticles (AuNPs) were conjugated to anti-TB antibodies using both physical and covalent conjugation techniques to detect mycolic acid TB antigens at different concentrations using UV-vis spectroscopy and Fourier-transform infrared (FTIR) spectroscopy. Physical adsorption or direct conjugation relies on electrostatic interactions between the antibody and the AuNP, whereas covalent conjugation uses chemical linkers that react with specific chemical groups on the molecule to be conjugated [17]. Spectroscopy is a technique used to measure the interaction of molecules with electromagnetic radiation [18]. Light in the near-ultraviolet (UV) and visible (vis) range of the electromagnetic spectrum has an energy of about 150 - 400 kJ mol^{-1} [19]. This energy promotes electrons from the ground state to an excited state. A spectrum is obtained when the absorption of light is measured as a function of its frequency or wavelength [19]. Molecules with electrons in delocalized aromatic systems often absorb light in the near-UV (150–400 nm) or the visible (400–800 nm) region [20]. Spectroscopic measurements are very sensitive and non-destructive, and only require small amounts of sample for analysis [19]. Absorption spectroscopy is therefore an excellent technique for analysing amongst others ligand-binding reactions such as antibody-antigen binding reactions applied in our study. The obtained results show that LSPR and FTIR were able to detect differences between AuNPs before and after conjugation with anti-TB antibodies. New peaks were also observed on the FTIR spectra upon introduction of the mycolic acid TB analyte.

2. MATERIALS AND METHODS

2.1 Characterization of AuNPs

Gold nanourchins were characterized using TEM to study their morphology and size. The characterized AuNPs were subsequently used for covalent and physical conjugation with anti-TB antibodies.

2.2 UV-vis spectroscopy

2.2.1 Covalent coupling of antibodies to AuNPs

NHS (N-hydroxysuccinimide) (Sigma-Aldrich, 56480) and EDC (1-Ethyl-3-(3-dimethylaminopropyl)-carbodiimide) (Sigma-Aldrich, E7750) with similar molar ratio were added to a heterobifunctional polyethylene glycol (SH-PEG-COOH) (Sigma-Aldrich, 757845) in ultrapure water and shaken for an hour. The pH of this reaction mixture was adjusted to 7.4 using 10x phosphate buffered saline (PBS) and the *anti-mycobacterium tuberculosis antibody* was added to the solution. The reaction mixture was further incubated for 2 hours before filtering with a 50 kDA filter to remove any by-products. The final SH-PEG-IgG conjugated solution was obtained after washing with 1x PBS twice. Then, 12µL of the SH-PEG-IgG conjugate was added to 200µL of AuNPs and incubated for an hour to form AuNPs-IgG conjugate confirmed using NanoDrop ND-1000 spectrophotometer.

2.2.2 Direct conjugation of antibodies by electrostatic attraction

Anti-mycobacterium tuberculosis antibody (Abcam, ab 905) was added to AuNPs (Sigma-Aldrich, 797707). The mixture was wrapped in foil and incubated on a shaking incubator at room temperature for 30 minutes (min) to form AuNPs-IgG bioconjugate. Mycolic acid from *mycobacterium tuberculosis* (bovine strain) (Sigma-Aldrich, M4537) TB antigen analyte were prepared in hexane. Serial dilutions of the analyte were prepared and introduced to the bioconjugate.

In order to verify the applicability of the bioconjugates as well as their differences in diagnostic assays, both bioconjugates produced by the two conjugation strategies were evaluated using NanoDrop spectrophotometer. The absorption spectra of the AuNPs were recorded before and after conjugation. Absorbance spectra of mycolic acid TB antigen as the analyte were recorded at different concentrations. Origin Pro software was used to plot the acquired data.

Downloaded From: https://www.spiedigitallibrary.org/conference-proceedings-of-spie on 11 May 2021
Terms of Use: https://www.spiedigitallibrary.org/terms-of-use

2.3 Fourier-transform infrared (FTIR) spectroscopy

FTIR measurements were obtained on a Perkin Elmer Spectrum 100 FTIR spectrometer equipped with a DTGS detector. The spectra were measured in the 4000 to 550 cm^{-1} wavenumber region. Prior to data acquisition, the spectrometer plate and crystal were thoroughly cleaned with tissue and iso-propanol, and also cleaned in between sample analysis. The spectrum of air was used as background before each sample analysis. The background and sample spectra were taken in a room with temperature around 21 - 23°C, at a spectral resolution of 4 cm^{-1} and to each measurement 32 scans were performed. The original FTIR spectra were baseline corrected using Perkin Elmer Spectrum software.

3. RESULTS AND DISCUSSION

3.1 Characterization of AuNPs

The morphology and size of AuNPs functionalized with anti-TB antibodies were evaluated. Figure 1 shows the TEM image of bare AuNPs used in this study. Under TEM analysis, the AuNPs appeared multibranched with spiky uneven surfaces. This is a typical characteristic of gold nanourchins. The AuNPs had an average size of 90 nm. The spikes found in this type of AuNPs causes a red shift in the surface plasmon peak and a larger enhancement of the electromagnetic field at the tips of the spikes compared to spherical nanoparticles.

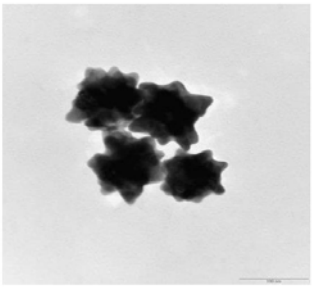

Figure 1: Transmission electron microscope image of gold nanourchins nanoparticles. The AuNPs were an average size of 90 nm, and displayed a multibranched shape with a spiky uneven surface.

3.2 UV-vis absorption spectroscopy

UV-vis absorption spectroscopy was used to characterize AuNPs conjugated to anti-TB antibodies using the covalent conjugation method (figure 2) and the direct conjugation method (figure 3) in the presence and absence of the mycolic acid TB antigen. In this study we used EDC and NHS chemistry bioconjugation for covalent coupling of anti-TB antibodies to polyethylene glycol (SH-PEG-COOH). EDC and NHS activate the carboxyl groups on the particle surface to form an intermediate that can subsequently react with primary amine groups on the specific antibody. Bioconjugation occurs upon successful binding of the monoclonal antibodies to the AuNPs surface, thus resulting in LSPR spectrum red-shift that is an increase in wavelength by a few nanometres [17]. Figure 2 and 3 show UV-vis spectrum of AuNPs, AuNPs conjugated to anti-TB antibodies (TB bioconjugate), the TB bioconjugate with mycolic acid TB antigen at different concentrations of 0.5mg/ml (sample 1), 0.06mg/ml (sample 2) and 0.008mg/ml (sample 3).

Downloaded From: https://www.spiedigitallibrary.org/conference-proceedings-of-spie on 11 May 2021
Terms of Use: https://www.spiedigitallibrary.org/terms-of-use

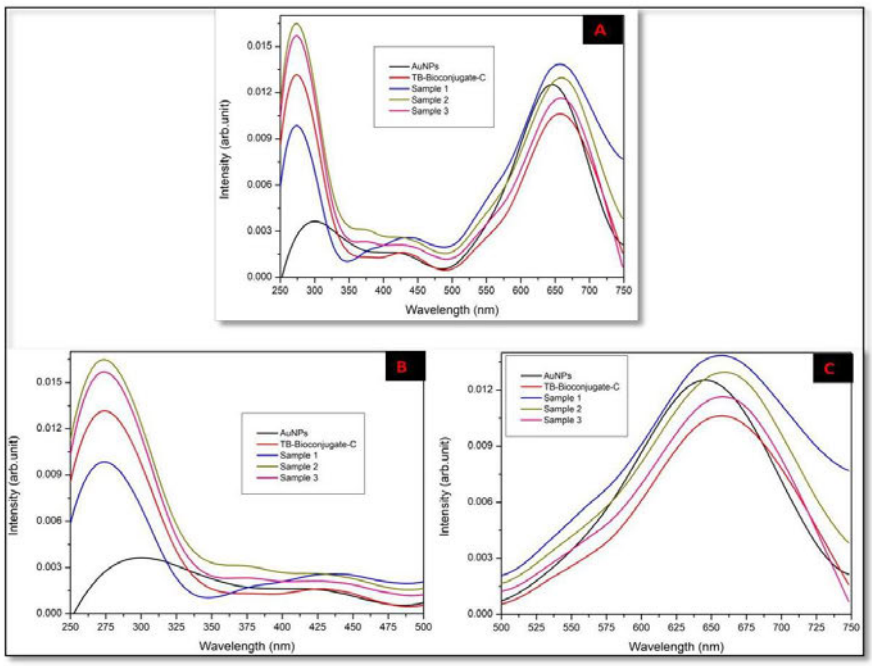

Figure 2: Absorption spectra of AuNPs covalently conjugated with TB antibody in the presence of mycolic acid at different concentrations. Sample 1 consists of the bioconjugate and 0.5mg/ml of mycolic acid, while sample 2 and 3 consists of 0.06mg/ml and 0.008mg/ml of mycolic acid respectively.

The absorption spectra around 280nm region on figure 2A and 3A indicate the behaviour of the bioconjugated anti-TB antibodies. The absorbance of UV radiation by intrinsic chromophores is a commonly used method, particularly useful is absorbance at 280 nm (A_{280}), which offers high specificity, as it arises strictly from tryptophan and tyrosine residues. Thus, the molar absorptivity for a protein at 280 nm can be accurately estimated directly from its amino acid sequence [21]. In our study, a decline at a wavelength around 280nm was observed with a decrease in the concentration of the TB antigen analyte (figure 2B and 3B).

Downloaded From: https://www.spiedigitallibrary.org/conference-proceedings-of-spie on 11 May 2021
Terms of Use: https://www.spiedigitallibrary.org/terms-of-use

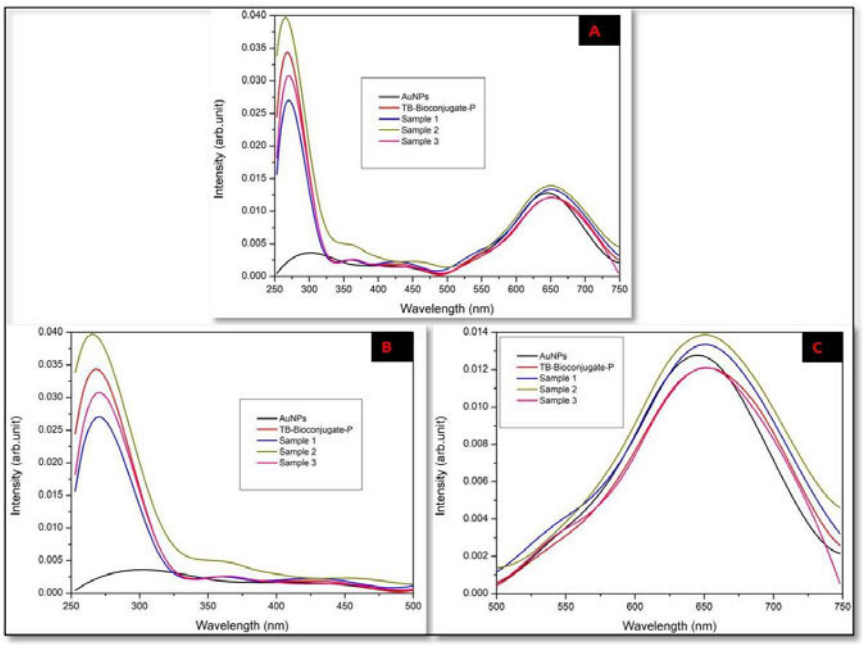

Figure 3: Absorption spectra of AuNPs physically conjugated with TB antibody in the presence of mycolic acid at different concentrations. Sample 1 consists of the bioconjugate and 0.5mg/ml of mycolic acid, while sample 2 and 3 consists of 0.06mg/ml and 0.008mg/ml of mycolic acid respectively.

The AuNPs showed their characteristic plasmony peak at a wavelength of 646nm and after bioconjugation with anti-TB antibody there was a red shift in the wavelength. The red shift observed in this study was 12nm for covalent coupling of anti-TB antibodies (figure 2C) and 6nm for direct conjugation of antibodies by electrostatic attraction (figure 3C). A red shift is a result of increased amounts of organic molecules anchored to the surface of the AuNP [17]. The red shift is attributed to the fact that the antibody replaces the negative charge citrate capping on the surface of citrate stabilized colloidal gold nanoparticles [17]. Sample 1 containing the highest concentration of the analyte showed the highest absorption intensity and sample 3 containing the lowest concentration of the analyte showed the lowest absorption intensity of the analytes. A red shift was clearly observed when the AuNPs spectra were compared to the bioconjugate and the samples containing the analyte.

3.3 Fourier-transform infrared spectroscopy

FTIR was carried out to identify the possible biomolecules involved in the bioconjugation of AuNPs with anti-TB antibodies and the introduction of mycolic acid analyte. To analyse the molecular bonds formed between the AuNPs, anti-TB antibody and the analyte, we performed FTIR using a sample of AuNPs, physical and covalent bioconjugates only, and the bioconjugates containing the highest concentration of the analyte (0.5mg/ml). Since mycolic acids are unique long chain fatty acids found in the lipid-rich cell walls of mycobacteria, we were expecting to detect fatty acids or lipid bands from the FTIR spectra. In our study we used the same liquid samples used for UV-vis spectroscopy to perform FTIR spectroscopy. Figure 4 and 5 shows FTIR spectra of covalent and physical adsorption bioconjugation. The

Downloaded From: https://www.spiedigitallibrary.org/conference-proceedings-of-spie on 11 May 2021
Terms of Use: https://www.spiedigitallibrary.org/terms-of-use

spectra were the same for both methods of bioconjugation; however the representation of fatty acid peaks is not very prominent on figure 4 yet prominent and broad on figure 5.

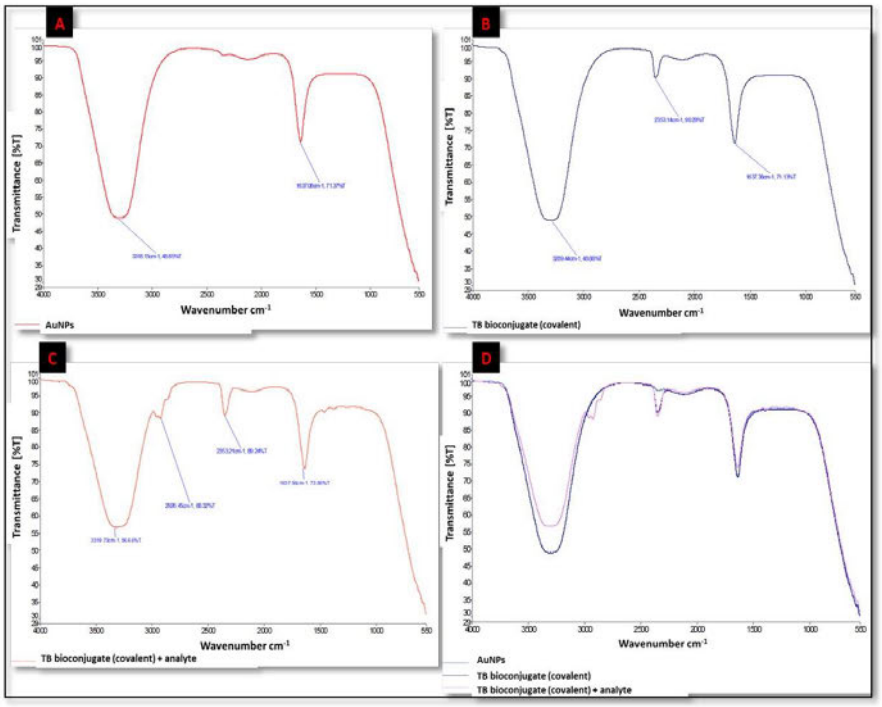

Figure 4: FTIR spectra of AuNPs (A), covalently attached TB bioconjugate (B), the bioconjugate in the presence of the analyte (mycolic acid, 0.5mg/ml) (C), and (D) is the merged comparison of the three spectra.

Figure 4A shows the AuNPs FTIR spectrum with two intense bands at 3318 cm^{-1} and 1637 cm^{-1}, and a less prominent peak at 2352 cm^{-1}. Since we used an aqueous sample, the intense broad band present in all samples at 3318 cm^{-1} on figure 4A, 3289 cm^{-1} on figure 4B and 3319 cm^{-1} was due to stretching and bending of O-H groups in water. The second intense band at 1637 cm^{-1} noted in all samples was caused by O-H-O scissors bending in water. Further, a smaller band located at 2353 cm^{-1} is present in all samples but not so prominent on the spectrum of AuNPs however becomes more prominent with the introduction of anti-TB antibodies and mycolic acid TB antigens on the surface of the metallic nanoparticles. This band is the result of coupling of scissors-bending and the broad band in the near-infrared region [22]. The band at 2926 cm^{-1} corresponds to asymmetric stretching of CH_2 in fatty acids [2]. And therefore FTIR was success in detecting the bioconjugation of anti-TB antibodies to AuNPs.

Downloaded From: https://www.spiedigitallibrary.org/conference-proceedings-of-spie on 11 May 2021
Terms of Use: https://www.spiedigitallibrary.org/terms-of-use

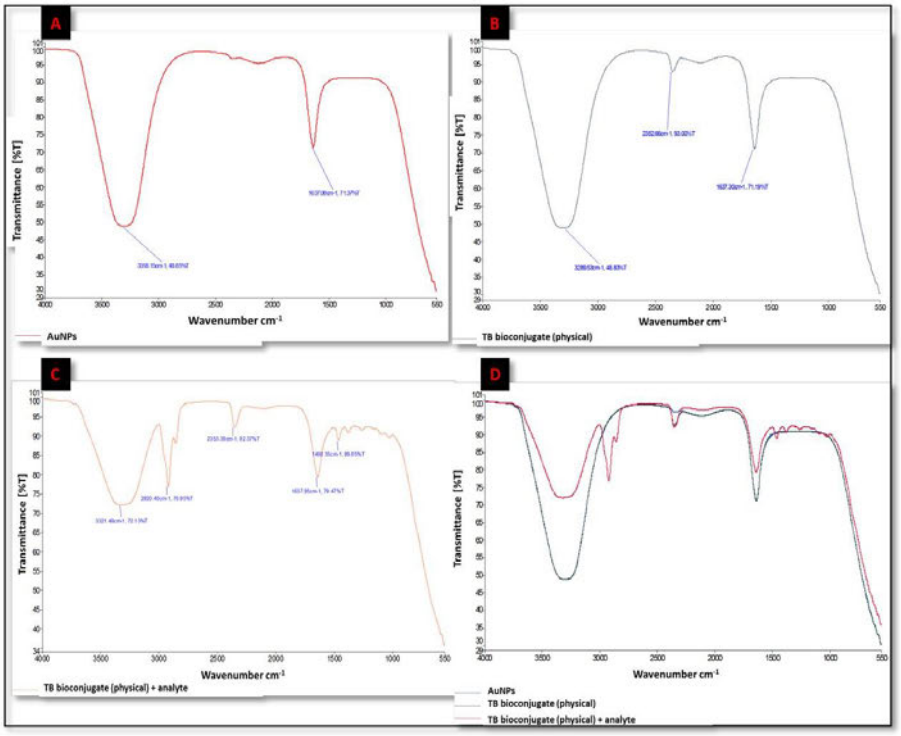

Figure 5: FTIR spectra of AuNPs (A), physically adsorbed TB bioconjugate (B), the bioconjugate in the presence of the analyte (mycolic acid, 0.5mg/ml) (C), and (D) is the merged comparison of the three spectra.

Figure 5A shows the AuNPs FTIR spectrum with bands at 3318 cm^{-1}, 1637 cm^{-1} and a not so prominent band at 2353 cm^{-1} similar to figure 4A explained above. The introduction of mycolic acid analyte resulted in additional peaks at 2920 cm^{-1} representing asymmetric stretching of CH_2 in fatty acids, and 2850 cm^{-1} representing symmetric stretching of CH_2 in fatty acids [23]. These results are also consistent with other publications. On Figure 4D and 5D it is clear that the introduction of the analyte did not only introduce new peaks but also resulted in a shift in wavenumbers and an increase in transmission intensity which is very significant for diagnostic purposes.

4. CONCLUSION

In conclusion, anti-TB antibodies were successfully conjugated to AuNPs using two different conjugation strategies namely covalent conjugation using NHS, EDC and PEG, and physical conjugation by electrostatic attraction. Both methods produced similar results on UV-vis spectroscopy and FTIR spectroscopy techniques. Mycolic acid TB antigens successfully reacted with anti-TB antibodies for diagnostic purposes and concentration differences of the analyte were determined using both detection techniques. Concentration differences of the analyte play a significant role in determination of detection limit of the analyte. These conjugation strategies will play a crucial role in improvement of the sensitivity of our custom-built optical systems such as the surface plasmon resonance (SPR) system, the DNA hybridization biosensor and the immunosensor. Subsequent studies will include studies of the binding affinity and

Downloaded From: https://www.spiedigitallibrary.org/conference-proceedings-of-spie on 11 May 2021
Terms of Use: https://www.spiedigitallibrary.org/terms-of-use

orientation of the anti-TB antibodies to AuNPs using both conjugation strategies, and also studies of the amount of antibodies bound to the surface of the AuNPs which determines the quantity of analytes binding to the antibodies significant for diagnostic detection limit assays of the analyte.

5. REFERENCES

[1] Sun, W., Yuan, S., Huang, H., Liu, N., & Tan, Y. (2017). A label-free biosensor based on localized surface plasmon resonance for diagnosis of tuberculosis. *Journal of Microbiological Methods*, *142*(September), 41–45. https://doi.org/10.1016/j.mimet.2017.09.007

[2] Tsai, T., Huang, C., Chen, C., Shen, S., Wang, M., Cheng, C., & Chen, C. (2017). *Diagnosis of Tuberculosis Using Colorimetric Gold Nanoparticles on a Paper-Based Analytical Device*. https://doi.org/10.1021/acssensors.7b00450

[3] Golichenari, B., Nosrati, R., Farokhi-fard, A., Maleki, M. F., Mohammad, S., Hayat, G., Vaziri, F. (2019). Critical Reviews in Biotechnology Electrochemical-based biosensors for detection of Mycobacterium tuberculosis and tuberculosis biomarkers tuberculosis and tuberculosis biomarkers. *Critical Reviews in Biotechnology*, *0*(0), 1–22. https://doi.org/10.1080/07388551.2019.1668348

[4] Chen, H., Liu, F., & Koh, K. (2013). *Sensitive detection of tuberculosis using nanoparticle-enhanced surface plasmon resonance*. 431–436. https://doi.org/10.1007/s00604-013-0943-5

[5] Chang, C., Lin, H., Lai, M., Shieh, T., & Peng, C. (2018). Flexible Localized Surface Plasmon Resonance Sensor with Metal – Insulator – Metal Nanodisks on PDMS Substrate. *Scientific Reports*, (July), 1–8. https://doi.org/10.1038/s41598-018-30180-8

[6] Unser, S., Bruzas, I., He, J., & Sagle, L. (2015). *Localized Surface Plasmon Resonance Biosensing: Current Challenges and Approaches*. 15684–15716. https://doi.org/10.3390/s150715684

[7] Hammond, J. L., Bhalla, N., Rafiee, S. D., & Estrela, P. (2014). *Localized Surface Plasmon Resonance as a Biosensing Platform for Developing Countries*. (July). https://doi.org/10.3390/bios4020172

[8] Samsuri, N. D., Mukhtar, W. M., Rozana, A., Rashid, A., Dasuki, K. A., Rahman, A., & Awangku, H. (2017). *Synthesis methods of gold nanoparticles for Localized Surface Plasmon Resonance (LSPR) sensor applications*. *01002*, 1–5. https://doi.org/10.1051/epjconf/201716201002

[9] Li, Z., Leustean, L., Inci, F., Zheng, M., Demirci, U., & Wang, S. (2019). Plasmonic-based platforms for diagnosis of infectious diseases at the point- of-care. *Biotechnology Advances*, *37*(8), 107440. https://doi.org/10.1016/j.biotechadv.2019.107440

[10] Bonyár, A., Lednický, T., & Hubálek, J. (2016). LSPR nanosensors with highly ordered gold nanoparticles fabricated on nanodimpled aluminium templates. *Procedia Engineering*, *168*, 1160–1163. https://doi.org/10.1016/j.proeng.2016.11.390

[11] Baek, S. H., Song, H. W., Lee, S., Kim, J., Kim, Y. H., Wi, J., Kwak, M. K. (2020). *Gold Nanoparticle-Enhanced and Roll-to-Roll Nanoimprinted LSPR Platform for Detecting Interleukin-10*. *8*(May). https://doi.org/10.3389/fchem.2020.00285

[12] Aamouche, A., & Goormaghtigh, E. (2008). *FTIR-ATR biosensor based on self-assembled phospholipids surface : Haemophilia factor VIII diagnosis*. *22*, 223–234. https://doi.org/10.3233/SPE-2008-0351

[13] Ferreira, I. C. C., Aguiar, M. G., Silva, A. T. F., Santos, L. D., Santos, D. W., Goulart, L. R., Maia, Y. C. P. (2020). *Attenuated Total Reflection-Fourier Transform Infrared (ATR-FTIR) Spectroscopy Analysis of Saliva for Breast Cancer Diagnosis*. *2020*.

[14] Su, K., & Lee, W. (2020). *Fourier Transform Infrared Spectroscopy as a Cancer Screening and Diagnostic Tool : A Review*.

[15] Lewis, P. D., Lewis, K. E., Ghosal, R., Bayliss, S., Lloyd, A. J., Wills, J., Mur, L. A. J. (2010). *Evaluation of FTIR Spectroscopy as a diagnostic tool for lung cancer using sputum*.

[16] Santos, M. C. D., Morais, C. L. M., & Lima, K. M. G. (2020). *ATR-FTIR spectroscopy for virus identification : A powerful alternative*. *9*, 103–118. https://doi.org/10.3233/BSI-200203

[17] Oliveira, J. P., Prado, A. R., Keijok, W. J., Wagnner, P., Antunes, P., Yapuchura, E. R., Guimarães, C. (2019). *Impact of conjugation strategies for targeting of antibodies in gold nanoparticles for ultrasensitive detection of*

Downloaded From: https://www.spiedigitallibrary.org/conference-proceedings-of-spie on 11 May 2021
Terms of Use: https://www.spiedigitallibrary.org/terms-of-use

17 β -estradiol. (September), 1–8. https://doi.org/10.1038/s41598-019-50424-5
[18] Penner, M. H. (2010). *Basic Principles of Spectroscopy*. https://doi.org/10.1007/978-1-4419-1478-1
[19] Schmid, F., & Beer, L. (2001). *Biological Macromolecules : Spectrophotometry Concentrations*. 1–4.
[20] Tomovska, R., Agirre, A., Veloso, A., & Leiza, J. R. (2014). Characterization Techniques for Polymeric Materials. In *Chemistry, Molecular Sciences and Chemical Engineering*. https://doi.org/10.1016/B978-0-12-409547-2.10910-2
[21] Anthis, N. J., & Clore, G. M. (2013). *Sequence-specific determination of protein and peptide concentrations by absorbance at 205 nm*. *22*, 851–858. https://doi.org/10.1002/pro.2253
[22] Mojet, B. L., Ebbesen, S. D., Denmark, I. F., & Lefferts, L. (2010). *ChemInform Abstract : Light at the Interface : The Potential of Attenuated In-situ characterization of heterogeneous catalysts themed issue Guest editor Bert M . Weckhuysen*. (December). https://doi.org/10.1039/c0cs00014k
[23] Corneli, S., Corte, L., Roscini, L., Paolo, A. Di, Colabella, C., Petrucci, L., Mazzone, P. (2019). *Spectroscopic Characterization of Bovine , Avian and Johnin Purified Protein Derivative (PPD) with High-Throughput Fourier Transform InfraRed-Based Method*.

Downloaded From: https://www.spiedigitallibrary.org/conference-proceedings-of-spie on 11 May 2021
Terms of Use: https://www.spiedigitallibrary.org/terms-of-use

PROCEEDINGS OF SPIE

SPIEDigitalLibrary.org/conference-proceedings-of-spie

Optical biosensing of mycobacterium tuberculosis for point-of-care diagnosis

Maphanga, Charles, Manoto, Sello, Ombinda-Lemboumba, Saturnin, Hlekelele, Lerato, Mthunzi-Kufa, Patience

Charles Maphanga, Sello Manoto, Saturnin Ombinda-Lemboumba, Lerato Hlekelele, Patience Mthunzi-Kufa, "Optical biosensing of mycobacterium tuberculosis for point-of-care diagnosis," Proc. SPIE 11251, Label-free Biomedical Imaging and Sensing (LBIS) 2020, 112510R (20 February 2020); doi: 10.1117/12.2545842

SPIE.

Event: SPIE BiOS, 2020, San Francisco, California, United States

Downloaded From: https://www.spiedigitallibrary.org/conference-proceedings-of-spie on 11 May 2021 Terms of Use: https://www.spiedigitallibrary.org/terms-of-use

Optical biosensing of mycobacterium tuberculosis for point-of-care diagnosis

Charles Maphanga [1*], Sello Manoto [1], Saturnin Ombinda-Lemboumba [1], Lerato Hlekelele [3], Patience Mthunzi-Kufa [1,2,4]

[1]Council for Scientific and Industrial Research, National Laser Centre, P O BOX 395, Pretoria, 0001, South Africa

[2]College of Science, Engineering and Technology, Department of Physics, NB Pityana Building, University of South Africa, Science Campus, Florida, 1710, South Africa

[3]Council for Scientific and Industrial research, Material Science and Manufacturing, Meiring Naude Road, Brummeria, Pretoria, 0184

[4]University of KwaZulu-Natal, H Block, Westville Campus, University Road, Westville, Durban, 3209

ABSTRACT

An optical biosensor is a compact analytical device formed by a bio-recognition sensing element integrated to an optical transducer system which translates a signal into a readable outcome that is measured by the detector. The target analyte interacts with an immobile bio-recognition element giving rise to a signal proportionate to the concentration of a measured analyte. Optical biosensors offer great advantages over conventional analytical techniques. Specifically, they can provide multiple capabilities such as user-friendly operation, real-time analysis, rapid response, high sensitivity and specificity, portability, label-free detection and cost-effectiveness. As a result, they possess suitable features critical for point-of-care diagnostics. In this study, a home-build surface plasmon resonance (SPR) optical biosensor device was used to analyse interactions between the bio-recognition sensing element and an analyte on the biosensing layer. The transducer consisted of silica dioxide (SiO_2) substrate layer where a thin layer of gold was deposited. Mycolic acid antigens from *mycobacterium tuberculosis* (bovine strain) were immobilised on the biosensing layer and used as bio-recognition sensing elements to capture tuberculosis (TB) antibodies (analyte). From our findings, it was realised that the mycolic acid successfully captured TB antibodies resulting in a detectable signal which paves a way for the development of the point-of-care device.

Keywords: Optical biosensor, bio-recognition, mycolic acid, *mycobacterium tuberculosis*, point-of-care.

*Corresponding author: CMaphanga@csir.co.za

Label-free Biomedical Imaging and Sensing (LBIS) 2020, edited by Natan T. Shaked, Oliver Hayden, Proc. of SPIE Vol. 11251, 112510R · © 2020 SPIE
CCC code: 1605-7422/20/$21 · doi: 10.1117/12.2545842

Downloaded From: https://www.spiedigitallibrary.org/conference-proceedings-of-spie on 11 May 2021
Terms of Use: https://www.spiedigitallibrary.org/terms-of-use

1. INTRODUCTION

Tuberculosis (TB) is a contagious disease caused by *Mycobacterium tuberculosis* (MTb) [1]. The infection usually lasts throughout life as latent infection in more than 90% of infected individuals and can occur in any organ of the body as extrapulmonary TB, however it is most common in the lungs as pulmonary TB infection [1,2,3]. MTb is an airborne bacillus and can spread through microscopic droplets or particles called droplet nuclei generated when a person with untreated active pulmonary TB coughs, sneezes, talks, or sings [4,5]. People who become infected with TB have approximately 10% risk of developing active TB during the course of their lives with greater risk in the first two years after infection and a much higher risk in HIV/TB co-infected individuals [6]. Active pulmonary TB can cause symptoms such as bad cough that lasts for 3 weeks or longer, chest pain, coughing up bloody sputum, night sweat, loss of appetite, weight loss, weakness or fatigue, chills, and fever [7].

Although TB is a preventable and treatable disease, globally it still remains a cause of more than a million deaths each year [8]. In 2017, TB caused approximately 1.3 million deaths among HIV-negative individuals and an additional 300 000 deaths among HIV-positive individuals. There were also 10 million new reported cases of TB infection worldwide [9]. The estimated incidence of TB infections is high in both Asia and Africa, and the sub-Saharan Africa has the highest estimated TB incidence [10]. The notable high rate of TB in the sub-Saharan Africa is influenced by the high prevalence of HIV infection. More than half of TB cases in most sub-Saharan African countries are in HIV infected individuals [10]. People living with HIV are much more susceptible to contract extrapulmonary TB [11].

Currently, there are numerous methods used for screening and diagnosing TB. Diagnosis is primarily dependent on initial clinical assessment, chest radiography or chest x-ray (CXR), and subsequent laboratory confirmation by various bacteriologic studies. Most common techniques used to diagnose TB include purified protein derivative (PPD) – tuberculin skin test or Mantoux test (screening test), direct microscopy, TB culture and various nucleic acid amplification tests (NAATs) [12]. Most of these have several limitations. The Mantoux test can only be used to diagnose latent TB and has a potential for high number of false positive results caused by, but not limited to previous Bacillus Calmette–Guérin (BCG) vaccination, infection with non-tuberculous mycobacteria, and incorrect interpretation of reaction [12,13,14,15]. Direct microscopy is an acid-fast bacilli (AFB) sputum smear test and its major limitation is low sensitivity and specificity [15,16]. Since MTB is a slow-growing and fastidious bacterium which requires specialised media, the average time to detect growth on culture media is 2 – 6 weeks [12]. Therefore the long turn-around-time (TAT) is a major limitation. The NAAT is a molecular test that can rapidly detect genetic material of MTB from respiratory specimen; however this test cannot be used to monitor treatment response because it detects both viable and non-viable tuberculous mycobacteria, is not cost-effective, and requires specialised infrastructure and highly trained personnel [12].

Therefore, there is a need for a cost-effective, rapid, reliable (high sensitivity and specificity), user-friendly, and robust POC device for diagnosing both pulmonary and extrapulmonary TB. This technique will detect mycobacteria in real-time and is based on surface plasmon resonance (SPR) optical biosensing and a biosensor chip immobilised with mycolic acid to capture TB antibodies. The home-build SPR system monitors or probe changes in the refractive index at the sensing surface containing immobilised bio-recognition element (mycolic acid) and the analyte (TB antibodies). During the interaction on the sensing surface, an optical signal is generated by the change in refractive index between the two binding species and subsequently converted to a readable output displayed on a multimeter. This kind of real-time detection devices using rechargeable batteries will be easy to operate by primary healthcare providers and will also be of great value in resource limited areas with poor healthcare infrastructure.

Downloaded From: https://www.spiedigitallibrary.org/conference-proceedings-of-spie on 11 May 2021
Terms of Use: https://www.spiedigitallibrary.org/terms-of-use

2. MATERIALS AND METHODS

2.1 The SPR setup

The home-build SPR setup (figure 1) used in this study was based on the Kretschmann configuration and consisted of a 640 nm coherent cube laser with an average output power of 60 mW. The incident beam was passed through a neutral density (ND) filter, a half-wave plate and a polarizing beam splitter in order to control the power and also enable selection of the p-polarisation of the laser beam. The Au-coated biosensing layer containing immobilised bio-recognition element and an analyte was illuminated by the collimated p-polarized incident beam through the BK7 equilateral glass prism with the refractive index n = 1.517. The reflected beam was collected using a photodiode and the intensity was read with a multimeter.

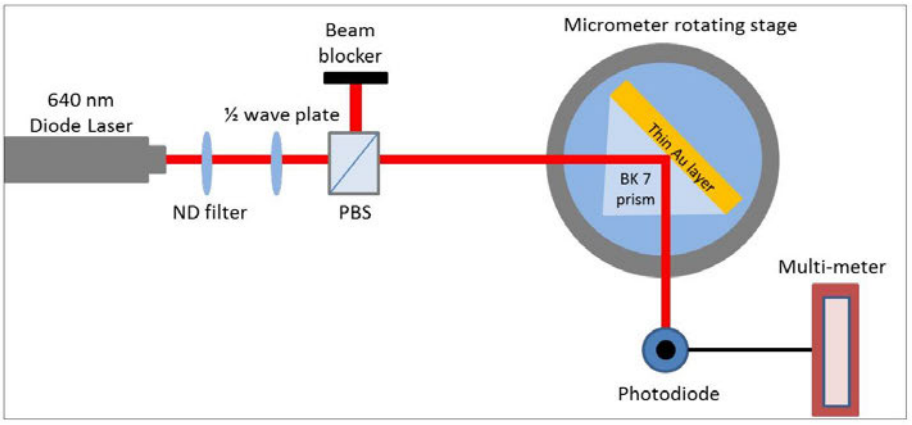

Figure 1: A schematic representation of the home-build Kretschmann configuration surface plasmon resonance (SPR) optical biosensing setup.

2.2 The biosensor chip

2.2.1 Preparation of substrates

Hydrophobic glass slides (SiO_2) were activated with piranha solution (H_2O_2: H_2SO_4, 7:3 v/v) for 45 minutes at 75°C to generate Si – OH bonds. Subsequently the glass slides were washed thoroughly with ultrapure water (resistivity of 18 MΩ) and blow dried with nitrogen gas. After activation procedure, the activated glass slides were immersed in 1% (3-Aminopropyl) triethoxysilane (APTES) (Sigma-Aldrich, A3648) in a vertical coplin jar and incubated at room temperature overnight. Post incubation, the glass slides where washed thoroughly by sonication in absolute ethanol for 5 minutes and followed by sonication in ultrapure water (resistivity of 18 MΩ) for 5 minutes. The clean glass slides blown with nitrogen (N2) gas and further dried at 90°C for 1 hour. Silanized glass slides where used immediately to immobilise stearic acid (STA) (Sigma-Aldrich, S4745) on the glass surface or stored in a vacuum for future use. Gold slides coated by electron beam evaporation were used as biosensor chips. The Au chip was washed with absolute ethanol and blow dried with N_2 gas prior to incubation with 10 mM cysteamine (Cys) (Sigma-Aldrich, M9768) in absolute ethanol for 18 hours to form Au-Cys monolayer, and followed by covalent attachment of stearic acid (Sigma-Aldrich, S4751) using carbodiimide coupling chemistry to form an amide bond.

Downloaded From: https://www.spiedigitallibrary.org/conference-proceedings-of-spie on 11 May 2021
Terms of Use: https://www.spiedigitallibrary.org/terms-of-use

2.2.2 *Mycolic acid monolayer and immobilization of antibodies*

Mycolic acids (MAs) from *mycobacterium tuberculosis* (bovine strain) (Sigma-Aldrich, M4537) TB antigens were immobilised on STA monolayer by incubating the biosensor chip in a solution of 0.5 mg/ml of MAs in hexane over night at room temperature. Post incubation the biosensor chip was rinsed thoroughly with 1x phosphate buffered saline (PBS) (Sigma-Aldrich, D1283) to remove physically adsorbed MA, and subsequently incubated in a solution of 1% bovine serum albumin (BSA) (Roche Diagnostics, 10711454001) blocking agent in 1x PBS for an hour prior to addition of primary antibodies. *Anti-mycobacterium tuberculosis antibody* (Abcam, ab905) prepared in 1x PBS was used as primary antibody and added on the MA monolayer and incubated overnight. For fluorescence imaging, a secondary fluorescently labelled *goat anti-rabbit IgG H&L (Alexa Fluor)* (Abcam, ab150077) was introduced to the primary antibody for 2 hours prior to microscope imaging. For SPR biosensing, the secondary *goat anti-rabbit IgG H&L* antibody (Abcam, ab6702) was conjugated to AuNPs (Sigma-Aldrich, 797707) as detailed below.

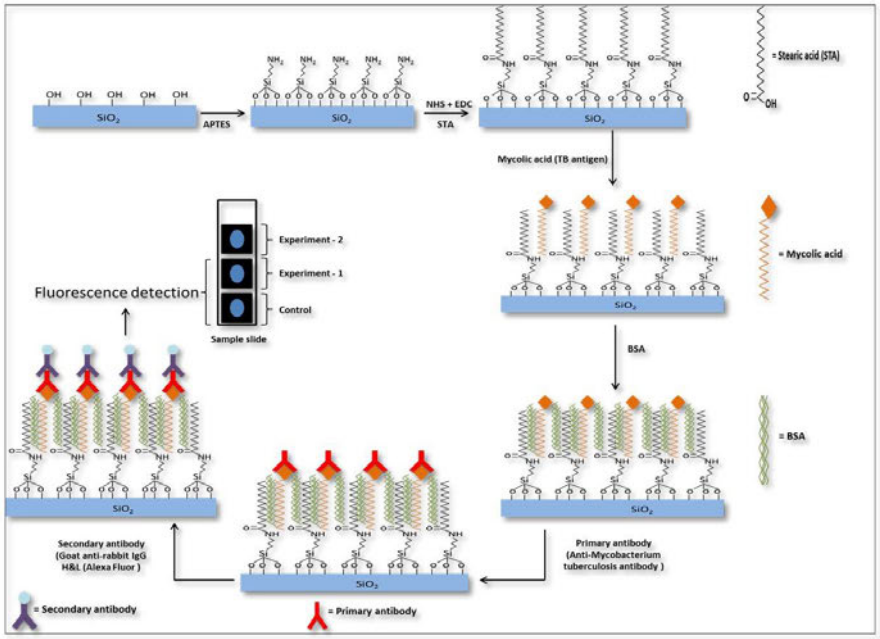

Figure 2: Schematic representation of the biosensor chip developed in-house for TB diagnosis using immobilised mycolic acid antigens to capture TB antibodies. Schematic key steps include the following: (1) treatment of hydrophilic silica glass with APTES (3-Aminopropyl) triethoxysilane) silane, (2) covalent attachment of STA (stearic acid) and forming amide bonds using NHS (N-hydroxysuccinimide) and EDC (1-Ethyl-3-(3-dimethylaminopropyl)-carbodiimide), (3) development of a self-assembled monolayer (SAM) of mycolic acid (MA) through inter-molecular forces existing between STA and MA, (4) addition of 1% bovine serum albumin (BSA) to prevent non-specific binding of molecules, (5) binding of TB primary antibody to MA, (6) binding of secondary antibody to primary antibody, (7) fluorescence detection (experiment-1), (8) optical biosensor detection (experiment-2). For optical detection this steps were performed on Au-coated surface deposited on a glass substrate, and the secondary antibody was functionalised on AuNPs to enhance refractive index and improved sensitivity of the assay.

Downloaded From: https://www.spiedigitallibrary.org/conference-proceedings-of-spie on 11 May 2021
Terms of Use: https://www.spiedigitallibrary.org/terms-of-use

2.2.3 *AuNPs – goat anti-rabbit IgG H&L conjugation*

NHS (N-hydroxysuccinimide) (Sigma-Aldrich, 56480) and EDC (1-Ethyl-3-(3-dimethylaminopropyl)-carbodiimide) (Sigma-Aldrich, E7750) with similar molar ratio were added to a heterobifunctional polyethylene glycol (SH-PEG-COOH) (Sigma-Aldrich, 757845) in ultrapure water and shaken for an hour. The pH of this reaction mixture was adjusted to 7.4 using 10x PBS and the *goat anti-rabbit IgG H&L* secondary antibody was added to the solution. The reaction mixture was incubated for additional 2 hours before filtering with a 50 kDA filter to remove any by-products. The final SH-PEG-IgG conjugated solution was obtained after washing with 1x PBS twice. Then, 12µL of the SH-PEG-IgG conjugate was added to 200µL of AuNPs and incubated for an hour to form AuNPs-IgG conjugate confirmed using NanoDrop.

2.2.4 *UV/VIS absorption spectroscopy*

The absorption spectra of the AuNPs before and after conjugation were immediately recorded using the NanoDrop ND-1000 spectrophotometer. Several UV/VIS spectra were recorded before and after conjugation.

2.3 Fluorescence imaging

For fluorescence imaging, bright-field microscopy was performed using the inverted light microscope (CKX41, Olympus) (excitation wavelength = 495 nm, and emission wavelength = 519 nm). The CCD camera attached to the microscopy enabled image capture to study changes before and after introduction of a fluorescently labelled secondary antibody.

2.4 Scanning Electron Microscopy (SEM) and Energy-dispersive X-ray (EDX) spectroscopy

The SEM was performed to study the surface morphology post immobilization of the AuNPs-IgG conjugate to the biosensor chip containing immobilised primary antibodies. Four sample reactions were prepared. Sample 1 consisted of AuNPs only, sample 2 consisted of conjugated AuNPs-IgG, sample 3 and 4 were dilutions from sample 2 in 1x PBS whereby sample 3 was a 50% dilution of sample 2, and sample 4 was a 50% dilution of sample 3. The EDX spectrographs of sample 1 – 4 were obtained using the SEM device.

3. RESULTS AND DISCUSSION

3.1 UV/VIS absorption spectroscopy

Successful conjugation of AuNPs with the secondary antibody plays a crucial role in enhancing the refractive index on the sensing layer of the biosensor chip resulting in enhanced sensitivity of the detection system. The confirmation of successful conjugation of *goat anti-rabbit IgG H&L* secondary antibody was performed using UV/VIS absorption spectroscopy. Figure 3 depicts spectra of AuNPs before and after conjugation with the antibody.

Downloaded From: https://www.spiedigitallibrary.org/conference-proceedings-of-spie on 11 May 2021
Terms of Use: https://www.spiedigitallibrary.org/terms-of-use

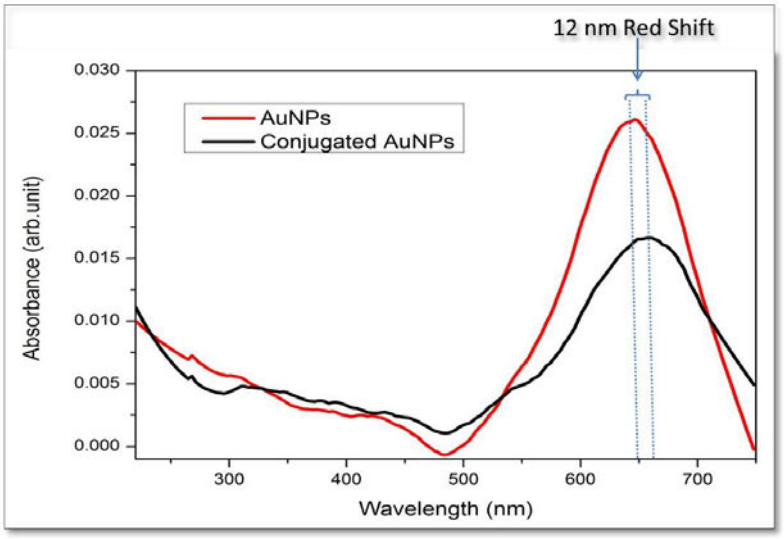

Figure 3: A graphical representation of UV/VIS absorption spectrograph for conjugation of AuNPs to secondary antibody. The red line represents spectra of AuNPs before conjugation, and the black line represents successful AuNPs conjugation with secondary antibody.

The spectra illustrate that there was a 12 nm red shift and a drop in the absorption intensity after the conjugation of AuNPs to the IgG antibody. The AuNPs showed absorption at 650 nm wavelength and the AuNPs-IgG conjugate at 662 nm. AuNPs have unique optical properties that can be easily manipulated compared to bulk gold. These special characteristics provide a plethora of advantages especially in biosensing and diagnostic imaging. One of the major attributes is the interchange of light with electrons on its exterior [17]. The resonance wavelength and bandwidth of the AuNPs is dependent on the shape, particle size, the refractive index of the surrounding media and also the temperature. The shift in the AuNPs-IgG conjugate spectra might be as a result of the changes in the dielectric environment surrounding the AuNPs.

3.2 Fluorescence microscopy

Fluorescence microscopy (figure 4) was performed as proof of concept for the use of MA TB antigens to capture TB antibodies.

Downloaded From: https://www.spiedigitallibrary.org/conference-proceedings-of-spie on 11 May 2021
Terms of Use: https://www.spiedigitallibrary.org/terms-of-use

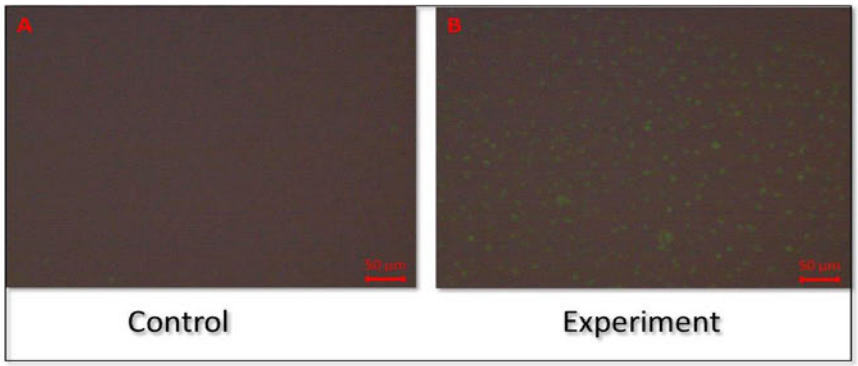

Figure 4: Fluorescence images of mycolic acid TB antigens reaction with a primary TB antibody and a fluorescently labelled secondary antibody. Image A is the control and Image B is the experiment showing green fluorescence.

In image A is a control where primary TB antibody was not added to the biosensor chip and only secondary fluorescently labelled antibody was added. Following a wash step with 1x PBS, the physically bound secondary antibody was washed off resulting in no fluorescence detection. However, image B is the experiment where primary TB antibody successfully attached to the mycolic acid on the surface of the biosensor chip, and subsequent addition of a fluorescently labelled secondary antibody and washing with 1x PBS resulted in fluorescence detection. This is an indication of a successful chemical reaction between mycolic acid and TB antibody.

3.3 Scanning Electron Microscopy (SEM) and Energy-dispersive X-ray (EDX) spectroscopy

i. SEM

Mycolic acids TB antigens were immobilised on the STA monolayer through intermolecular forces existing between the fatty acid long chains of the two structures resulting in a self-assembled monolayer. The illustration is depicted on figure 2.

Downloaded From: https://www.spiedigitallibrary.org/conference-proceedings-of-spie on 11 May 2021
Terms of Use: https://www.spiedigitallibrary.org/terms-of-use

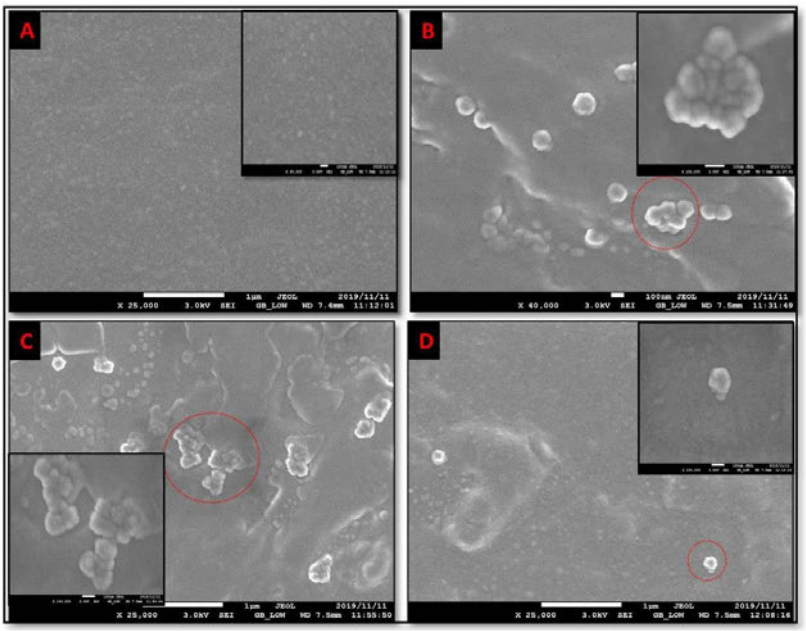

Figure 5: SEM images of AuNPs and AuNPs-IgG conjugate. Image A (sample 1) is the control where AuNPs where added on a biosensor chip without primary Tb antibody. After washing with 1x PBS the physically bound AuNPs where removed from the surface since they had no complementary binding species. Image B (sample 2) is a picture of successfully attached AuNPs-IgG conjugate. Sample 3 (image C) and 4 (Image D) are dilutions from sample 2 whereby sample 3 is a 50% dilution of sample 2, and sample 4 is a 50% dilution of sample 3.

Briefly, addition of the primary antibody resulted in a reaction with the MA, and subsequent attachment of the AuNPs-IgG secondary antibody depicted on figure 5. This is shown by the SEM images of non-uniform distribution of AuNPs between samples 2 – 4 with occasional aggregation. No AuNPs were visualised in sample 1 due to the lack primary antibody in the sample to react with the AuNPs-IgG. The morphology of the AuNPs seen on the SEM images shows the presence of spike nanoantenna-type shapes which is a typical feature of the Nano-Urchins AuNPs used in this study. Nano-Urchins enhance the plasmonic resonance effect, and thus improve the optical limiting effect.

ii. EDX

EDX with chromium (Cr) coating was used to qualitatively determine the elemental compositions of the AuNPs and the conjugated AuNPs-IgG samples (figure 6 and 7). The EDX spectra of the four samples showed all the expected elemental compositions. All samples showed Cr, C, O, Na, Al, Si, Cl, K, Ti with an exception of sample 2 that had quantifiable value for Au. Sample 3 and 4 which are dilutions of sample 2 contained AuNPs on SEM however the amounts could not be quantified.

Downloaded From: https://www.spiedigitallibrary.org/conference-proceedings-of-spie on 11 May 2021
Terms of Use: https://www.spiedigitallibrary.org/terms-of-use

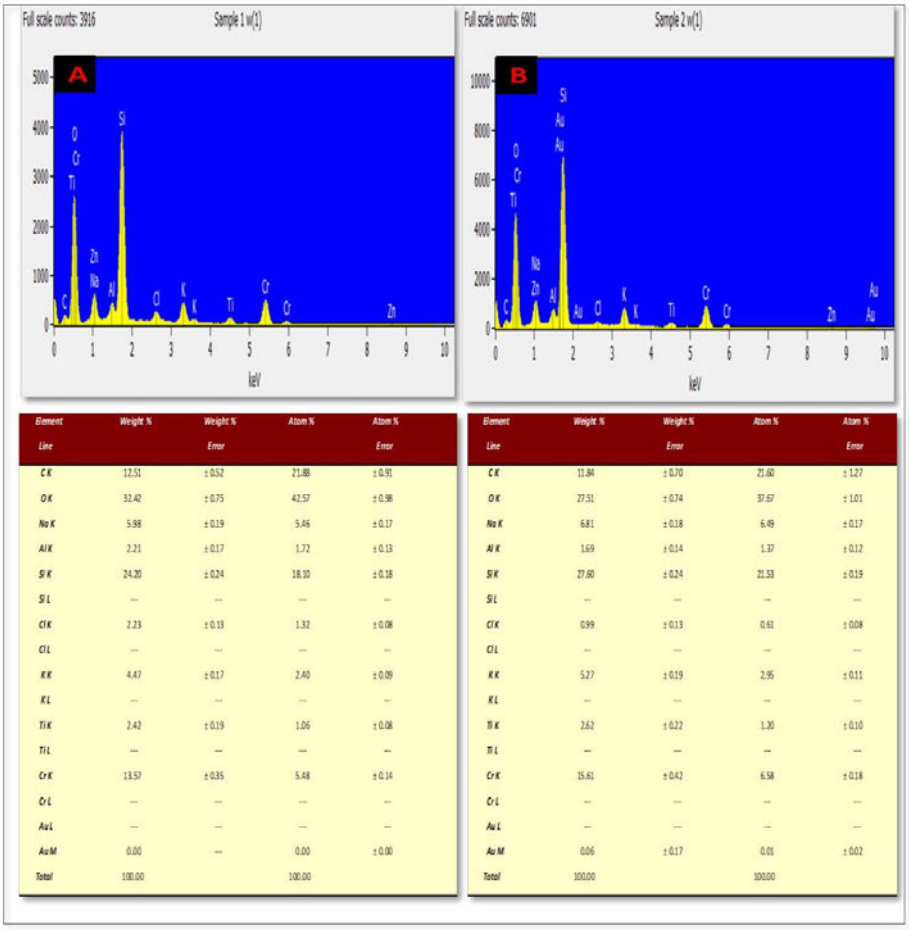

Element Line	Weight %	Weight % Error	Atom %	Atom % Error
C K	12.51	± 0.52	21.88	± 0.91
O K	32.42	± 0.75	42.57	± 0.98
Na K	5.98	± 0.19	5.46	± 0.17
Al K	2.21	± 0.17	1.72	± 0.13
Si K	24.20	± 0.24	18.10	± 0.18
Si L	---	---	---	---
Cl K	2.23	± 0.13	1.32	± 0.08
Cl L	---	---	---	---
K K	4.47	± 0.17	2.40	± 0.09
K L	---	---	---	---
Ti K	2.42	± 0.19	1.06	± 0.08
Ti L	---	---	---	---
Cr K	13.57	± 0.35	5.48	± 0.14
Cr L	---	---	---	---
Au L	---	---	---	---
Au M	0.00	---	0.00	± 0.00
Total	100.00		100.00	

Element Line	Weight %	Weight % Error	Atom %	Atom % Error
C K	11.84	± 0.70	21.60	± 1.27
O K	27.51	± 0.74	37.67	± 1.01
Na K	6.81	± 0.18	6.49	± 0.17
Al K	1.69	± 0.14	1.37	± 0.12
Si K	27.60	± 0.24	21.53	± 0.19
Si L	---	---	---	---
Cl K	0.99	± 0.13	0.61	± 0.08
Cl L	---	---	---	---
K K	5.27	± 0.19	2.95	± 0.11
K L	---	---	---	---
Ti K	2.62	± 0.22	1.20	± 0.10
Ti L	---	---	---	---
Cr K	15.61	± 0.42	6.58	± 0.18
Cr L	---	---	---	---
Au L	---	---	---	---
Au M	0.06	± 0.17	0.01	± 0.02
Total	100.00		100.00	

Figure 6: EDX spectrographs of sample 1 and 2 as seen on figure 5 above. This assay plays a crucial role in identifying elements contained on the biosensor chip when an analyte interacts with a bio-recognition element, specifically to identify whether the surface contains gold (Au). Image A (sample 1) is a spectrograph of the control with corresponding elements percentage values listed on the table. Au was not detected in sample 1. Image B is a spectrograph of sample 2 (AuNPs-IgG) where Au was detected.

Downloaded From: https://www.spiedigitallibrary.org/conference-proceedings-of-spie on 11 May 2021
Terms of Use: https://www.spiedigitallibrary.org/terms-of-use

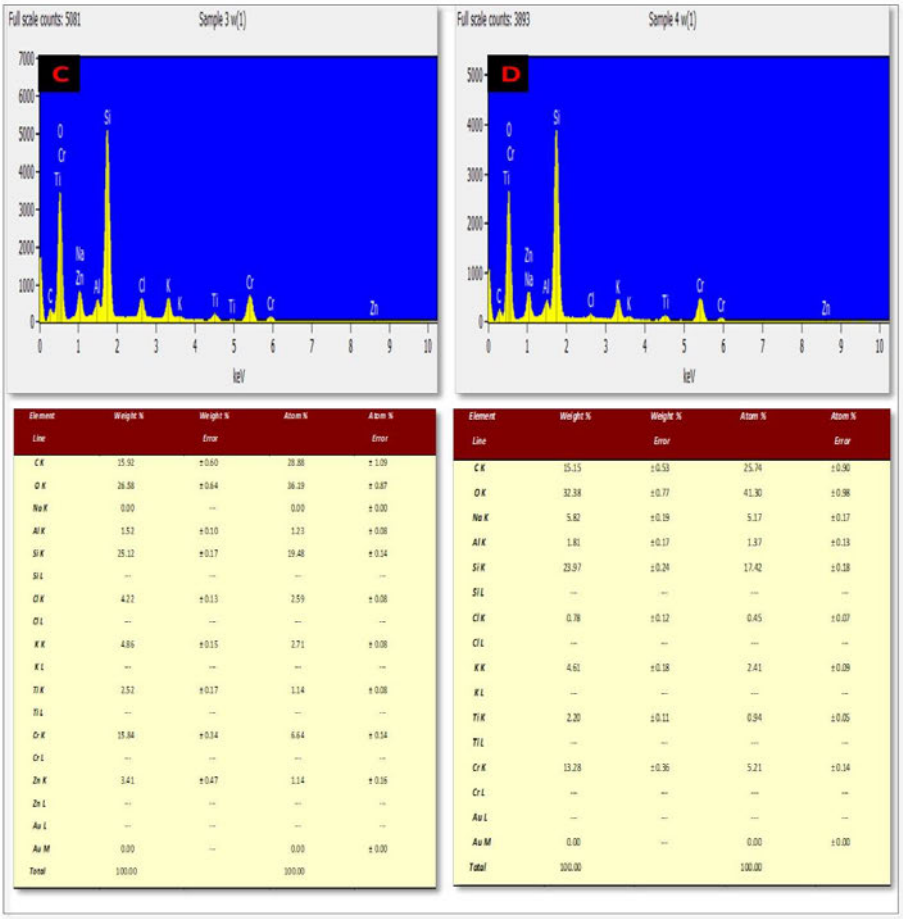

Element Line	Weight %	Weight % Error	Atom %	Atom % Error
C K	15.92	±0.60	28.88	±1.09
O K	26.58	±0.64	36.19	±0.87
Na K	0.00	---	0.00	±0.00
Al K	1.52	±0.10	1.23	±0.08
Si K	25.12	±0.17	19.48	±0.14
Si L	---	---	---	---
Cl K	4.22	±0.13	2.59	±0.08
Cl L	---	---	---	---
K K	4.86	±0.15	2.71	±0.08
K L	---	---	---	---
Ti K	2.52	±0.17	1.14	±0.08
Ti L	---	---	---	---
Cr K	15.84	±0.14	6.64	±0.14
Cr L	---	---	---	---
Zn K	3.41	±0.47	1.14	±0.16
Zn L	---	---	---	---
Au L	---	---	---	---
Au M	0.00	---	0.00	±0.00
Total	100.00		100.00	

Element Line	Weight %	Weight % Error	Atom %	Atom % Error
C K	15.15	±0.53	25.74	±0.90
O K	32.38	±0.77	41.30	±0.98
Na K	5.82	±0.19	5.17	±0.17
Al K	1.81	±0.17	1.37	±0.13
Si K	29.97	±0.24	17.42	±0.18
Si L	---	---	---	---
Cl K	0.78	±0.12	0.45	±0.07
Cl L	---	---	---	---
K K	4.61	±0.18	2.41	±0.09
K L	---	---	---	---
Ti K	2.20	±0.11	0.94	±0.05
Ti L	---	---	---	---
Cr K	13.28	±0.36	5.21	±0.14
Cr L	---	---	---	---
Au L	---	---	---	---
Au M	0.00	---	0.00	±0.00
Total	100.00		100.00	

Figure 7: EDX spectrographs of sample 3 and 4 as depicted on figure 5 above. Image C is a spectrograph of sample 3 and image D is a spectrograph of sample 4. Even though AuNPs where visualised under SEM on figure 5 for both samples, the amount of Au present on the surface was not enough to be quantified when during EDX spectroscopy.

3.4 SPR biosensing

Figure 8 shows the results of the SPR biosensing experiments using the home-build Kretschmann optical setup. Here, five sample reactions where prepared on a biosensor chip coated with primary TB antibody immobilised on a MA monolayer.

Downloaded From: https://www.spiedigitallibrary.org/conference-proceedings-of-spie on 11 May 2021
Terms of Use: https://www.spiedigitallibrary.org/terms-of-use

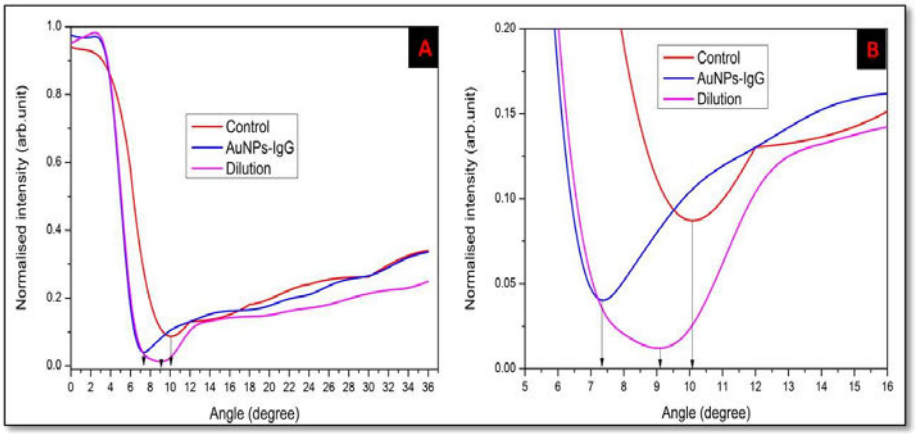

Figure 8: Surface plasmon resonance (SPR) biosensing of a biosensor chip immobilised with mycolic acid (MA) TB antigens used to capture primary TB antibodies. A conjugated secondary antibody (AuNPs-IgG) was allowed to chemically react with the immobilised primary antibody trapped by the MA self-assembled monolayer. SPR angle shift was compare between the control, the conjugated secondary antibody, and the dilution. Image B is an expanded version of image A.

Figure 8 shows SPR results of the control, the conjugated secondary antibody (AuNPs-IgG), and a 1:1 dilution of the conjugated AuNPs-IgG. In the control, 1x PBS was added on the biosensor surface containing immobilised primary TB antibodies. Based on the SPR angle analysis a left shift was observed. The SPR angle for the control, diluted conjugated AuNPs-IgG and the conjugated AuNPs-IgG was 10.1°, 9.1°, and 7.3° respectively. The SPR angle shift between the control and the diluted conjugated AuNPs-IgG was 1° and between the control and the conjugated AuNPs-IgG was 2.8°. The higher SPR angle shift between the control and the conjugated AuNPs-IgG was due to the higher refractive index of the biosensor chip surface resulting from high concentration of AuNPs. A decline in the SPR angle between the control and the diluted conjugated AuNPs-IgG was observed. This was due to a reduction in the concentration of AuNPs in the diluted conjugated AuNPs-IgG, thus reducing the refractive index of the sensing surface.

4. CONCLUSION

In conclusion, the mycolic acid from *mycobacterium tuberculosis* (bovine strain) antigen was successfully immobilised on the biosensor chip with the assistance of stearic acid forming a self-assembled monolayer. This MA monolayer chemically reacted with the *anti-mycobacterium tuberculosis* primary antibody, thus further reacting with the *goat anti-rabbit IgG H&L (Alexa Fluor)* secondary antibody and produced fluorescence. In addition, it also reacted with the conjugated *goat anti-rabbit IgG H&L* and resulted in a red shift and decrease in absorption intensity on UV/VIS spectroscopy. An SPR angle shift was also realised when the primary antibody reacted with the conjugated secondary antibody (AuNPs-IgG). The conjugated secondary antibody was captured by the primary antibody and visible on SEM and EDX spectroscopy. Further optimization of the home-build SPR biosensor device will be implemented for robust optical biosensor diagnosis of TB for future applications in point-of-care diagnosis. Improving the uniformity of the sensing surface is also required.

Downloaded From: https://www.spiedigitallibrary.org/conference-proceedings-of-spie on 11 May 2021
Terms of Use: https://www.spiedigitallibrary.org/terms-of-use

5. REFERENCES

[1] Barberis, I. et al. (2017) 'The history of tuberculosis: from the first historical records to the isolation of Koch's bacillus.', Journal of preventive medicine and hygiene, 58(1), pp. E9–E12. Available at: http://www.ncbi.nlm.nih.gov/pubmed/28515626%0Ahttp://www.pubmedcentral.nih.gov/articlerender.fcgi?artid=PMC5432783.

[2] Frith, J. (2014) 'History of Tuberculosis. Part 1 – Phthisis, consumption and the White Plague', Journal of Military and Veterans' Health, 22(2), pp. 29–35. Available at: http://www.atsjournals.org/doi/abs/10.1164/ajrccm/140.6.1788.

[3] Highsmith, H. Y., Starke, J. R. and Mandalakas, A. M. (2018) 'Tuberculosis', Kendig's Disorders of the Respiratory Tract in Children, pp. 475-497.e5. doi: 10.1016/B978-0-323-44887-1.00029-8.

[4] Hinman, A. R. et al. (1994) 'Guidelines for Preventing the Transmission of Mycobacterium tuberculosis in Health-Care Facilities, 1994 Writer-Editor Visual Information Specialists', 43(Cdc). Available at: https://www.cdc.gov/mmwr/pdf/rr/rr4313.pdf.

[5] Knechel, N. A. (2009) 'Tuberculosis: Pathophysiology, clinical features, and diagnosis', Critical Care Nurse, 29(2), pp. 34–43. doi: 10.4037/ccn2009968.

[6] Ahmad, S. (2011) 'Pathogenesis, immunology, and diagnosis of latent mycobacterium tuberculosis infection', Clinical and Developmental Immunology, 2011. doi: 10.1155/2011/814943.

[7] https://www.cdc.gov/features/tbsymptoms/index.html

[8] Kyu, H. H. et al. (2018) 'Global, regional, and national burden of tuberculosis, 1990-2016: Results from the Global Burden of Diseases, Injuries, and Risk Factors 2016 Study', The Lancet Infectious Diseases, pp. 1329–1349. doi: 10.1016/S1473-3099(18)30625-X.

[9] Global WHO report on tuberculosis 2018.

[10] King, L. and Ahuja, S. (2006) 'TB and HIV Coinfection: Current Trends, Diagnosis and Treatment Update', 11(2), pp. 17–23.

[11] Broderick, A. (1996) 'Tuberculosis and HIV co-infection', AIDSlink, (38), p. 1,3. Available at: http://www.ncbi.nlm.nih.gov/pubmed/12290909.

[12] Nachiappan, A. C. et al. (2017) 'Pulmonary Tuberculosis: Role of Radiology in Diagnosis and Management', RadioGraphics, 37(1), pp. 52–72. doi: 10.1148/rg.2017160032.

[13] Centers for Disease Control and Prevention (2011) 'How is the TST Read? How Are TST Reactions Interpreted? Classification of the Tuberculin Skin Test Reaction', p. 2. Available at: https://www.cdc.gov/tb/publications/factsheets/testing/skintesting.pdf.

[14] Nayak, S. and Acharjya, B. (2012) 'Mantoux test and its interpretation.', Indian journal of dermatology, 57(1), pp. 3–8. doi: 10.4103/0019-5154.92666.

[15] Center for Disease Control and Prevention (2013) 'Mantoux tuberculin skin test Facilitator Guide', (November), pp. 2–30. Available at: https://www.cdc.gov/tb/education/mantoux/pdf/mantoux.pdf.

[16] Department of Heath Republic of South Africa (2014) South Africa TB Guidelines.

[17] Shafiqa, A. R., Abdul Aziz, A. and Mehrdel, B. (2018) 'Nanoparticle Optical Properties: Size Dependence of a Single Gold Spherical Nanoparticle', *Journal of Physics: Conference Series*, 1083(1). doi: 10.1088/1742-6596/1083/1/012040.

Downloaded From: https://www.spiedigitallibrary.org/conference-proceedings-of-spie on 11 May 2021
Terms of Use: https://www.spiedigitallibrary.org/terms-of-use

7. REFERENCES

[1] I. Barberis, N.L. Bragazzi, L. Galluzzo, M. Martini, The history of tuberculosis: from the first historical records to the isolation of Koch's bacillus., J. Prev. Med. Hyg. 58 (2017) E9–E12. http://www.ncbi.nlm.nih.gov/pubmed/28515626%0Ahttp://www.pubmedcentral.nih.gov/articlerender.fcgi?artid=PMC5432783.

[2] W. Sun, S. Yuan, H. Huang, N. Liu, Y. Tan, A label-free biosensor based on localized surface plasmon resonance for diagnosis of tuberculosis, J. Microbiol. Methods. 142 (2017) 41–45. https://doi.org/10.1016/j.mimet.2017.09.007.

[3] A.R. Hinman, M. Director, D.M. James Hughes, H. Linda Rosenstock, E.B. Program Office Stephen Thacker, D.A. Richard Goodman, M. Editor, R.J. Wilson, P.C. Bourque Sandra L Ford Morie M Higgins Peter M Jenkins, Guidelines for Preventing the Transmission of Mycobacterium tuberculosis in Health-Care Facilities, 1994 Writer-Editor Visual Information Specialists, 43 (1994). https://www.cdc.gov/mmwr/pdf/rr/rr4313.pdf.

[4] N.A. Knechel, Tuberculosis: Pathophysiology, clinical features, and diagnosis, Crit. Care Nurse. 29 (2009) 34–43. https://doi.org/10.4037/ccn2009968.

[5] S. Ahmad, Pathogenesis, immunology, and diagnosis of latent mycobacterium tuberculosis infection, Clin. Dev. Immunol. 2011 (2011). https://doi.org/10.1155/2011/814943.

[6] T. Tsai, C. Huang, C. Chen, S. Shen, M. Wang, C. Cheng, C. Chen, Diagnosis of Tuberculosis Using Colorimetric Gold Nanoparticles on a Paper-Based Analytical Device, (2017). https://doi.org/10.1021/acssensors.7b00450.

[7] J. Frith, History of Tuberculosis. Part 1 – Phthisis, consumption and the White Plague, J. Mil. Veterans. Health. 22 (2014) 29–35.

http://www.atsjournals.org/doi/abs/10.1164/ajrccm/140.6.1788.

[8] H.Y. Highsmith, J.R. Starke, A.M. Mandalakas, Tuberculosis, Kendig's Disord. Respir. Tract Child. (2018) 475-497.e5. https://doi.org/10.1016/B978-0-323-44887-1.00029-8.

[9] R. Bansal, D. Sharma, R. Singh, Tuberculosis and its Treatment: An Overview, Mini-Reviews Med. Chem. 18 (2016) 58–71. https://doi.org/10.2174/1389557516666160823160010.

[10] J. Minion, E. Leung, E. Talbot, K. Dheda, M. Pai, D. Menzies, Diagnosing tuberculosis with urine lipoarabinomannan: Systematic review and meta-analysis, Eur. Respir. J. 38 (2011) 1398–1405. https://doi.org/10.1183/09031936.00025711.

[11] E.W. Chang, A.L. Page, M. Bonnet, Light-emitting diode fluorescence microscopy for tuberculosis diagnosis: A meta-analysis, Eur. Respir. J. 47 (2016) 929–937. https://doi.org/10.1183/13993003.00978-2015.

[12] L. King, S. Ahuja, TB and HIV Coinfection: Current Trends, Diagnosis and Treatment Update, 11 (2006) 17–23.

[13] B. Acharya, A. Acharya, S. Gautam, S.P. Ghimire, G. Mishra, N. Parajuli, B. Sapkota, Advances in diagnosis of Tuberculosis: an update into molecular diagnosis of Mycobacterium tuberculosis, Mol. Biol. Rep. 47 (2020) 4065–4075. https://doi.org/10.1007/s11033-020-05413-7.

[14] M. Pai, M.P. Nicol, C.C. Boehme, Tuberculosis Diagnostics: State of the Art and Future Directions, Microbiol. Spectr. 4 (2016). https://doi.org/10.1128/microbiolspec.tbtb2-0019-2016.

[15] S. Oommen, N. Banaji, Laboratory diagnosis of tuberculosis: Advances in technology and drug susceptibility testing, Indian J. Med. Microbiol. 35 (2017) 323–331. https://doi.org/10.4103/ijmm.IJMM_16_204.

[16] Z. Li, L. Leustean, F. Inci, M. Zheng, U. Demirci, S. Wang, Plasmonic-based platforms

for diagnosis of infectious diseases at the point- of-care, Biotechnol. Adv. 37 (2019) 107440. https://doi.org/10.1016/j.biotechadv.2019.107440.

[17] J.L. Hammond, N. Bhalla, S.D. Rafiee, P. Estrela, Localized surface plasmon resonance as a biosensing platform for developing countries, Biosensors. 4 (2014) 172–188. https://doi.org/10.3390/bios4020172.

[18] S.H. Baek, H.W. Song, S. Lee, J.E. Kim, Y.H. Kim, J.S. Wi, J.G. Ok, J.S. Park, S. Hong, M.K. Kwak, H.J. Lee, S.W. Nam, Gold Nanoparticle-Enhanced and Roll-to-Roll Nanoimprinted LSPR Platform for Detecting Interleukin-10, Front. Chem. 8 (2020). https://doi.org/10.3389/fchem.2020.00285.

[19] S.M. Shamah, B.T. Cunningham, Label-free cell-based assays using photonic crystal optical biosensors, Analyst. 136 (2011) 1090–1102. https://doi.org/10.1039/c0an00899k.

[20] D. Threm, Y. Nazirizadeh, M. Gerken, Photonic crystal biosensors towards on-chip integration, J. Biophotonics. 5 (2012) 601–616. https://doi.org/10.1002/jbio.201200039.

[21] S. Romano, A. Lamberti, M. Masullo, E. Penzo, S. Cabrini, I. Rendina, V. Mocella, Optical biosensors based on photonic crystals supporting bound states in the continuum, Materials (Basel). 11 (2018) 1–11. https://doi.org/10.3390/ma11040526.

[22] J. Divya, S. Selvendran, A. Sivanantha Raja, Photonic crystal-based optical biosensor: A brief investigation, Laser Phys. 28 (2018). https://doi.org/10.1088/1555-6611/aab7d2.

[23] B.T. Cunningham, M. Zhang, Y. Zhuo, L. Kwon, C. Race, Recent Advances in Biosensing with Photonic Crystal Surfaces: A Review, IEEE Sens. J. 16 (2016) 3349–3366. https://doi.org/10.1109/JSEN.2015.2429738.

[24] World Health Organisation, WHO Global Tuberculosis Report, 2022, 2022.

[25] J.K. Sia, J. Rengarajan, Immunology of mycobacterium tuberculosis infections, Gram-Positive Pathog. (2019) 1056–1086. https://doi.org/10.1128/9781683670131.ch64.

[26] C.M. Gill, L. Dolan, L.M. Piggott, A.M. McLaughlin, New developments in tuberculosis diagnosis and treatment, Breathe. 18 (2022) 1–15. https://doi.org/10.1183/20734735.0149-2021.

[27] (WHO) World Health Organization, Global TB Report, 2023.

[28] WHO, Tuberculosis in the WHO African Region: 2023 progress update, Tuberc. WHO African Reg. 2023 Prog. Updat. (2023).

[29] A. Natarajan, P.M. Beena, A. V. Devnikar, S. Mali, A systemic review on tuberculosis, Indian J. Tuberc. 67 (2020) 295–311. https://doi.org/10.1016/j.ijtb.2020.02.005.

[30] S. Gagneux, Ecology and evolution of Mycobacterium tuberculosis, Nat. Rev. Microbiol. 16 (2018) 202–213. https://doi.org/10.1038/nrmicro.2018.8.

[31] Barnes D, Historical perspectives on the etiology of tuberculosis, Microbes Infect. 2 (2000) 431–440. https://doi.org/10.1016/S1286-4579(00)00323-3.

[32] A. Sakula, Robert Koch: centnary of the discovery of the tubercle bacillus, 1882, (1982) 246–251.

[33] E. Cambau, M. Drancourt, Steps towards the discovery of *Mycobacterium tuberculosis* by Robert, Clin. Microbiol. Infect. 20 (2014) 196–201.

[34] N.W. Schluger, The pathogenesis of tuberculosis: The first one hundred (and twenty-three) years, Am. J. Respir. Cell Mol. Biol. 32 (2005) 251–256. https://doi.org/10.1165/rcmb.F293.

[35] Rajni, L.S. Meena, Unique characteristic features of mycobacterium tuberculosis in relation to immune system, Am. J. Immunol. 7 (2011) 62–69. https://doi.org/10.3844/ajisp.2011.1.8.

[36] M. Daffé, H. Marrakchi, Unraveling the structure of the mycobacterial envelope, Gram-Positive Pathog. (2019) 1087–1095. https://doi.org/10.1128/9781683670131.ch65.

[37] M. Daffé, A. Quémard, H. Marrakchi, Mycolic Acids: From Chemistry to Biology,

2019. https://doi.org/10.1007/978-3-319-50430-8_18.

[38] A.T. Vincent, S. Nyongesa, I. Morneau, M.B. Reed, E.I. Tocheva, F.J. Veyrier, The mycobacterial cell envelope: A relict from the past or the result of recent evolution?, Front. Microbiol. 9 (2018) 1–9. https://doi.org/10.3389/fmicb.2018.02341.

[39] R.E. Lee, P.J. Brennan, G.S. Besra, Mycobacterium tuberculosis cell envelope, Curr. Top. Microbiol. Immunol. 215 (1996) 1–27. https://doi.org/10.1007/978-3-642-80166-2_1.

[40] R. Kalscheuer, A. Palacios, I. Anso, J. Cifuente, J. Anguita, W.R. Jacobs, M.E. Guerin, R. Prados-Rosales, The Mycobacterium tuberculosis capsule: A cell structure with key implications in pathogenesis, Biochem. J. 476 (2019) 1995–2016. https://doi.org/10.1042/BCJ20190324.

[41] S.H. Lee, Tuberculosis infection and latent tuberculosis, Tuberc. Respir. Dis. (Seoul). 79 (2016) 201–206. https://doi.org/10.4046/trd.2016.79.4.201.

[42] T.A. Yates, P.Y. Khan, G.M. Knight, J.G. Taylor, T.D. McHugh, M. Lipman, R.G. White, T. Cohen, F.G. Cobelens, R. Wood, D.A.J. Moore, I. Abubakar, The transmission of Mycobacterium tuberculosis in high burden settings, Lancet Infect. Dis. 16 (2016) 227–238. https://doi.org/10.1016/S1473-3099(15)00499-5.

[43] G.B. Migliori, C.W.M. Ong, L. Petrone, L. D'ambrosio, R. Centis, D. Goletti, The definition of tuberculosis infection based on the spectrum of tuberculosis disease, Breathe. 17 (2021) 1–12. https://doi.org/10.1183/20734735.0079-2021.

[44] R.D. Turner, G.H. Bothamley, Cough and the transmission of tuberculosis, J. Infect. Dis. 211 (2015) 1367–1372. https://doi.org/10.1093/infdis/jiu625.

[45] M. Keikha, S. Soleimanpour, M. Eslami, B. Yousefi, M. Karbalaei, The mystery of tuberculosis pathogenesis from the perspective of T regulatory cells, Meta Gene. 23 (2020). https://doi.org/10.1016/j.mgene.2019.100632.

[46] H. Getahun, A. Matteelli, R.E. Chaisson, M. Raviglione, Latent Mycobacterium tuberculosis Infection , N. Engl. J. Med. 372 (2015) 2127–2135. https://doi.org/10.1056/nejmra1405427.

[47] C. Bussi, M.G. Gutierrez, Mycobacterium tuberculosis infection of host cells in space and time, FEMS Microbiol. Rev. 43 (2019) 341–361. https://doi.org/10.1093/femsre/fuz006.

[48] U. Mack, G.B. Migliori, M. Sester, H.L. Rieder, S. Ehlers, D. Goletti, A. Bossink, K. Magdorf, C. Holscher, B. Kampmann, S.M. Arend, A. Detjen, G. Bothamley, J.P. Zellweger, H. Milburn, R. Diel, P. Ravn, F. Cobelens, P.J. Cardona, B. Kan, I. Solovic, R. Duarte, D.M. Cirillo, C. Lange, LTBI: Latent tuberculosis infection or lasting immune responses to M. tuberculosis? A TBNET consensus statement, Eur. Respir. J. 33 (2009) 956–973. https://doi.org/10.1183/09031936.00120908.

[49] G. Delogu, M. Sali, G. Fadda, The biology of mycobacterium tuberculosis infection, Mediterr. J. Hematol. Infect. Dis. 5 (2013). https://doi.org/10.4084/mjhid.2013.070.

[50] F. Bozzano, F. Marras, A. De Maria, Immunology of tuberculosis, Mediterr. J. Hematol. Infect. Dis. 6 (2014). https://doi.org/10.4084/MJHID.2014.027.

[51] S. Ehrt, D. Schnappinger, K.Y. Rhee, Metabolic principles of persistence and pathogenicity in Mycobacterium tuberculosis, Nat. Rev. Microbiol. 16 (2018) 496–507. https://doi.org/10.1038/s41579-018-0013-4.

[52] S. Ehrt, D. Schnappinger, K.Y. Rhee, Metabolic principles of persistence and pathogenicity in Mycobacterium tuberculosis, Nat. Rev. Microbiol. 16 (2018) 496–507. https://doi.org/10.1038/s41579-018-0013-4.

[53] S.M.L. and M.D. Rossman, Pulmonary tuberculosis., Am. Soc. Microsc. 26 (2017) 75–78.

[54] I.A.C. and O. Bah-Sow, Pulmonary tuberculosis: diagnosis and treatment, Br. Med. J.

332 (2006) 1194–7. https://doi.org/10.1136/bmj.1.3507.523-b.

[55] Q. He, S. Cai, J. Wu, O. Hu, L. Liang, Z. Chen, Determination of tuberculosis-related volatile organic biomarker methyl nicotinate in vapor using fluorescent assay based on quantum dots and cobalt-containing porphyrin nanosheets, Microchim. Acta. 189 (2022) 1–10. https://doi.org/10.1007/s00604-022-05212-w.

[56] N.M. Zetola, C. Modongo, O. Matsiri, T. Tamuhla, B. Mbongwe, K. Matlhagela, E. Sepako, A. Catini, G. Sirugo, E. Martinelli, R. Paolesse, C. Di Natale, Diagnosis of pulmonary tuberculosis and assessment of treatment response through analyses of volatile compound patterns in exhaled breath samples, J. Infect. 74 (2017) 367–376. https://doi.org/10.1016/j.jinf.2016.12.006.

[57] S. Sethi, R. Nanda, T. Chakraborty, Clinical application of volatile organic compound analysis for detecting infectious diseases, Clin. Microbiol. Rev. 26 (2013) 462–475. https://doi.org/10.1128/CMR.00020-13.

[58] UNSAID, UNAIDS Data 2018, Program. HIV/AIDS. (2018) 1–376. http://www.unaids.org/sites/default/files/media_asset/unaids-data-2018_en.pdf%0Ahttp://www.unaids.org/sites/default/files/media_asset/20170720_Data_book_2017_en.pdf.

[59] I. du Preez, L. Luies, D.T. Loots, The application of metabolomics toward pulmonary tuberculosis research, Tuberculosis. 115 (2019) 126–139. https://doi.org/10.1016/j.tube.2019.03.003.

[60] T. Nawrath, G.F. Mgode, B. Weetjens, S.H.E. Kaufmann, S. Schulz, The volatiles of pathogenic and nonpathogenic mycobacteria and related bacteria, Beilstein J. Org. Chem. 8 (2012) 290–299. https://doi.org/10.3762/bjoc.8.31.

[61] A. Scott-Thomas, M. Epton, S. Chambers, Validating a breath collection and analysis system for the new tuberculosis breath test, J. Breath Res. 7 (2013).

https://doi.org/10.1088/1752-7155/7/3/037108.

[62] J.G. Peter, G. Theron, R. Van Zyl-Smit, A. Haripersad, L. Mottay, S. Kraus, A. Binder, R. Meldau, A. Hardy, K. Dheda, Diagnostic accuracy of a urine lipoarabinomannan strip-test for TB detection in HIV-infected hospitalised patients, Eur. Respir. J. 40 (2012) 1211–1220. https://doi.org/10.1183/09031936.00201711.

[63] L. Nakiyingi, V.M. Moodley, Y.C. Manabe, M.P. Nicol, M. Holshouser, D.T. Armstrong, W. Zemanay, W. Sikhondze, O. Mbabazi, B.A.S. Nonyane, M. Shah, M.L. Joloba, D. Alland, J.J. Ellner, S.E. Dorman, Diagnostic accuracy of a rapid urine lipoarabinomannan test for tuberculosis in HIV-infected adults, J. Acquir. Immune Defic. Syndr. 66 (2014) 270–279. https://doi.org/10.1097/QAI.0000000000000151.

[64] S. Jakhar, R. Sakamuri, D. Vu, P. Dighe, L.R. Stromberg, L. Lilley, N. Hengartner, B.I. Swanson, E. Moreau, S.E. Dorman, H. Mukundan, Interaction of amphiphilic lipoarabinomannan with host carrier lipoproteins in tuberculosis patients: Implications for blood-based diagnostics, PLoS One. 16 (2021) 1–15. https://doi.org/10.1371/journal.pone.0243337.

[65] M. Correia-Neves, G. Fröberg, L. Korshun, S. Viegas, P. Vaz, N. Ramanlal, J. Bruchfeld, B. Hamasur, P. Brennan, G. Källenius, Biomarkers for tuberculosis: The case for lipoarabinomannan, ERJ Open Res. 5 (2019) 1–13. https://doi.org/10.1183/23120541.00115-2018.

[66] T. Tuuminen, Urine as a specimen to diagnose infections in twenty-first century: Focus on analytical accuracy, Front. Immunol. 3 (2012) 1–6. https://doi.org/10.3389/fimmu.2012.00045.

[67] P.K. Drain, E. Losina, S.M. Coleman, J. Giddy, D. Ross, J.N. Katz, K.A. Freedberg, I. V. Bassett, Clinic-based urinary lipoarabinomannan as a biomarker of clinical disease severity and mortality among antiretroviral therapy-naive human immunodeficiency

virus-infected adults in South Africa, Open Forum Infect. Dis. 4 (2017) 1–9. https://doi.org/10.1093/ofid/ofx167.

[68] J. Flores, J.C. Cancino, L. Chavez-Galan, Lipoarabinomannan as a Point-of-Care Assay for Diagnosis of Tuberculosis: How Far Are We to Use It?, Front. Microbiol. 12 (2021). https://doi.org/10.3389/fmicb.2021.638047.

[69] S.D. Lawn, Point-of-care detection of lipoarabinomannan (LAM) in urine for diagnosis of HIV-associated tuberculosis: A state of the art review, BMC Infect. Dis. 12 (2012). https://doi.org/10.1186/1471-2334-12-103.

[70] P. Tucci, G. González-Sapienza, M. Marin, Pathogen-derived biomarkers for active tuberculosis diagnosis, Front. Microbiol. 5 (2014) 1–6. https://doi.org/10.3389/fmicb.2014.00549.

[71] P. De, A.G. Amin, B. Graham, S.L. Martiniano, S.M. Caceres, K.R. Poch, M.C. Jones, M.T. Saavedra, K.C. Malcolm, J.A. Nick, D. Chatterjee, Urine lipoarabinomannan as a marker for low-risk of NTM infection in the CF airway, J. Cyst. Fibros. 19 (2020) 801–807. https://doi.org/10.1016/j.jcf.2020.06.016.

[72] R. Wood, K. Racow, L.G. Bekker, K. Middelkoop, M. Vogt, B.N. Kreiswirth, S.D. Lawn, Lipoarabinomannan in urine during tuberculosis treatment: Association with host and pathogen factors and mycobacteriuria, BMC Infect. Dis. 12 (2012). https://doi.org/10.1186/1471-2334-12-47.

[73] S. Bjerrum, E. Kenu, M. Lartey, M.J. Newman, K.K. Addo, A.B. Andersen, I.S. Johansen, Diagnostic accuracy of the rapid urine lipoarabinomannan test for pulmonary tuberculosis among HIV-infected adults in Ghana-findings from the DETECT HIV-TB study, BMC Infect. Dis. 15 (2015) 1–10. https://doi.org/10.1186/s12879-015-1151-1.

[74] A. Wood, S. Barizuddin, C.M. Darr, C.J. Mathai, A. Ball, K. Minch, A. Somoskovi, B. Hamasur, J.T. Connelly, B. Weigl, A. Andama, A. Cattamanchi, K. Gangopadhyay, S.

Bok, S. Gangopadhyay, Ultrasensitive detection of lipoarabinomannan with plasmonic grating biosensors in clinical samples of HIV negative patients with tuberculosis, PLoS One. 14 (2019) 1–12. https://doi.org/10.1371/journal.pone.0214161.

[75] B. Hamasur, J. Bruchfeld, P. VanHelden, G. Källenius, S. Svenson, A sensitive urinary lipoarabinomannan test for tuberculosis, PLoS One. 10 (2015) 1–11. https://doi.org/10.1371/journal.pone.0123457.

[76] G. Suwanpimolkul, K. Kawkitinarong, W. Manosuthi, J. Sophonphan, S. Gatechompol, P.J. Ohata, S. Ubolyam, T. Iampornsin, P. Katerattanakul, A. Avihingsanon, K. Ruxrungtham, Utility of urine lipoarabinomannan (LAM) in diagnosing tuberculosis and predicting mortality with and without HIV: prospective TB cohort from the Thailand Big City TB Research Network, Int. J. Infect. Dis. 59 (2017) 96–102. https://doi.org/10.1016/j.ijid.2017.04.017.

[77] R.F. Luo, N. Banaei, Molecular approaches and biomarkers for detection of mycobacterium tuberculosis, Clin. Lab. Med. 33 (2013) 553–566. https://doi.org/10.1016/j.cll.2013.03.012.

[78] C. Green, J.F. Huggett, E. Talbot, P. Mwaba, K. Reither, A.I. Zumla, Rapid diagnosis of tuberculosis through the detection of mycobacterial DNA in urine by nucleic acid amplification methods, Lancet Infect. Dis. 9 (2009) 505–511. https://doi.org/10.1016/S1473-3099(09)70149-5.

[79] S.R. Umansky, L.D. Tomei, Transrenal DNA testing: Progress and perspectives, Expert Rev. Mol. Diagn. 6 (2006) 153–163. https://doi.org/10.1586/14737159.6.2.153.

[80] H. Bordelon, P.K. Russ, D.W. Wright, F.R. Haselton, A Magnetic Bead-Based Method for Concentrating DNA from Human Urine for Downstream Detection, PLoS One. 8 (2013). https://doi.org/10.1371/journal.pone.0068369.

[81] V. V. Sinkov, O.B. Ogarkov, A.O. Plotnikov, N.E. Gogoleva, S.N. Zhdanova, V.L.

Pervanchuk, N.L. Belkova, M.E. Koshcheev, T.A. Thomas, J. Liu, E.Y. Zorkaltseva, S.K. Heysell, Metagenomic analysis of mycobacterial transrenal DNA in patients with HIV and tuberculosis coinfection, Infect. Genet. Evol. 77 (2020) 104057. https://doi.org/10.1016/j.meegid.2019.104057.

[82] A. Oreskovic, N.D. Brault, N. Panpradist, J.J. Lai, B.R. Lutz, Analytical Comparison of Methods for Extraction of Short Cell-Free DNA from Urine, J. Mol. Diagnostics. 21 (2019) 1067–1078. https://doi.org/10.1016/j.jmoldx.2019.07.002.

[83] K. Patel, M. Nagel, M. Wesolowski, S. Dees, E. Rivera-Milla, C. Geldmacher, K. Dheda, M. Hoelscher, I. Labugger, Evaluation of a Urine-Based Rapid Molecular Diagnostic Test with Potential to Be Used at Point-of-Care for Pulmonary Tuberculosis: Cape Town Cohort, J. Mol. Diagnostics. 20 (2018) 215–224. https://doi.org/10.1016/j.jmoldx.2017.11.005.

[84] W.R. Magdalena Druszczynska, Sebastian Wawrocki, Rafal Szewczyk, Mycobacteria-derived biomarker for tuberculosis diagnosis, Indian J. Med. Res. 146 (2017) 700–707. https://doi.org/DOI: 10.4103/ijmr.IJMR_1441_16.

[85] Z. Zhang, Y. Pen, R.G. Edyvean, S.A. Banwart, R.M. Dalgliesh, M. Geoghegan, Adhesive and conformational behaviour of mycolic acid monolayers, Biochim. Biophys. Acta - Biomembr. 1798 (2010) 1829–1839. https://doi.org/10.1016/j.bbamem.2010.05.024.

[86] G.K. Schleicher, C. Feldman, Y. Vermaak, J.A. Verschoor, Prevalence of anti-mycolic acid antibodies in patients with pulmonary tuberculosis co-infected with HIV, Clin. Chem. Lab. Med. 40 (2002) 882–887. https://doi.org/10.1515/CCLM.2002.156.

[87] S. Vander Beken, J.R. Al Dulayymi, T. Naessens, G. Koza, M. Maza-Iglesias, R. Rowles, C. Theunissen, J. De Medts, E. Lanckacker, M.S. Baird, J. Grooten, Molecular structure of the Mycobacterium tuberculosis virulence factor, mycolic acid, determines

the elicited inflammatory pattern, Eur. J. Immunol. 41 (2011) 450–460. https://doi.org/10.1002/eji.201040719.

[88] N.S. Mathebula, J. Pillay, G. Toschi, J.A. Verschoor, K.I. Ozoemena, Recognition of anti-mycolic acid antibody at self-assembled mycolic acid antigens on a gold electrode: A potential impedimetric immunosensing platform for active tuberculosis, Chem. Commun. (2009) 3345–3347. https://doi.org/10.1039/b905192a.

[89] P.A. Steck, B.A. Schwartz, M.S. Rosendahl, G.R. Gray, Mycolic acids. A reinvestigation, J. Biol. Chem. 253 (1978) 5625–5629. https://doi.org/10.1016/s0021-9258(17)30312-5.

[90] S.T. Thanyani, V. Roberts, D.G.R. Siko, P. Vrey, J.A. Verschoor, A novel application of affinity biosensor technology to detect antibodies to mycolic acid in tuberculosis patients, J. Immunol. Methods. 332 (2008) 61–72. https://doi.org/10.1016/j.jim.2007.12.009.

[91] R.A. Omar, N. Verma, P.K. Arora, Development of ESAT-6 Based Immunosensor for the Detection of Mycobacterium tuberculosis, Front. Immunol. 12 (2021) 1–12. https://doi.org/10.3389/fimmu.2021.653853.

[92] J. Xie, Z. Mu, B. Yan, J. Wang, J. Zhou, L. Bai, An electrochemical aptasensor for Mycobacterium tuberculosis ESAT-6 antigen detection using bimetallic organic framework, Microchim. Acta. 188 (2021). https://doi.org/10.1007/s00604-021-05058-8.

[93] S. Gupta, V. Kakkar, DARPin based GMR Biosensor for the detection of ESAT-6 Tuberculosis Protein, Tuberculosis. 118 (2019) 101852. https://doi.org/10.1016/j.tube.2019.07.003.

[94] J. Xie, Z. Mu, B. Yan, J. Wang, J. Zhou, L. Bai, An electrochemical aptasensor for Mycobacterium tuberculosis ESAT-6 antigen detection using bimetallic organic framework, Microchim. Acta. 188 (2021). https://doi.org/10.1007/s00604-021-05058-8.

[95] H.S. Clemmensen, N.P.H. Knudsen, R. Billeskov, I. Rosenkrands, G. Jungersen, C. Aagaard, P. Andersen, R. Mortensen, Rescuing ESAT-6 Specific CD4 T Cells From Terminal Differentiation Is Critical for Long-Term Control of Murine Mtb Infection, Front. Immunol. 11 (2020) 1–14. https://doi.org/10.3389/fimmu.2020.585359.

[96] E. Rodríguez-Hernández, L.I. Quintas-Granados, S. Flores-Villalva, J.G. Cantó-Alarcón, F. Milián-Suazo, Application of antigenic biomarkers for Mycobacterium tuberculosis, J. Zhejiang Univ. Sci. B. 21 (2020) 856–870. https://doi.org/10.1631/jzus.B2000325.

[97] S. Mukherjee, S. Perveen, A. Negi, R. Sharma, Evolution of tuberculosis diagnostics: From molecular strategies to nanodiagnostics, Tuberculosis. 140 (2023) 102340. https://doi.org/10.1016/j.tube.2023.102340.

[98] E. Barbier, F. Mougari, M. Lubetzki, M. Rochelet, Rapid electrochemical detection of Mycobacterium tuberculosis in sputum by measuring Ag85 activity with disposable carbon sensors, Talanta. 253 (2023) 123927. https://doi.org/10.1016/j.talanta.2022.123927.

[99] W.R. Druszczynska, Magdalena, Sebastian Wawrocki, Rafal Szewczyk, Mycobacteria-derived biomarkers for tuberculosis diagnosis, Indian J. Med. Res. 146 (2017) 700–707. https://doi.org/10.4103/ijmr.IJMR.

[100] B. Murphy, E. Dempsey, Evaluation of an Ag85B Immunosensor with Potential for Electrochemical Mycobacterium Tuberculosis Diagnostics Evaluation of an Ag85B Immunosensor with Potential for Electrochemical Mycobacterium Tuberculosis Diagnostics, (2020). https://doi.org/10.1149/2162-8777/aba993.

[101] W. Yan, H. Zhou, H. Yan, Characterization of and advanced diagnostic methods for ocular tuberculosis and tuberculosis, Int. J. Ophthalmol. 11 (2020) 1820–1826. https://doi.org/10.18240/ijo.2020.11.21.

[102] E. Kamra, P.K. Mehta, Current updates in diagnosis of male urogenital tuberculosis, Expert Rev. Anti. Infect. Ther. 00 (2021) 1–16. https://doi.org/10.1080/14787210.2021.1902305.

[103] O.V. Uhuo, T.T. Waryo, S.F. Douman, K.C. Januarie, K.C. Nwambaekwe, M.M. Ndipingwi, P. Ekwere, E.I. Iwuoha, Bioanalytical methods encompassing label-free and labeled tuberculosis aptasensors: A review, Anal. Chim. Acta. 1234 (2022) 340326. https://doi.org/10.1016/j.aca.2022.340326.

[104] E. Kamra, P.K. Mehta, Current updates in diagnosis of male urogenital tuberculosis, Expert Rev. Anti. Infect. Ther. 00 (2021) 1–16. https://doi.org/10.1080/14787210.2021.1902305.

[105] T.E. Chiliza, M. Pillay, K. Naidoo, B. Pillay, Immunoscreening of the M . tuberculosis F15 / LAM4 / KZN secretome library against TB patients ′ sera identi fi es unique active- and latent-TB speci fi c biomarkers, Tuberculosis. 115 (2019) 161–170. https://doi.org/10.1016/j.tube.2019.03.005.

[106] T.E. Chiliza, M. Pillay, K. Naidoo, B. Pillay, Immunoscreening of the M . tuberculosis F15 / LAM4 / KZN secretome library against TB patients ′ sera identi fi es unique active- and latent-TB speci fi c biomarkers, Tuberculosis. 115 (2019) 161–170. https://doi.org/10.1016/j.tube.2019.03.005.

[107] H. Mukundan, S. Kumar, D.N. Price, S.M. Ray, Y.J. Lee, S. Min, S. Eum, J. Kubicek-Sutherland, J.M. Resnick, W.K. Grace, A.S. Anderson, S.H. Hwang, S.N. Cho, L.E. Via, C. Barry, R. Sakamuri, B.I. Swanson, Rapid detection of Mycobacterium tuberculosis biomarkers in a sandwich immunoassay format using a waveguide-based optical biosensor, Tuberculosis. 92 (2012) 407–416. https://doi.org/10.1016/j.tube.2012.05.009.

[108] L. Fan, D. Li, S. Zhang, L. Yao, X. Hao, J. Gu, H. Li, J. Niu, Z. Zhang, C. Zhu, Parallel

tests using culture, Xpert MTB/RIF, and SAT-TB in sputum plus bronchial alveolar lavage fluid significantly increase diagnostic performance of smear-negative pulmonary tuberculosis, Front. Microbiol. 9 (2018) 1–7. https://doi.org/10.3389/fmicb.2018.01107.

[109] CDC, Treatment of Tuberculosis Disease, Nat. Genet. 45 (2013) 1183–1189.

[110] E. Maclean, M. Kohli, S.F. Weber, A. Suresh, Advances in Molecular Diagnosis of Tuberculosis, J. Clin. Microbiol. 58 (2020).

[111] A.Y. Vittor, J.M. Garland, R.H. Gilman, Molecular diagnosis of TB in the HIV positive population, Ann. Glob. Heal. 80 (2014) 476–485. https://doi.org/10.1016/j.aogh.2015.01.001.

[112] B.J. Marais, W. Brittle, K. Painczyk, A.C. Hesseling, N. Beyers, E. Wasserman, D. Van Soolingen, R.M. Warren, Use of light-emitting diode fluorescence microscopy to detect acid-fast bacilli in sputum, Clin. Infect. Dis. 47 (2008) 203–207. https://doi.org/10.1086/589248.

[113] A. Ojha, S. Banik, S.K. Melanthota, N. Mazumder, Light emitting diode (LED) based fluorescence microscopy for tuberculosis detection: a review, Lasers Med. Sci. 35 (2020) 1431–1437. https://doi.org/10.1007/s10103-019-02947-6.

[114] A.S. Khan, S. Ali, M.T. Khan, S. Ahmed, Y. Khattak, Abduljabbar, M. Irfan, W. Sajjad, Comparison of GeneXpert MTB/RIF assay and LED-FM microscopy for the diagnosis of extra pulmonary tuberculosis in Khyber Pakhtunkhwa, Pakistan, Brazilian J. Microbiol. 49 (2018) 909–913. https://doi.org/10.1016/j.bjm.2018.02.011.

[115] M. Ashraf, A. Namaji, S. Maheshkumar, S.D. Nadgir, Comparison of Ziehl – Neelsen light microscopy and fluorescent (light-emitting diode) microscopy with solid culture for the diagnosis of tuberculosis with special reference to extrapulmonary cases, (2020) 613–619. https://doi.org/10.4103/ejcdt.ejcdt.

[116] R.M. Anthony, A.H.J. Kolk, S. Kuijper, P.R. Klatser, Light emitting diodes for

auramine O fluorescence microscopic screening of Mycobacterium tuberculosis, Int. J. Tuberc. Lung Dis. 10 (2006) 1060–1062.

[117] WHO, Fluorescent light-emitting diode (LED) microscopy for diagnosis of tuberculosis Policy statement, Who. (2011) 1–12. http://whqlibdoc.who.int/publications/2011/9789241501613_eng.pdf.

[118] J. Minion, H. Sohn, M. Pai, Light-emitting diode technologies for TB diagnosis: What is on the market?, Expert Rev. Med. Devices. 6 (2009) 341–345. https://doi.org/10.1586/erd.09.26.

[119] Z. Khatun, M. Kamal, C.K. Roy, T. Sultana, M.Q. Rahman, M.B.A.S. Azad, A.N.N. Ahmed, Usefulness of light emitting diode (LED) fluorescent microscopy as a tool for rapid and effective method for the diagnosis of pulmonary tuberculosis, Bangladesh Med. Res. Counc. Bull. 37 (2011) 7–10. https://doi.org/10.3329/bmrcb.v37i1.7792.

[120] M. Bhalla, Z. Sidiq, P.P. Sharma, R. Singhal, V.P. Myneedu, R. Sarin, Performance of light-emitting diode fluorescence microscope for diagnosis of tuberculosis, Int. J. Mycobacteriology. 2 (2013) 174–178. https://doi.org/10.1016/j.ijmyco.2013.05.001.

[121] S. Shenai, J. Minion, V. Vadwai, T. Tipnis, S. Shetty, A. Salvi, Z. Udwadia, M. Pai, C. Rodrigues, Evaluation of light emitting diode-based fluorescence microscopy for the detection of mycobacteria in a tuberculosis-endemic region, Int. J. Tuberc. Lung Dis. 15 (2011) 483–488. https://doi.org/10.5588/ijtld.10.0229.

[122] A. Whitelaw, J. Peter, H. Sohn, D. Viljoen, G. Theron, M. Badri, V. Davids, M. Pai, K. Dheda, Comparative cost and performance of light-emitting diode microscopy in HIV-tuberculosis-co-infected patients, Eur. Respir. J. 38 (2011) 1393–1397. https://doi.org/10.1183/09031936.00023211.

[123] G.S. and C.M. M. Cruciani, C. Scarparo, M. Malena, O. Bosco, Meta-Analysis of BACTEC MGIT 960 and BACTEC 460 TB, with or without Solid Media, for Detection

of Mycobacteris, J. Clin. Microbiol. 42 (2004) 2321–2325. https://doi.org/10.1128/JCM.42.5.2321.

[124] C. Rodrigues, J. Jani, S. Shenai, P. Thakkar, S. Siddiqi, A. Mehta, Drug susceptibility testing of Mycobacterium tuberculosis against second-line drugs using the BACTEC MGIT 960 System, Int. J. Tuberc. Lung Dis. 12 (2008) 1449–1455.

[125] C. Rodrigues, S. Shenai, M. Sadani, N. Sukhadia, M. Jani, K. Ajbani, A. Sodha, A. Mehta, Evaluation of the bactec MGIT 960 TB system for recovery and identification of mycobacterium tuberculosis complex in a high volume tertiary care centre, Indian J. Med. Microbiol. 27 (2009) 217–221. https://doi.org/10.4103/0255-0857.53203.

[126] S. Rishi, P. Sinha, B. Malhotra, N. Pal, A Comparative Study for the Detection of Mycobacteria By Bactec Mgit 960, Lowenstein Jensen Media and Direct AFB Smear Examination, Indian J. Med. Microbiol. 25 (2007) 383–386. https://doi.org/10.1016/s0255-0857(21)02056-9.

[127] Á. Somoskövi, C. Ködmön, Á. Lantos, Z. Bártfai, L. Tamási, J. Füzy, P. Magyar, Comparison of recoveries of Mycobacterium tuberculosis using the automated BACTEC MGIT 960 system, the BACTEC 460 TB system, and Lowenstein- Jensen medium, J. Clin. Microbiol. 38 (2000) 2395–2397. https://doi.org/10.1128/.38.6.2395-2397.2000.

[128] J.H. Chin, A.K. Musubire, N. Morgan, J. Pellinen, S. Grossman, J.M. Bhatt, V. Wadda, W. Ssengooba, Xpert MTB/RIF Ultra for Detection of Mycobacterium tuberculosis in Cerebrospinal Fluid, J. Clin. Microbiol. 57 (2019) 8–10. https://doi.org/10.1128/JCM.00249-19.

[129] N.C. Bahr, E. Nuwagira, E.E. Evans, F. V. Cresswell, P. V. Bystrom, A. Byamukama, S.C. Bridge, A.S. Bangdiwala, D.B. Meya, C.M. Denkinger, C. Muzoora, D.R. Boulware, D.A. Williams, K. Taseera, D. Nyehangane, M. Ivan, P. Orikiriza, J. Rhein,

K.H. Hullsiek, A. Musubire, K. Pastick, P. Nabeta, J. Mwesigye, R. Rajasingham, Diagnostic accuracy of Xpert MTB/RIF Ultra for tuberculous meningitis in HIV-infected adults: a prospective cohort study, Lancet Infect. Dis. 18 (2018) 68–75. https://doi.org/10.1016/S1473-3099(17)30474-7.

[130] L.S. Rebecca H. Berhanu, Anura David, Pedro da Silva, Kate Shearer, Ian Sanne, Wendy Stevens, Performance of Xpert MTB/RIF, Xpert Ultra, and Abbott RealTime MTB for Diagnosis of Pulmonary Tuberculosis in a High-HIV-Burden Setting, J. Clin. Microbiol. 56 (2018) 1–11.

[131] O. Opota, J. Mazza-Stalder, G. Greub, K. Jaton, The rapid molecular test Xpert MTB/RIF ultra: towards improved tuberculosis diagnosis and rifampicin resistance detection, Clin. Microbiol. Infect. 25 (2019) 1370–1376. https://doi.org/10.1016/j.cmi.2019.03.021.

[132] S.E. Dorman, S.G. Schumacher, D. Alland, P. Nabeta, D.T. Armstrong, B. King, S.L. Hall, S. Chakravorty, D.M. Cirillo, N. Tukvadze, N. Bablishvili, W. Stevens, L. Scott, C. Rodrigues, M.I. Kazi, M. Joloba, L. Nakiyingi, M.P. Nicol, Y. Ghebrekristos, I. Anyango, W. Murithi, R. Dietze, R. Lyrio Peres, A. Skrahina, V. Auchynka, K.K. Chopra, M. Hanif, X. Liu, X. Yuan, C.C. Boehme, J.J. Ellner, C.M. Denkinger, S.E. Dorman, S.G. Schumacher, D. Alland, P. Nabeta, D.T. Armstrong, B. King, S.L. Hall, S. Chakravorty, N. Tukvadze, N. Bablishvili, W. Stevens, L. Scott, C. Rodrigues, M.I. Kazi, M. Joloba, L. Nakiyingi, Y. Ghebrekristos, I. Anyango, W. Murithi, R. Dietze, R.L. Peres, A. Skrahina, V. Auchynka, K.K. Chopra, M. Hanif, X. Liu, X. Yuan, C.C. Boehme, J.J. Ellner, C.M. Denkinger, Y.C. Manabe, D. Hom, R. Aspindzelashvili, A. David, U. Surve, L.H. Kamulegeya, S. Nabweyambo, S. Surtie, N. Hapeela, K.P. Cain, J. Agaya, K.D. McCarthy, P. Marques-Rodrigues, L.G. Schmidt Castellani, P.S. Almeida, P.P.L. de Aguiar, V. Solodovnikova, X. Ruan, L. Liang, G. Zhang, H. Zhu, Y.

Xie, Xpert MTB/RIF Ultra for detection of Mycobacterium tuberculosis and rifampicin resistance: a prospective multicentre diagnostic accuracy study, Lancet Infect. Dis. 18 (2018) 76–84. https://doi.org/10.1016/S1473-3099(17)30691-6.

[133] G. Wang, S. Wang, G. Jiang, X. Yang, M. Huang, F. Huo, Y. Ma, G. Dai, W. Li, X. Chen, H. Huang, Xpert MTB/RIF Ultra improved the diagnosis of paucibacillary tuberculosis: A prospective cohort study, J. Infect. 78 (2019) 311–316. https://doi.org/10.1016/j.jinf.2019.02.010.

[134] World Health Organization, Meeting Report of a Technical Expert Consultation: Non-inferiority analysis of Xpert MTB/RIF Ultra compared to Xpert MTB/RIF, (2017) 10. http://apps.who.int/bookorders.

[135] K. Sharma, M. Sharma, R. Shree, M. Modi, M. Goyal, D. Narang, A. Sharma, V. Lal, N. Sharma, P. Ray, Xpert MTB/RIF ultra for the diagnosis of tuberculous meningitis: A diagnostic accuracy study from India, Tuberculosis. 125 (2020) 101990. https://doi.org/10.1016/j.tube.2020.101990.

[136] S. Cheng, S.H. Pheng, S. Heng, G.B. Marks, A.L. Bañuls, T.E. Mao, A. Kerléguer, Evaluation of Loopamp Assay for the Diagnosis of Pulmonary Tuberculosis in Cambodia, Biomed Res. Int. 2020 (2020). https://doi.org/10.1155/2020/6828043.

[137] G. Sharma, R. Tewari, S.K. Dhatwalia, R. Yadav, D. Behera, S. Sethi, A loop-mediated isothermal amplification assay for the diagnosis of pulmonary tuberculosis, Lett. Appl. Microbiol. 68 (2019) 219–225. https://doi.org/10.1111/lam.13115.

[138] R. Yadav, P. Daroch, P. Gupta, P. Agarwal, A.N. Aggarwal, S. Sethi, Diagnostic accuracy of TB-LAMP assay in patients with pulmonary tuberculosis…a case-control study in northern India, Pulmonology. 28 (2022) 449–453. https://doi.org/10.1016/j.pulmoe.2020.10.007.

[139] C.K. Kim, E.A. Cho, D.M. Shin, S.W. Choi, S.Y. Shin, Comparative evaluation of the

loop-mediated isothermal amplification assay for detecting pulmonary tuberculosis, Ann. Lab. Med. 38 (2018) 119–124. https://doi.org/10.3343/alm.2018.38.2.119.

[140] T.H. Pham, J. Peter, F.C.Q. Mello, T. Parraga, N.T.N. Lan, P. Nabeta, E. Valli, T. Caceres, K. Dheda, S.E. Dorman, D. Hillemann, C.M. Gray, M.D. Perkins, Performance of the TB-LAMP diagnostic assay in reference laboratories: Results from a multicentre study, Int. J. Infect. Dis. 68 (2018) 44–49. https://doi.org/10.1016/j.ijid.2018.01.005.

[141] E.M. Bentaleb, M. Abid, M.D. El Messaoudi, B. Lakssir, E.M. Ressami, S. Amzazi, H. Sefrioui, H. Ait Benhassou, Development and evaluation of an in-house single step loop-mediated isothermal amplification (SS-LAMP) assay for the detection of Mycobacterium tuberculosis complex in sputum samples from Moroccan patients, BMC Infect. Dis. 16 (2016) 1–10. https://doi.org/10.1186/s12879-016-1864-9.

[142] R.K. Garg, Microbiological diagnosis of tuberculous meningitis: Phenotype to genotype, Indian J. Med. Res. 150 (2019) 448–457. https://doi.org/10.4103/ijmr.IJMR.

[143] K. Nagai, N. Horita, M. Yamamoto, T. Tsukahara, H. Nagakura, K. Tashiro, Y. Shibata, H. Watanabe, K. Nakashima, R. Ushio, M. Ikeda, A. Narita, A. Kanai, T. Sato, T. Kaneko, Diagnostic test accuracy of loop-mediated isothermal amplification assay for Mycobacterium tuberculosis: Systematic review and meta-analysis, Sci. Rep. 6 (2016) 3–9. https://doi.org/10.1038/srep39090.

[144] (WHO) World Health Organization, The use of molecular line probe assays for the detection of resistance to isoniazid and rifampicin. Policy update, WHO/HTM/TB/2016.12. World Heal. Organ. Geneva, Switz. (2016) 57. https://www.who.int/publications/i/item/9789241511261.

[145] S.B. Rufai, P. Kumar, A. Singh, S. Prajapati, V. Balooni, S. Singh, Comparison of xpert MTB/RIF with line probe assay for detection of rifampin-monoresistant mycobacterium tuberculosis, J. Clin. Microbiol. 52 (2014) 1846–1852.

https://doi.org/10.1128/JCM.03005-13.

[146] B.K. Singh, S.K. Sharma, R. Sharma, V. Sreenivas, V.P. Myneedu, M. Kohli, D. Bhasin, S. Sarin, Diagnostic utility of a line probe assay for multidrug resistant-TB in smear-negative pulmonary tuberculosis, PLoS One. 12 (2017) 1–9. https://doi.org/10.1371/journal.pone.0182988.

[147] H. Inan, M. Poyraz, F. Inci, M.A. Lifson, M. Baday, B.T. Cunningham, U. Demirci, Photonic crystals: Emerging biosensors and their promise for point-of-care applications, Chem. Soc. Rev. 46 (2017) 366–388. https://doi.org/10.1039/c6cs00206d.

[148] S. Mittal, T. Sharma, M. Tiwari, Surface plasmon resonance based photonic crystal fiber biosensors: A review, Mater. Today Proc. 43 (2021) 3071–3074. https://doi.org/10.1016/j.matpr.2021.01.405.

[149] L.M. Lechuga, Chapter 5 Optical biosensors, Compr. Anal. Chem. 44 (2005) 209–250. https://doi.org/10.1016/S0166-526X(05)44005-2.

[150] Y. Chen, J. Liu, Z. Yang, J.S. Wilkinson, X. Zhou, Optical biosensors based on refractometric sensing schemes: A review, Biosens. Bioelectron. 144 (2019) 111693. https://doi.org/10.1016/j.bios.2019.111693.

[151] S. Akgönüllü, A. Denizli, Recent advances in optical biosensing approaches for biomarkers detection, Biosens. Bioelectron. X. 12 (2022). https://doi.org/10.1016/j.biosx.2022.100269.

[152] D. Gowdhami, V.R. Balaji, M. Murugan, S. Robinson, G. Hegde, Photonic crystal based biosensors: an overview, ISSS J. Micro Smart Syst. 11 (2022) 147–167. https://doi.org/10.1007/s41683-022-00092-x.

[153] G. Pitruzzello, T.F. Krauss, Photonic crystal resonances for sensing and imaging, J. Opt. (United Kingdom). 20 (2018). https://doi.org/10.1088/2040-8986/aac75b.

[154] Y. Zhao, X. Zhao, Z. Gu, Photonic crystals in bioassays, Adv. Funct. Mater. 20 (2010)

2970–2988. https://doi.org/10.1002/adfm.201000098.

[155] X. Fan, I.M. White, S.I. Shopova, H. Zhu, J.D. Suter, Y. Sun, Sensitive optical biosensors for unlabeled targets: A review, Anal. Chim. Acta. 620 (2008) 8–26. https://doi.org/10.1016/j.aca.2008.05.022.

[156] P. Damborský, J. Švitel, J. Katrlík, Optical biosensors, Essays Biochem. 60 (2016) 91–100. https://doi.org/10.1042/EBC20150010.

[157] I. Abdulhalim, M. Zourob, A. Lakhtakia, Overview of Optical Biosensing Techniques, 2008. https://doi.org/10.1002/9780470061565.hbb040.

[158] I.M. Efimov, N.A. Vanyushkin, A.H. Gevorgyan, Defected photonic crystal-based sensor with enhanced performance, (n.d.).

[159] D. Dorfner, T. Zabel, T. Hürlimann, N. Hauke, L. Frandsen, U. Rant, G. Abstreiter, J. Finley, Photonic crystal nanostructures for optical biosensing applications, Biosens. Bioelectron. 24 (2009) 3688–3692. https://doi.org/10.1016/j.bios.2009.05.014.

[160] G. Zanchetta, R. Lanfranco, F. Giavazzi, T. Bellini, M. Buscaglia, Emerging applications of label-free optical biosensors, Nanophotonics. 6 (2017) 627–645. https://doi.org/10.1515/nanoph-2016-0158.

[161] C. Chen, J. Wang, Optical biosensors: An exhaustive and comprehensive review, Analyst. 145 (2020) 1605–1628. https://doi.org/10.1039/c9an01998g.

[162] C. Chang, H. Lin, M. Lai, T. Shieh, C. Peng, Flexible Localized Surface Plasmon Resonance Sensor with Metal – Insulator – Metal Nanodisks on PDMS Substrate, Sci. Rep. (2018) 1–8. https://doi.org/10.1038/s41598-018-30180-8.

[163] S. Unser, I. Bruzas, J. He, L. Sagle, Localized Surface Plasmon Resonance Biosensing: Current Challenges and Approaches, Sensors. 15 (2015) 15684–15716. https://doi.org/10.3390/s150715684.

[164] N.D. Samsuri, W.M. Mukhtar, A. Rozana, A. Rashid, K.A. Dasuki, A. Rahman, H.

Awangku, Synthesis methods of gold nanoparticles for Localized Surface Plasmon Resonance (LSPR) sensor applications, 01002 (2017) 1–5. https://doi.org/10.1051/epjconf/201716201002.

[165] A. Bonyár, T. Lednický, J. Hubálek, LSPR Nanosensors with Highly Ordered Gold Nanoparticles Fabricated on Nanodimpled Aluminium Templates, Procedia Eng. 168 (2016) 1160–1163. https://doi.org/10.1016/j.proeng.2016.11.390.

[166] A. Panda, P. Devi, N. Ayyanar, Investigation of transmission properties in defective one dimensional superconductive photonic crystal for ultralow level bioethanol detection, Optik (Stuttg). 245 (2021) 167733. https://doi.org/10.1016/j.ijleo.2021.167733.

[167] F. Bayat, S.A. Kandjani, H. Tajalli, Designing Real Time Biosensors and Chemical Sensors Based on Defective 1D Photonic Crystals, IEEE PHOTONICS Technol. 6 (2016). https://doi.org/10.1109/LPT.2016.2573852.

[168] N.R. Ramanujam, S.K. Patel, N.M. Reddy, S.A. Taya, D. Vigneswaran, M.S.M. Rajan, One-dimensional ring mirror-defect photonic crystal for detection of mycobacterium tuberculosis bacteria, Opt. - Int. J. Light Electron Opt. 219 (2020) 165097. https://doi.org/10.1016/j.ijleo.2020.165097.

[169] V.N. Konopsky, E. V. Alieva, Photonic crystal surface waves for optical biosensing, 2011 Int. Work. Biophotonics, BIOPHOTONICS 2011. 79 (2011) 4729–4735. https://doi.org/10.1109/IWBP.2011.5954807.

[170] E. Ozbay, I. Bulu, K. Aydin, Physics and applications of photonic crystals, 2 (2004) 87–95. https://doi.org/10.1016/j.photonics.2004.08.001.

[171] B. Suthar, Biosensor Application of One-Dimensional Photonic Crystal for Malaria Diagnosis, Plasmonics. (2020).

[172] D.M. Mattox, Physical vapor deposition (PVD) processes, Met. Finish. 98 (2000) 410–423. https://doi.org/10.1016/S0026-0576(00)80350-5.

[173] S.M. Rossnagel, Thin film deposition with physical vapor deposition and related technologies, J. Vac. Sci. Technol. A Vacuum, Surfaces, Film. 21 (2003) S74–S87. https://doi.org/10.1116/1.1600450.

[174] H. Usui, Preparation of Polymer Thin Films by Physical Vapor Deposition, Funct. Polym. Film. 1 (2011) 287–318. https://doi.org/10.1002/9783527638482.ch9.

[175] I.V. Shishkovsky, P.N. Lebedev, Chemical and physical vapor deposition methods for nanocoatings, Woodhead Publishing Limited, 2011. https://doi.org/10.1533/9780857094902.1.57.

[176] O. Knotek, F. Löffler, G. Krämer, Multicomponent and multilayer physically vapour deposited coatings for cutting tools, Surf. Coatings Technol. 54–55 (1992) 241–248. https://doi.org/10.1016/S0257-8972(09)90057-3.

[177] J.P. Oliveira, A.R. Prado, W.J. Keijok, P. Wagnner, P. Antunes, E.R. Yapuchura, M. Cesar, C. Guimarães, Impact of conjugation strategies for targeting of antibodies in gold nanoparticles for ultrasensitive detection of 17 β -estradiol, Sci. Rep. 9 (2019) 1–8. https://doi.org/10.1038/s41598-019-50424-5.

[178] R.A. Sperling, W.J. Parak, Surface modification, functionalization and bioconjugation of colloidal Inorganic nanoparticles, Philos. Trans. R. Soc. A Math. Phys. Eng. Sci. 368 (2010) 1333–1383. https://doi.org/10.1098/rsta.2009.0273.

[179] R. Sunasee, R. Narain, Covalent and Noncovalent Bioconjugation Strategies, Chem. Bioconjugates Synth. Charact. Biomed. Appl. 9781118359 (2014) 1–75. https://doi.org/10.1002/9781118775882.ch1.

[180] V.B. Borse, A.N. Konwar, R.D. Jayant, P.O. Patil, Perspectives of characterization and bioconjugation of gold nanoparticles and their application in lateral flow immunosensing, Drug Deliv. Transl. Res. 10 (2020) 878–902. https://doi.org/10.1007/s13346-020-00771-y.

[181] V. Biju, Chemical modifications and bioconjugate reactions of nanomaterials for sensing, imaging, drug delivery and therapy, Chem. Soc. Rev. 43 (2014) 744–764. https://doi.org/10.1039/c3cs60273g.

[182] P. Lilienfeld, Optical detection of particle contamination on surfaces: A review, Aerosol Sci. Technol. 5 (1986) 145–165. https://doi.org/10.1080/02786828608959085.

[183] M. Manzano, S. Viezzi, S. Mazerat, R.S. Marks, J. Vidic, Rapid and label-free electrochemical DNA biosensor for detecting hepatitis A virus, Biosens. Bioelectron. 100 (2018) 89–95. https://doi.org/10.1016/j.bios.2017.08.043.

[184] B. Santos Gomes, D.J. Morgan, W. Langbein, P. Borri, F. Masia, Biofunctionalisation of gallium arsenide with neutravidin, J. Colloid Interface Sci. 608 (2022) 2399–2406. https://doi.org/10.1016/j.jcis.2021.10.135.

[185] S. Stassi, V. Cauda, G. Canavese, D. Manfredi, I. Roppolo, P. Martino, Handbook of Nanomaterials Properties, 2014. https://doi.org/10.1007/978-3-642-31107-9.

[186] Y. Zou, H. Chen, Y. Li, X. Yuan, X. Zhao, W. Chen, F. Cao, N. Cai, X. Huang, F. Yang, W. Liu, Synthesis of mesoporous-silica coated multi-branched gold nanoparticles for surface enhanced Raman scattering evaluation of 4-bromomethcathinone, J. Saudi Chem. Soc. 23 (2019) 378–383. https://doi.org/10.1016/j.jscs.2018.11.005.

[187] M. He, B. Cao, X. Gao, B. Liu, J. Yang, Synthesis of multi-branched gold nanostructures and their surface-enhanced Raman scattering properties of 4-aminothiophenol, J. Mater. Res. 34 (2019) 2928–2934. https://doi.org/10.1557/jmr.2018.503.

[188] R. Peltomaa, B. Glahn-Martínez, E. Benito-Peña, M.C. Moreno-Bondi, Optical Biosensors for Label-Free Detection of Small Molecules, Sensors (Basel). 18 (2018). https://doi.org/10.3390/s18124126.

[189] J. Su, A.F.G. Goldberg, B.M. Stoltz, Label-free detection of single nanoparticles and

biological molecules using microtoroid optical resonators, Light Sci. Appl. 5 (2016) 2–7. https://doi.org/10.1038/lsa.2016.1.

[190] H. Maddali, C.E. Miles, J. Kohn, D.M. O'Carroll, Optical Biosensors for Virus Detection: Prospects for SARS-CoV-2/COVID-19, ChemBioChem. 22 (2021) 1176–1189. https://doi.org/10.1002/cbic.202000744.

[191] K. Singh, T. Agarwal, U. Kumar, S. Pal, A. Runthala, T.M. Pan, C.C. Wu, Optical biosensors for diabetes management: Advancing into stimuli-responsive sensing mechanisms, Smart Mater. Med. 4 (2023) 91–101. https://doi.org/10.1016/j.smaim.2022.08.003.

[192] C.L. Baird, D.G. Myszka, Current and emerging commercial optical biosensors, J. Mol. Recognit. 14 (2001) 261–268. https://doi.org/10.1002/jmr.544.

[193] Y.S. Sun, Optical biosensors for label-free detection of Biomolecular interactions, Instrum. Sci. Technol. 42 (2014) 109–127. https://doi.org/10.1080/10739149.2013.843060.

[194] M. Citartan, S.C.B. Gopinath, J. Tominaga, T.H. Tang, Label-free methods of reporting biomolecular interactions by optical biosensors, Analyst. 138 (2013) 3576–3592. https://doi.org/10.1039/c3an36828a.

[195] M.A. Cooper, Optical biosensors in drug discovery, Nat. Rev. Drug Discov. 1 (2002) 515–528. https://doi.org/10.1038/nrd838.

[196] J. Cao, T. Sun, K.T.V. Grattan, Gold nanorod-based localized surface plasmon resonance biosensors: A review, Sensors Actuators, B Chem. 195 (2014) 332–351. https://doi.org/10.1016/j.snb.2014.01.056.

[197] A.J. Haes, R.P. Van Duyne, A unified view of propagating and localized surface plasmon resonance biosensors, Anal. Bioanal. Chem. 379 (2004) 920–930. https://doi.org/10.1007/s00216-004-2708-9.

[198] B. Sepúlveda, P.C. Angelomé, L.M. Lechuga, L.M. Liz-Marzán, LSPR-based nanobiosensors, Nano Today. 4 (2009) 244–251. https://doi.org/10.1016/j.nantod.2009.04.001.

[199] E. Petryayeva, U.J. Krull, Localized surface plasmon resonance: Nanostructures, bioassays and biosensing-A review, Anal. Chim. Acta. 706 (2011) 8–24. https://doi.org/10.1016/j.aca.2011.08.020.

[200] M. Wang, M. Ye, J. Iocozzia, C. Lin, Z. Lin, Plasmon-mediated solar energy conversion via photocatalysis in noble metal/semiconductor composites, Adv. Sci. 3 (2015). https://doi.org/10.1002/advs.201600024.

[201] T.K. Sarkar, M.N. Abdallah, M. Salazar-Palma, W.M. Dyab, Surface Plasmons/Polaritons, Surface Waves, and Zenneck Waves: Clarification of the terms and a description of the concepts and their evolution., IEEE Antennas Propag. Mag. 59 (2017) 77–93. https://doi.org/10.1109/MAP.2017.2686079.

[202] S. Hayashi, T. Okamoto, Plasmonics: Visit the past to know the future, J. Phys. D. Appl. Phys. 45 (2012). https://doi.org/10.1088/0022-3727/45/43/433001.

[203] A.G. Brolo, Plasmonics for future biosensors, Nat. Photonics. 6 (2012) 709–713. https://doi.org/10.1038/nphoton.2012.266.

[204] H.H. Nguyen, J. Park, S. Kang, M. Kim, Surface plasmon resonance: A versatile technique for biosensor applications, Sensors (Switzerland). 15 (2015) 10481–10510. https://doi.org/10.3390/s150510481.

[205] S. Szunerits, R. Boukherroub, Sensing using localised surface plasmon resonance sensors, Chem. Commun. 48 (2012) 8999–9010. https://doi.org/10.1039/c2cc33266c.

[206] E. Hutter, J.H. Fendler, Exploitation of localized surface plasmon resonance, Adv. Mater. 16 (2004) 1685–1706. https://doi.org/10.1002/adma.200400271.

[207] K.M. Mayer, J.H. Hafner, Localized surface plasmon resonance sensors, Chem. Rev.

111 (2011) 3828–3857. https://doi.org/10.1021/cr100313v.

[208] J. Langer, D.J. de Aberasturi, J. Aizpurua, R.A. Alvarez-Puebla, B. Auguié, J.J. Baumberg, G.C. Bazan, S.E.J. Bell, A. Boisen, A.G. Brolo, J. Choo, D. Cialla-May, V. Deckert, L. Fabris, K. Faulds, F. Javier García de Abajo, R. Goodacre, D. Graham, A.J. Haes, C.L. Haynes, C. Huck, T. Itoh, M. Käll, J. Kneipp, N.A. Kotov, H. Kuang, E.C. Le Ru, H.K. Lee, J.F. Li, X.Y. Ling, S.A. Maier, T. Mayerhöfer, M. Moskovits, K. Murakoshi, J.M. Nam, S. Nie, Y. Ozaki, I. Pastoriza-Santos, J. Perez-Juste, J. Popp, A. Pucci, S. Reich, B. Ren, G.C. Schatz, T. Shegai, S. Schlücker, L.L. Tay, K. George Thomas, Z.Q. Tian, R.P. van Duyne, T. Vo-Dinh, Y. Wang, K.A. Willets, C. Xu, H. Xu, Y. Xu, Y.S. Yamamoto, B. Zhao, L.M. Liz-Marzán, Present and future of surface-enhanced Raman scattering, ACS Nano. 14 (2020) 28–117. https://doi.org/10.1021/acsnano.9b04224.

[209] S. Badilescu, M. Packirisamy, Plasmonic biosensors on a chip for point-of-care applications, Electrochem. Soc. Interface. 28 (2019) 65–69. https://doi.org/10.1149/2.F09193IF.

[210] J.N. Anker, W.P. Hall, O. Lyandres, N.C. Shah, J. Zhao, R.P. Van Duyne, Biosensing with plasmonic nanosensors, Nanosci. Technol. A Collect. Rev. from Nat. Journals. 7 (2009) 308–319. https://doi.org/10.1142/9789814287005_0032.

[211] T. Chung, S.Y. Lee, E.Y. Song, H. Chun, B. Lee, Plasmonic nanostructures for nano-scale bio-sensing, Sensors. 11 (2011) 10907–10929. https://doi.org/10.3390/s111110907.

[212] M. Soler, M.C. Estevez, M. Cardenosa-Rubio, A. Astua, L.M. Lechuga, How Nanophotonic Label-Free Biosensors Can Contribute to Rapid and Massive Diagnostics of Respiratory Virus Infections: COVID-19 Case, ACS Sensors. 5 (2020) 2663–2678. https://doi.org/10.1021/acssensors.0c01180.

[213] A. Ahmed, J. V. Rushworth, N.A. Hirst, P.A. Millner, Biosensors for whole-cell bacterial detection, Clin. Microbiol. Rev. 27 (2014) 631–646. https://doi.org/10.1128/CMR.00120-13.

[214] S.H. Khatami, S. Karami, H.R. Siahkouhi, M. Taheri-Anganeh, J. Fathi, M.B. Aghazadeh Ghadim, S. Taghvimi, Z. Shabaninejad, G. Tondro, N. Karami, L. Dolatshah, E. Soltani Fard, A. Movahedpour, M.H. Darvishi, Aptamer-based biosensors for Pseudomonas aeruginosa detection, Mol. Cell. Probes. 66 (2022) 101865. https://doi.org/10.1016/j.mcp.2022.101865.

[215] M. Soler, C.S. Huertas, L.M. Lechuga, Label-free plasmonic biosensors for point-of-care diagnostics: a review, Expert Rev. Mol. Diagn. 19 (2019) 71–81. https://doi.org/10.1080/14737159.2019.1554435.

[216] Y. Wang, J. Zhou, J. Li, Construction of Plasmonic Nano-Biosensor-Based Devices for Point-of-Care Testing, Small Methods. 1 (2017) 1–13. https://doi.org/10.1002/smtd.201700197.

[217] W. Wang, Y. You, S. Gunasekaran, LSPR-based colorimetric biosensing for food quality and safety, Compr. Rev. Food Sci. Food Saf. 20 (2021) 5829–5855. https://doi.org/10.1111/1541-4337.12843.

[218] N. Khansili, G. Rattu, P.M. Krishna, Label-free optical biosensors for food and biological sensor applications, Sensors Actuators, B Chem. 265 (2018) 35–49. https://doi.org/10.1016/j.snb.2018.03.004.

[219] P.S. Parsamehr, M. Zahed, M.A. Tofighy, T. Mohammadi, M. Rezakazemi, Preparation of novel cross-linked graphene oxide membrane for desalination applications using (EDC and NHS)-activated graphene oxide and PEI, Desalination. 468 (2019) 114079. https://doi.org/10.1016/j.desal.2019.114079.

[220] A.R. Shafiqa, A. Abdul Aziz, B. Mehrdel, Nanoparticle Optical Properties: Size

Dependence of a Single Gold Spherical Nanoparticle, J. Phys. Conf. Ser. 1083 (2018). https://doi.org/10.1088/1742-6596/1083/1/012040.

[221] X. Zhang, Plasmon extinguishment by bandedge shift identified as a second-order spectroscopic differentiation, Nanophotonics. 10 (2021) 1329–1335. https://doi.org/10.1515/nanoph-2020-0603.

[222] F. Schmid, L. Beer, Biological Macromolecules : Spectrophotometry Concentrations, (2001) 1–4.

[223] R. Tomovska, A. Agirre, A. Veloso, J.R. Leiza, Characterization Techniques for Polymeric Materials, Elsevier Inc., 2014. https://doi.org/10.1016/B978-0-12-409547-2.10910-2.

[224] S.L. Manoto, A. El-Hussein, R. Malabi, L. Thobakgale, S. Ombinda-Lemboumba, Y.A. Attia, M.A. Kasem, P. Mthunzi-Kufa, Exploring optical spectroscopic techniques and nanomaterials for virus detection, Saudi J. Biol. Sci. 28 (2021) 78–89. https://doi.org/10.1016/j.sjbs.2020.08.034.

[225] S. Link, M.A. El-Sayed, Optical Properties and Ultrafast Dynamics of Metallic Nanocrystals, Annu. Rev. Phys. Chem. 54 (2003) 331–366. https://doi.org/10.1146/annurev.physchem.54.011002.103759.

[226] F. Ruffino, M.G. Grimaldi, Morphological characteristics of Au films deposited on Ti: A combined SEM-AFM study, Coatings. 8 (2018). https://doi.org/10.3390/coatings8040121.

[227] Q. Yu, H. Huang, X. Peng, Z. Ye, Ultrathin free-standing close-packed gold nanoparticle films: Conductivity and Raman scattering enhancement, Nanoscale. 3 (2011) 3868–3875. https://doi.org/10.1039/c1nr10578g.

[228] O.M. Bakr, B.H. Wunsch, F. Stellacci, High-Yield Synthesis of Multi-Branched Urchin-Like Gold Nanoparticles, Chem. Mater. 18 (2016) 3297–3301.

[229] A. Candreva, E. Morrone, M. La Deda, Gold Sea Urchin-Shaped Nanoparticles: Synthesis and Characterization of Energy Transducer Candidates, Plasmonics. 18 (2023) 291–298. https://doi.org/10.1007/s11468-022-01751-3.

[230] J.H. Lee, B.C. Kim, B.K. Oh, J.W. Choi, Highly sensitive electrical detection of HIV-1 virus based on scanning tunneling microscopy, J. Nanosci. Nanotechnol. 15 (2015) 1117–1122. https://doi.org/10.1166/jnn.2015.9336.

[231] A. Aamouche, E. Goormaghtigh, FTIR-ATR biosensor based on self-assembled phospholipids surface : Haemophilia factor VIII diagnosis, Spectroscopy. 22 (2008) 223–234. https://doi.org/10.3233/SPE-2008-0351.

[232] I.C.C. Ferreira, M.G. Aguiar, A.T.F. Silva, L.D. Santos, D.W. Santos, L.R. Goulart, T.G. Ara, R. Sabino-silva, Y.C.P. Maia, Attenuated Total Reflection-Fourier Transform Infrared (ATR-FTIR) Spectroscopy Analysis of Saliva for Breast Cancer Diagnosis, J. Oncol. 2020 (2020) 1–11.

[233] K. Su, W. Lee, Fourier Transform Infrared Spectroscopy as a Cancer Screening and Diagnostic Tool : A Review, MDPI Cancers. 12 (2020) 2–19.

[234] P.D. Lewis, K.E. Lewis, R. Ghosal, S. Bayliss, A.J. Lloyd, J. Wills, R. Godfrey, P. Kloer, L.A.J. Mur, Evaluation of FTIR Spectroscopy as a diagnostic tool for lung cancer using sputum, BioMed Cent. (2010).

[235] M.C.D. Santos, C.L.M. Morais, K.M.G. Lima, ATR-FTIR spectroscopy for virus identification : A powerful alternative, Biomed. Spectrosc. Imaging. 9 (2020) 103–118. https://doi.org/10.3233/BSI-200203.

[236] S. Gurunathan, J.W. Han, J.H. Park, J.H. Kim, A green chemistry approach for synthesizing biocompatible gold nanoparticles, Nanoscale Res. Lett. 9 (2014) 1–11. https://doi.org/10.1186/1556-276X-9-248.

[237] M. Lee, H.S. Gwak, B.D. Park, S.T. Lee, Synthesis of mycolic acid biosurfactants and

their physical and surface-active properties, JAOCS, J. Am. Oil Chem. Soc. 82 (2005) 181–188. https://doi.org/10.1007/s11746-005-5170-8.

[238] N. Hari, V.P. Nair, FTIR spectroscopic analysis of leaf extract in hexane in Jasminum azoricum L., Int. J. Sci. Res. Technol. 4 (2018) 170–172. www.ijsrst.com.

[239] H. Wang, K.Q. Zhang, Photonic crystal structures with tunable structure color as colorimetric sensors, Sensors (Switzerland). 13 (2013) 4192–4213. https://doi.org/10.3390/s130404192.

[240] V.N. Konopsky, T. Karakouz, E. V. Alieva, C. Vicario, S.K. Sekatskii, G. Dietler, Photonic crystal biosensor based on optical surfacewaves, Sensors (Switzerland). 13 (2013) 2566–2578. https://doi.org/10.3390/s130202566.

[241] O. Tokel, F. Inci, U. Demirci, Advances in plasmonic technologies for point of care applications, Chem. Rev. 114 (2014) 5728–5752. https://doi.org/10.1021/cr4000623.

[242] E. Luan, H. Shoman, D.M. Ratner, K.C. Cheung, L. Chrostowski, Silicon photonic biosensors using label-free detection, Sensors (Switzerland). 18 (2018) 1–42. https://doi.org/10.3390/s18103519.

[243] A.L. Washburn, R.C. Bailey, Photonics-on-a-chip: Recent advances in integrated waveguides as enabling detection elements for real-world, lab-on-a-chip biosensing applications, Analyst. 136 (2011) 227–236. https://doi.org/10.1039/c0an00449a.

[244] N.L. Kazanskiy, S.N. Khonina, M.A. Butt, A. Kaźmierczak, R. Piramidowicz, State-of-the-art optical devices for biomedical sensing applications—a review, Electron. 10 (2021) 1–29. https://doi.org/10.3390/electronics10080973.

[245] M.C. Estevez, M. Alvarez, L.M. Lechuga, Integrated optical devices for lab-on-a-chip biosensing applications, Laser Photonics Rev. 6 (2012) 463–487. https://doi.org/10.1002/lpor.201100025.

[246] J. Derbali, F. AbdelMalek, S.S.A. Obayya, H. Bouchriha, R. Letizia, Design of a

compact photonic crystal sensor, Opt. Quantum Electron. 42 (2011) 463–472. https://doi.org/10.1007/s11082-010-9429-4.

[247] Y. Khan, A. Samad, U. Iftikhar, S. Kumar, N. Ullah, J. Sultan, H. Ali, M.L. Haider, Mathematical modeling of photonic crystal based optical filters using machine learning, 2018 Int. Conf. Comput. Electron. Electr. Eng. ICE Cube 2018. (2019) 1–5. https://doi.org/10.1109/ICECUBE.2018.8610986.

[248] V. Chaudhery, S. George, M. Lu, A. Pokhriyal, B.T. Cunningham, Nanostructured surfaces and detection instrumentation for photonic crystal enhanced fluorescence, Sensors (Switzerland). 13 (2013) 5561–5584. https://doi.org/10.3390/s130505561.

[249] L. Sun, H. Lin, K.L. Kohlstedt, G.C. Schatz, C.A. Mirkin, Design principles for photonic crystals based on plasmonic nanoparticle superlattices, Proc. Natl. Acad. Sci. U. S. A. 115 (2018) 7242–7247. https://doi.org/10.1073/pnas.1800106115.

[250] T. Prasad, R. Rengarajan, D.M. Mittleman, V.L. Colvin, Advanced photonic crystal architectures from colloidal self-assembly techniques, Opt. Mater. (Amst). 27 (2005) 1250–1254. https://doi.org/10.1016/j.optmat.2004.11.019.

[251] C. Pacholski, Photonic crystal sensors based on porous silicon, Sensors (Switzerland). 13 (2013) 4694–4713. https://doi.org/10.3390/s130404694.

[252] C. Maphanga, S. Manoto, S. Ombinda-lemboumba, Y. Ismail, Localized surface plasmon resonance biosensing of Mycobacterium tuberculosis biomarker for TB diagnosis, Sens. Bio-Sensing Res. 39 (2023) 100545. https://doi.org/10.1016/j.sbsr.2022.100545.